# MATRIX STRUCTURE FOR INFORMATION-DRIVEN POLARIMETER DESIGN

by

Andrey S. Alenin

---

A Dissertation Submitted to the Faculty of the

COLLEGE OF OPTICAL SCIENCES

In Partial Fulfillment of the Requirements
For the Degree of

DOCTOR OF PHILOSOPHY

In the Graduate College

THE UNIVERSITY OF ARIZONA

2015

THE UNIVERSITY OF ARIZONA
GRADUATE COLLEGE

As members of the Dissertation Committee, we certify that we have read the dissertation prepared by Andrey S. Alenin entitled Matrix Structure for Information-Driven Polarimeter Design and recommend that it be accepted as fulfilling the dissertation requirement for the Degree of Doctor of Philosophy.

_____     Date: March 2, 2015
 Russell Chipman

_____     Date: March 2, 2015
 J. Scott Tyo

_____     Date: March 2, 2015
 Matthew Kupinski

_____     Date: March 2, 2015

_____     Date: March 2, 2015

Final approval and acceptance of this dissertation is contingent upon the candidate's submission of the final copies of the dissertation to the Graduate College.
I hereby certify that I have read this dissertation prepared under my direction and recommend that it be accepted as fulfilling the dissertation requirement.

_____     Date: March 2, 2015
 Dissertation Director: J. Scott Tyo

## STATEMENT BY AUTHOR

This dissertation has been submitted in partial fulfillment of requirements for an advanced degree at the University of Arizona and is deposited in the University Library to be made available to borrowers under rules of the Library.

SIGNED:    Andrey S. Alenin

ACKNOWLEDGEMENTS

I would like to acknowledge my family: my mom for always being there, my dad for in-spiring me to be better, and my siblings for their encouragement. Without them, none of this would have been possible.

I would like to thank Dr. J. Scott Tyo for giving me the opportunity to perform inde-pendent research in his lab, as well as providing guidance throughout my graduate work. I would also like to thank Dr. Russell Chipman and Dr. Matthew Kupinski for agreeing to be on my committee and offering advice on the topics of my dissertation.

I would like to thank all of my colleagues in Advanced Sensing Laboratory (ASL) and College of Optical Sciences (OSC), especially Charles LaCasse and Israel Vaughn, with whom I've spent countless hours discussing topics of physical optics, polarization and methods of reconstruction.

I would also like thank my girlfriend, Geraldine Longo, for her endless support and patience.

Finally, I would like to acknowledge all of my friends, a list that is too long to enumerate and any attempt of which would insult more through exclusion than it would honor those listed.

DEDICATION

*Посвящается моим родителям, Сергею и Рите.*

TABLE OF CONTENTS

TABLE OF CONTENTS – *Continued*

LIST OF FIGURES

LIST OF FIGURES – *Continued*

LIST OF FIGURES – *Continued*

LIST OF FIGURES – *Continued*

LIST OF FIGURES – *Continued*

LIST OF TABLES

LIST OF TABLES – *Continued*

ABSTRACT

Estimating the polarization of light has been shown to have merit in a wide variety of applications between UV and LWIR wavelengths. These tasks include target identification, estimation of atmospheric aerosol properties, biomedical and other applications. In all of these applications, polarization sensing has been shown to assist in discrimination ability; however, due to the nature of many phenomena, it is difficult to add polarization sensing everywhere. The goal of this dissertation is to decrease the associated penalties of using polarimetry, and thereby broaden its applicability to other areas.

First, the class of channeled polarimeter systems is generalized to relate the Fourier domains of applied modulations to the resulting information channels. The quality of reconstruction is maximized by virtue of using linear system manipulations rather than arithmetic derived by hand, while revealing system properties that allow for immediate performance estimation. Besides identifying optimal systems in terms of equally weighted variance (EWV), a way to redistribute the error between all the information channels is presented. The result of this development often leads to superficial changes that can improve signal-to-noise-ration (SNR) by up to a factor of three compared to existing designs in the literature.

Second, the class of partial Mueller maitrx polarimeters (pMMPs) is inspected in regards to their capacity to match the level of discrimination performance achieved by full systems. The concepts of structured decomposition and the reconstructables matrix are developed to provide insight into Mueller subspace coverage of pMMPs, while yielding a pMMP basis that allows the formation of ten classes of pMMP systems. A method for evaluating such systems while considering a multi-objective optimization of noise resilience and space coverage is provided. An example is presented for which the number of measurements was reduced to half.

Third, the novel developments intended for channeled and partial systems are com-

bined to form a previously undiscussed class of channeled partial Mueller matrix polarimeters (c-pMMPs). These systems leverage the gained understanding in manipulating the structure of the measurement to design modulations such that the desired pieces of information are mapped into channels with favorable reconstruction characteristics.

CHAPTER 1

INTRODUCTION

This dissertation pertains to matrix structure of the information reconstruction techniques, which are pivotal to the design of a polarimeter, a device intended for measuring the polarization of light. Estimating the polarization of light has been shown to have merit in a wide variety of applications between UV and LWIR wavelengths (Tyo et al. (2006)). These tasks can be categorized into target identification (Cheng et al. (1994); Tyo et al. (1996); Goudail and Tyo (2011); Hoover and Tyo (2007)), estimation of atmospheric aerosol properties (Diner et al. (2007)), as well as biomedical applications (Jacques et al. (1999); Baldwin (2004); Zhao et al. (2009)). In all of these applications, polarization sensing has been shown to assist in discrimination ability; however, due to the nature of many phenomena, it is difficult to add polarization sensing everywhere. The goal of this dissertation is to decrease the associated penalties of using polarimetry, and thereby broaden its applicability to other areas.

Because current state of the art detectors are incapable of detecting polarization directly, a series of indirect measurements need to be made and then combined to reveal the underlying polarization properties. In the most general sense, polarimeter design involves making a number of choices with regards to selection of those indirect measurements that fit the specifics of the phenomenological nature of the extant scattering events in a particular measurement task. Many designs use a sequentially generated set of testing conditions, which are commonly referred to as modulation. These testing conditions are often modulated in one of three domains: time, space or wavelength (LaCasse et al. (2011a)). Additionally, multiple modulation domains can be used simultaneously to balance the resolution loss across domains. The optimal selection is unlikely to present itself without a careful analysis of the domains that the intended target and its background occupy. As the field of polarimetry expands to include more estimation and discrimination tasks, the need for appropriate selection of both the type of the system, as well as the modulation

domains, becomes critical to constructing a successful system.

With polarization being a rich physical process, it contains many parameters concerning different aspects of the kind of transformations that light goes through. Depending on the task, some of these parameters are essential, while others may prove to be extraneous. This dissertation will discuss how to select measurements such that the relevance of information derived from a measurement is maximized. The concept of creating partial systems is interesting in that it allows one to derive a comparable amount of relevant information, while taking fewer measurements, generally resulting in a simpler system.

## 1.1  Polarized Light

Light is an electromagnetic wave and there are several quantifiable physical properties that describe it. The most immediately useful ones are direction of propagation, field intensity and frequency. In fact, if one only ever had to describe plane-wave radiation, i.e.,

$$\vec{E}(\vec{r}, t) = \Re\left\{\vec{E}_o e^{+i(\vec{k}\cdot\vec{r} - \omega t)}\right\}, \tag{1.1}$$

then one would not need to consider anything else. $\vec{E}_o$ would describe the orientation and magnitude of the electrical field, while $\vec{k}$ and $\omega$ would give the direction of propagation and spectral information, and temporal frequency within the four dimensional universe described by $(\vec{r}, t)$ coordinates, respectively. However, in the great majority of scenarios, there is a plurality of plane-waves interfering together. This interference of electromagnetic fields is what gives rise to the importance of the study of coherence and polarization.

An abundant selection of tasks are successfully analyzed with the limited case of incoherent polarization. A common way to describe said incoherent optical polarization is with a set of Stokes parameters, represented in a form of a vector,

$$\underline{\mathbf{S}} = \begin{bmatrix} s_0 \\ s_1 \\ s_2 \\ s_3 \end{bmatrix} = \frac{\epsilon_o c}{2} \begin{bmatrix} \langle |E_x|^2 + |E_y|^2 \rangle \\ \langle |E_x|^2 - |E_y|^2 \rangle \\ 2\Re\{\langle E_x E_y^* \rangle\} \\ 2\Im\{\langle E_x E_y^* \rangle\} \end{bmatrix} = \begin{bmatrix} I_H + I_V \\ I_H - I_V \\ I_{+45} - I_{-45} \\ I_R - I_L \end{bmatrix}. \tag{1.2}$$

In Equation 1.2, the Stokes vector is represented in the form stemming from the underlying

electric field, as well as a set of intensity difference measurements. For latter, we can understand the four components as: $s_0$ is the total intensity, $s_1$ is the prevalence of horizontally polarized light ($I_H$) over vertically polarized light ($I_V$), $s_2$ is the prevalence of linearly polarized light at $+45°$ ($I_{+45}$) over linearly polarized light at $-45°$ ($I_{-45}$) and $s_3$ is the prevalence of right circularly polarized light ($I_R$) over left circularly polarized light ($I_L$). An additional condition,

$$s_0 \geqslant \sqrt{s_1^2 + s_2^2 + s_3^2}, \tag{1.3}$$

forces the polarization state to lie within the Poincaré sphere, which is depicted in Figure 1.1. Other polarization products derived from the original four are often useful. A normalized set of Stokes parameters,

$$\underline{\bar{\mathbf{S}}} = \begin{bmatrix} \bar{s}_1 \\ \bar{s}_2 \\ \bar{s}_3 \end{bmatrix} = \begin{bmatrix} s_1/s_0 \\ s_2/s_0 \\ s_3/s_0 \end{bmatrix}, \tag{1.4}$$

is useful when the variation of the degree of polarization in space or time differs from the variation of absolute intensity, $s_0$. This is typical for a laser, where the power fluctuations do not necessarily reflect on degree of polarization fluctuations. These normalized parameters can be combined to form Degree of Polarization (DoP),

$$\mathrm{DoP} = \sqrt{\bar{s}_1^2 + \bar{s}_2^2 + \bar{s}_3^2} = \frac{\sqrt{s_1^2 + s_2^2 + s_3^2}}{s_0}, \tag{1.5}$$

Degree of Linear Polarization (DoLP),

$$\mathrm{DoLP} = \sqrt{\bar{s}_1^2 + \bar{s}_2^2} = \frac{\sqrt{s_1^2 + s_2^2}}{s_0}, \tag{1.6}$$

while Degree of Circular Polarization (DoCP) is just $\bar{s}_3$. Another product of interest is angle of linear polarization,

$$\mathrm{AoLP} = \frac{1}{2} \arctan\left(\frac{s_2}{s_1}\right), \tag{1.7}$$

which is often used in tandem with DoLP to convert from the Cartesian set of coordinates to the more natural polar corrdinates, as dictated by the geometry of the Poincaré sphere.
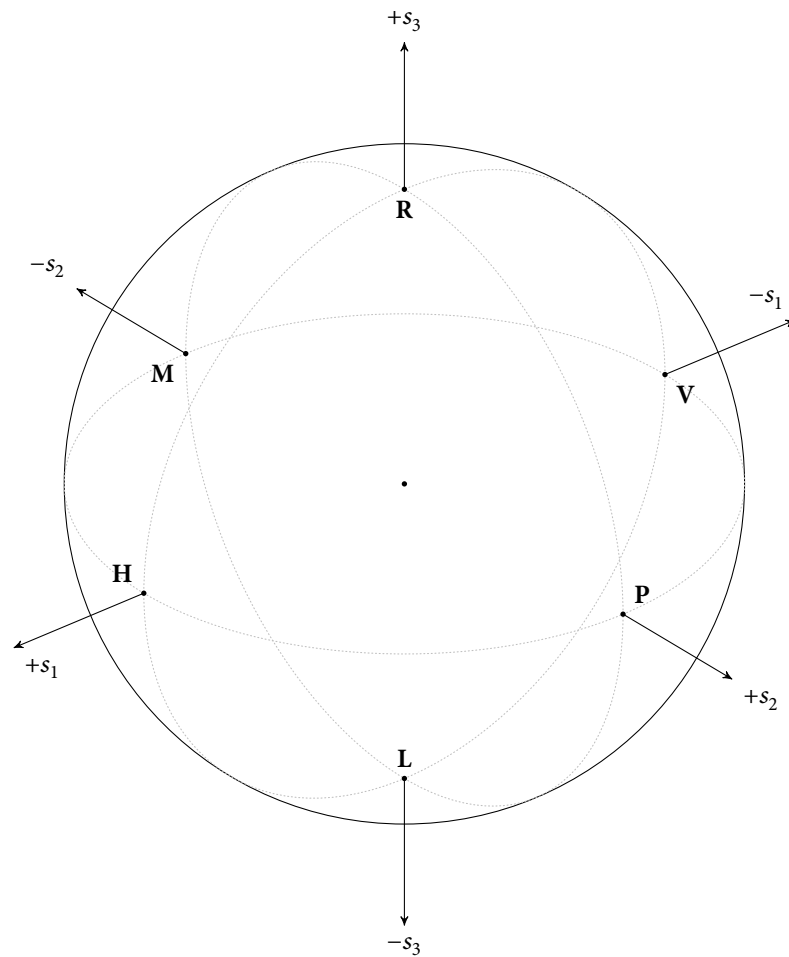
Figure 1.1: Poincaré Sphere. H denotes horizontally polarized light; V denotes vertically polarized light; P denotes +45° light; M denotes −45° light; R denotes right circularly polarized light; L denotes left circularly polarized light.

Passing through a medium or interacting with a surface has the potential to change the polarization state of light. This effect is characterized by a Mueller matrix, which maps the input Stokes vector into an output Stokes vector by way of a $4 \times 4$ real transformation (Chipman (2009b)):

$$\underline{S}_{out} = \underline{\underline{M}}\,\underline{S}_{in},  \tag{1.8}$$

where

$$\underline{\underline{M}} = \begin{bmatrix} m_{00} & m_{01} & m_{02} & m_{03} \\ m_{10} & m_{11} & m_{12} & m_{13} \\ m_{20} & m_{21} & m_{22} & m_{23} \\ m_{30} & m_{31} & m_{32} & m_{33} \end{bmatrix}.  \tag{1.9}$$

Given the context of Equation 1.8, the intended goal can either be to know the Stokes vector, a property of the light, or the Mueller matrix, a property of the surface that the light reflects from or a medium that the light propagates through. The necessary procedure to measure both are discussed in the following sections.

## 1.2 Stokes Polarimetry

The polarization state has to be inferred from a series of indirect measurements. In the case of a Stokes polarimeter, these indirect measurements are made by passing light of an unknown polarization state through a series of predetermined analyzing polarization states or vectors:

$$\underline{A}_n = \begin{bmatrix} a_0 & a_1 & a_2 & a_3 \end{bmatrix}_n^T,  \tag{1.10}$$

which are themselves Stokes vectors, and are subject to the same constraint posed by Equation 1.3. The detector then records intensities — projections of the unknown state onto each of the analyzing vectors,

$$I_n = \underline{A}_n^T \underline{S},  \tag{1.11}$$

which can be equivalently rewritten as

$$\underline{I} = \underline{\underline{W}}\,\underline{S},  \tag{1.12}$$

where $\underline{\underline{\mathbf{W}}}$ is a collected matrix of all analyzing vectors,

$$\underline{\underline{\mathbf{W}}} = \begin{bmatrix} \underline{\mathbf{A}}_1 & \underline{\mathbf{A}}_2 & \cdots & \underline{\mathbf{A}}_N \end{bmatrix}^{\mathrm{T}}. \tag{1.13}$$

It is possible to reconstruct the necessary vector orientation of the polarization state and thereby calculate the unknown state's Stokes parameters by inverting the process (Chipman (2009c)) and estimating the Stokes vector to be

$$\hat{\underline{\mathbf{S}}} = \underline{\underline{\mathbf{W}}}^{+}(\underline{\mathbf{I}} + \vec{\underline{\mathbf{n}}}) \tag{1.14}$$

where $\underline{\underline{\mathbf{W}}}^{+}$ is the pseudoinverse, or the Data Reduction Matrix (DRM) and $\vec{\underline{\mathbf{n}}}$ represents additive noise. Because additive noise is prevalent, most of this dissertation will limit itself to considering a Gaussian noise model as a representative example. However, Chapter 6 will consider a multiplicative noise model for purposes of optimizing overdetermined Stokes polarimeters, where diverse analyzing vector sets are shown to provide an advantage.

## 1.3 Mueller Polarimetry

For Mueller matrix polarimeters, a similar procedure is followed, but now the generating vectors

$$\underline{\mathbf{G}}_n = \begin{bmatrix} g_0 & g_1 & g_2 & g_3 \end{bmatrix}_n^{\mathrm{T}}, \tag{1.15}$$

are prearranged and calibrated to provide a known set of testing conditions from which the Muller matrix can be inferred. The $n^{\mathrm{th}}$ measurement of intensity in the Mueller polarimeter is

$$I_n = \underline{\mathbf{A}}_n^{\mathrm{T}} \underline{\underline{\mathbf{M}}} \underline{\mathbf{G}}_n. \tag{1.16}$$

The constituent parts of the system that are responsible for setting $\underline{\mathbf{G}}_n$ and $\underline{\mathbf{A}}_n$ are called Polarization State Generator(PSG) and Polarization State Analyzer(PSA), respectively. It has been shown that Equation 1.16 can be equivalently expressed as (Chipman (2009a))

$$I_n = \underline{\mathbf{D}}'^{\mathrm{T}}_n \underline{\mathbf{M}}', \tag{1.17}$$

where $\underline{\mathbf{D}}'_n$ is the dyad product reshaped into a vector,

$$\underline{\mathbf{D}}'_n = \text{vec}\left(\underline{\mathbf{A}}_n \underline{\mathbf{G}}_n^{\mathrm{T}}\right) = \underline{\mathbf{A}}_n \otimes \underline{\mathbf{G}}_n = \begin{bmatrix} a_0 g_0 \\ a_0 g_1 \\ a_0 g_2 \\ a_0 g_3 \\ a_1 g_0 \\ a_1 g_1 \\ a_1 g_2 \\ a_1 g_3 \\ a_2 g_0 \\ a_2 g_1 \\ a_2 g_2 \\ a_2 g_3 \\ a_3 g_0 \\ a_3 g_1 \\ a_3 g_2 \\ a_3 g_3 \end{bmatrix}_n , \tag{1.18}$$

and $\underline{\mathbf{M}}'$ is the Mueller matrix reshaped into a Mueller vector,

$$\underline{\mathbf{M}}' = \text{vec}\left(\underline{\underline{\mathbf{M}}}\right) = \begin{bmatrix} m_{00} \\ m_{01} \\ m_{02} \\ m_{03} \\ m_{10} \\ m_{11} \\ m_{12} \\ m_{13} \\ m_{20} \\ m_{21} \\ m_{22} \\ m_{23} \\ m_{30} \\ m_{31} \\ m_{32} \\ m_{33} \end{bmatrix}. \tag{1.19}$$

In the above equations, $\otimes$ is the Kronecker (direct) product, and vec($\underline{\underline{\mathbf{M}}}$) creates a column vector by reordering the matrix $\underline{\underline{\mathbf{M}}}$ into a vector in a row-by-row fashion. Equation 1.17 shows that a single measurement of the is a projection of the unknown Mueller matrix onto a known basis vector in $\mathbb{R}^{16}$. This procedure removes the need for considering high-dimensional tensor manipulations. By taking a collection of such projections, the unknown matrix – or portions of it in the case of partial systems – can be determined in a least-squares sense. The series of $N$ measurements in a polarimeter is

$$\underline{\mathbf{I}} = \begin{bmatrix} I_1 \\ I_2 \\ \vdots \\ I_N \end{bmatrix} = \begin{bmatrix} \underline{\mathbf{D}}'^{\mathrm{T}}_1 \underline{\mathbf{M}}' \\ \underline{\mathbf{D}}'^{\mathrm{T}}_2 \underline{\mathbf{M}}' \\ \vdots \\ \underline{\mathbf{D}}'^{\mathrm{T}}_N \underline{\mathbf{M}}' \end{bmatrix} + \vec{\underline{\mathbf{n}}} = \underline{\underline{\mathbf{W}}}\,\underline{\mathbf{M}}' + \vec{\underline{\mathbf{n}}}. \tag{1.20}$$

where $\underline{\underline{\mathbf{W}}}'$ is a collected matrix of all the effective dyads,

$$\underline{\underline{\mathbf{W}}}' = \begin{bmatrix} \underline{\mathbf{D}}'_1 & \underline{\mathbf{D}}'_2 & \cdots & \underline{\mathbf{D}}'_N \end{bmatrix}^{\mathrm{T}}. \tag{1.21}$$

Similar to Stokes polarimeters, reconstruction is performed as $\underline{\mathbf{M}}'$,

$$\hat{\underline{\mathbf{M}}}' = \underline{\underline{\mathbf{W}}}'^{+}(\underline{\mathbf{I}} + \vec{\mathbf{n}}), \tag{1.22}$$

where $\underline{\underline{\mathbf{W}}}'^{+}$ is the pseudoinverse of $\underline{\underline{\mathbf{W}}}'$ and $\vec{\mathbf{n}}$ represents additive noise. To keep the notation as clear as possible, $i$ and $j$ will be used as matrix indices, while $k$ will be used as the unfolded vector index. To go from one to the other,

$$k = 4i + j \tag{1.23}$$

or

$$i = \lfloor k/4 \rfloor, \tag{1.24a}$$

$$j = k - 4i. \tag{1.24b}$$

## 1.4   Matrix Pseudoinverse

Since both Stokes and Mueller polarimetry propose indirect measurements as a means to arrive at the underlying information of need, the process of information-mapping matrix is important for each and save for occupying a different geometrical space, the two can be approached in the same mathematical sense. Thus, the number of measurements will be denoted as $N$ and the total number of information parameters as $K$, where $K$ is 4 and 16 for Stokes and Mueller polarimeters, respectively. The measurement matrix is then $N \times K$. Since a true matrix inverse only exists for a square matrix, the only time it is possible to be completely unambiguous about how to combine measurements is when $N = K$. In order to handle the cases where $N \neq K$, a robust way to consistently calculate a pseudo-inverse is needed, such that the error introduced into the reconstructed information is minimized.

One way is to use the Moore-Penrose pseudoinverse, which in polarimetry literature is often written as

$$\underline{\underline{\mathbf{W}}}^{+} = \left( \underline{\underline{\mathbf{W}}}^{\mathrm{T}} \underline{\underline{\mathbf{W}}} \right)^{-1} \underline{\underline{\mathbf{W}}}^{\mathrm{T}} = \left( \underline{\underline{\mathbf{W}}}^{\mathrm{T}} \underline{\underline{\mathbf{W}}} \right) \backslash \underline{\underline{\mathbf{W}}}^{\mathrm{T}}, \tag{1.25}$$

with the latter calculation usually being more numerically stable, since the inverse is not being calculated. However, the columns of $\underline{\underline{W}}$ must be linearly independent for that explicit definition to hold, which requires $N \geqslant K$. Since one of the foci of this dissertation is design of partial systems, an alternative expression for the pseudoinverse is preferred — one that provides more computational control when handling the case when $N < K$.

Instead, use Singular Value Decomposition (SVD) to decompose the measurement matrix,

$$\underline{\underline{W}} = \underline{\underline{U}}\,\underline{\underline{\Sigma}}\,\underline{\underline{V}}^{\mathrm{T}}, \tag{1.26}$$

where matrices $\underline{\underline{U}}$ and $\underline{\underline{V}}$ are $N \times N$ and $K \times K$ real, orthonormal matrices, respectively, and $\underline{\underline{\Sigma}}$ is the $N \times K$ reduced diagonal matrix containing the $\min(N, K)$ singular values $\sigma_1 \geq \sigma_2 \geq \ldots \geq \sigma_{\min(N,K)}$. To be completely general at this point, it is deliberate that nothing is said about the relative magnitudes of those singular values and the rank of the system. The pseudoinverse can then be written as

$$\underline{\underline{W}}^{+} = \underline{\underline{V}}\,\underline{\underline{\Sigma}}^{+}\,\underline{\underline{U}}^{\mathrm{T}}, \tag{1.27}$$

where $\underline{\underline{\Sigma}}^{+}$ is the $K \times N$ reduced diagonal matrix containing the inverse of the singular values. The advantage of this method is that $N < K$ cases are handled better by only keeping track of $\min(N, K)$ singular values and taking the inverse of only the sufficiently large singular values. As will become clearer later, it is also much easier to perform additional culling of singular values and the corresponding left- and right-column matrices. This additional control serves the purpose of enabling the understanding of the process that is required for successful structure manipulation.

1.5    Polarization Components

This section introduces Mueller matrices of the most common polarization elements (Chipman (2009b)).

A linear diattenuator applies a different amount of attenuation to the intensities in two orthogonal directions. The Mueller matrix of a linear diattenuator is

$$
\underline{\underline{\mathbf{M}}}_{\mathrm{LD}}(\alpha, \beta, \theta) = \frac{1}{2}
\begin{bmatrix}
\alpha & \beta \cos(2\theta) & \beta \sin(2\theta) & 0 \\
\beta \cos(2\theta) & \alpha \cos^2(2\theta) + \gamma \sin^2(2\theta) & (\alpha - \gamma) \cos(2\theta) \sin(2\theta) & 0 \\
\beta \sin(2\theta) & (\alpha - \gamma) \cos(2\theta) \sin(2\theta) & \alpha \sin^2(2\theta) + \gamma \cos^2(2\theta) & 0 \\
0 & 0 & 0 & \gamma
\end{bmatrix},
$$

(1.28)

where $\alpha = q + r$, $\beta = q - r$, and $\gamma = 2\sqrt{qr}$, of which $q$ and $r$ represent the fractions of intensity maintained for the two orthogonal polarizations of light. If $q = 1$ and $r = 0$ is assumed, then the element simplifies to the ideal linear polarizer,

$$
\underline{\underline{\mathbf{M}}}_{\mathrm{LP}}(\theta) = \frac{1}{2}
\begin{bmatrix}
1 & \cos(2\theta) & \sin(2\theta) & 0 \\
\cos(2\theta) & \cos(2\theta)^2 & \cos(2\theta) \sin(2\theta) & 0 \\
\sin(2\theta) & \cos(2\theta) \sin(2\theta) & \sin(2\theta)^2 & 0 \\
0 & 0 & 0 & 0
\end{bmatrix}.
$$

(1.29)

Another commonly used polarization element is a linear retarder. Instead of differently attenuating the two orthogonal polarizations of light, a different amount of phase is accumulated for two orthogonal directions in passing through the element. The Mueller matrix of a linear retarder is

$$
\underline{\underline{\mathbf{M}}}_{\mathrm{LR}}(\delta, \theta) =
\begin{bmatrix}
1 & 0 & 0 & 0 \\
0 & c^2(2\theta) + c(\delta) s^2(2\theta) & c(2\theta) s(2\theta) v(\delta) & -s(2\theta) s(\delta) \\
0 & c(2\theta) s(2\theta) v(\delta) & c(\delta) c^2(2\theta) + s^2(2\theta) & c(2\theta) s(\delta) \\
0 & s(2\theta) s(\delta) & -c(2\theta) s(\delta) & c(\delta)
\end{bmatrix},
$$

(1.30)

where $\theta$ is orientation of the retarder and $\delta$ is its retardance, which is the difference between the applied phases. It suffices to know the phase difference, since absolute phase is of very

limited concern in Stokes polarimetry, and optics in general. To show the complete matrix, some shorthands were used: $c(x) = \cos(x)$, $s(x) = \sin(x)$ and $v(x) = \text{versin}(x) = 1 - \cos(x)$.

## 1.6 Polarimeter Types

There exist a number of different polarimeter designs, but there is no one best design for every intended measurement task. This section will introduce the types of polarimeters this dissertation will predominantly focus on and discuss each one's strengths and weaknesses.

For the purposes of keeping the descriptions in this section concise, only the Stokes versions of these polarimeters will be considered. The Mueller versions can be trivially derived by mirroring the components used on the PSA side to the ones used on the PSG side. Furthermore, the restriction of looking at a given PSA or PSG bodes well for natural introduction of hybrid modulation in Mueller matrix polarimeters.

### 1.6.1 Division of Time

Perhaps the most common type of polarimeter is one of the type of Division of Time. This is because the method by which the different measurements are achieved is relatively simple and readily accessible. Provided that there exists an avenue by which to differently orient various polarization elements, it is possible to take several measurements with different configurations. A properly selected set of measurements is one is able to reconstruct the underlying polarization signature with sufficient noise resilience.

If the main advantage of Division of Time polarimeters is their simplicity, the disadvantage is the need for some sort of mechanical or electro-optic adjustment to construct additional measurements. This type of polarimeters intrinsically applies a stronger temporal bandwidth constraint than the constraint for the underlying detector. This is because the adjustments take time and unless the object is completely controlled and stationary, the non-simultaneous capture means that for a moving object the measurements from different times will be combined, causing motion blur.

One example of a Division of Time polarimeter is the Rotating Analyzer (RA) po-

Figure 1.2: RA Polarimeter. (Animation available in the digital version)

larimeter, the layout of which is shown in Figure 1.2. Although it can be analyzed for a general diattenuator, it is simplified here to feature an idealized polarizer, which allows the analyzing vector to be written as

$$\underline{\mathbf{A}}_{\text{RA}}(\phi) = \left( \begin{bmatrix} 1 & 0 & 0 & 0 \end{bmatrix} \underline{\underline{\mathbf{M}}}_{\text{LP}}(\phi) \right)^{\text{T}} = \begin{bmatrix} 1 \\ \cos(2\phi) \\ \sin(2\phi) \\ 0 \end{bmatrix}. \tag{1.31}$$

Figure 1.3: RR Polarimeter. (Animation available in the digital version)

Another example of a Division of Time polarimeter is the Rotating Retarder (RR) po-larimeter, the layout of which is shown in Figure 1.3. Again, using an ideal polarizer in place of a linear diattenuator, allows the analyzing vector of the RR polarimeter to be writ-ten as

$$
\underline{\mathbf{A}}_{RR}(\phi, \theta, \delta) = \left( \begin{bmatrix} 1 & 0 & 0 & 0 \end{bmatrix} \underline{\underline{\mathbf{M}}}_{LP}(\phi) \underline{\underline{\mathbf{M}}}_{LR}(\delta, \theta) \right)^{\mathrm{T}} =
$$

$$
= \begin{bmatrix} 1 \\ \cos(2\phi)(\cos(2\theta)^2 + \cos(\delta)\sin(2\theta)^2) + \frac{1}{2}\sin(4\theta)\sin(2\phi)(1 - \cos(\delta)) \\ \sin(2\phi)(\cos(\delta)\cos(2\theta)^2 + \sin(2\theta)^2) + \frac{1}{2}\sin(4\theta)\cos(2\phi)(1 - \cos(\delta)) \\ \sin(2\phi - 2\theta)\sin(\delta) \end{bmatrix}.
$$

$$(1.32)$$

Note that in Equations 1.31 and 1.32, $\begin{bmatrix} 1 & 0 & 0 & 0 \end{bmatrix}$ can be thought of as the idealized analyzing vector of the detector, which is assumed to be perfectly sensitive to $s_0$.
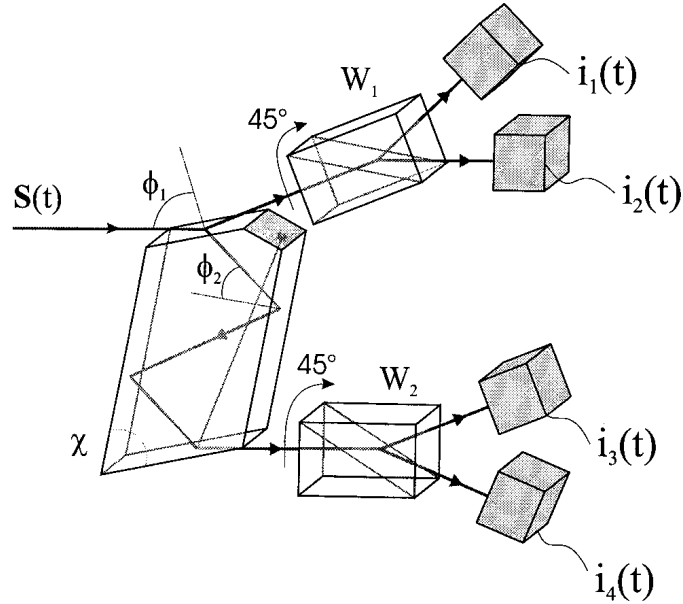
Figure 1.4: Reproduced from Compain and Drevillon (1998). Principle of a visible–near-infrared DOAP with an uncoated dielectric prism. The light beam is separated first into two by a prism then into four by two Wollaston prisms (W1 and W2) oriented at 45° with respect to the plane of incidence. Stokes vector $\underline{\mathbf{S}}$ is determined from the four intensities $i_1$–$i_4$.

### 1.6.2  Division of Focal Plane

A polarimeter of the type of Division of Focal Plane (DoFP) uses different segments of the focal plane to impose a set of different test conditions to determine the incoming state of polarization. In a way, this type of a polarimeter is a continuation of Division of Amplitude (DoA) polarimeters that use beam splitters to split the beam into several and associate a different analyzing vector in each hand of the system, like in the system depicted in Figure 1.4. Although the measurements can be made simultaneously, there is a particular amount of bulkiness that is unavoidable and alignment might require some time to get right. Conventionally DoFP can be treated as DoA system, where the different hands of the setup intersect and use the same detector.

The class of DoFP polarimeters was enabled by advances in detector lithography process. It is achieved by associating analyzing vectors directly with each pixel in a particular pattern. This polarimeter has been nicknamed "microgrid" because the most com-

$$\underline{\mathbf{A}}(m,n) = \frac{1}{2} \begin{bmatrix} 1 \\ \frac{1}{2}\left(\cos(m\pi) + \cos(n\pi)\right) \\ \frac{1}{2}\left(\cos(m\pi) - \cos(n\pi)\right) \\ 0 \end{bmatrix}$$
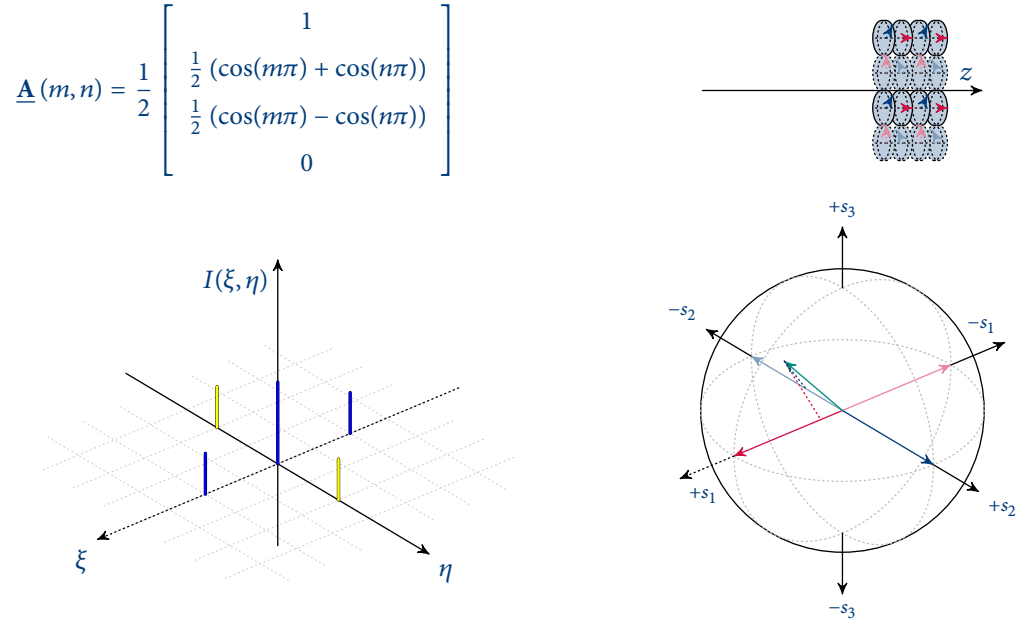
Figure 1.5: Microgrid Polarimeter. Each pixel has a polarizer at $0°/45°/90°/135°$.

mon pattern of the imposed pattern of polarization components is that of a repeated $2 \times 2$ pixel structure, referred to as the superpixel, a diagram of which can be seen in Figure 1.7. Each superpixel contains four pixels with applied linear polarizers that individually let in $0°/45°/90°/135°$ polarized light. Mathematically, the analyzing vector of $(m,n)$ pixel can be described as:

$$\underline{\mathbf{A}}(m,n) = \begin{bmatrix} 1 \\ \frac{1}{2}(\cos(m\pi) + \cos(n\pi)) \\ \frac{1}{2}(\cos(m\pi) - \cos(n\pi)) \\ 0 \end{bmatrix}. \tag{1.33}$$

Other structured patterns exist. MSPI polarimeter uses a $3 \times 1$ superpixel, measuring $s_0$, $I_H$ and $I_V$ (Diner et al. (2007)). Peltzer suggested a pattern that substitutes the polarizer on one of the pixels in the $2 \times 2$ structure with a circular-polarization sensitive structure that enables a microgrid polarimeter to estimate $s_3$ as well (Peltzer et al. (2011)). A microgrid polarimeter can be adjusted in a number of ways, but at this point the above description suffices. In Chapter 6 it will be parametrized further.

Figure 1.6: Microgrid and RR polarimeter. (Animation available in the digital version)

Finally, provided that the patterns of polarization selection properties are arranged periodically, DoFP can also be treated as a channeled system, which are discussed in the next subsection.

### 1.6.3 Channeled

Channeled polarimeters measure polarization by modulating the measured intensity in order to create polarization-dependent channels in tempporal, spatial, spectral or angular domains that can be demodulated to reveal the desired polarization information. Channeled modulations can be either temporal, spatial or spectral. However, transforming temporal modulation into channels is less conducive because the number of temporal measurements is often limited to the bare minimum needed for reconstruction. Thus, transforming information is unlikely to pose an advantage that would stem from linking various data together. Spatial and spectral channels, on the other hand, can be extremely useful, since polarization information can be modulated onto two independent dimensions of the detector and be captured simultaneously. This class of system has been introduced by Oka (Oka and

Kato (1999)). In that system, the spatial modulation frequencies are determined by the thicknesses of the birefringent prisms. The diagram of that system can be seen in Figure 2.5. Using notation employed later on in the dissertation, we can describe the system with a vector of modulations carried in each element of the analyzing vector,

$$
\underline{\mathbf{f}}_{\underline{\mathbf{A}}} = \begin{bmatrix} 1 \\ \cos(2\pi\xi_o x) \\ \sin(2\pi\xi_o x)\cos(2\pi\eta_o y) \\ \sin(2\pi\xi_o x)\sin(2\pi\eta_o y) \end{bmatrix}, \tag{1.34}
$$

where $\xi_o$ and $\eta_o$ represent the two carrier frequencies at the center of the information bands.

## 1.7 Contents Summary

This dissertation is organized as follows. Chapter 2 introduces the most prevalent pieces of prior work, on top of which this dissertation innovates. First, Chapter 3 generalizes the concept of channeled polarimetry with the measurement matrix completely defining the system evaluation. This introduction enables abstraction of channeled system design by extracting the necessary components for analysis. Second, Chapter 4 proposes the concept of structured decomposition in order to determine the space coverage as well as noise resilience within the Mueller element combinations of interest. A basis is developed to allow for a family of efficient partial systems in terms of rank and number of measurements. Third, Chapter 5 combines the concepts of Chapter 3 and Chapter 4 to construct channeled partial Mueller matrix polarimeters, a class of previously unstudied polarimeters. Fourth, Chapter 6 provides insight into the geometrical distributions of analyzing vectors for overdetermined Stokes polarimeters, which is useful for systems where non-additive noise is dominant. Finally, Chapter 7 concludes this dissertation.
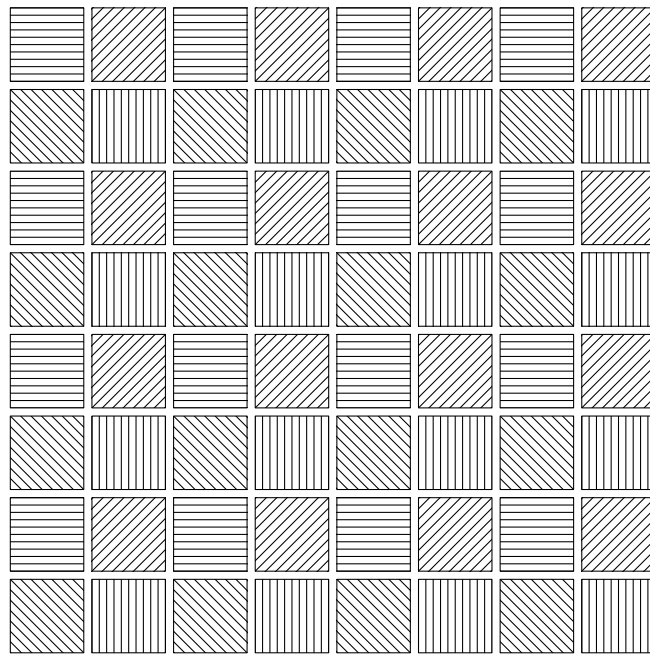
Figure 1.7: Microgrid Focal Plane Array (FPA) diagram. Each superpixel contains four pixels with linear polarizers at 0°/45°/90°/135°. The four pixels constitute a set of four analyzing vectors that is able to reconstruct the linear state of polarization of light.

CHAPTER 2

PRIOR WORK

Because this dissertation's focus is on the evaluation of different types of polarimeters, it is appropriate to introduce some of the prior efforts in the field. This chapter will go over literature pertaining to polarimetric system evaluation, as well as various previously used system designs. The goal of this dissertation is then to build on top of the building blocks shown here.

## 2.1    System Evaluation

One way to objectively analyze the system is by considering its signal-to-noise ratio (SNR). Because, for independent variables, standard deviations add in root-sum-square (RSS) fashion, it also follows that for multiple reconstruction channels of information, it is common to add noise variances, rather than noise standard deviations. Sabatke applied this evaluation to polarimeters by introducing equally weighted variance (EWV) as an evaluation figure of merit for Stokes polarimeters (Sabatke et al. (2000)). The metric is a sum of variances within each of the Stokes parameters and can be calculated directly from $\underline{\underline{\mathbf{W}}}^{+}$ by computing

$$\text{EWV} = \sum_{j=0}^{3} \sum_{k=0}^{N-1} (\underline{\underline{\mathbf{W}}}^{+})_{j,k}^{2} = \text{tr}\left( (\underline{\underline{\mathbf{W}}}^{+})^{\text{T}} \underline{\underline{\mathbf{W}}}^{+} \right) = \sum_{j=0}^{R-1} \frac{1}{\mu_{j}^{2}}, \tag{2.1}$$

where $j$ denotes the Stokes component, $k$ denotes the measurement and $\mu_{j}$ refers to the singular value. Sabatke applied that metric to optimize a RR polarimeter, as depicted in Figure 1.3. His results yielded a retarder with $\delta = 132°$ and orientations at $\pm 15.1°$ and $\pm 51.7°$ with respect to the polarizer's orientation. The resulting analyzing vectors produced an approximation to the regular tetrahedron inscribed inside the Poincaré sphere as can be seen in Figure 2.1. While their results in Figure 2.2 show that use of optimal retardance provides a vast improvement over using a quarterwave plate.
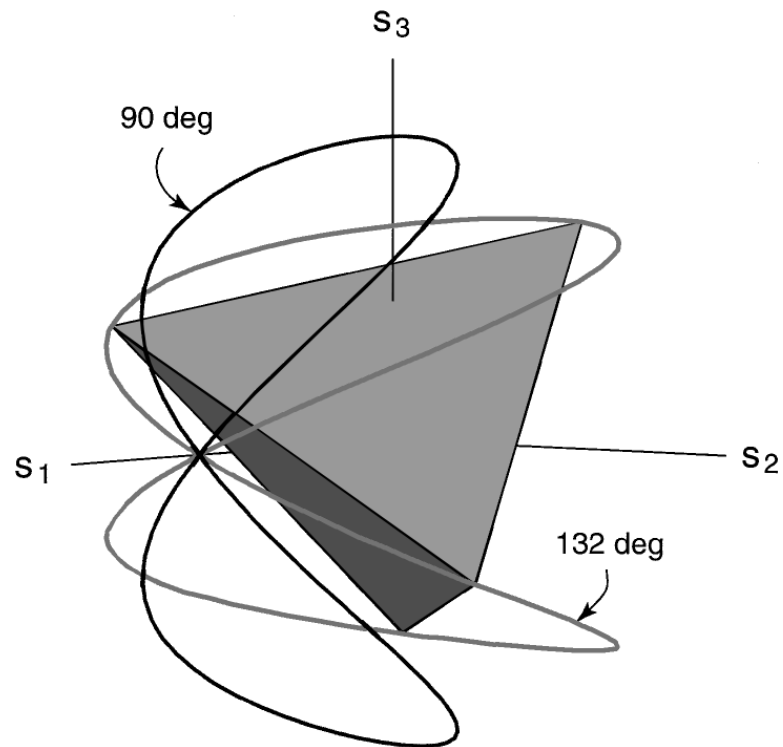
Figure 2.1: Reproduced from Sabatke et al. (2000). Curves for retardances of 90° and 132°, showing an inscribed regular tetrahedron in the curve of 132°. The tetrahedron vertices correspond to retarder angles of ±51.7° and ±15.1°.
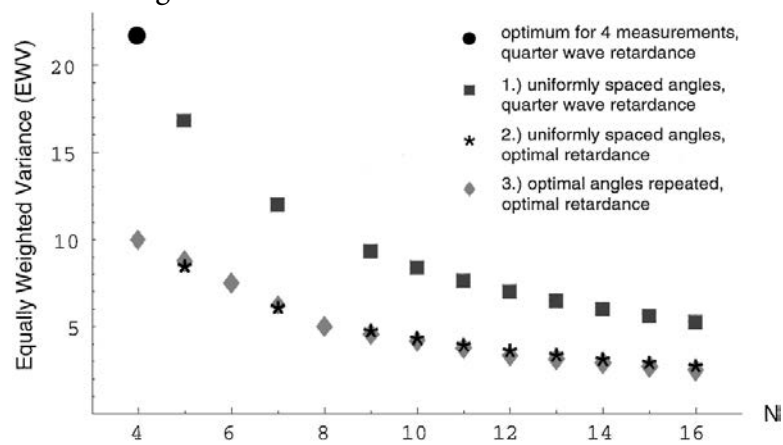


Figure 2.2: Reproduced from Sabatke et al. (2000). Comparison of multiple measurement techniques, showing values of the EWV figure of merit as a function of the number N of measurements for cases (1)–(3) described in text. Missing points at $N = 4, 6, 8$ in the data for cases (1) and (2) are due to singularities in the measurement matrices. A single data point (•) is also shown for a four-measurement procedure using a quarterwave plate.

Another way to approach the problem is to focus on its mathematical properties and use the tools of numerical analysis to estimate the stability of the inverse problem. This is commonly done through calculating condition number of the matrix,

$$\text{CN} = \left\| \underline{\underline{\mathbf{W}}} \right\| \cdot \left\| \underline{\underline{\mathbf{W}}}^+ \right\| = \left| \frac{\lambda_{\max}(\underline{\underline{\mathbf{W}}})}{\lambda_{\min}(\underline{\underline{\mathbf{W}}})} \right|, \tag{2.2}$$

which Tyo applied to Stokes polarimeters (Tyo (2002)). His results for a RR polarimeter yielded the same retardance and orientations, agreeing with the result shown by Sabatke's application of EWV. The subtle point to make to differentiate the two is to stress that the two methods intrinsically choose different norms, which affects the metric's space and thus the approach of the optimization to the minimum. If the particular arrangement of a given system cannot obtain the theoretical minimum, then it is possible and quite likely that the best solutions dictated by EWV and by CN are going to be different. However, because the RR polarimeter is able to achieve the theoretical minimum, the different norms agree on the minimum as can be seen in Figure 2.3.

Although the metrics were first applied to Stokes polarimeters, the principles of evaluating noise resilience in the different channels or the numerical stability of a given problem are directly transferable to problems with a greater number of information channels. In order to analyze Mueller matrix polarimeters, Twietmeyer adapted the concepts that Sabatke and Tyo applied to Stokes polarimeters (Twietmeyer and Chipman (2008)). Her optimization considered a dual rotating retarder (DRR) polarimeter, which can be equivalently thought of as two mirrored RR polarimeters comprising the PSA and the PSG. The results of said optimization yield retarders with retardance $\delta = 127°$ as can be seen in Figure 2.4.

## 2.2 Channeled Systems

The first examples of added polarization sensitivity were achieved through combining multiple temporal measurements. In effect, this technique shares of temporal bandwidth between time and polarization and only for perfectly static scenes is the motion blur negligible. However, when the scene's temporal content is restricting for a DoT polarimeter, a
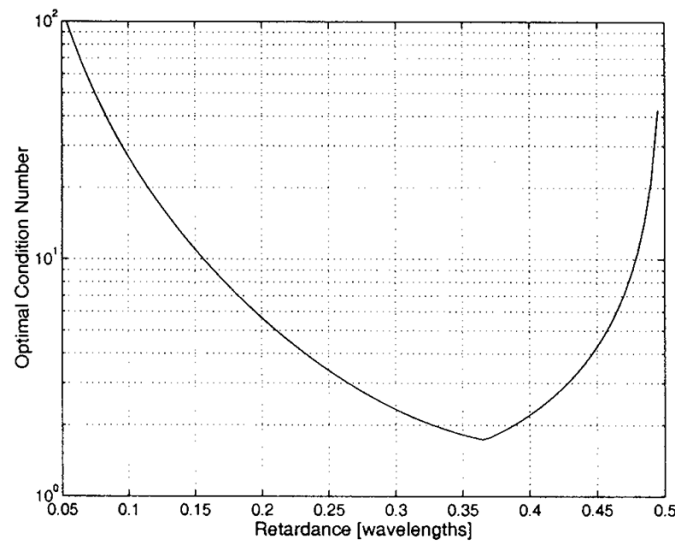
Figure 2.3: Reproduced from Tyo (2002). Optimal condition number for four-measurement rotating compensator systems. There is a clear optimum at $\delta = 0.3661\lambda$. [Tyo] obtained the optimization by minimizing the $L_2$ condition number of the system matrices, but achieved the same result as Sabatke et al. (2000) where the equal-weighted variance–equivalent to the Frobenius condition number of the system matrices–was minimized.
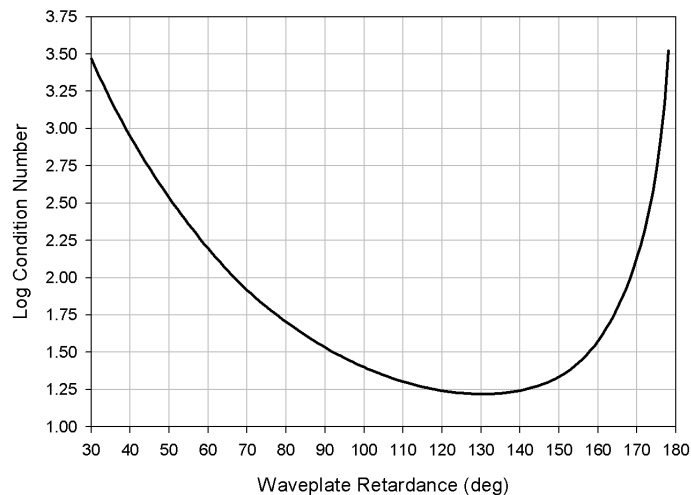


Figure 2.4: Reproduced from Twietmeyer and Chipman (2008). Base 10 log of the condition number as a function of waveplate retardance [$\delta$] for the DRR polarimeter. The optimum solution is a retardance of 127°; condition number increases significantly with distance from the optimum solution.

different approach is needed. Much like temporal bandwidth being used to share temporal and polarization information, other domains can be shared as well, namely, spectral and spatial. The advantage of using those domains for purposes of adding polarization sensitivity is that they can both be mapped to the spatial extent of a detector, thus enabling one-snapshot systems.

### 2.2.1 Stokes Polarimeters

Channeled polarimeters were introduced by Oka and Kato (1999), with the proposed system's layout shown in Figure 2.5. In their treatment, they were able to define and construct a system that measures a polarization-dependent spectrum as seen in Figure 2.6,

$$
\begin{aligned}
P(\sigma) = \frac{s_0(\sigma)}{2} + \frac{s_1(\sigma)}{2} & \cos(2\pi L_2 \sigma + \Phi_2(\sigma)) + \\
& + \frac{|s_{23}(\sigma)|}{4} \cos(2\pi(L_1 - L_2)\sigma + \Phi_1(\sigma) + \Phi_2(\sigma) + \arg(s_{23}(\sigma))) + \\
& - \frac{|s_{23}(\sigma)|}{4} \cos(2\pi(L_1 + L_2)\sigma + \Phi_1(\sigma) + \Phi_2(\sigma) + \arg(s_{23}(\sigma)))
\end{aligned}
\tag{2.3}
$$

where $s_{23}(\sigma) = s_2(\sigma) - is_3(\sigma)$, $\Phi_1(\sigma)$ and $\Phi_2(\sigma)$ are total phase terms of retarders denoted $R_1$ and $R_2$, and $L_i$ are the OPD distances stemming from modulation frequencies of the respective retarders. By taking the Fourier transform of the modulated spectrum represented in terms of wavenumber, channels emerge in the optical path difference (OPD):

$$
\begin{aligned}
C(h) = \frac{1}{2}A_0(h) + \frac{1}{4}A_1(h - L_2) & + \frac{1}{4}A_1^*(-h - L_2) + \\
& + \frac{1}{8}A_2(h - (L_1 - L_2)) + \frac{1}{8}A_2^*(-h - (L_1 - L_2)) + \\
& - \frac{1}{8}A_3(h - (L_1 + L_2)) - \frac{1}{8}A_3^*(-h - (L_1 + L_2)),
\end{aligned}
\tag{2.4}
$$

where $h$ represents OPD. The Stokes parameters are contained within:

$$
A_0(h) = \mathcal{F}^{-1}\{s_0\}, \tag{2.5a}
$$

$$
A_1(h) = \mathcal{F}^{-1}\{s_1(\sigma)\exp(i\Phi_2(\sigma))\}, \tag{2.5b}
$$

$$
A_2(h) = \mathcal{F}^{-1}\{s_{23}(\sigma)\exp(i(\Phi_1(\sigma) - \Phi_2(\sigma)))\}, \tag{2.5c}
$$

$$
A_3(h) = \mathcal{F}^{-1}\{s_{23}(\sigma)\exp(i(\Phi_1(\sigma) + \Phi_2(\sigma)))\}, \tag{2.5d}
$$
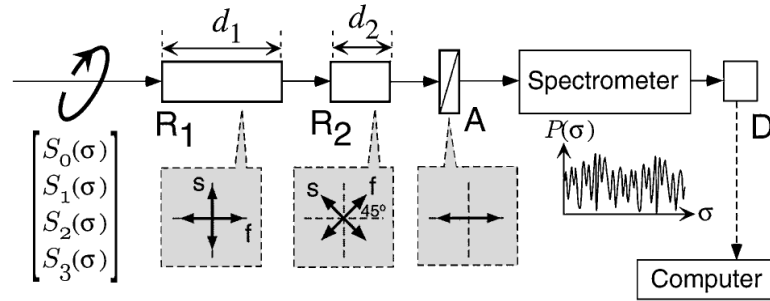
Figure 2.5: Reproduced from Oka and Kato (1999). Schematic of the spectroscopic polarimeter with a channeled spectrum.
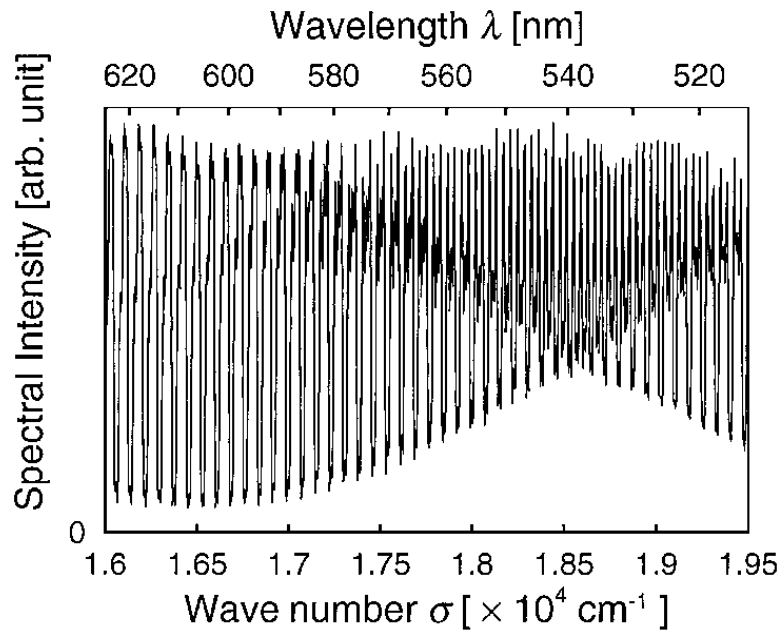


Figure 2.6: Reproduced from Oka and Kato (1999). Measured channeled spectrum $P(\sigma)$.

and can be found by taking the Fourier transforms of each of the channels resulting in the estimates shown in Figure 2.8. Note that even though there are seven channels, only three (first, second and fourth in Equation 2.4) of them are being used to produce the estimates.

Oka has also built a channeled polarimeter that uses birefringent prism pairs to encode polarization into $x$- and $y$-axes of the detector's spatial domain (Oka and Kaneko (2003)). The layout of this system can be seen in Figures 2.9 and 2.10. The typical intensity can be seen in Figure 2.11, which clearly shows the imposed modulation pattern, which results
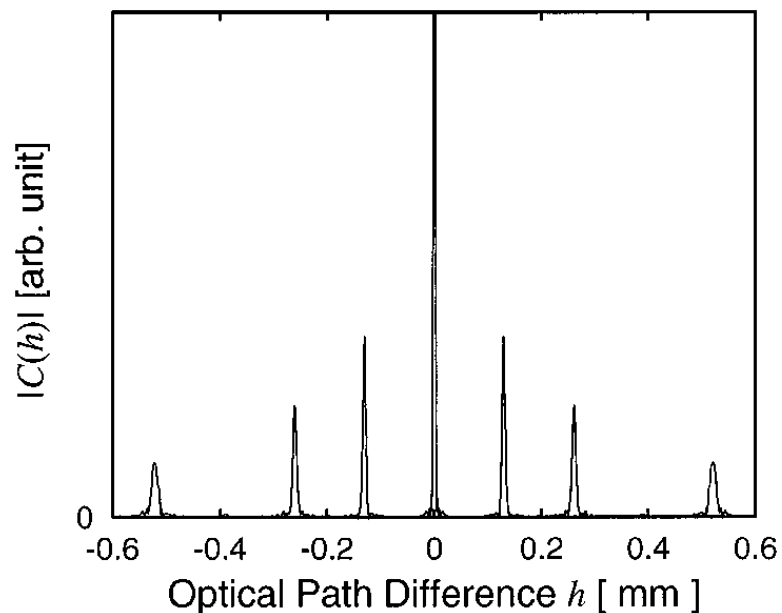
Figure 2.7: Reproduced from Oka and Kato (1999). Magnitude of autocorrelation function $C(h)$. The seven components included in $C(h)$ are separated over the $h$ axis.
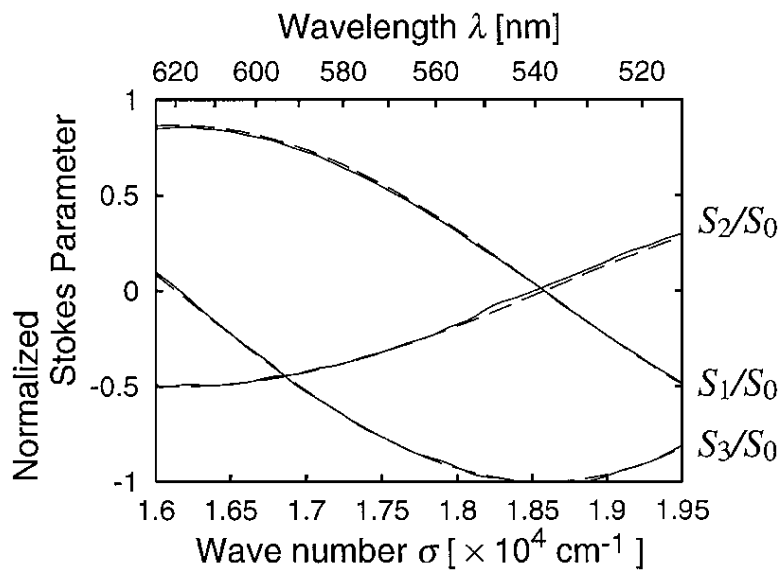


Figure 2.8: Reproduced from Oka and Kato (1999). Normalized Stokes parameters. Solid and dashed curves show the experimentally obtained and theoretically calculated values, respectively.

in the $3 \times 3$ arrangement of channels seen in Figure 2.12. Although the channels occupy a dffierent domain, they are exceptionally similar to the system of Oka and Kato (1999):

$$\tilde{I}(f_x, f_y) = \frac{1}{2}A_0(f_x, f_y) + \frac{1}{4}A_1(f_x - U, f_y) + \frac{1}{4}A_1^*(-f_x - U, -f_y)+$$
$$+ \frac{1}{8}A_{23}(f_x - U, f_y + U) + \frac{1}{8}A_{23}^*(-f_x - U, -f_y + U)+$$
$$- \frac{1}{8}A_{23}^*(f_x - U, f_y - U) - \frac{1}{8}A_{23}(-f_x - U, -f_y - U). \quad (2.6)$$

The principle by which the Stokes estimates are produced remain the same. Once again, only three terms in Equation 2.6 are used to estimate the Stokes parameters, a feature that is common to prior channeled system treatments.
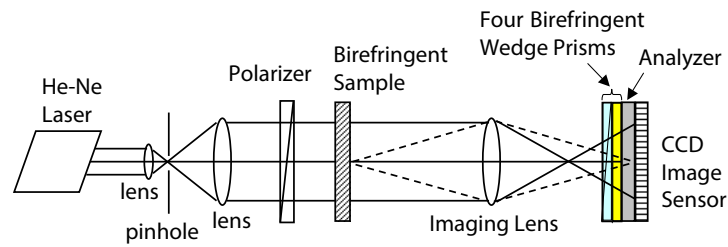
Figure 2.9: Reproduced from Oka and Kaneko (2003). Schematic of the imaging polarimeter using birefringent wedge prisms.
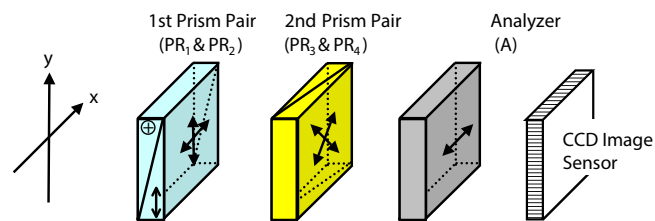


Figure 2.10: Reproduced from Oka and Kaneko (2003). Configuration of the block of the polarimetric devices.



Figure 2.11: Reproduced from Oka and Kaneko (2003). Intensity pattern with mesh-like fringes.
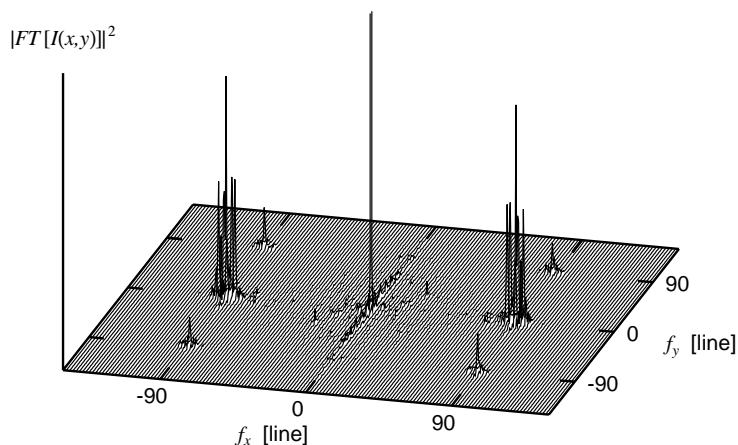
Figure 2.12: Reproduced from Oka and Kaneko (2003). Power spectrum of the intensity pattern.
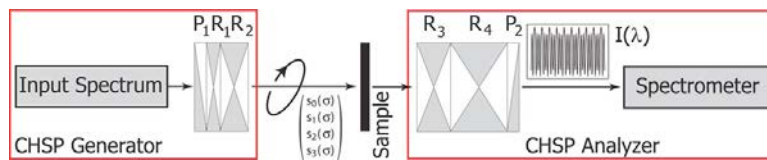


Figure 2.13: Reproduced from Hagen et al. (2007). Basic layout of the snapshot Mueller matrix spectropolarimeter. Retarders 1 and 4 have their fast axes oriented at $45°$, retarders 2 and 3 at $0°$. Polarizers 1 and 2 both have their transmission axes oriented at $0°$.
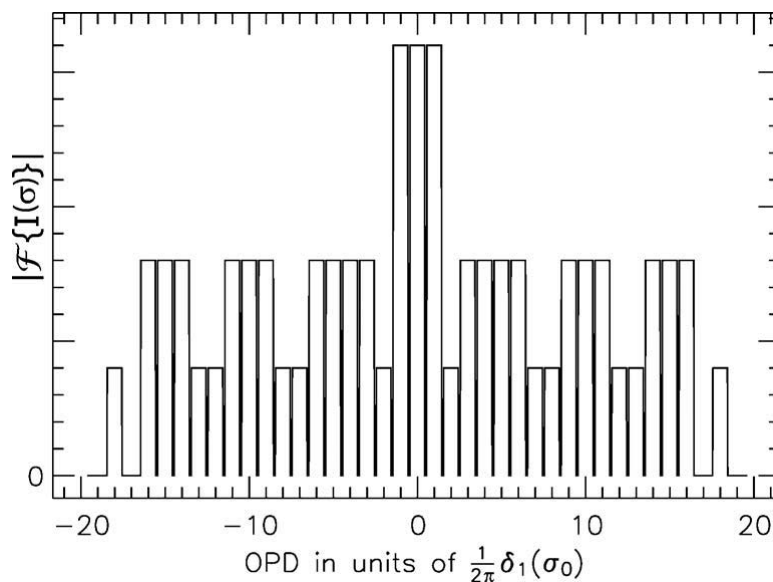


Figure 2.14: Reproduced from Hagen et al. (2007). Fourier domain, 37 channels $C_n$.

### 2.2.2    Mueller Matrix Polarimeters

Oka's designs for Stokes polarimeters were followed by naturally extended Mueller matrix polarimeter designs, including those of Hagen et al. (2007), Dubreuil et al. (2007) and Kudenov et al. (2012). The polarimeter presented by Hagen et al. (2007) is an extension of the polarimeter developed by Oka and Kato (1999). The PSA and the PSG follow exactly the same principle of using high order retarders to separate information into channels. The PSA in Hagen's polarimeter features retarders that are five times thicker than their PSG counterparts, as can be seen in Figure 2.13. The measured intensity of Hagen's polarimeter is

$$
\begin{aligned}
I(\sigma) = \; & m_{00} \\
& + m_{01} \cos(c_1\sigma) \\
& + m_{02} \sin(c_1\sigma) \sin(c_2\sigma) \\
& + m_{03} \sin(c_1\sigma) \cos(c_2\sigma) \\
& + m_{10} \cos(c_4\sigma) \\
& + m_{11} \cos(c_1\sigma) \cos(c_4\sigma) \\
& + m_{12} \sin(c_1\sigma) \sin(c_2\sigma) \cos(c_4\sigma) \\
& + m_{13} \sin(c_1\sigma) \cos(c_2\sigma) \cos(c_4\sigma) \\
& + m_{20} \sin(c_3\sigma) \sin(c_4\sigma) \\
& + m_{21} \cos(c_1\sigma) \sin(c_3\sigma) \sin(c_4\sigma) \\
& + m_{22} \sin(c_1\sigma) \sin(c_2\sigma) \sin(c_3\sigma) \sin(c_4\sigma) \\
& + m_{23} \sin(c_1\sigma) \cos(c_2\sigma) \sin(c_3\sigma) \sin(c_4\sigma) \\
& - m_{30} \cos(c_3\sigma) \sin(c_4\sigma) \\
& - m_{31} \cos(c_1\sigma) \cos(c_3\sigma) \sin(c_4\sigma) \\
& - m_{32} \sin(c_1\sigma) \sin(c_2\sigma) \cos(c_3\sigma) \sin(c_4\sigma) \\
& - m_{33} \sin(c_1\sigma) \cos(c_2\sigma) \cos(c_3\sigma) \sin(c_4\sigma),
\end{aligned}
\tag{2.7}
$$

where the argument can be expanded into

$$c_i\sigma = 2\pi\tau_i\sigma = 2\pi d_o d_i \lambda_o B\sigma \longrightarrow \tau_i = d_o d_i \lambda_o B, \tag{2.8}$$

where $\tau$ is OPD, $d_o$ is the global retarder factor, $d_i$ is the individual retarder factor, $\lambda_o$ is the center wavelength of the retarder and $B$ is birefringence (index difference). Figure 2.14 shows the relative magnitudes of each information channel in the Fourier-domain, while Table 2.1 defines the contents of each channel and Table 2.2 proposes a reconstruction routine for the Mueller elements. From the reconstruction, it is readily seen that only 21 of the 37 channels are being used to reconstruct the underlying polarization information. Figure 2.15 shows the simulation result for the snapshot channeled spectropolarimeter in question.

Another similar system was proposed by Dubreuil et al. (2007), which uses the effective $\underline{\mathbf{d}}$ = ( 1  1  5  5 ) instead of Hagen's $\underline{\mathbf{d}}$ = ( 1  2  5  10 ). Its setup can be seen in Figure 2.16, while its intensity output is shown in Figure 2.17. This system will not be inspected in greater detail here because of its similarities to Hagen's polarimeter, but its performance will be commented on in Chapter 3.

The last channeled system of interest for this dissertation is the one developed by Kudenov et al. (2012). It does to the system of Oka and Kaneko (2003) what Hagen did to the system of Oka and Kato (1999). The spatial modulation is now done in the PSG, as well as the PSA with analyzer's frequencies being double that of the generator's, as depicted in

Figure 2.18. The resulting polarization-modulated intensity can be expressed as

$$
\begin{aligned}
I(x, y) =& |A_1| \cos[\kappa\alpha(1x + 3y) + A_1^a] \\
&+ |A_2| \cos[\kappa\alpha(3x - 3y) + A_2^a] \\
&+ |A_3| \cos[\kappa\alpha(1x + 1y) + A_3^a] \\
&+ |A_4| \cos[\kappa\alpha(3x - 1y) + A_4^a] \\
&+ |A_5| \cos[\kappa\alpha(1x - 1y) + A_5^a] \\
&+ |A_6| \cos[\kappa\alpha(3x + 1y) + A_6^a] \\
&+ |A_7| \cos[\kappa\alpha(1x - 3y) + A_7^a] \\
&+ |A_8| \cos[\kappa\alpha(3x + 3y) + A_8^a] \\
&+ |A_9| \cos[\kappa\alpha(1x + 2y) + A_9^a] \\
&+ |A_{10}| \cos[\kappa\alpha(3x - 2y) + A_{10}^a] \\
&+ |A_{11}| \cos[\kappa\alpha(1x - 2y) + A_{11}^a] \\
&+ |A_{12}| \cos[\kappa\alpha(3x + 2y) + A_{12}^a] \\
&+ |A_{13}| \cos[\kappa\alpha(2x - 2y) + A_{13}^a] \\
&+ |A_{14}| \cos[\kappa\alpha(2x + 2y) + A_{14}^a] \\
&+ |A_{15}| \cos[\kappa\alpha(1x) + A_{15}^a] \\
&+ |A_{16}| \cos[\kappa\alpha(2y) + A_{16}^a] + A_{17},
\end{aligned}
\tag{2.9}
$$

where $\kappa\alpha$ are the global modulation coefficients and $|A_i|$s and $A_i^a$s correspond to the magnitudes and phases of the channels shown in Figure 2.19, respectively. The channel contents are shown Table 2.3 and Kudenov's proposed reconstruction is shown in Table 2.4. As with other systems, not all channels containing a given Mueller matrix element are used for reconstruction of that element. The simulation of Kudenov's polarimeter can be seen in Figure 2.20, which clearly shows the reduced spatial resolution within the reconstruction due to sharing of that domain with the polarization information.

Table 2.1: Reproduced from Hagen et al. (2007). Fourier-Domain channels $C_n$ encoding the Mueller matrix elements for the 1-2-5-10 configuration. The OPD numbers listed for the channels are given in terms of multiples of $\text{OPD}_1(\sigma_0)$, the mean OPD of the thinnest retarder.

| $C_n$ | Channel Content $\times(64/S_{in,0})$ |
|---|---|
| 0 | $16m_{00}$ |
| $\pm 1$ | $8m_{01} + 4m_{02} \pm 4im_{03}$ |
| $\pm 2$ | $-m_{22} \pm im_{23} \mp im_{32} - m_{33}$ |
| $\pm 3$ | $-4m_{02} \mp 4im_{03}$ |
| $\pm 4$ | $2m_{21} + m_{22} \mp im_{23} \pm 2im_{31} \pm im_{32} + m_{33}$ |
| $\pm 5$ | $4m_{20} \pm 4im_{30}$ |
| $\pm 6$ | $2m_{21} + m_{22} \pm 1m_{23} \pm 2im_{31} \pm im_{32} - m_{33}$ |
| $\pm 7$ | $-2m_{12} \pm 2im_{13}$ |
| $\pm 8$ | $-m_{22} \mp im_{23} \mp im_{32} + m_{33}$ |
| $\pm 9$ | $4m_{11} + 2m_{12} \mp 2im_{13}$ |
| $\pm 10$ | $8m_{10}$ |
| $\pm 11$ | $4m_{11} + 2m_{12} \pm 2im_{13}$ |
| $\pm 12$ | $m_{22} \mp im_{23} \mp im_{32} - m_{33}$ |
| $\pm 13$ | $-2m_{12} \mp 2im_{13}$ |
| $\pm 14$ | $-2m_{21} - m_{22} \pm im_{23} \pm 2im_{31} + im_{32} + m_{33}$ |
| $\pm 15$ | $-4m_{20} \pm 4im_{30}$ |
| $\pm 16$ | $-2m_{21} - m_{22} \mp im_23 \pm 2im_{31} \pm im_{32} - m_{33}$ |
| $\pm 18$ | $m_{22} \pm im_{23} \mp im_{32} + m_{33}$ |

Table 2.2: Reproduced from Hagen et al. (2007). Spectrally resolved Mueller matrix elements $m_{ij}(\sigma)$ obtained by operating on spectral- domain Channels $c_n$. These are given in terms of the Fourier-domain channels by $c_n = [1/s_{in,0}(\sigma)]\mathcal{F}^{-1}\{w(\text{OPD})C_n(\text{OPD})\}$, for windowing function $w$.

| $m_{ij}(\sigma)$ | | $m_{ij}(\sigma)$ | |
|---|---|---|---|
| $m_{00}(\sigma) =$ | $4c_0$ | $m_{20}(\sigma) =$ | $16\Re[c_5]$ |
| $m_{01}(\sigma) =$ | $8(c_1 + c_3)$ | $m_{21}(\sigma) =$ | $32\Re[c_2 + c_4]$ |
| $m_{02}(\sigma) =$ | $-16\Re[c_3]$ | $m_{22}(\sigma) =$ | $-32\Re[c_2 + c_8]$ |
| $m_{03}(\sigma) =$ | $16\Re[c_1]$ | $m_{23}(\sigma) =$ | $32\Im[c_2 - c_8]$ |
| $m_{10}(\sigma) =$ | $8c_{10}$ | $m_{30}(\sigma) =$ | $16\Re[c_5]$ |
| $m_{11}(\sigma) =$ | $16(c_7 + c_9)$ | $m_{31}(\sigma) =$ | $16\Im[c_2 + c_4 + c_6 + c_8]$ |
| $m_{12}(\sigma) =$ | $-32\Re[c_7]$ | $m_{32}(\sigma) =$ | $-32\Im[c_2 + c_8]$ |
| $m_{13}(\sigma) =$ | $32\Im[c_7]$ | $m_{33}(\sigma) =$ | $32\Re[c_8 - c_2]$ |

51
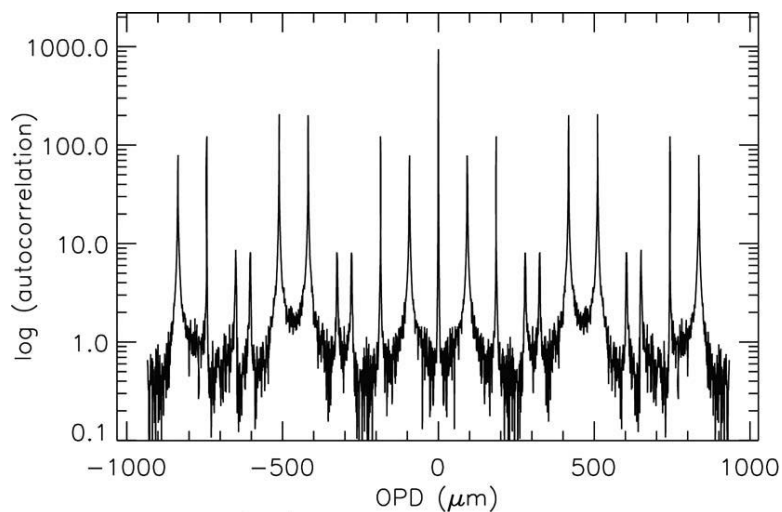


(a) The Fourier-domain representation of the measured spectrum.
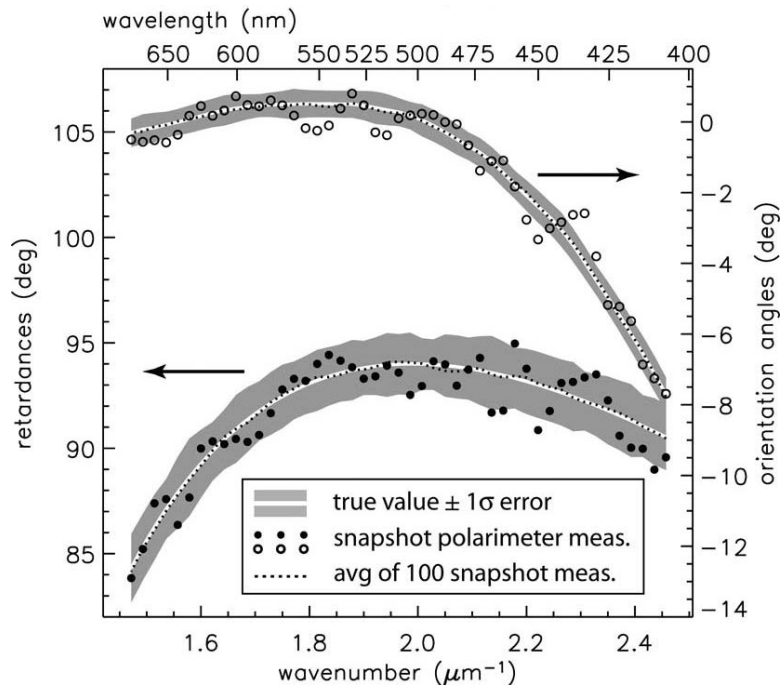


(b) The retardance $\delta(\sigma)$ and orientation angle $\theta(\sigma)$ of the sample reconstructed from the measured Mueller matrix elements. The error bars are obtained from the standard deviation of data taken over 100 instances of Poisson noise.

Figure 2.15: Reproduced from Hagen et al. (2007). Simulated measurement of an achromatic polymer retarder using a snapshot Mueller matrix polarimeter.
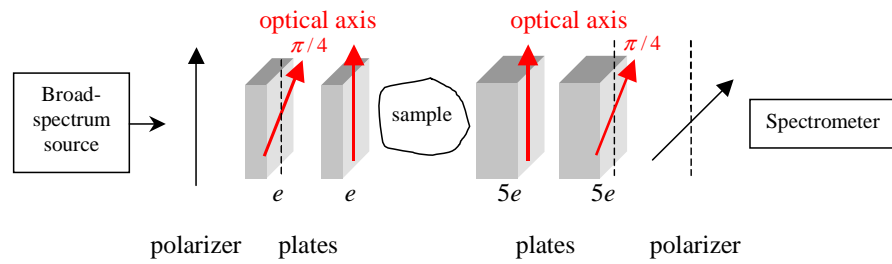
Figure 2.16: Reproduced from Dubreuil et al. (2007). Snapshot Mueller polarimeter for the configuration ( $e$ $e$ $5e$ $5e$ ).
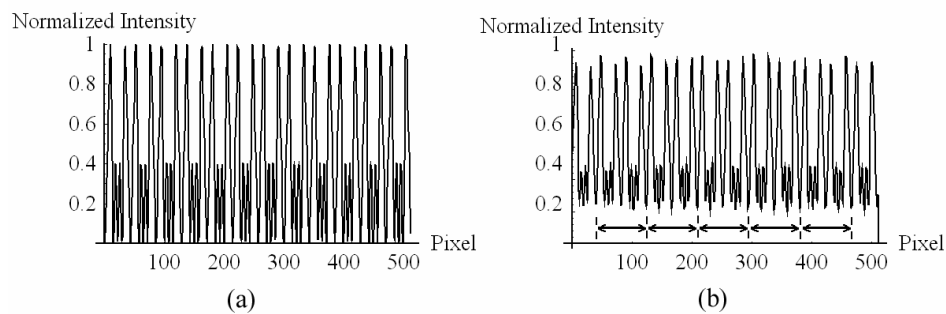


Figure 2.17: Reproduced from Dubreuil et al. (2007). Theoretical (a) and experimental (b) signals given by the snapshot Mueller polarimeter. The experimental signal is split into 5 zones for which the instantaneous frequency will be studied.
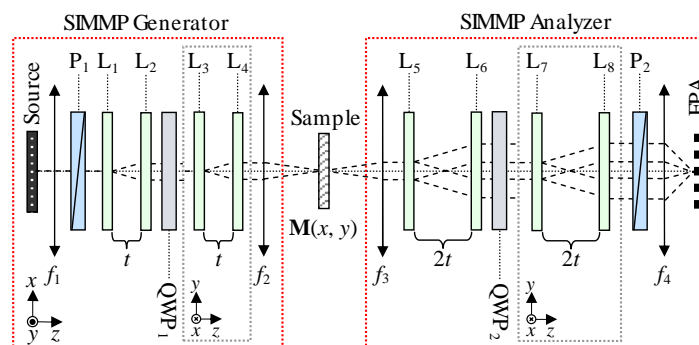


Figure 2.18: Reproduced from Kudenov et al. (2012). SIMMP optical configuration. PGs $L_1$, $L_2$, $L_5$ and $L_6$ shear the beam along $x$ while $L_3$, $L_4$, $L_7$ and $L_8$ shear along $y$. $P_1$ and $P_2$ are linear polarizers at 45° while two quarter wave-plates, $QWP_1$ and $QWP_2$, have fast axes oriented at 45° and 0°, respectively. All PGs have identical grating periods $\Lambda$ and the generator's and analyzer's PGs are separated by a distance $t$ and $2t$, respectively.

Table 2.3: Reproduced from Kudenov et al. (2012). Coefficient definitions for the intensity pattern. $C_{k,cal} = A_{rk}(C_{sk}/C_{rk})(C_{r17}/C_{s17})$.

| $A_k =$ | Coefficient $\times(S_{0,in}(x, y)/16)$ |
|---------|------------------------------------------|
| $A_1 =$ | $-m_{12} - m_{21} - im_{11} + im_{22} + 2m_{31} + 2im_{32}$ |
| $A_2 =$ | $-m_{12} + m_{21} + im_{11} + im_{22}$ |
| $A_3 =$ | $-m_{12} + m_{21} - im_{11} + im_{22} - 2m_{31} - 2im_{32} - 4m_{02} + 4im_{01}$ |
| $A_4 =$ | $-m_{12} - m_{21} - im_{11} + im_{22}$ |
| $A_5 =$ | $-m_{12} - m_{21} - im_{11} + im_{22} - 2m_{31} + 2im_{32} - 4m_{02} + 4im_{01}$ |
| $A_6 =$ | $-m_{12} + m_{21} + im_{11} + im_{22}$ |
| $A_7 =$ | $-m_{12} + m_{21} + im_{11} + im_{22} + 2m_{31} + 2im_{32}$ |
| $A_8 =$ | $-m_{12} - m_{21} - im_{11} + im_{22}$ |
| $A_9 =$ | $-2m_{23} - 2im_{13} - 4m_{33}$ |
| $A_{10} =$ | $-2m_{23} + 2im_{13}$ |
| $A_{11} =$ | $-2m_{23} - 2im_{13} + 4m_{33}$ |
| $A_{12} =$ | $2m_{23} + 2im_{13}$ |
| $A_{13} =$ | $4m_{10} - 4im_{20}$ |
| $A_{14} =$ | $4m_{10} - 4im_{20}$ |
| $A_{15} =$ | $8im_{03}$ |
| $A_{16} =$ | $8im_{30}$ |
| $A_{17} =$ | $8m_{00}$ |

Table 2.4: Reproduced from Kudenov et al. (2012). Mueller Matrix Solutions from the Fourier domain.

| $m_{ij} =$ | Channel Combinations $\times|C_{r17}|/|C_{s17}|$ |
|-----------|--------------------------------------------------|
| $m_{00} =$ | $|C_{s17}|/|C_{r17}|$ |
| $m_{01} =$ | $-2\Im[A_{r2}C_{s2}/C_{r2} - A_{r3}C_{s3}/C_{r3} - A_{r5}C_{s5}/C_{r5} + A_{r8}C_{s8}/C_{r8}]$ |
| $m_{02} =$ | $-2\Re[A_{r1}C_{s1}/C_{r1} + A_{r3}C_{s3}/C_{r3} + A_{r5}C_{s5}/C_{r5} + A_{r7}C_{s7}/C_{r7}] - m_{23}/2$ |
| $m_{03} =$ | $-2\Im[A_{r15}C_{s15}/C_{r15}]$ |
| $m_{10} =$ | $4\Re[A_{r13}C_{s13}/C_{r13} + A_{r14}C_{s14}/C_{r13}]$ |
| $m_{11} =$ | $4\Im[A_{r2}C_{s2}/C_{r2} - A_{r4}C_{s4}/C_{r4} + A_{r6}C_{s6}/C_{r6} - A_{r8}C_{s8}/C_{r8}]$ |
| $m_{12} =$ | $-4\Re[A_{r2}C_{s2}/C_{r2} + A_{r4}C_{s4}/C_{r4} + A_{r6}C_{s6}/C_{r6} - A_{r8}C_{s8}/C_{r8}]$ |
| $m_{13} =$ | $-4\Im[A_{r9}C_{s9}/C_{r9} + A_{r11}C_{s11}/C_{r11}]$ |
| $m_{20} =$ | $-2\Im[A_{r13}C_{s13}/C_{r13} + A_{r14}C_{s14}/C_{r14}]$ |
| $m_{21} =$ | $-4\Re[A_{r1}C_{s1}/C_{r1} - A_{r3}C_{s3}/C_{r3} + A_{r5}C_{s5}/C_{r5} - A_{r7}C_{s7}/C_{r7}]$ |
| $m_{22} =$ | $4\Im[A_{r2}C_{s2}/C_{r2} + A_{r4}C_{s4}/C_{r4} + A_{r6}C_{s6}/C_{r6} + A_{r8}C_{s8}/C_{r8}]$ |
| $m_{23} =$ | $4\Re[A_{r10}C_{s10}/C_{r10} + A_{r12}C_{s12}/C_{r12}]$ |
| $m_{30} =$ | $2\Im[A_{r16}C_{s16}/C_{r16}]$ |
| $m_{31} =$ | $4\Re[A_{r1}C_{s1}/C_{r1} - A_{r4}C_{s4}/C_{r4} - A_{r6}C_{s6}/C_{r6} + A_{r7}C_{s7}/C_{r7}]$ |
| $m_{32} =$ | $-4\Im[A_{r1}C_{s1}/C_{r1} - A_{r4}C_{s4}/C_{r4} - A_{r6}C_{s6}/C_{r6} + A_{r7}C_{s7}/C_{r7}]$ |
| $m_{33} =$ | $-2\Re[A_{r9}C_{s9}/C_{r9} - A_{r11}C_{s11}/C_{r11}]$ |
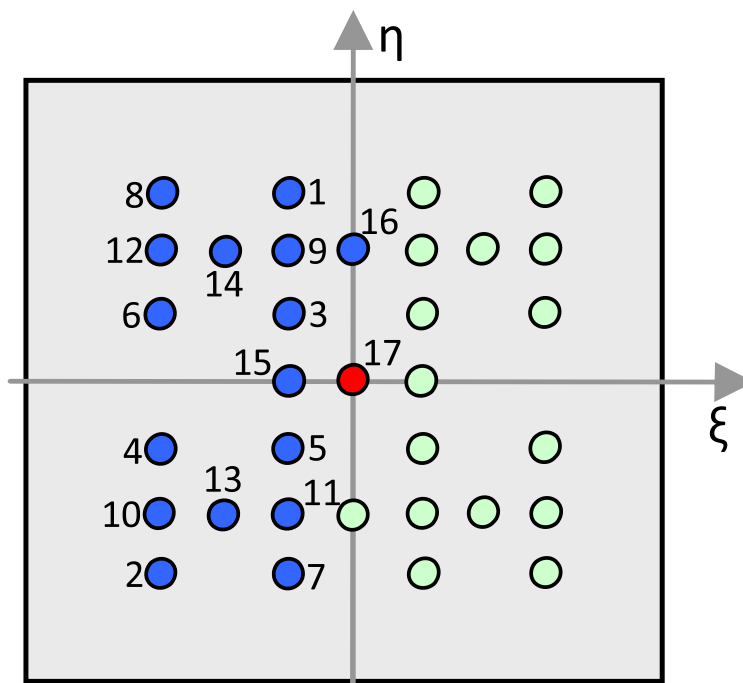
Figure 2.19: Reproduced from Kudenov et al. (2012). Fourier domain of a channeled image obtained from the SIMMP. Channel numbers correspond to the $k$ subscripts of the $A_k$ coefficients per Table 2.3. Only the non-conjugated channels are numbered for clarity.
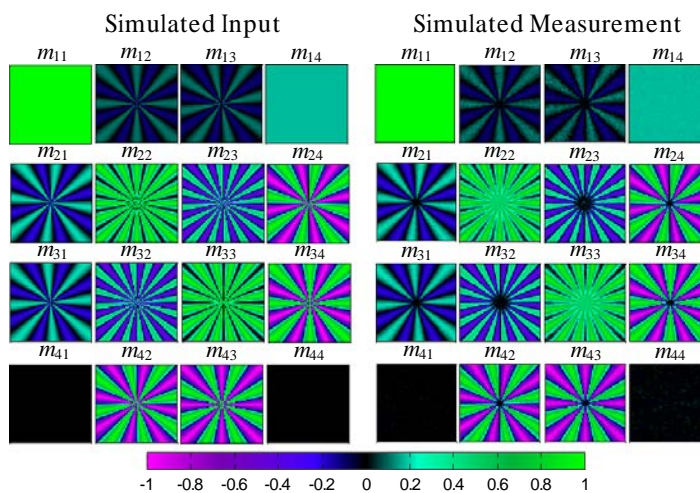


Figure 2.20: Reproduced from Kudenov et al. (2012). Simulated input (left) and measured (right) Mueller matrix of the quarter-wave vortex retarder.

## 2.3   Partial Systems

Although literature regarding partial polarimeters might seem limited, there are a number of developed applications that construct a partial system without necessarily treating it as such. Directly from Equation 1.2, it follows that if one is to measure $I_H$ and $I_V$, a partial system that is able to reconstruct $s_0$ and $s_1$ is created. Jacques's Pol measurement, for example, can be thought of as a primitive partial Stokes Vector Polarimeter (pSVP) (Jacques et al. (1999)),

$$\text{Pol} = \frac{I_{\parallel} - I_{\perp}}{I_{\parallel} + I_{\perp}} = \frac{s_1 \cos(\alpha) + s_2 \sin(\alpha)}{s_0}, \tag{2.10}$$

where $\alpha$ defines which direction is parallel and which is perpendicular with respect to the measurement. The DoFP discussed in Chapter 1 is another extension of the principle of taking a selection of canonical measurements to produce the estimate. Treating a mircogrid polarimeter as a conventional polarimeter rather than a channeled one is equivalent to reconstructing three information channels from four measurements, thereby constituting a partial measurement as well.

Developing a partial Stokes polarimeter does not require an overly elaborate consideration because there are relatively few degrees of freedom to be measured and thus, considered. Goudail and his co-workers have focused their attention on making single-measurement systems in order to enhance contrast for a given scene (Goudail and Tyo (2011); Anna et al. (2011a,b)). This dissertation, however, deals with the broader topic of making partial Mueller Matrix polarimeters (pMMPs) that were recently introduced (Hoover and Tyo (2007); Tyo et al. (2010); Alenin and Tyo (2012); Vaughn et al. (2012b)).

Hoover and Tyo (2007) created various textures on ABS polymer coupons by delivering different levels of laser fluences. Performing principal component analysis (PCA), authors deduced the following three polarization channels as being the most important for discrimination:

$$c_1 = -m_{11} + m_{22} + m_{33}, \tag{2.11a}$$

$$c_2 = -0.3(m_{01} + m_{10}) - 0.6(m_{11} - m_{22}) - m_{33}, \tag{2.11b}$$

$$c_3 = -m_{01} - m_{10} - 0.5(m_{22} - m_{33}), \tag{2.11c}$$

which grouped the different objects into clusters shown in Figure 2.21. Figure 2.23 shows the corresponding non-linear curve fitting. The reduced space was shown to be sufficient in separating the objects, which bodes well for pMMPs.

Finally, Tyo's subsequent publication has introduced the concept of pMMPs (Tyo et al. (2010)). By relying on Chipman's formalism (Chipman (2009b)), a set of canonical pMMP was identified. By properly selecting measurement conditions, a four-block pMMP was developed that is able to measure the following channels:

$$c_1 = m_{00}, \tag{2.12a}$$

$$c_2 = m_{i0}, \tag{2.12b}$$

$$c_3 = m_{0j}, \tag{2.12c}$$

$$c_4 = m_{ij}, \tag{2.12d}$$

where $0 < i, j \leq 3$. The premise of that paper is summarized well in Figure 2.22. Chapter 4 will show that the achieved space coverage by Tyo et al. (2010) is fairly sparse and will develop a much broader set of systems in the process.
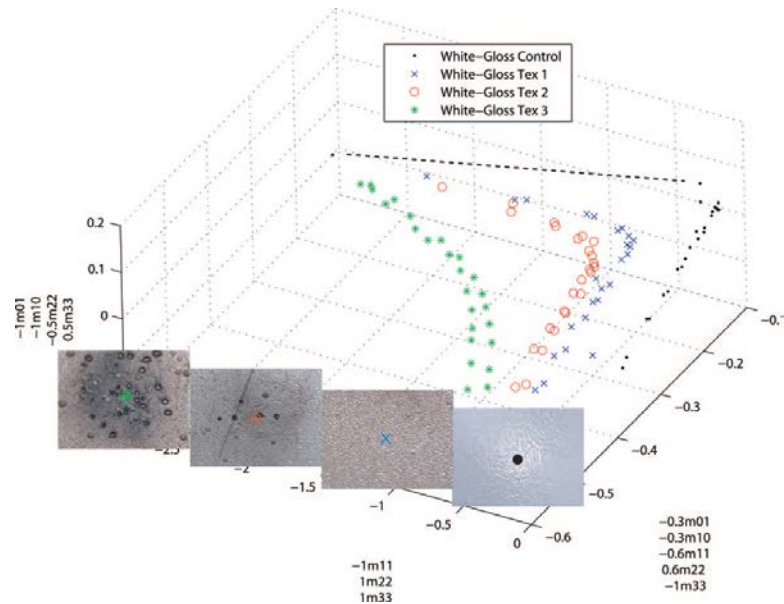
Figure 2.21: Reproduced from Hoover and Tyo (2007). Cluster diagram of data due to a family of textures on a white-gloss paint projected onto three principalcomponent channels. The dashed line indicates where data around the specular peak of the control sample is expected to fall.
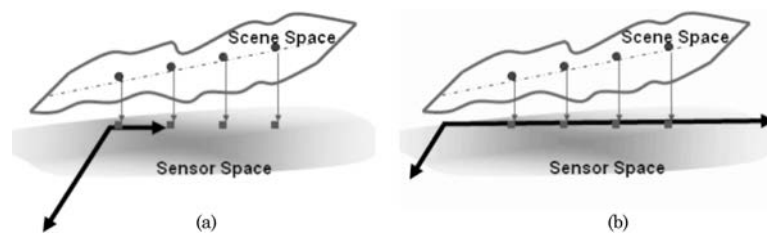


Figure 2.22: Reproduced from Tyo et al. (2010). These two one-dimensional scene spaces have the same angle with respect to the sensor space. However, the space in (a) projects into a direction in sensor space with poor SNR and the scene space in (b) projects into a direction in sensor space with good SNR.
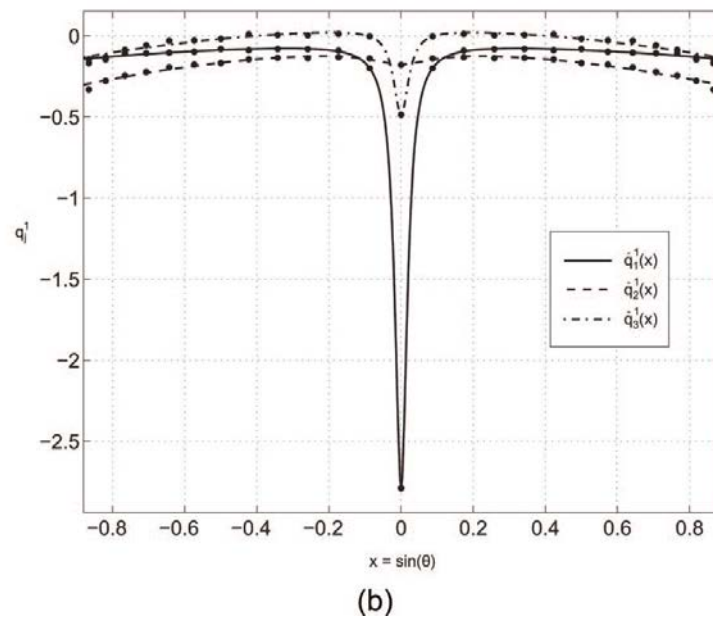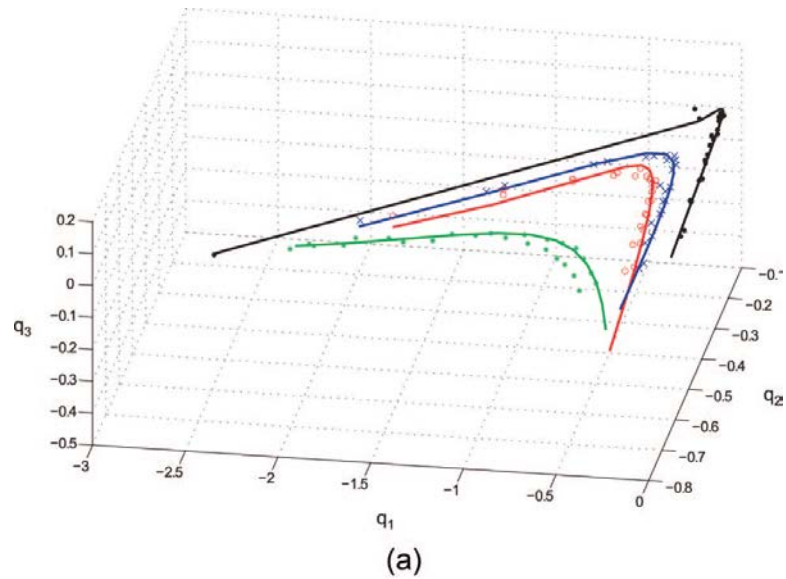
Figure 2.23: Reproduced from Hoover and Tyo (2007). Nonlinear fitting results. (a) Three-dimensional polynomial estimates overlaid on the data projections of Figure 2.21. (b) Control-sample data and estimate projections onto each of the principal-component channels as functions of the probe angle.

CHAPTER 3

GENERALIZED CHANNELED POLARIMETRY

The concepts of SNR optimality have been explored for conventional active and passive polarimeters using the Data Reduction Matrix (DRM) formalism (Chipman (2009a); Tyo (2002); Twietmeyer and Chipman (2008)), but they have not been applied to the class of channeled polarimeters that have emerged recently. Channeled or modulated polarimeters, the polarization states that define the measurement either spatially, temporally, spectrally, (LaCasse et al. (2011a)) or more than one simultaneously (LaCasse et al. (2011b)). Every one of those harmonic modulations will split the information in the corresponding Fourier domains, creating weighted copies of the Fourier transform of the data at the modulation's carrier frequencies. These multiplexed copies are called channels. Oka and his coworkers (Oka and Kato (1999); Oka and Kaneko (2003); Okabe et al. (2007)) have popularized the design concepts that go into making a channeled system, which were then further developed by Hagen et al. (2007), Kudenov et al. (2007, 2012) and others. This chapter introduces a toolkit to describe, analyze and optimize such systems, and investigates channeled polarimeters from the literature to show how they can be improved.

## 3.1    Introduction

There has been a number of proposed channeled systems in the past (Oka and Kato (1999); Oka and Kaneko (2003); Okabe et al. (2007); Kudenov et al. (2007); Hagen et al. (2007); Kudenov et al. (2012)) whose designs and corresponding reconstruction techniques were derived by hand. Lemaillet et al. (2008) proposed a way to optimize a spectrally channeled system by introducing linear algebraic inversions to map the information. Their effort, however, focused on one kind of system and stopped short of providing a complete solution to deal with any channeled polarimeter. This chapter describes the generalized methods that can be used to model channeled information mapping and guide the reconstruction.

A great advantage of a spatially or a spectrally channeled systems is the possibility of constructing a snapshot polarimeter. This reduces the temporal bandwidth penalties and removes the need for complex image registration that would be required in a temporally modulated system. In terms of object bandwidth, a snapshot channeled system favors temporal resolution at the cost of introducing stricter band limit constraints in other domains.

A common 2D FPA detector will be considered, which enables access to up to two modulation types to be mapped onto the two orthogonal axes. In addition to having no modulation, either spatial and spectral modulations cane be mapped into either $x$- or $y$-axes of the detector. Although the methods introduced here are general enough to be used with any channel structure on any orthogonal coordinate system, this chapter will focus on Cartesian coordinates, implying that the channels lie on a rectangular grid.

For the sake of completeness, temporal modulation is also considered. Such a system will obviously lose its snapshot nature, but it is conceivable that some middle ground solution could be found, whereby a very limited number of temporal measurements are made with intent of balancing the resolution loss among all possible modulation dimensions (LaCasse et al. (2011b,a)). Thus, a conventional detector will allow to split polarization information into a three dimensional structure of channels that can be manipulated to reconstruct the polarization information. When presented with a small number of temporal measurements, the resultant temporal frequency channels may contain as few as one data point. In those cases it may be prohibitive and unnecessary to work with the data in the Fourier domain; instead measurements can be used as information "channels" themselves with a clear benefit that they will contain modulation information more compactly.

### 3.1.1 Sinusoidal Channel Splitting

For typical channeled systems, $a_i$ and $g_j$ in Equations 1.10 and 1.15 are composed of a number of periodic functions. Every sinusoidal modulation splits the element information in $m_{ij}$ into two channels at certain frequencies within the Fourier domain of the modulation. For the available modulation dimensions of $x$, $y$, $\sigma$ (wavenumber) and $t$, the corresponding frequency dimensions will be called $\xi$, $\eta$, $\tau$ (optical path difference (OPD)) and $\nu$. Only the relevant equations for the $x$–$\xi$ pair will be shown, since all others can be obtained trivially.

The following Fourier transform pairs are well known (Alenin and Tyo (2014)):

$$1(x) \longleftrightarrow \delta(\xi), \tag{3.1a}$$

$$\cos(2\pi\xi_i x) \longleftrightarrow \tfrac{1}{2}[\delta(\xi + \xi_i) + \delta(\xi - \xi_i)], \tag{3.1b}$$

$$\sin(2\pi\xi_i x) \longleftrightarrow \tfrac{i}{2}[\delta(\xi + \xi_i) - \delta(\xi - \xi_i)]. \tag{3.1c}$$

In the general case, the modulation functions have multiple modulating frequencies as

$$f_M(x) = \prod_{m=1}^{M} {}^{\cos}_{\sin}(2\pi\xi_m x), \tag{3.2}$$

where ${}^{\cos}_{\sin}$ denotes that the function could either be a cosine or a sine. When $M$ sinusoids are multiplied together, a $2^M \times 2^M$ matrix can be created that will describe all the possible combinations of either $\pm\xi_m$ of the $\delta$-function, as well as distinguish between a cosine and a sine. Each sub-function will have a phasor that, when multiplied together, will yield the net phase of the particular channel-weight. This "look-up-table" can be created by means of an outer product of two matrices:

$$\underline{\underline{\mathbf{F}}}_M \equiv \begin{bmatrix} \underline{\mathbf{f}}_1 & \underline{\mathbf{f}}_2 & \cdots & \underline{\mathbf{f}}_M \end{bmatrix}, \tag{3.3a}$$

$$\underline{\underline{\mathbf{O}}}_M \equiv \begin{bmatrix} \underline{\mathbf{o}}_1 & \underline{\mathbf{o}}_2 & \cdots & \underline{\mathbf{o}}_M \end{bmatrix}, \tag{3.3b}$$

where $f_{m,k}$ is 0 for cosine and 1 for sine, while $o_{m,\ell}$ is $-1$ for $-\xi_i$ and $+1$ for $+\xi_i$. $\underline{\underline{\mathbf{F}}}_M$ and $\underline{\underline{\mathbf{O}}}_M$ are both $2^M \times M$ in size. The Frequency Phase Matrix (FPM) is then,

$$\underline{\underline{\mathbf{P}}}_M \equiv \frac{1}{2^M} \exp\left[\frac{-i\pi}{2}\left(\underline{\underline{\mathbf{F}}}_M \underline{\underline{\mathbf{O}}}_M^{\mathrm{T}}\right)\right]. \tag{3.4}$$

Cases of $M = 1, \ldots, 5$ are shown in Figure 3.1. Given any modulation, the rows can be extracted from an appropriately-sized FPM and the coefficients placed at the contributing frequencies, thereby creating $\underline{\mathbf{q}}^{\mathrm{T}}$. Note that this vector matches the uniform sampling of the underlying grid and has $2\xi_{max} + 1$ elements.

For some polarimeters the induced modulation may be more complicated than the one prescribed by Equation 3.2. For example, Diner et al. (2007) describe a system that employs components applying Bessel function modulation. In order to treat those modulation schemes, an addition of modulating functions can be allowed, effectively treating
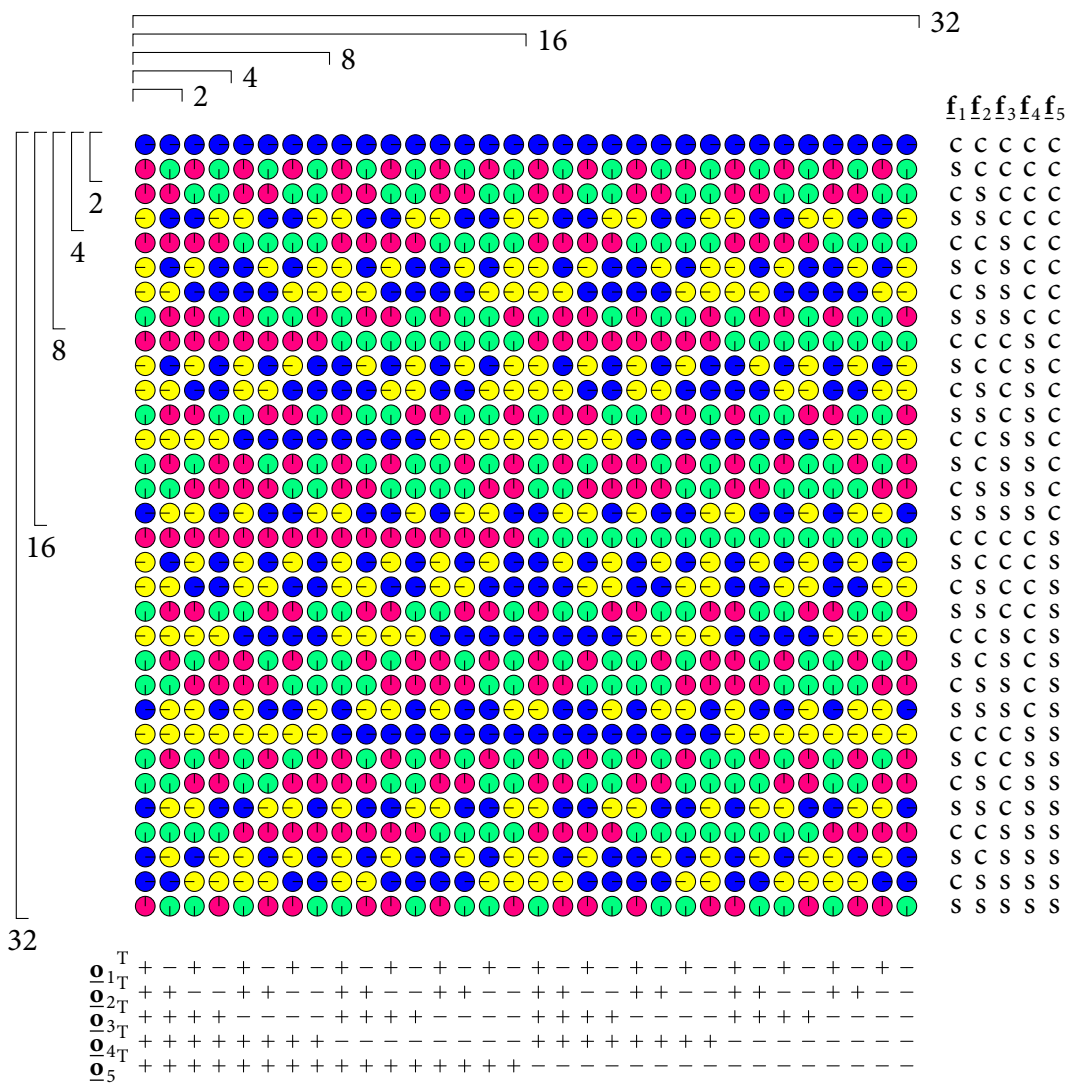
Figure 3.1: First five FPMs. The circles represent the polar form of the coefficients: ● = +1, ● = +i, ● = −1, ● = −i. Each FPM has an omitted weight of $2^{-M}$. If $\xi_i = \xi_j$, then $\delta(\xi \pm \cdots + \xi_i - \xi_j \pm \cdots)$ and $\delta(\xi \pm \cdots - \xi_i + \xi_j \pm \cdots)$ will combine and change the magnitude of the impulse at that frequency. The side brackets denoted with 2/4/8/16/32 can be used as crop guidelines for obtaining FPMs for $M = 1/2/3/4/5$.

individual FPMs as a basis set. The total FPM can be decomposed into $L$ sub-FPMs,

$$\underline{\underline{P}}_{\text{total}} = \underline{\underline{P}}_{M_1} + \underline{\underline{P}}_{M_2} + \cdots + \underline{\underline{P}}_{M_L}, \tag{3.5}$$

which can be calculated separately and simply added together. The involved frequency coefficients will be potentially more complicated, but they should present no additional computational challenge within the prescribed methods.

There are several ways by which to combine modulations in multiple domains into a total structure of channels. If each dimension's structure is already determined, they can combined using a Kronecker product,

$$\underline{\mathbf{q}}_{\{\tau\}} \otimes \underline{\mathbf{q}}_{\{\omega\}} \otimes \underline{\mathbf{q}}_{\{\xi\}} \otimes \underline{\mathbf{q}}_{\{\eta\}}. \tag{3.6}$$

On the other hand, if the order of modulation dimensions alternates between elements, convolution can be used to create the $N$-dimensional cloud of channels that would then need to be unfolded into a vector.

As an example, consider four polarization modulation elements that operate over $x/y/x/y$, or equivalently modulate into $\xi/\eta/\xi/\eta$. The total vector is then

$$\text{vec}\left(\underline{\mathbf{q}}_{\{\xi_{e_1}\}} *_n \underline{\mathbf{q}}_{\{\eta_{e_2}\}} *_n \underline{\mathbf{q}}_{\{\xi_{e_3}\}} *_n \underline{\mathbf{q}}_{\{\eta_{e_4}\}}\right), \tag{3.7}$$

where $*_n$ redundantly implies that the vectors are differently oriented or, more generally, can be described as degenerate $N$-dimensional structures. In this example, $\underline{\mathbf{q}}_{\{\xi_{e_1}\}}$ and $\underline{\mathbf{q}}_{\{\xi_{e_3}\}}$ are row vectors, while $\underline{\mathbf{q}}_{\{\eta_{e_2}\}}$ and $\underline{\mathbf{q}}_{\{\eta_{e_4}\}}$ are column vectors. The result of the convolution operation is a matrix and needs to be unfolded using the vec operation defined above. The choice of row/column over column/row addressing is arbitrary at first, but once chosen must be maintained consistently.

The total vector can also be generated by recognizing that the modulation patterns can be viewed as either a test dyad or a projection target. By treating it as a dyad, $\underline{\underline{D}} = \underline{\underline{A}}\,\underline{\underline{G}}^{\mathrm{T}}$, its Fourier transform can be inspected, $\mathcal{F}\{\underline{\underline{D}}\} = \mathcal{F}\{\underline{\underline{A}}\} * \mathcal{F}\{\underline{\underline{G}}\}^{\mathrm{T}}$, with $*$ now being a matrix convolution (same as multiplication, but every product is replaced with convolution between the same elements and added as before). That allows PSG and PSA modulations to be combined as

$$\underline{\mathbf{q}}_{m_{ij}} = \text{vec}\left(\underline{\mathbf{q}}_{g_i} * \underline{\mathbf{q}}_{a_j}\right). \tag{3.8}$$

Finally, after using any of these methods to construct the Mueller element modulation vectors, all 16 of them need to be combined into the corresponding $\underline{\underline{\mathbf{Q}}}$ matrix

$$\underline{\underline{\mathbf{Q}}} = \begin{bmatrix} \underline{\mathbf{q}}^{\mathrm{T}}_{\{\tau,\omega,\xi,\eta\};m_{00}} \\ \underline{\mathbf{q}}^{\mathrm{T}}_{\{\tau,\omega,\xi,\eta\};m_{01}} \\ \underline{\mathbf{q}}^{\mathrm{T}}_{\{\tau,\omega,\xi,\eta\};m_{02}} \\ \underline{\mathbf{q}}^{\mathrm{T}}_{\{\tau,\omega,\xi,\eta\};m_{03}} \\ \underline{\mathbf{q}}^{\mathrm{T}}_{\{\tau,\omega,\xi,\eta\};m_{10}} \\ \underline{\mathbf{q}}^{\mathrm{T}}_{\{\tau,\omega,\xi,\eta\};m_{11}} \\ \underline{\mathbf{q}}^{\mathrm{T}}_{\{\tau,\omega,\xi,\eta\};m_{12}} \\ \underline{\mathbf{q}}^{\mathrm{T}}_{\{\tau,\omega,\xi,\eta\};m_{13}} \\ \underline{\mathbf{q}}^{\mathrm{T}}_{\{\tau,\omega,\xi,\eta\};m_{20}} \\ \underline{\mathbf{q}}^{\mathrm{T}}_{\{\tau,\omega,\xi,\eta\};m_{21}} \\ \underline{\mathbf{q}}^{\mathrm{T}}_{\{\tau,\omega,\xi,\eta\};m_{22}} \\ \underline{\mathbf{q}}^{\mathrm{T}}_{\{\tau,\omega,\xi,\eta\};m_{23}} \\ \underline{\mathbf{q}}^{\mathrm{T}}_{\{\tau,\omega,\xi,\eta\};m_{30}} \\ \underline{\mathbf{q}}^{\mathrm{T}}_{\{\tau,\omega,\xi,\eta\};m_{31}} \\ \underline{\mathbf{q}}^{\mathrm{T}}_{\{\tau,\omega,\xi,\eta\};m_{32}} \\ \underline{\mathbf{q}}^{\mathrm{T}}_{\{\tau,\omega,\xi,\eta\};m_{33}} \end{bmatrix}^{\mathrm{T}} \tag{3.9}$$

that maps an input Mueller vector into a channel vector,

$$\mathcal{F}\{\underline{\mathbf{C}}\} = \underline{\underline{\mathbf{Q}}}\,\mathcal{F}\{\underline{\mathbf{M}}'\}, \tag{3.10}$$

where $\underline{\mathbf{C}}$ describes the channels contents. However, since channels are measured directly, the opposite operation is desired. To do that, the pseudo inverse of $\underline{\underline{\mathbf{Q}}}$ can be obtained much like in DRM. By correctly arranging Fourier transform operations around the multiplication, the reverse mapping can be used to get back to the Mueller elements' information,

$$\underline{\mathbf{M}}' = \mathcal{F}^{-1}\left\{\underline{\underline{\mathbf{Q}}}^{+}\,\mathcal{F}\{\underline{\mathbf{C}}\}\right\}. \tag{3.11}$$

An important piece of insight can be obtained if $\underline{\underline{\mathbf{Q}}}$ is recognized to not be that much different from $\underline{\underline{\mathbf{D}}}'$; however, whereas before multiple dyads were constructed against which

Figure 3.2: Modulations for each Mueller element as a convolution of modulations in the respective PSG and PSA elements and the corresponding rearrangement of channel modulations into the total $\underline{\underline{\mathbf{Q}}}$ matrix. In this example, a verbose $7 \times 7$ grid of frequencies is defined, and empty channels are constructed where the information exists for any Mueller element. (Animation available in the digital version)

to test the Mueller object, it is now possible to have a very limited number of dyads. This is because the particular modulation choices create a multi-dimensional "pointer" that can be unfolded to the full $\underline{\underline{\mathbf{Q}}}$ representation. As an example of $\underline{\underline{\mathbf{Q}}}$ construction, consider the modulations and their reordering in Figure 3.2.

### 3.1.2 Snapshot Channels

A snapshot measurement implies that there is no temporal modulation, which consequently means that no additional (other than the exposure time) temporal band-limit constraints are placed on the captured scene. If each dimension on the 2D detector can carry spatial, spectral or no modulation, a verbose set of nine snapshot channeled systems can be created, as depicted in Figure 3.3. These nine systems can be further separated into two
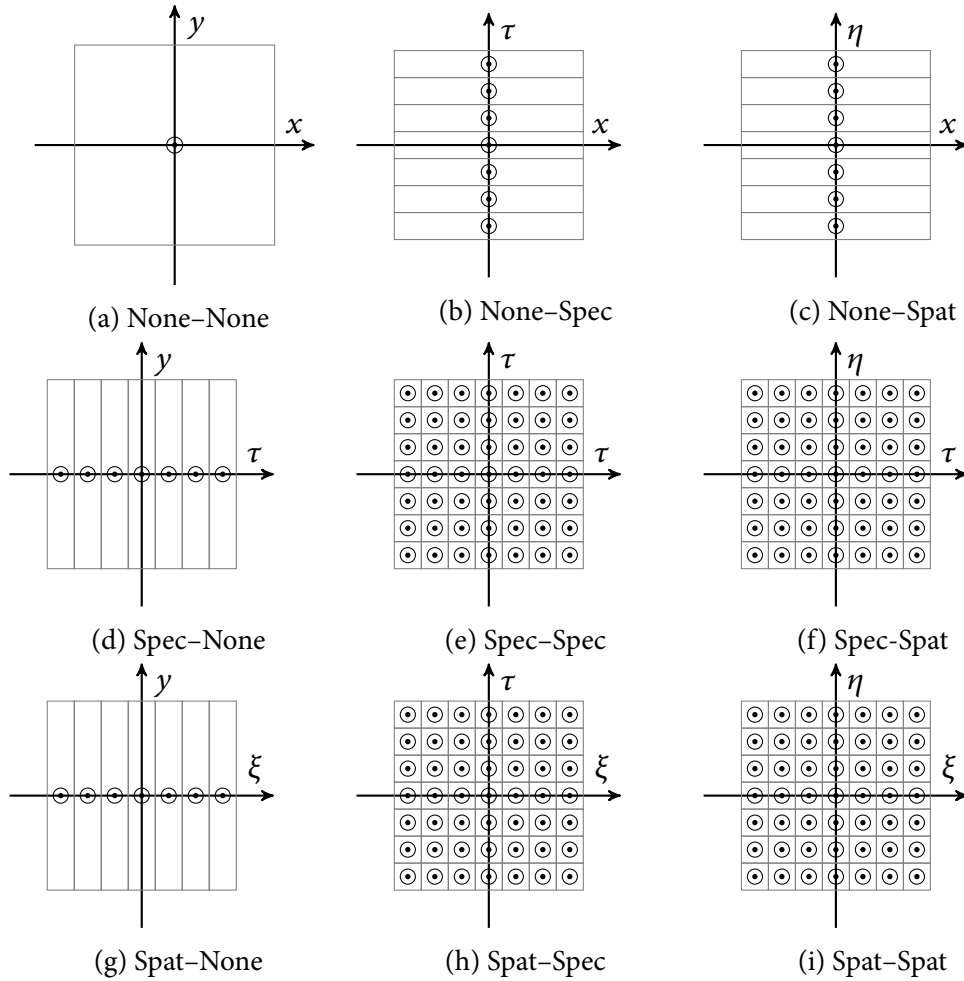
Figure 3.3: Snapshot systems. Case (a) provides no modulation. Case (e) is not straightforward to implement physically. Case pairs (b)/(d), (c)/(g) and (f)/(h) are essentially equivalent.

classes: one-dimension-modulating (b/c/d/g) and two-dimension-modulating (e/f/h/i). An example of each will be studied.

Further developing the consideration of physical realizability, several snapshot measurements can be taken. This gives an easy access to a third modulation dimension — time. Provided that the temporal modulation is captured in even time steps, the Fourier transform can be used to create the corresponding channels. However, since in most cases this will create more channels than the original data, with all channels being a single pixel, using the Fourier coefficients does not present any advantage. Instead, the captured snap-

(a) Six snapshots with 25 $\xi$–$\eta$ channels each    (b) Ten snapshots with 9 $\tau$–$y$ channels each
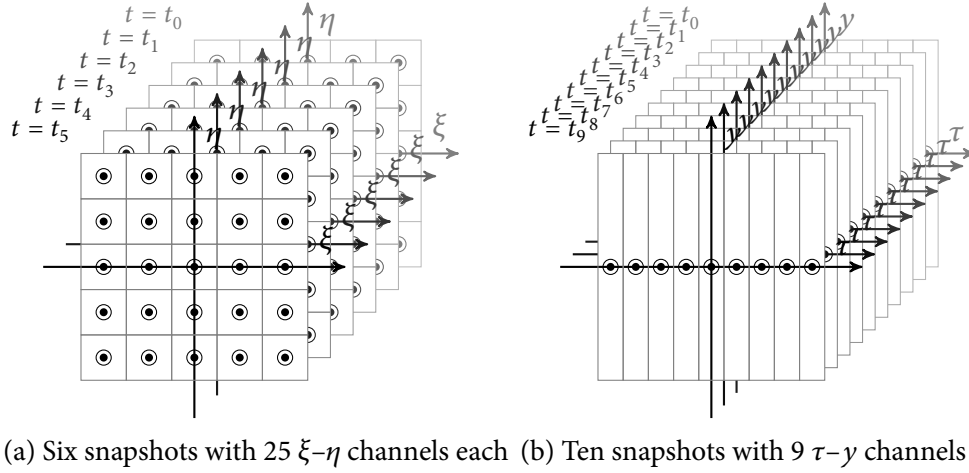
Figure 3.4: Hypothetical multi-snapshot systems that can be analyzed with the proposed formalism.

shots themselves can be used as "direct channels", or simply, projection targets like in the $\underline{\underline{\mathbf{W}}}'$ formalism, namely,

$$\underline{\underline{\mathbf{Q}}}_{\text{total}} = \begin{bmatrix} \underline{\underline{\mathbf{Q}}}_{t_1}^{\mathrm{T}} & \underline{\underline{\mathbf{Q}}}_{t_2}^{\mathrm{T}} & \cdots & \underline{\underline{\mathbf{Q}}}_{t_N}^{\mathrm{T}} \end{bmatrix}^{\mathrm{T}}. \tag{3.12}$$

This removes the need to have evenly spaced samples, yet maintains the compressed nature of $\underline{\underline{\mathbf{Q}}}$. Figure **??** demonstrates the kinds of systems this alteration can handle. Note that even though only temporal modulation is represented with direct channels, it is possible to treat other domain modulations similarly. For example, if one subdivides the FPA into a small number of sections performing different polarization analyses, it might be preferred to treat those sections as direct channels.

### 3.1.3  Channeled Reconstruction

Much like the reconstruction described in Section 1.4, an SVD method is used to calculate the pseudoinverse for reasons of its numerical stability and higher capacity for manipulation. First, $\underline{\underline{\mathbf{Q}}}$ is decomposed as

$$\underline{\underline{\mathbf{Q}}} = \underline{\underline{\mathbf{U}}}_{\mathbf{Q}}\,\underline{\underline{\mathbf{\Sigma}}}_{\mathbf{Q}}\,\underline{\underline{\mathbf{V}}}_{\mathbf{Q}}^{\dagger}, \tag{3.13}$$

where the matrices $\underline{\underline{\mathbf{U}}}$ and $\underline{\underline{\mathbf{V}}}$ are $N_C \times N_C$ and $16 \times 16$ complex, orthonormal matrices, respectively, with $N_C$ denoting the number of constructed channels. Provided that the

system is full as opposed to partial, $\underline{\underline{\Sigma}}$ is a $N_C \times 16$ reduced diagonal matrix containing the 16 singular values $\sigma_1 \geq \sigma_2 \geq \ldots \geq \sigma_{16} > 0$. The pseudoinverse can be written as

$$\underline{\underline{Q}}^+ = \underline{\underline{V}}_Q \underline{\underline{\Sigma}}_Q^+ \underline{\underline{U}}_Q^\dagger, \tag{3.14}$$

where $\underline{\underline{\Sigma}}^+$ is the $16 \times N_C$ reduced diagonal matrix with the inverses of the singular values.

## 3.2 Examples

This section discusses systems, for which the intensity can be written generally as

$$I(\vec{\vartheta}) = \sum_{i=0}^{3} \sum_{j=0}^{3} f_{a_i}(\vec{\vartheta}) m_{ij}(\vec{\vartheta}) f_{g_j}(\vec{\vartheta}), \tag{3.15}$$

where $\vec{\vartheta}$ is used to denote a set of domains where the information is modulated. The two functions, $f_{a_i}(\vec{\vartheta})$ and $f_{g_j}(\vec{\vartheta})$, define the polarimeter design and can be used to derive $\underline{\underline{Q}}$ using methods outlined in Section 3.1.1.

By simplifying the generation of polarimeter design, the idealized SNR can be calculated from $\underline{\underline{Q}}$ directly, without performing full simulations of the system. Simply changing the way the problem is written allows for introduction of more optimization parameters that can help find an optimal polarimeter. Several systems from the literature are examined to see how the introduced concepts could help increase their performance.

Sabatke introduced Equally Weighted Variance (EWV) as an appropriate metric to evaluate Stokes polarimetersSabatke et al. (2000), and Twietmeyer later adopted a similar metric for use with Mueller polarimeters.Twietmeyer and Chipman (2008) In the context of Equation 1.21,

$$\text{EWV} = \text{tr}\left[\underline{\underline{K}}_{\underline{\underline{W}}'^+}\right] = \sum_{k=0}^{15} 1/\sigma_{\underline{\underline{W}}'^+,k}^2, \tag{3.16}$$

where $\underline{\underline{K}}_{\underline{\underline{W}}'^+}$ is the covariance matrix $\underline{\underline{W}}'^+ \underline{\underline{W}}'^{+\mathrm{T}}$. To use EWV for channeled systems, the calculation merely needs to be performed with $\underline{\underline{Q}}^+$ instead of $\underline{\underline{W}}'^+$.

Without needing to establish any particulars of a system first, a general statement can be made that if the channel structures form an orthogonal basis set, the system will be optimal. This optimality arises from the fact that channel cross-talk is eliminated when $\underline{\underline{K}}$ is diagonal. To investigate the lower limit of the EWV, orthogonality is simply assumed. In

order to describe the surface of the Poincaré sphere, two parameters are needed — azimuth and elevation angles. To modulate sufficiently, two carrier frequencies associated with the two spherical parameters in both the PSG and the PSA need to be introduced.

As a result, modulation based on spherical coordinate mapping provides the smallest number of carrier frequencies, while remaining physically realizable, i.e.,

$$\underline{\mathbf{f}}_{\underline{\mathbf{G}}} = \begin{bmatrix} 1 \\ \cos(2\pi\vartheta_1\tilde{\vartheta}_1) \\ \sin(2\pi\vartheta_1\tilde{\vartheta}_1)\cos(2\pi\vartheta_2\tilde{\vartheta}_2) \\ \sin(2\pi\vartheta_1\tilde{\vartheta}_1)\sin(2\pi\vartheta_2\tilde{\vartheta}_2) \end{bmatrix}, \tag{3.17a}$$

$$\underline{\mathbf{f}}_{\underline{\mathbf{A}}} = \begin{bmatrix} 1 \\ \cos(2\pi\vartheta_3\tilde{\vartheta}_3) \\ \sin(2\pi\vartheta_3\tilde{\vartheta}_3)\cos(2\pi\vartheta_4\tilde{\vartheta}_4) \\ \sin(2\pi\vartheta_3\tilde{\vartheta}_3)\sin(2\pi\vartheta_4\tilde{\vartheta}_4) \end{bmatrix}, \tag{3.17b}$$

where $\vartheta_i$ are modulation domains, and $\tilde{\vartheta}_i$ are the corresponding carrier frequencies. The insight of Figure 3.1 allows a simple writing down of the number of frequencies present in each PSG/PSA element as $\underline{\mathbf{n}}_A = \underline{\mathbf{n}}_G = \begin{bmatrix} 1 & 2 & 4 & 4 \end{bmatrix}^{\mathrm{T}}$. Assuming independence, the minimal EWV follows,

$$\mathrm{EWV}_{\min} = \sum \underline{\mathbf{n}}_G \otimes \underline{\mathbf{n}}_A, \tag{3.18}$$

which for the assumed modulation is equal to 121. A better EWV is mathematically possible, but would require that $\underline{\mathbf{n}}_A$ and $\underline{\mathbf{n}}_G$ contain fewer modulating frequencies. Quite expectedly, a more efficient modulation than the one stemming from spherical coordinates was not found, as all of them required a Degree of Polarization (DoP) greater than 1, thereby violating the condition specified in Equation 1.3.

### 3.2.1   One Dimensional Channeled Systems

In order to treat single dimension systems generally, the rigorous channel creation description needs to be forgone for now and the initial discussion limited to frequency ratios. Given spherical mapping's implied proper selection of sines and cosines for modulation

Table 3.1: Channeled system designs with the lowest EWV for a given number of channels. The corresponding bandwidth of a system will be proportional to $\frac{1}{N_C}$.

| $N_C$ | $\text{EWV}_{\text{min}}$ | Configuration |
|---|---|---|
| 19 | 350.5664 | ( 3  1  3  2 ) |
| 21 | 259.1667 | ( 2  1  2  5 ) |
| 23 | 176.8039 | ( 2  1  2  6 ) |
| 25 | 169.5152 | ( 2  1  2  7 ) |
| 27 | 158.1018 | ( 2  1  3  7 ) |
| 29 | 137.6667 | ( 3  2  1  8 ) |
| 31 | 137.3810 | ( 2  1  3  9 ) |
| 33 | 121.0000 | ( 1  4  2  9 ) |
| 35 | 126.7143 | ( 2  1  4  10 ) |
| 37 | 121.0000 | ( 2  1  4  11 ) |
| 39 | 121.0000 | ( 2  1  4  12 ) |
| $41 + 2n$ | 121.0000 | ( 2  1  5  $12 + n$ ), $n \in \mathbb{N}_0$ |

functions, the polarimeter configuration can be described with

$$\underline{\mathbf{d}} = ( \ \tilde{\vartheta}_1 \quad \tilde{\vartheta}_2 \quad \tilde{\vartheta}_3 \quad \tilde{\vartheta}_4 \ ), \tag{3.19}$$

which is a vector containing the proportional modulation frequencies in order of the polarization elements. The total number of channels produced is

$$N_C = 1 + 2 \sum_{i=1}^{4} d_i. \tag{3.20}$$

To find optimal configurations, a number of optimizations were run that were constrained to have a particular number of channels. The results of those optimizations are summarized in Table 3.1.

Now consider the spectral-none channeled polarimeter proposed by Hagen et al. (2007), which can be seen in Figure 2.13. The polarimeter uses two thick retarders in both the PSG and the PSA to modulate in wavenumber. Using Equation 3.15, the system

can be described with the following modulation sets,

$$\underline{\mathbf{f}}_{\mathbf{G}} = \begin{bmatrix} 1 \\ \cos(c_1\sigma) \\ \sin(c_1\sigma)\sin(c_2\sigma) \\ \sin(c_1\sigma)\cos(c_2\sigma) \end{bmatrix}, \quad (3.21a)$$

$$\underline{\mathbf{f}}_{\mathbf{A}} = \begin{bmatrix} 1 \\ \cos(c_4\sigma) \\ \sin(c_3\sigma)\sin(c_4\sigma) \\ \cos(c_3\sigma)\sin(c_4\sigma) \end{bmatrix}. \quad (3.21b)$$

The argument

$$c_i\sigma = 2\pi\tau_i\sigma = 2\pi d_o d_i \lambda_o B\sigma, \quad \tau_i = d_o d_i \lambda_o B \quad (3.22)$$

contains the global thickness factor, $d_o$, individual retarder thickness factor, $d_i$, center wavelength, $\lambda_o$, and birefringence, $B$. The vector $\underline{\mathbf{d}}$ contains all the modulation information in the form of proportional frequencies from Equation 3.19. Now, the modulations are no longer in an arbitrary relation to one another — the positions and orientations of the retarders and polarizers in the system determine that selection. This chapter only concerns itself with the mathematics of the design and as such, only the details that make the discussion complete are presented.

Hagen chooses $\underline{\mathbf{d}} = ( 1 \quad 2 \quad 5 \quad 10 )$, meaning $N_C = 37$. The resulting channels are shown in Table 2.1, and the proposed reconstruction scheme is shown in Table 2.2. From the proposed reconstruction, it is seen that some measurements are ignored for the sake of algebraic simplicity — only channels $c_0 - c_{10}$ are referenced, with real and imaginary operators constituting the use of conjugates. Thus, instead of using all 37 channels, only 21 are used. An alternative method would be to recognize the modulation induced by retarders, construct an appropriate FPM, look up the coefficients and construct $\underline{\underline{\mathbf{Q}}}$ by placing them at the contributing frequencies. The resultant $\underline{\underline{\mathbf{Q}}}$ and its inverse can be seen in Figure 3.5. Those matrices represent Tables 2.1 and 2.2 more compactly. The system in Figure 3.6 was found using trial-and-error to see if other arrangements of the same elements can produce better results. The system in Figure 3.7 was found through optimization with

(a) $\underline{\underline{Q}}$           (b) $\underline{\underline{Q}}^+$
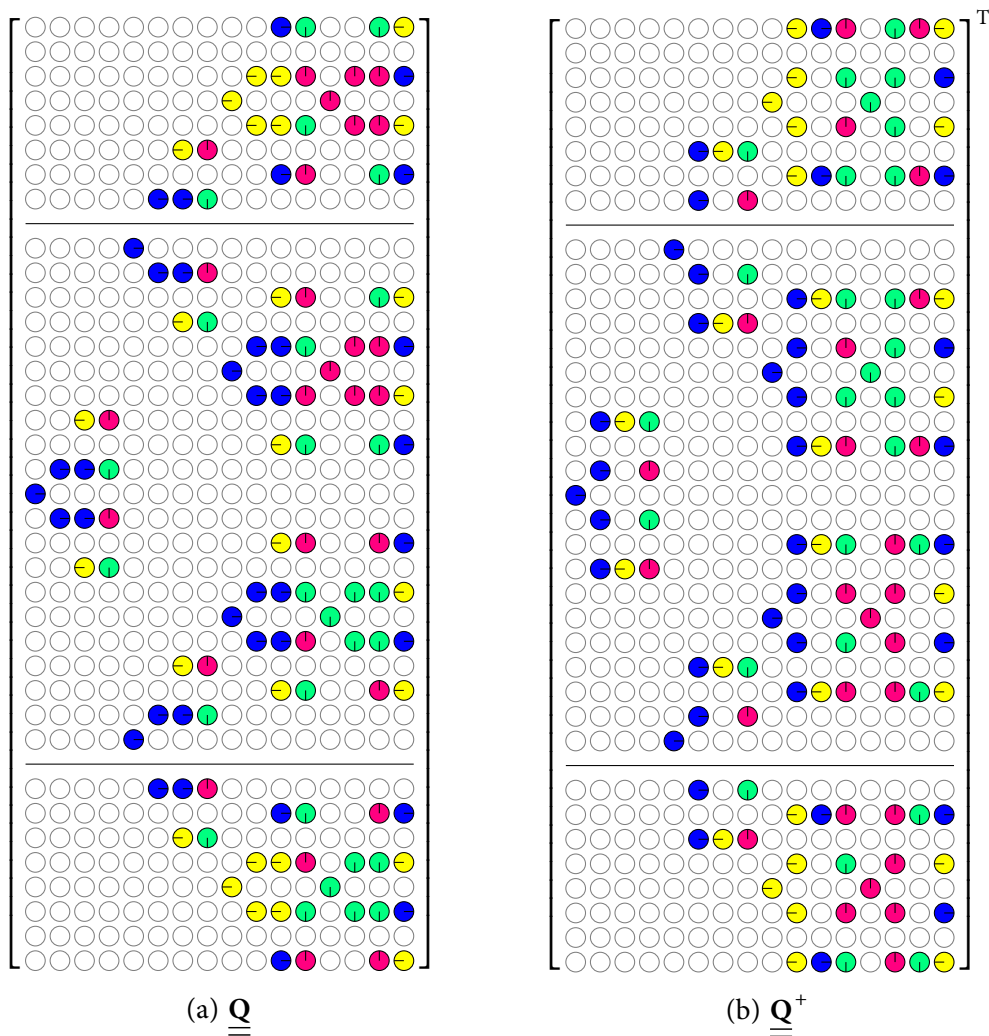
Figure 3.5: Polarimeter proposed by Hagen et al. (2007), with $\underline{d}$ = ( 1  2  5  10 ). This representation shows channels as rows and Mueller elements as columns. The matrix containing 21 cropped channels can be seen between the two horizontal lines and has an EWV of 355; including the other 16 channels lowers the EWV to 187. These extra channels must be measured to prevent aliasing. The distinction is whether the data contained within these channels is used in reconstruction, after the Fourier transform of the measured intensity was found.
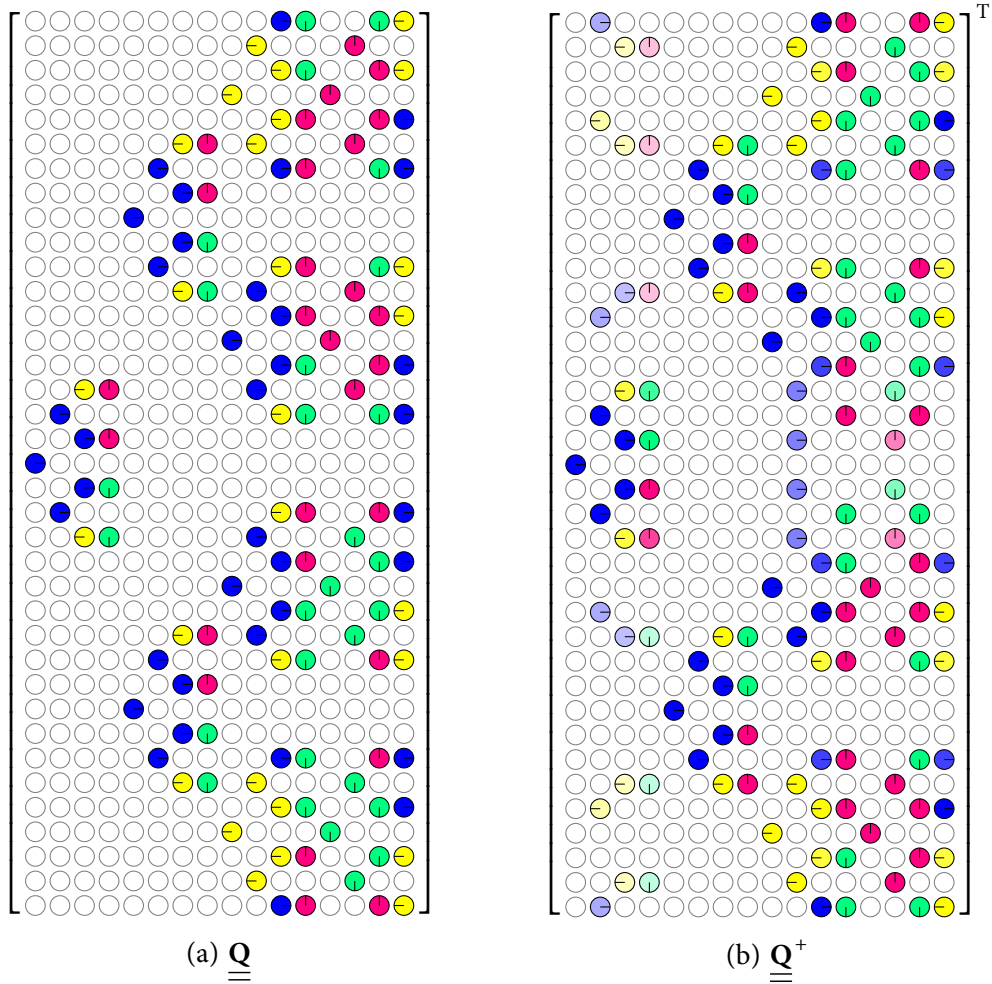
Figure 3.6: Resultant $\underline{\underline{Q}}$ matrix with the first two elements swapped. The configuration is now $\underline{d}$ = ( 2  1  5  10 ), with all 37 channels occupied. EWV is lowered to $130\frac{4}{7}$.

$N_C$ = 37 constraint. Changing to $\underline{d}$ = ( 2  1  4  11 ) has the effect of "orthogonalizing" the channels so that the PSA-channels are available independently from PSG-channels in the Fourier domain, i.e. at different carrier frequencies, a characteristic that has been empirically observed to be indicative of optimality. Considering all the channels in Figure 3.5 lowers EWV by 47.3%, while the systematic approach to measurement selection brings another 35.3% reduction to EWV. In total, EWV was reduced to 34.1% of its original value, suggesting that the polarimeter's SNR is almost three times higher.

Finally, Figure 3.8 shows the covariance matrix, $\underline{\underline{K}}_{\underline{\underline{Q}}^+}$, for the three systems with $N_C$ =

(a) $\underline{\underline{\mathbf{Q}}}$
(b) $\underline{\underline{\mathbf{Q}}}^{+}$
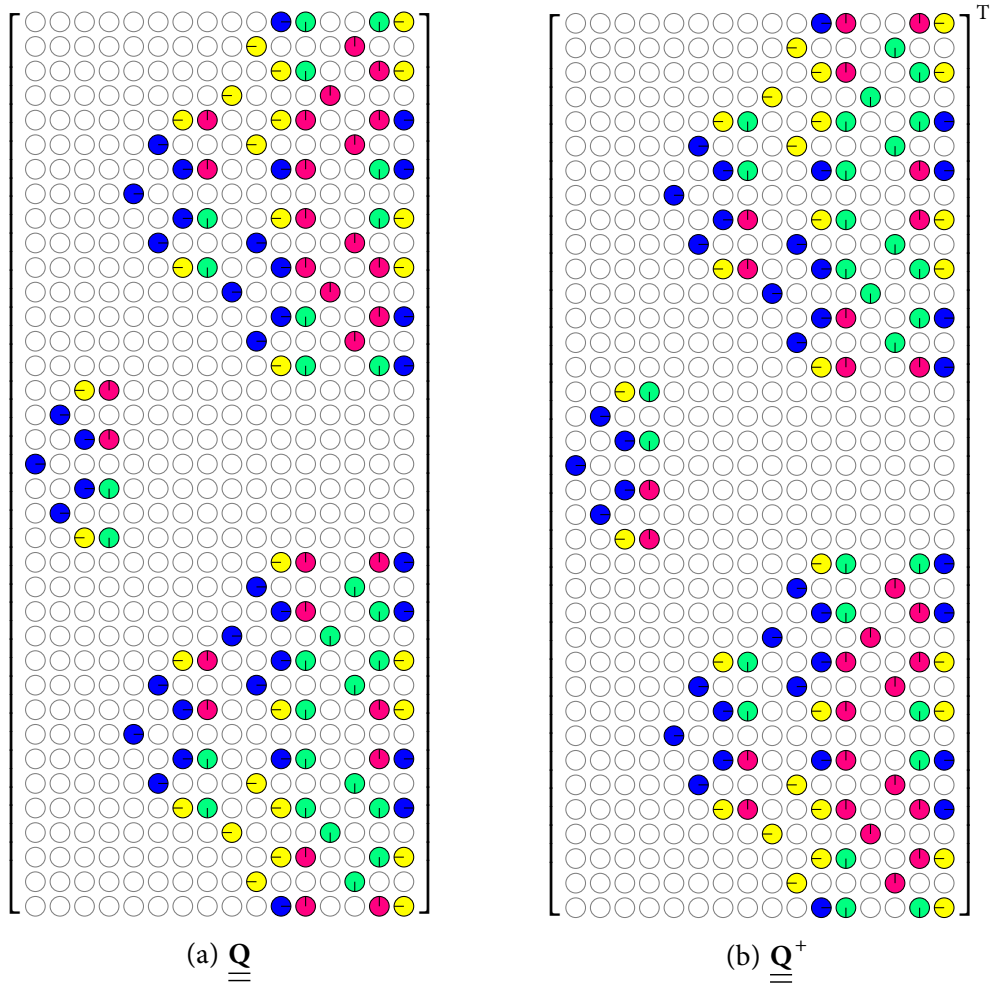
Figure 3.7: Further thickness adjustments can produce an optimal $\underline{\underline{\mathbf{Q}}}$ with $\underline{\mathbf{d}}$ = ( 2  1  4  11 ) and EWV = 121, while keeping the same number of channels.

(a) $\underline{\mathbf{d}}$ = ( 1  2  5  10 )    (b) $\underline{\mathbf{d}}$ = ( 2  1  5  10 )    (c) $\underline{\mathbf{d}}$ = ( 2  1  4  11 )
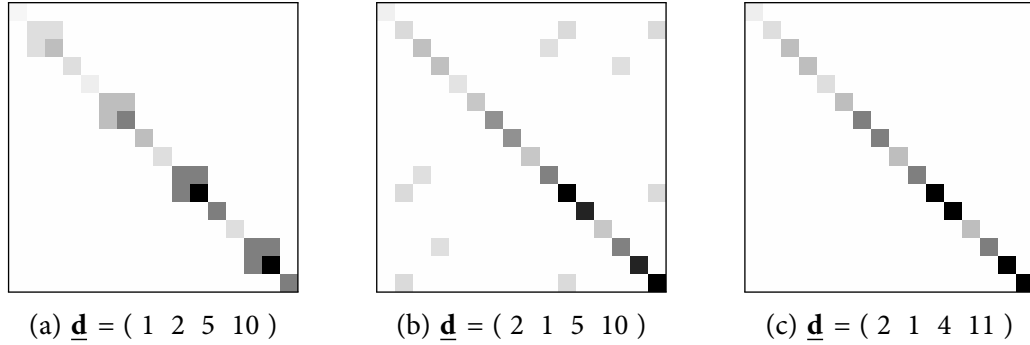
Figure 3.8: $\underline{\underline{\mathbf{K}}}_{\underline{\mathbf{Q}}^+}$ for different spectrally channeled configurations.

37. Since the number of channels is the same, spectral resolution remained unchanged as well.

Table 3.1 mentions an optimal system with $\underline{\mathbf{d}}$ = ( 1  4  2  9 ) and $N_C$ = 33. Choosing this system does not impact the SNR of the reconstructed polarization channels, but has the added benefit of enabling one to increase $d_o$ so as to widen the channel bandwidth. The resultant $\underline{\underline{\mathbf{Q}}}$ and its inverse can be seen in Figure 3.9. Once again, the fact that the channels that contain PSG modulation information are free of any contribution from the rest of the Mueller elements is crucial to ensuring the system's optimality.

There are other one-dimensional channeled systems in prior literature. Dubreuil et al. (2007) proposed a system with an effective $\underline{\mathbf{d}}$ = ( 1  1  5  5 ), meaning a total of 21 channels. The $\underline{\underline{\mathbf{Q}}}$ matrix and its inverse for that system can be seen in Figure 3.10. Evaluating the system with the methods outline in this treatment, reveals an EWV of 441, while the results in Table 3.1 show that a system with $\underline{\mathbf{d}}$ = ( 2  1  2  7 ) has the same number of channels but 70.2% higher SNR. Inspecting the corresponding $\underline{\underline{\mathbf{Q}}}$ matrix, it is readily seen that Dubreuil's system has many channels canceling one another, thereby reducing the amount of information carried through.

### 3.2.2  Two Dimensional Channeled Systems

Like in the previous example of one dimensional channel systems, two modulating frequencies are needed to separate the elements within both the PSG and the PSA sufficiently. Instead of considering a single design vector ($\underline{\mathbf{d}}$), it is more appropriate to consider two

(a) $\underline{\underline{Q}}$          (b) $\underline{\underline{Q}}^+$
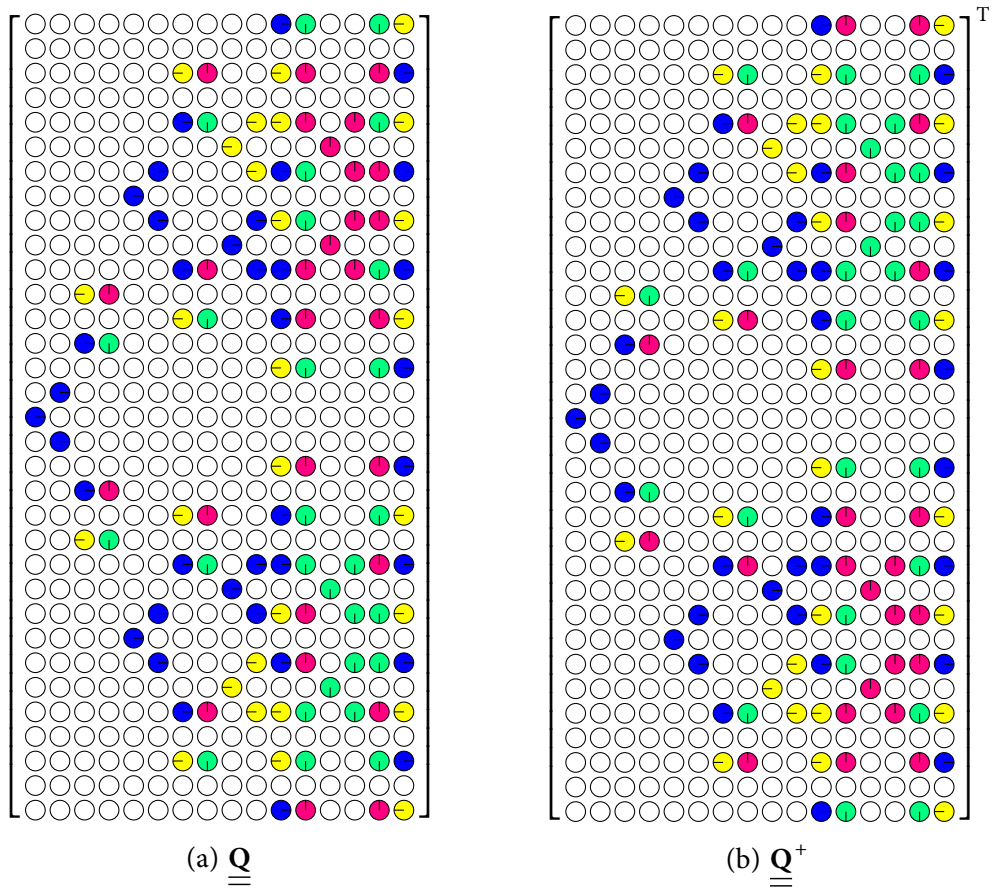
Figure 3.9: Resultant $\mathbf{Q}$ matrix of a system with $\underline{\mathbf{d}} = (\ 1\ \ 4\ \ 2\ \ 9\ )$. All 33 channels are occupied, while EWV is maintained at 121.

(a) $\underline{\underline{\mathbf{Q}}}$          (b) $\underline{\underline{\mathbf{Q}}}^+$
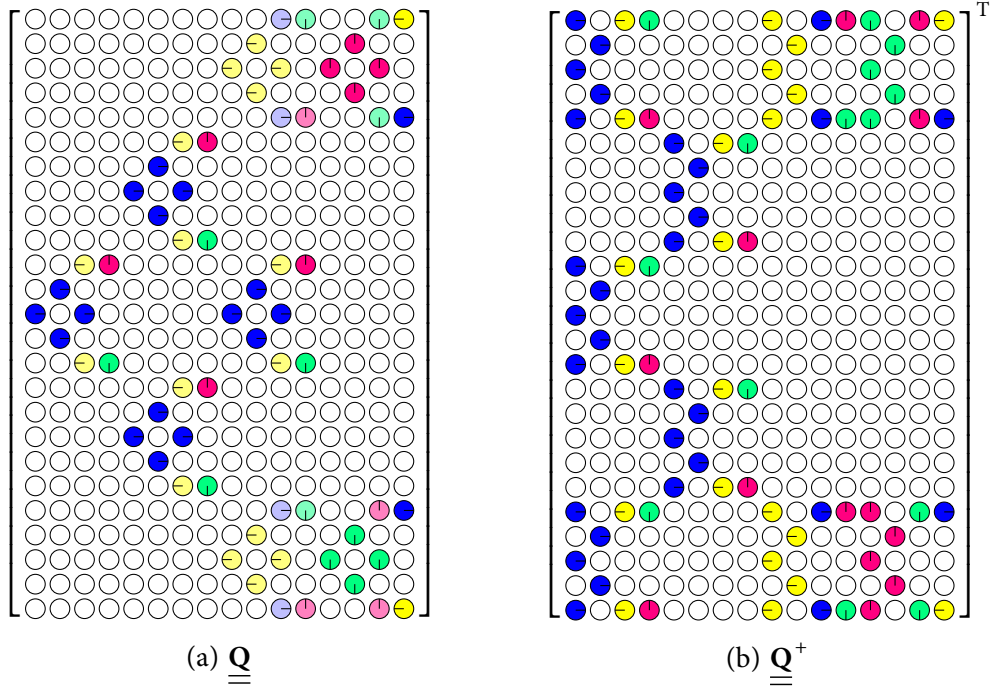
Figure 3.10: Resultant $\underline{\underline{\mathbf{Q}}}$ matrix of a system with $\underline{\mathbf{d}} = (\,1 \quad 1 \quad 5 \quad 5\,)$. The system features 25 channels and an $\overline{\mathrm{EWV}}$ of 441.

proportional frequency vectors, $\underline{\mathbf{a}} = (\,\tilde{\vartheta}_1 \quad \tilde{\vartheta}_2\,)$ and $\underline{\mathbf{g}} = (\,\tilde{\vartheta}_3 \quad \tilde{\vartheta}_4\,)$, which translates to having

$$N_x = 1 + 2\sum_{i=1}^{4}\tilde{\vartheta}_i(\vartheta_i \overset{?}{=} x), \tag{3.23a}$$

$$N_y = 1 + 2\sum_{i=1}^{4}\tilde{\vartheta}_i(\vartheta_i \overset{?}{=} y). \tag{3.23b}$$

First, it is possible to study the lowest attainable EWV without assuming anything about the type of modulation applied or the order of dimensions. Keeping those parameters variable, genetic algorithm optimizations were run to find systems with the best EWV given a specified number of $x$- and $y$- channels. The result can be seen in Table 3.2. Note that full Mueller Matrix polarimeters do not exist for $3 \times (3, 5, 7, 9)$ or $(3, 5, 7, 9) \times 3$ two-dimensional arrangements. The most balanced solution appears to be $N_x = N_y = 7$, as it posits the same bandwidth constraint on the two dimensions, while being a sub-class of systems with the lowest number of channels that achieves optimality.

As a representative example, consider the spatial-spatial channeled polarimeter de-

(a) $\underline{\underline{\mathbf{Q}}}$          (b) $\underline{\underline{\mathbf{Q}}}^+$
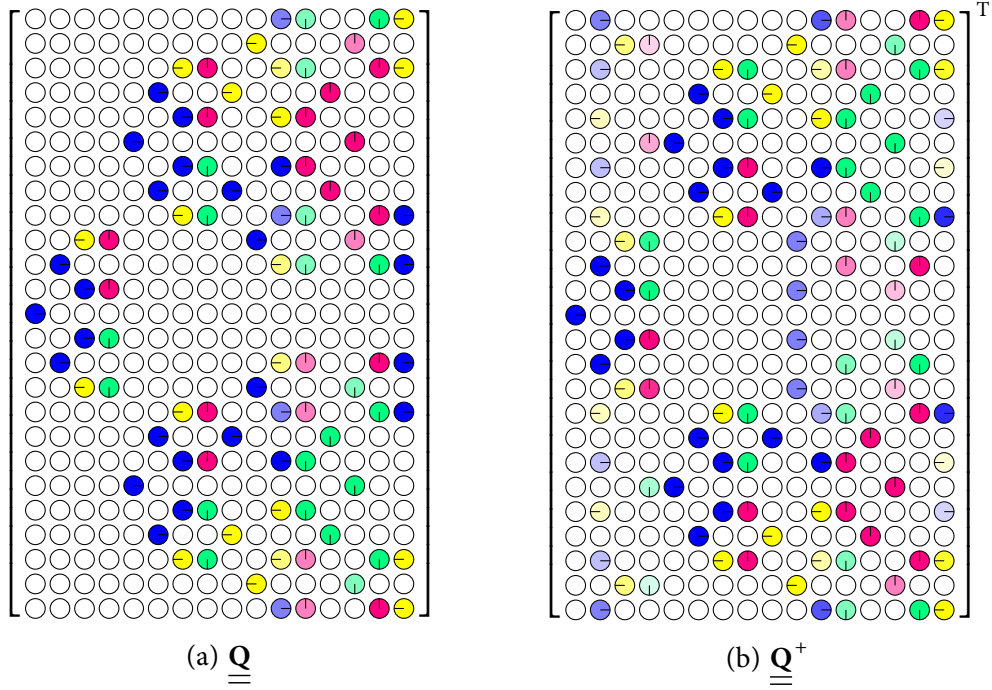
Figure 3.11: Resultant $\underline{\underline{\mathbf{Q}}}$ matrix of a system with $\underline{\mathbf{d}} = (\ 2 \quad 1 \quad 2 \quad 7\ )$. The system features 25 channels and an EWV of $169\frac{17}{33}$.

Table 3.2: Minimum achievable EWV for $N_y \times N_x$ channel arrangement.

| $N_y \backslash^{N_x}$ | 3 | 5 | 7 | 9 | 11 | 13 |
|---|---|---|---|---|---|---|
| 3 | — | — | — | — | 147.67 | 131.67 |
| 5 | — | 441.00 | 171.67 | 147.67 | 147.67 | 131.67 |
| 7 | — | 171.67 | 121.00 | 121.00 | 121.00 | 121.00 |
| 9 | — | 147.67 | 121.00 | 121.00 | 121.00 | 121.00 |
| 11 | 147.67 | 147.67 | 121.00 | 121.00 | 121.00 | 121.00 |
| 13 | 131.67 | 131.67 | 121.00 | 121.00 | 121.00 | 121.00 |

scribed by Kudenov et al. (2012), an example of a system in Figure 3.3i. The modulation is achieved via polarization gratings that separate the different Mueller matrix elements onto patterns of frequencies that are determined by the spacing of the elements. The intensity can be similarly represented as in Equation 3.15 with $\vec{\vartheta} = (\ x\ \ y\ \ y\ \ x\ )$. Kudenov used:

$$\mathbf{\underline{f}_G} = \begin{bmatrix} 1 \\ \cos(2\pi y) \\ \sin(2\pi y)\cos(2\pi x) \\ \sin(2\pi y)\sin(2\pi x) \end{bmatrix}, \tag{3.24a}$$

$$\mathbf{\underline{f}_A} = \begin{bmatrix} 1 \\ \cos(4\pi x) \\ \sin(4\pi x)\cos(4\pi y) \\ \sin(4\pi x)\sin(4\pi y) \end{bmatrix}. \tag{3.24b}$$

Figure 3.12 shows a comparison between three systems with the only difference being the order of modulation. The merit of introducing $\underline{\underline{\mathbf{Q}}}$ is clear; better performance is achieved virtually for free, using the same polarization elements arranged in a different order. Systems in Figure 3.12 were found by optimizing using genetic algorithms, while continuously relaxing the design restrictions.

Although a symmetrical (x/y/y/x & 1/1/2/2) modulation design shown in Figure 3.14 may seem intuitive, it is possible to improve the design as evidenced by the polarimeter in Figure 3.12c, which is shown in greater detail in Figures 3.13 and 3.15. First, in Figure 3.12b, an asymmetrical order of modulations (x/y/x/y & 1/1/2/2) improves EWV by 27.8%. Then, in Figure 3.12c, it is improved by another 19.9% by splitting the modulation into one dimensional structures for the PSG and the PSA (x/x/y/y & 2/1/2/1). In total, EWV was reduced to 57.9% of its original value. Although not as large of an improvement as in the previous example, it is, nonetheless, significant. The reason for the EWV improvements lies in how the channels interfere. From the comparison of Figure 3.12, it can be noted that the better systems "focus" the reconstruction onto the diagonal of $\underline{\underline{\mathbf{K}}}_{\underline{\underline{Q}}}$, which matches the fundamental expectation that the most orthogonal set of structures will produce an optimal system.
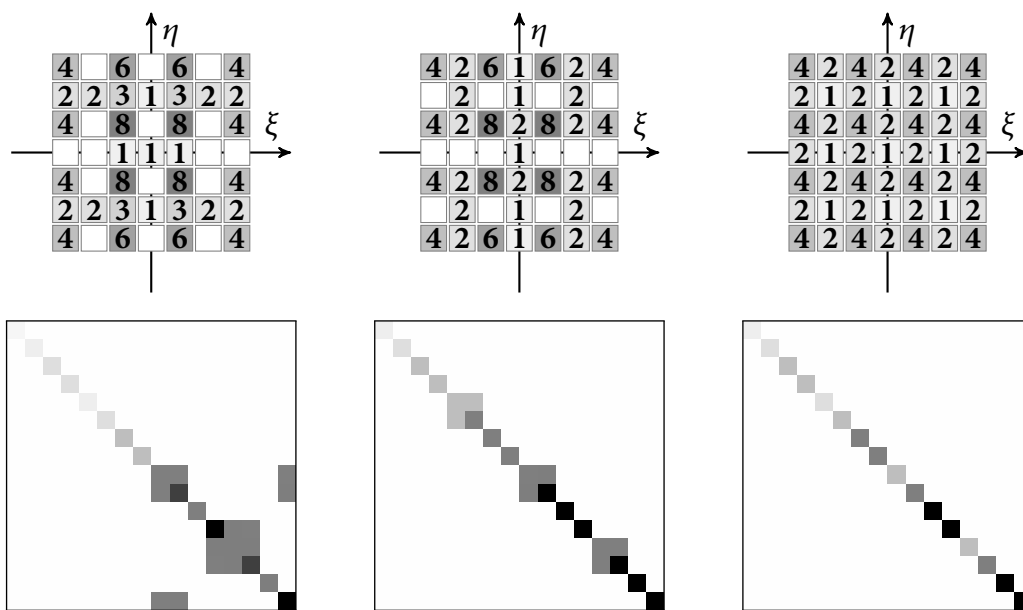
(a) $a_1 = a_2 = 2g_1 = 2g_2 = 2$, $x/y/y/x$, 33/49 channels used, EWV = 209

(b) $a_1 = a_2 = 2g_1 = 2g_2 = 2$, $x/y/x/y$, 35/49 channels used, EWV = 151

(c) $a_1 = 2a_2 = g_1 = 2g_2 = 2$, $x/x/y/y$, 49/49 channels used, EWV = 121

Figure 3.12: Top: $\xi/\eta$ plane of channels (the number inside each channel corresponds to the number of Mueller elements contained within). Bottom: $\underline{\underline{\mathbf{K}}}_{\underline{\underline{Q}}^+}$.
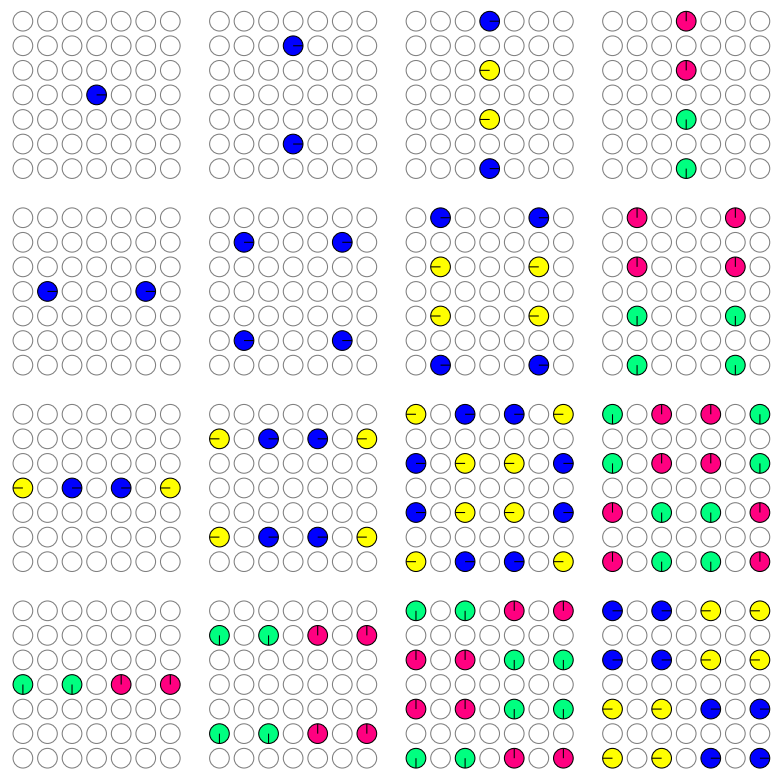
Figure 3.13: Frequency grid of the Mueller modulation. $\xi$ and $\eta$ are the $x$- and $y$-axes, respectively.

(a) $\underline{\underline{\mathbf{Q}}}$    (b) $\underline{\underline{\mathbf{Q}}}^{+}$
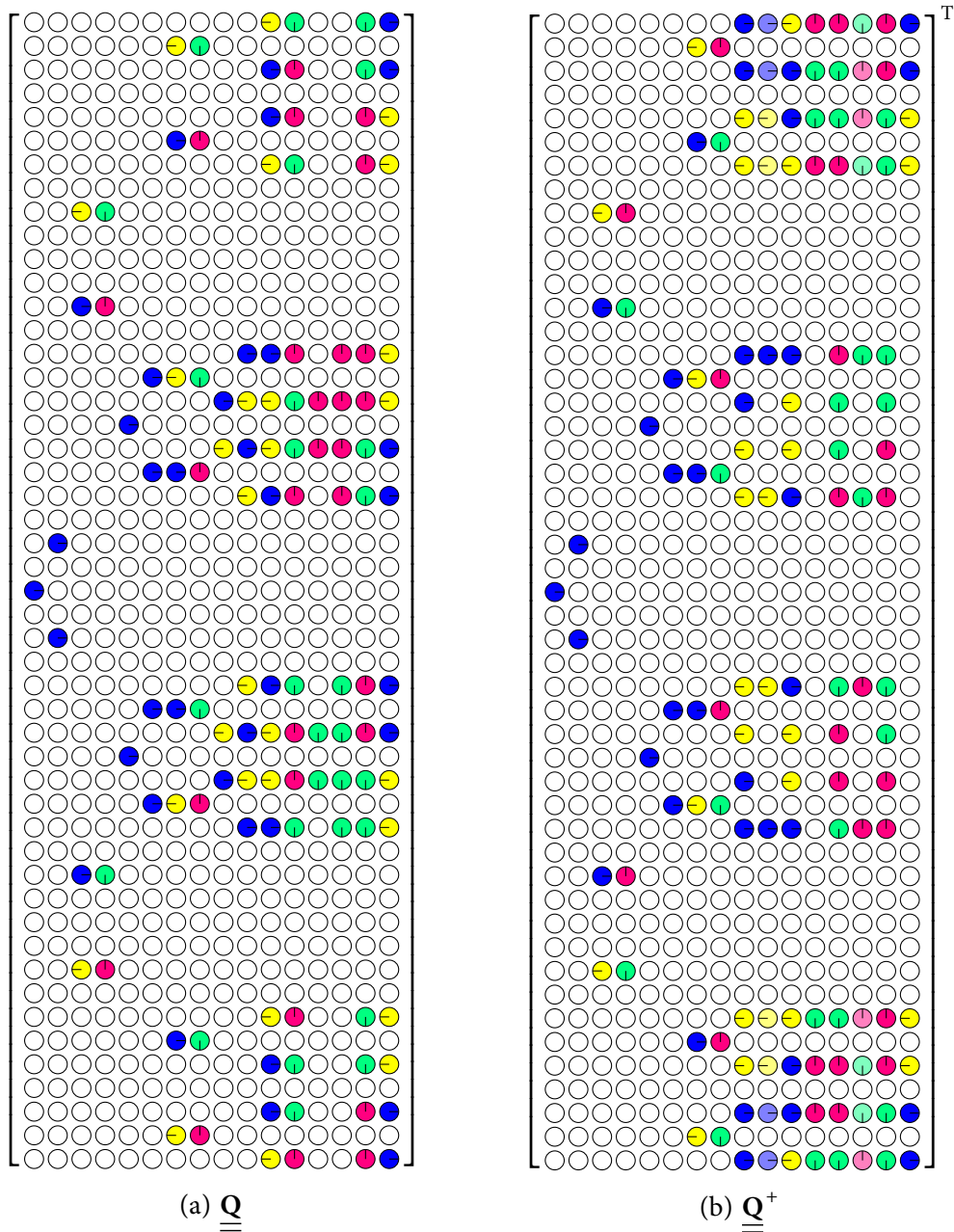
Figure 3.14: Equivalent representation using the introduced formalism of the spatially channeled polarimeter from Kudenov's work. Though the modulation configuration produces a total of 49 channels, only 33 channels are occupied with information; the rest are empty. This configuration has EWV = 209.

(a) $\underline{\underline{\mathbf{Q}}}$          (b) $\underline{\underline{\mathbf{Q}}}^{+}$

Figure 3.15: Spatially channeled polarimeter with an optimal modulation configuration. This system only changes the order and the dimensions of modulations while keeping the frequencies intact, which maintains the same number of channels. This design allows for all 49 channels to carry information and leads to this configuration having EWV = 121.

### 3.2.3 Multiple Snapshot Polarimeter

The columns of $\underline{\underline{\mathbf{Q}}}$ matrix represent nothing more than unfolded dyad elements that contain modulations within each Mueller channel projection target. Thus, once the system's spectral and/or spatial modulations are determined, the associated channel structures can be rotated via a unitary transformation that remixes the channel structures in the PSG and PSA as

$$\underline{\underline{\mathbf{Q}}}_\theta = \left[ \underline{\underline{\mathbf{U}}}_A \mathcal{F}\{\underline{\mathbf{A}}\} \right] * \left[ \mathcal{F}\{\underline{\mathbf{G}}\}^{\mathrm{T}} \underline{\underline{\mathbf{U}}}_G \right]. \tag{3.25}$$

Applying $\underline{\underline{\mathbf{U}}}_G$ and $\underline{\underline{\mathbf{U}}}_A$ maintains the channels' relative orientation, thereby maintaining the EWV. Looking at the Mueller matrix of a linear retarder in Equation 1.30, it can be shown that $|\det(\underline{\underline{\mathbf{LR}}}(\delta,\theta))| = 1$, which means it is a unitary transformation. Using the notation of Equation 3.18, the variances within the reconstructions of all 16 elements can be expressed with the number of modulations present. The sandwich retarders rotate each channel structure, which can be represented by defining $\underline{\mathbf{n}}_G(\delta_G,\theta_G)$ and $\underline{\mathbf{n}}_A(\delta_A,\theta_A)$:

$$\underline{\mathbf{n}}_G(\delta_G,\theta_G) = \left( \underline{\underline{\mathbf{M}}}_{\mathrm{LR}}(\delta_G,\theta_G) \circ \underline{\underline{\mathbf{M}}}_{\mathrm{LR}}(\delta_G,\theta_G) \right) \begin{bmatrix} 1 & 2 & 4 & 4 \end{bmatrix}^{\mathrm{T}} =$$

$$= \begin{bmatrix} 1 \\ 2\left[ c^2(2\theta_G) + c(\delta_G)\, s^2(2\theta_G) \right]^2 + 4\, s^2(2\theta_G)\, s^2(\delta_G) + s^2(4\theta_G)\, v^2(\delta_G) \\ 4\left[ s^2(2\theta_G) + c(\delta_G)\, c^2(2\theta_G) \right]^2 + 4\, c^2(2\theta_G)\, s^2(\delta_G) + \frac{1}{2}\, s^2(4\theta_G)\, v^2(\delta_G) \\ 4 - 2\, s^2(2\theta_G)\, s^2(\delta_G) \end{bmatrix},$$

$$\tag{3.26a}$$

$$\underline{\mathbf{n}}_A(\delta_A,\theta_A) = \left( \underline{\underline{\mathbf{M}}}_{\mathrm{LR}}(\delta_A,\theta_A) \circ \underline{\underline{\mathbf{M}}}_{\mathrm{LR}}(\delta_A,\theta_A) \right) \begin{bmatrix} 1 & 2 & 4 & 4 \end{bmatrix}^{\mathrm{T}} =$$

$$= \begin{bmatrix} 1 \\ 2\left[ c^2(2\theta_A) + c(\delta_A)\, s^2(2\theta_A) \right]^2 + 4\, s^2(2\theta_A)\, s^2(\delta_A) + s^2(4\theta_A)\, v^2(\delta_A) \\ 4\left[ s^2(2\theta_A) + c(\delta_A)\, c^2(2\theta_A) \right]^2 + 4\, c^2(2\theta_A)\, s^2(\delta_A) + \frac{1}{2}\, s^2(4\theta_A)\, v^2(\delta_A) \\ 4 - 2\, s^2(2\theta_A)\, s^2(\delta_A) \end{bmatrix},$$

$$\tag{3.26b}$$

where $\circ$ represents the Hadamard product, which is necessary for correct weighing of variances and the same shorthands are used as before: $c(x) = \cos(x)$, $s(x) = \sin(x)$ and $v(x) =$

Figure 3.16: Effect of $\delta_G = \delta_A = \frac{\pi}{2}$, $\theta_G \propto t$ and $\theta_A \propto t/5$ on the mixture of channel structures. Each channel structure features an EWV of 121 with the variance being traded off between Mueller element reconstructions. (Animation available in the digital version)

versin$(x) = 1 - \cos(x)$. The variances can still be evaluated as $\underline{\mathbf{n}}_G(\delta_G, \theta_G) \otimes \underline{\mathbf{n}}_A(\delta_A, \theta_A)$ and their sum will remain unchanged at 121. This enables one to adjust the distribution of noise power between Mueller elements and follows the concepts of preferential treatment of information without creating a partial system. This development also leads to a fairly straightforward construction of a multiple snapshot system by positioning the two retarders to different orientations for each successive measurement. Using Equation 3.12 gives the total $\underline{\underline{\mathbf{Q}}}$.

Figure 3.16 shows the effect on channel constructs after placing two $\frac{\lambda}{4}$-plates before PSG and after PSA and rotating them at rates of one and five. Each structure within the animation corresponds to an optimal system with EWV of 121. Figure 3.17 shows $(\theta_A, \theta_G)$ while scanning through different values of $\delta_A = \delta_G$. The impact of this development is the ability to redistribute the variance in case a preferential weighing of Mueller elements is needed.

Optimizations of 64 differently configured spatial–spatial channeled polarimeters were

Figure 3.17: Shuffled variance (blue/yellow for $+12/-12$) as a function of $\theta_A$, $\theta_G$ and $\delta_G = \delta_A$. (Animation available in the digital version)

Table 3.3: Results for different number of temporal snapshots. Row/Column labels refer to each element's modulating frequencies in PSG/PSA, respectively. Order of modulation domains is an optimization variable. For example, 1 snapshot with $\vec{\vartheta} = (\ 1\ \ 2\ \ 1\ \ 2\ )$ produces EWV = 133. For those constraints, optimization routine found $\vec{\vartheta} = (\ y\ \ x\ \ x\ \ y\ )$. The outside retarder orientations, $\theta_A$ and $\theta_G$, are plateau dimensions when number of measurements is unity, hence they do not play a significant role.

|     | 1/1   | 2/1   | 1/2   | 2/2   |
|-----|-------|-------|-------|-------|
| 1/1 | 441.0 | 171.7 | 214.9 | 151.0 |
| 2/1 | 171.7 | 121.0 | 147.7 | 147.7 |
| 1/2 | 214.9 | 147.7 | 133.0 | 214.9 |
| 2/2 | 151.0 | 147.7 | 214.9 | 441.0 |

(a) 1 snapshot — 49 channels

|     | 1/1   | 2/1   | 1/2   | 2/2   |
|-----|-------|-------|-------|-------|
| 1/1 | 60.00 | 53.50 | 53.60 | 53.60 |
| 2/1 | 53.50 | 53.57 | 54.28 | 53.50 |
| 1/2 | 53.60 | 54.28 | 56.22 | 59.08 |
| 2/2 | 53.60 | 53.50 | 59.08 | 60.00 |

(b) 2 snapshots — 98 channels

|     | 1/1   | 2/1   | 1/2   | 2/2   |
|-----|-------|-------|-------|-------|
| 1/1 | 36.26 | 35.50 | 35.32 | 35.00 |
| 2/1 | 35.50 | 34.00 | 34.50 | 34.77 |
| 1/2 | 35.32 | 34.50 | 35.20 | 35.95 |
| 2/2 | 35.00 | 34.77 | 35.95 | 36.49 |

(c) 3 snapshot — 147 channels

|     | 1/1   | 2/1   | 1/2   | 2/2   |
|-----|-------|-------|-------|-------|
| 1/1 | 25.33 | 25.48 | 25.52 | 25.65 |
| 2/1 | 25.48 | 25.22 | 25.61 | 25.61 |
| 1/2 | 25.52 | 25.61 | 25.78 | 26.16 |
| 2/2 | 25.65 | 25.61 | 26.16 | 25.94 |

(d) 4 snapshots — 196 channels

run. The number of snapshots was constrained to be 1, 2, 3 or 4, with $\vec{\theta}_G$ and $\vec{\theta}_A$ defining each snapshots' sandwich retarders as optimization variables. Additionally, the verbose grid of $\vec{\tilde{\vartheta}}$ frequencies, $(\ \tilde{\vartheta}_1\ \ \tilde{\vartheta}_2\ ) = (\ \tilde{\vartheta}_3\ \ \tilde{\vartheta}_4\ ) = \{(\ 1\ \ 1\ ),(\ 1\ \ 2\ ),(\ 2\ \ 1\ ),(\ 2\ \ 2\ )\}$ was searched, which would correspond to $N_x$ and $N_y$ as 5, 7, 7, and 9, respectively. With frequencies set, the distinction was the corresponding dimension into which the data were mapped, $\vec{\vartheta}$, which was an optimization variable in the optimization. A genetic algorithm was used to find the lowest EWV. The results are shown in Table 3.3.

From these results, it can be gathered that as the number of temporal measurements grows, the importance of the spatial frequencies and order of modulations diminishes. This bodes well if this phenomenon is understood as a continuously growing temporal bandwidth constraint allowing simplification of the spatial multiplexing.

## 3.3   Conclusion

Introducing $\underline{\underline{\mathbf{Q}}}$ and methods for generating it automatically allows description of a wide range of similar systems with a handful of parameters and removes the need to handle reconstruction by hand. Furthermore, analysis of $\underline{\underline{\mathbf{Q}}}$ reveals certain design metrics immediately instead of having to run an elaborate simulation. The end result is that a more optimal system can be found often without requiring the use of any extra elements, while injecting the optimization procedure before element selection allows for a better selection overall.

The premise of applying the same concepts presented in this chapter to partial Mueller Matrix Polarimeters (pMMPs) is of great interest and will be a topic of Chapter 5. To evaluate such systems the concept of EWV would have to be generalized to a Weighted Variance, where instead of treating all information equally, certain information can be deemed to be most important for the particular task.

CHAPTER 4

PARTIAL POLARIMETER DESIGN

Partial Mueller matrix polarimeters (pMMPs) are active sensing instruments that probe a scattering process with a set of polarization states and analyze the scattered light with a second set of polarization states. Unlike conventional Mueller matrix polarimeters, pMMPs do not attempt to reconstruct the entire Mueller matrix. With proper choice of generator and analyzer states, a subset of the Mueller matrix space can be reconstructed with fewer measurements than that of the full Mueller matrix polarimeter. This chapter considers the structure of the Mueller matrix and the ability to probe it using a reduced numbers of measurements. Analysis tools are developed to relate the particular choice of generator and analyzer polarization states to the portion of Mueller matrix space that the instrument measures. Additionally, an optimization method is introduced to balance the signal-to-noise-ratio of the resulting instrument with the ability of that instrument to accurately measure a particular set of desired polarization components. In the process, 10 classes of pMMP systems are identified, the space coverage of which is immediately known. A numerical example is used to demonstrate the theory where a partial polarimeter is designed for the task of monitoring the damage state of a material as presented earlier by Hoover and Tyo (2007). It is shown that the polarimeter can be reduced to making eight measurements while still covering the Mueller matrix subspace spanned by the objects.

## 4.1 Introduction

The Mueller matrix is a common method to characterize polarimetric optical scattering properties. The Mueller matrix gives the scattered Stokes parameters in terms of the incident Stokes parameters, thereby fully describing the optical interaction, at least for spatially incoherent fields (Chipman (2009b)).

Numerous authors have studied the structure of the Mueller matrix, and much is

known about how the various Mueller matrix elements relate to the physical properties of diattenuation, retardance, and depolarization (Gil (2007); Chipman (2009b)). It should be clear that not all $4 \times 4$ real matrices are physically realizable from Equation 1.3. A physical Mueller matrix must map real sets of Stokes parameters into real sets of Stokes parameters, but there are other conditions that must also be met as recently discussed by Gil (2007).

Much of the literature on Mueller matrices is concerned with methods to decompose the Mueller matrix in order to understand its structure and relate it to scattering properties. In the class of series decompositions, the Mueller matrix is broken up into discrete diattenuating, retarding, and depolarizing layers, and the result is a product of Mueller matrices that describe the effects of the whole. Lu and Chipman (1996) developed a series decomposition that writes the Mueller matrix as a non-unique cascade of pure diattenuation, retardance, and depolarization Mueller matrices. Ossikovski and colleagues developed a different decomposition that eliminated the order-dependence of the Lu-Chipman decomposition by creating a decomposition that is symmetric through the Minkowski metric tensor $\underline{\underline{G}} = \mathrm{diag}(1, -1, -1, -1)$ (Ossikovski (2009)). It's clear that while one can use either of these decompositions (or any other), they may not actually represent the physics of any particular process.

The limit of series decompositions is the class of differential decompositions (Ossikovski (2012)). These split the Mueller matrix into differential slices in an attempt to identify its fundamental characteristics. Noble and Chipman (Noble and Chipman (2012); Chipman (2009b)) use the method of matrix roots to uncover a fundamental differential Mueller matrix that can be written in terms of 15 Mueller matrix generators - three for retardance, three for diattenuation, and nine for depolarization. Ossikovski developed a logarithmic decomposition of the Mueller matrix (Ossikovski (2011)) that operates using a different formalism, but produces an equivalent outcome to that of the matrix roots decomposition (Ossikovski (2012)).

A third class of decomposition is the class of additive decompositions that consider the Mueller matrix as an ensemble average of parallel scattering processes that are added incoherently. Gil provides a recent review that covers the general cases of the trivial, spectral, and arbitrary decompositions (Gil (2007)). The most famous parallel decomposition is that

of Cloude, who demonstrated that an arbitrary Mueller matrix could be written as a super-position of not more than four pure Mueller-Jones matrices (Cloude (1986)). Ossikovski has demonstrated rigorously that in the limit of weakly depolarizing Mueller matrices, all decompositions return identical polarization properties to first order (Ossikovski (2012)). However, for more general depolarizing matrices, the various methods return different results for the "fundamental" properties or retardance and diattenuation of a Mueller matrix under test.

All of these classes of decompositions are important for understanding the fundamental properties of the Mueller matrix. However, measurement of the Mueller matrix requires consideration of a different basis set altogether. A Mueller matrix polarimeter operates by using a polarization state generator (PSG) to illuminate the sample with a controlled state of polarization. The polarimeter then measures the intensity passed through a polarization state analyzer (PSA) set to a second polarization state. Through a suitably diverse set of illumination and analysis states, the elements of the Mueller matrix can be determined (Chipman (2009c)). Much as is the case in Stokes polarimetry (Tyo (2002)), the measurement corresponding to each pair of PSG/PSA states can be thought of as a projection onto a basis vector, and then the unknown Mueller matrix can be estimated through a least-squares inversion process that produces an additive decomposition. Once the problem is cast in this manner, the design of a measurement system then becomes an optimization problem where a particular measurement basis is chosen in order to highlight specific aspects of the Mueller matrix. At least 16 measurements are needed in order to reconstruct the full Mueller matrix in general (Chipman (2009c)), while the choice of specific illumination states can help balance the signal-to-noise ratio (SNR) and/or error in particular Mueller matrix elements (Twietmeyer and Chipman (2008); Vaughn and Hoover (2008)). Going one step further, a partial Mueller matrix polarimeter (pMMP) can be designed that allows certain elements or combinations of elements of the Mueller matrix to be recovered with fewer than 16 measurements while ignoring other elements that might not be necessary for a particular sensing problem (Tyo et al. (2010)). Hoover and his coworkers (Hoover and Tyo (2007); Vaughn et al. (2012a)) have demonstrated that reduced dimensionality sub-spaces of Mueller matrix space can be used to perform invariant target detection through

nonlinear model fitting. Goudail and his coworkers (Goudail and Beniere (2009); Goudail (2009); Goudail and Tyo (2011)) have demonstrated that a single-measurement pMMP is optimal for maximizing polarization contrast in a two-class detection problem with known class Mueller matrices.

In this chapter, the design of pMMPs that seek to measure certain aspects of the Mueller matrix that might be dictated by a particular sensing task is considered. The pMMP could be an imaging or non-imaging device, but the design of the instrument proceeds from knowledge of linear combinations of Mueller matrix elements that allow a particular task to be performed (Hoover and Tyo (2007); Tyo et al. (2010)). It is well known that it is not possible to measure a single Mueller matrix element or a single arbitrary combination of Mueller matrix elements in a single measurement due to the restrictions on the structure of the Stokes parameters of the PSG and PSA states. Previous authors (Tyo et al. (2010); Anna and Goudail (2012)) have considered specific optimization strategies designed to maximize performance on a particular task. This chapter approaches the more general two-part problem of a) identifying the proper subspace in which to make a detection decision and b) designing a pMMP to get as close as possible to a specified subspace of Mueller matrix space through careful selection of measurement states. In order to accomplish this, some of the details of the structure of the Mueller matrix and how they interact with the PSG and PSA, are discussed. Finally, a numerical optimization method is developed that produces the desired pMMP design.

The remainder of this chapter is organized as follows. Section 4.2 discusses the modifications to the mathematics of Mueller matrix polarimetry that are necessary to consider pMMPs. Section 4.3 considers the structure of a few pMMPs in a way that elucidates how the PSG and PSA interact with the Mueller matrix to build up a pMMP basis. Section 4.4 generalizes the patterns seen in Section 4.3 to a general class of $4ij$ pMMP systems, as well as develops various metrics by which to evaluate the noise resilience and the proximity of a $K$-dimensional subspace of Mueller matrix space to an $N$-measurement pMMP. Section 4.5 applies the developed concepts to an object discrimination task from the literature (Hoover and Tyo (2007)) and discusses the results. Section 4.7 concludes the chapter.

## 4.2 Structure of Partial Mueller Matrices

In the case of partial polarimeters, $N < 16$, and the maximum rank that the polarimeter can achieve is $N$. It is easy to demonstrate

$$\text{tr}\left(\underline{\underline{W}}^{+}\underline{\underline{W}}\right) = \text{rank}\left(\underline{\underline{W}}\right) = R. \tag{4.1}$$

In this chapter, the singular value decomposition (SVD)Golub and van Loan (1983) is used to compute the pseudoinverse. The SVD of $\underline{\underline{W}}$ yields

$$\underline{\underline{W}} = \underline{\underline{U}}\,\underline{\underline{\Sigma}}\,\underline{\underline{V}}^{\text{T}}. \tag{4.2}$$

The matrices $\underline{\underline{U}}$ and $\underline{\underline{V}}$ are $R \times R$ and $16 \times 16$ real, orthogonal matrices, respectively, and $\underline{\underline{\Sigma}}$ is a $R \times 16$ reduced diagonal matrix containing the $R$ singular values $\sigma_1 \geq \sigma_2 \geq \ldots \geq \sigma_R > 0$. The columns of $\underline{\underline{U}}$ span the range of the pseudoinverse, and the columns of $\underline{\underline{V}}$ span Mueller matrix space. The first $R$ columns correspond to the non-zero singular values and span the portion of Mueller matrix space that the pMMP can reconstruct. The pseudoinverse can be written as

$$\underline{\underline{W}}^{+} = \underline{\underline{V}}\,\underline{\underline{\Sigma}}^{+}\,\underline{\underline{U}}^{\text{T}}, \tag{4.3}$$

where $\underline{\underline{\Sigma}}^{+}$ is the $16 \times R$ reduced diagonal matrix containing the inverse of the singular values. The SVD pseudoinverse creates a "maximally orthogonal" inverse.

Examining the diagonal elements of $\underline{\underline{W}}^{+}\underline{\underline{W}}$ matrix tells how the information from the $N$ measurements contributes to the rank and how that information is distributed in the estimated Mueller matrix. Define the reconstructables matrix,

$$\underline{\underline{B}}^{'} = \text{vec}(\underline{\underline{B}}) = \text{diag}\left(\underline{\underline{W}}^{+}\underline{\underline{W}}\right). \tag{4.4}$$

Examples of such matrices will be considered in subsequent sections, but at this point it can said that $\underline{\underline{B}}$ relates the percentage of each Mueller matrix element that is reconstructed in the pMMP. In the limit of $N = 16$, the pMMP becomes a full polarimeter, $\underline{\underline{W}}^{+}\underline{\underline{W}} = \mathbb{I}_{16}$, and $\underline{\underline{B}}$ is a $4 \times 4$ matrix of all ones; all elements of the Mueller matrix can be reconstructed.

To understand the function of the pMMP, consider the multiplication of the matrix and its pseudoinverse

$$\underline{\underline{W}}^{+}\underline{\underline{W}} = \underline{\underline{V}}\,\underline{\underline{\Sigma}}^{+}\,\underline{\underline{U}}^{+}\,\underline{\underline{U}}\,\underline{\underline{\Sigma}}\,\underline{\underline{V}}^{+} = \underline{\underline{V}}\,\underline{\underline{\Sigma}}^{+}\,\underline{\underline{\Sigma}}\,\underline{\underline{V}}^{+}. \tag{4.5}$$

The matrix $\underline{\underline{\Sigma}}^{+}\underline{\underline{\Sigma}}$ is diagonal with the first $R$ elements equaling unity and the last $16 - R$ equaling zero. This permits the claim made in Equation 4.1. Thus,

$$\underline{\underline{W}}^{+}\underline{\underline{W}} = \underline{\underline{V}}'\underline{\underline{V}}'^{\mathrm{T}}, \tag{4.6}$$

where $\underline{\underline{V}}'$ is the $16 \times R$ matrix composed of the first $R$ columns of $\underline{\underline{V}}$. Another way of interpreting the SVD of $\underline{\underline{W}}$ is that $\underline{\underline{V}}'$ forms an orthogonal basis that spans the subspace of Mueller matrix space that forms the domain of the particular pMMP represented by $\underline{\underline{W}}$. Likewise, the columns of $\underline{\underline{V}}$ discarded by the SVD (corresponding to singular values of zero) span the remaining null space. However, as shown later, knowledge of the domain alone is not sufficient to predict performance, as the conditioning of the matrix $\underline{\underline{W}}$ is important in the presence of noise and error.

## 4.3    Examples of Partial Mueller Matrix Polarimeters

This analysis is restricted to pMMPs that use fully polarized PSG and PSA states. Goudail and Tyo (2011) demonstrated that partially polarized PSG and PSA states never improve contrast. Below a case where one or more PSG or PSA state is unpolarized is considered, allowing reconstruction of particular elements of the Mueller matrix with fewer measurements than would be necessary if all PSG and PSA states were fully polarized.

### 4.3.1    Canonical 4-Measurement pMMP

Consider the simple $N = 4$ measurement pMMP that measures the co-polarized and cross-polarized return for both vertically and horizontally polarized illumination. For compactness, the following notation for the analyzer and generator matrices is introduced

$$\underline{\underline{A}} \Rightarrow \tfrac{1}{2}\left[\; \rightarrow \quad \rightarrow \quad \uparrow \quad \uparrow \;\right], \tag{4.7a}$$

$$\underline{\underline{G}} \Rightarrow \left[\; \rightarrow \quad \uparrow \quad \rightarrow \quad \uparrow \;\right], \tag{4.7b}$$

where $\rightarrow = \left[\; 1 \quad 1 \quad 0 \quad 0 \;\right]^{\mathrm{T}}$ is the set of Stokes parameters for ideally horizontally polarized light and $\uparrow = \left[\; 1 \quad -1 \quad 0 \quad 0 \;\right]^{\mathrm{T}}$ is the set of Stokes parameters for ideally vertically polarized light. The presence of $\tfrac{1}{2}$ in the definitions of the analyzing vector is needed for

rigor; the polarization sensing systems in consideration dismiss half of the light if the input is unpolarized. The set of four PSG/PSA pairs in Equations 4.7a and 4.7b results in the instrument matrix

$$
\underline{\underline{W}} = \frac{1}{2} \begin{bmatrix} 1 & 1 & 0 & 0 & 1 & 1 & 0 & 0 & 0 & 0 & 0 & 0 & 0 & 0 & 0 & 0 \\ 1 & 1 & 0 & 0 & -1 & -1 & 0 & 0 & 0 & 0 & 0 & 0 & 0 & 0 & 0 & 0 \\ 1 & -1 & 0 & 0 & 1 & -1 & 0 & 0 & 0 & 0 & 0 & 0 & 0 & 0 & 0 & 0 \\ 1 & -1 & 0 & 0 & -1 & 1 & 0 & 0 & 0 & 0 & 0 & 0 & 0 & 0 & 0 & 0 \end{bmatrix} \tag{4.8}
$$

and the reconstructables matrix

$$
\underline{\underline{B}} = \begin{bmatrix} 1 & 1 & 0 & 0 \\ 1 & 1 & 0 & 0 \\ 0 & 0 & 0 & 0 \\ 0 & 0 & 0 & 0 \end{bmatrix}. \tag{4.9}
$$

This is the well known result that four measurements are needed to reconstruct four Mueller matrix elements, and that these four elements must come in a "block" pattern within the Mueller matrix (Tyo et al. (2010)). A similar polarimeter could be obtained with a 4-measurment combination of any two of the six canonical states $\rightarrow$, $\uparrow$, $\nearrow$, $\nwarrow$, $\circlearrowright$, $\circlearrowleft$, where $\nearrow$ and $\nwarrow$ represent 45° and −45°, and $\circlearrowright$ and $\circlearrowleft$ represent right- and left circular polarization, respectively.

While this well-known result tells how to design a pMMP to reconstruct one of these groupings of four elements, it is not obvious how to add additional measurements to reconstruct additional elements, nor is it obvious how to design a pMMP to reconstruct linear combinations of elements rather than isolated elements.

## 4.3.2 Diagonal Depolarization Elements

Depolarization is a rich physical process that contains significant information about the random scattering properties (Chipman (2005)). Noble and Chipman (Noble and Chipman (2012); Chipman (2009b)) recently described the nine degrees of freedom for depolarization. Three of these correspond to randomness in the diattenuation properties of the Mueller matrix, three to randomness in the retardance properties of the Mueller matrix,

and three to "diagonal depolarization," which is related to randomness in geometric transformations as would happen in multiple scattering or rough surface scattering processes. Often, the diagonal depolarization elements are important for discrimination in both optical and radar tasks (Cloude and Pottier (1996)).

Section 4.3.1 shows that each canonical four-measurement polarimeter provides one diagonal element (in addition to $m_{00}$, which is involved in all MMPs). One obvious way to reconstruct the diagonal elements then would be to use a 12-measurement pMMP defined by the analyzer and generator matrices,

$$\underline{\underline{A}} \Rightarrow \tfrac{1}{2}\left[\; \rightarrow\;\; \rightarrow\;\; \uparrow\;\; \uparrow\;\; \nearrow\;\; \nearrow\;\; \nwarrow\;\; \nwarrow\;\; \circlearrowleft\;\; \circlearrowleft\;\; \circlearrowright\;\; \circlearrowright\;\right], \tag{4.10a}$$

$$\underline{\underline{G}} \Rightarrow \left[\; \rightarrow\;\; \uparrow\;\; \rightarrow\;\; \uparrow\;\; \nearrow\;\; \nwarrow\;\; \nearrow\;\; \nwarrow\;\; \circlearrowleft\;\; \circlearrowright\;\; \circlearrowleft\;\; \circlearrowright\;\right], \tag{4.10b}$$

which produces the following reconstructables matrix

$$\underline{\underline{B}} = \begin{bmatrix} 1 & 1 & 1 & 1 \\ 1 & 1 & 0 & 0 \\ 1 & 0 & 1 & 0 \\ 1 & 0 & 0 & 1 \end{bmatrix}. \tag{4.11}$$

In addition to the desired diagonal elements, the diattenuation and polarizance vectors (Lu and Chipman (1996)) are also measured. This 12-measurement pMMP only reconstructs 10 Mueller matrix elements, since each of the three canonical pMMPs redundantly reconstructs $m_{00}$. Because three reconstructions of $m_{00}$ are available, the SNR in that reconstructed element is a factor of $\sqrt{3}$ higher.

This redundancy can be addressed by eliminating one of the cross-polarized measurements in two of the canonical pMMPs so that

$$\underline{\underline{A}} = \tfrac{1}{2}\left[\; \rightarrow\;\; \rightarrow\;\; \uparrow\;\; \uparrow\;\; \nearrow\;\; \nwarrow\;\; \nwarrow\;\; \circlearrowleft\;\; \circlearrowright\;\; \circlearrowright\;\right], \tag{4.12a}$$

$$\underline{\underline{G}} = \left[\; \rightarrow\;\; \uparrow\;\; \rightarrow\;\; \uparrow\;\; \nearrow\;\; \nearrow\;\; \nwarrow\;\; \circlearrowleft\;\; \circlearrowleft\;\; \circlearrowright\;\right], \tag{4.12b}$$

which produces the same reconstructables matrix as Equation 4.11. In this case the elimination of redundancy allows 10 Mueller matrix elements to be reconstructed from 10 measurements.

The matrix of Equation 4.11 still unnecessarily reconstructs the first column and the first row of the Mueller matrix. The number of measurements can be lowered by further reducing two of the three canonical 4-measurement pMMPs to two-measurement pMMPs that make co-polarized measurements only, e. g.

$$\underline{\underline{A}} \Rightarrow \tfrac{1}{2} \left[ \; \rightarrow \quad \rightarrow \quad \uparrow \quad \uparrow \quad \nearrow \quad \nwarrow \quad \circlearrowright \quad \circlearrowleft \; \right], \tag{4.13a}$$

$$\underline{\underline{G}} \Rightarrow \left[ \; \rightarrow \quad \uparrow \quad \rightarrow \quad \uparrow \quad \nearrow \quad \nwarrow \quad \circlearrowright \quad \circlearrowleft \; \right], \tag{4.13b}$$

which produces the reconstructables matrix

$$\underline{\underline{B}} = \begin{bmatrix} 1 & 1 & \frac{1}{2} & \frac{1}{2} \\ 1 & 1 & 0 & 0 \\ \frac{1}{2} & 0 & 1 & 0 \\ \frac{1}{2} & 0 & 0 & 1 \end{bmatrix}. \tag{4.14}$$

Examination of $\underline{\underline{V}}$ can help to determine how the elements of $\underline{\underline{B}}$ correspond to reconstructed Mueller matrix channels as discussed in section 4.4. This pMMP can reconstruct the diagonal elements $m_{00}, m_{11}, m_{22}, m_{33}$ as well as the elements $m_{10}$ and $m_{01}$. In addition to these individual elements, the polarimeter can also reconstruct the linear combination channels $(m_{20} + m_{02})/\sqrt{2}$ and $(m_{30} + m_{03})/\sqrt{2}$. Although, not the case in this instance, the existence of reconstruction channels does not guarantee that these channels will have acceptable SNR. These items are discussed in greater detail below.

The polarimeter described by Equations 4.13a and 4.13b is the lowest dimensionality that was found that reconstructs all three of the diagonal elements with fully polarized analyzer and generator states. However, use of unpolarized measurements adds another degree of freedom and provides capacity for fewer measurements. Consider a system that makes six canonical, co-polarized measurements and one unpolarized measurement

$$\underline{\underline{A}} \Rightarrow \tfrac{1}{2} \left[ \; 2\bigcirc \quad \rightarrow \quad \uparrow \quad \nearrow \quad \nwarrow \quad \circlearrowright \quad \circlearrowleft \; \right], \tag{4.15a}$$

$$\underline{\underline{G}} \Rightarrow \left[ \; \bigcirc \quad \rightarrow \quad \uparrow \quad \nearrow \quad \nwarrow \quad \circlearrowright \quad \circlearrowleft \; \right], \tag{4.15b}$$

where $\bigcirc = \begin{bmatrix} 1 & 0 & 0 & 0 \end{bmatrix}^{\mathrm{T}}$. The reconstructables matrix for this polarimeter is

$$\underline{\underline{\mathbf{B}}} = \begin{bmatrix} 1 & \frac{1}{2} & \frac{1}{2} & \frac{1}{2} \\ \frac{1}{2} & 1 & 0 & 0 \\ \frac{1}{2} & 0 & 1 & 0 \\ \frac{1}{2} & 0 & 0 & 1 \end{bmatrix}. \tag{4.16}$$

The addition of the one unpolarized measurement allows the $m_{00}$ term to be reconstructed directly, obviating the need for the cross-polarized measurements indicated in Equations 4.13a and 4.13b.

Figures 4.1, 4.2 and 4.3 illustrate the reconstructions of the systems defined by Equations 4.10a and 4.10b, Equations 4.12a and 4.12b as well as Equations 4.13a and 4.13b. The simulation was performed with an artificial Mueller-matrix-like object. No extensive attention was paid to the physical realizability of the scene. That consideration does not pertain to the information mapping and thus does not affect measurement properties.
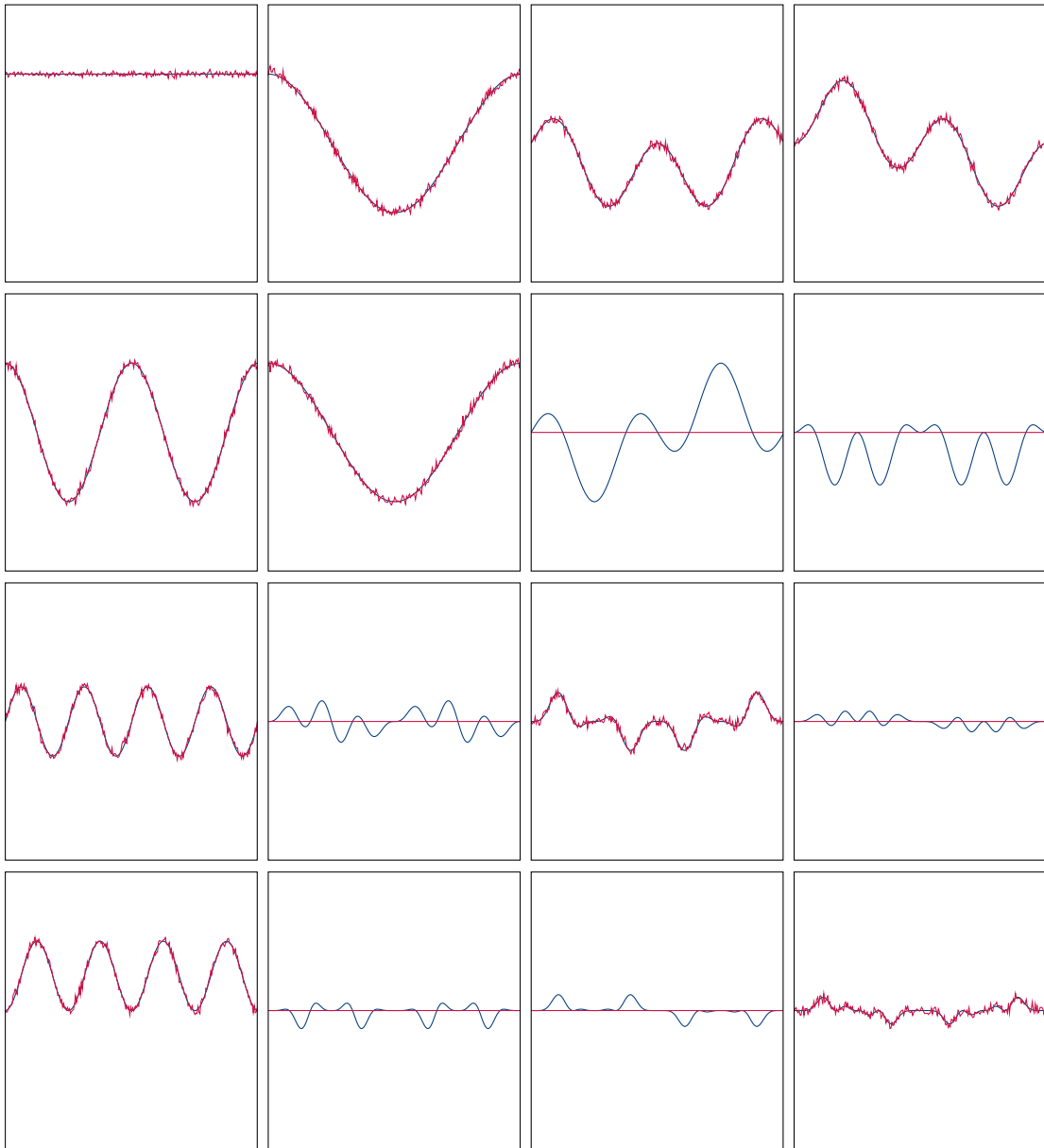
Figure 4.1: Partial reconstruction of a synthetic Mueller signal from the 12 measurements defined by Equations 4.10a and 4.10b. The associated reconstructables matrix can be seen in Equation 4.11. Note that the noise in $m_{00}$ appears to be lower than in any other channel. This is because each of the canonical four-blocks are capable of reconstructing that channel on their own and their contributions end up getting averaged with noise magnitude becoming $\frac{1}{\sqrt{3}}$ of the others.
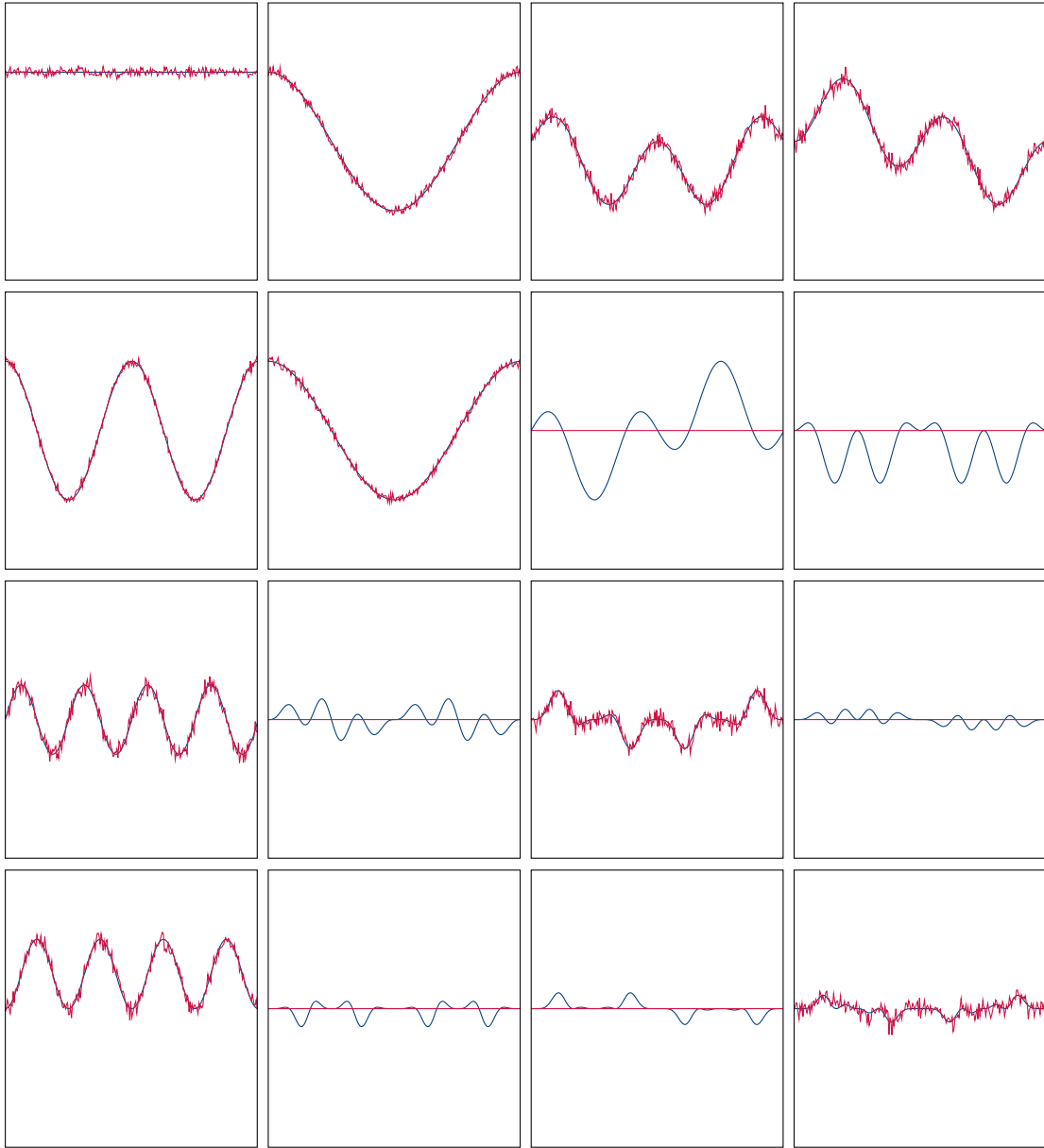
Figure 4.2: Partial reconstruction of a synthetic Mueller signal from the ten measurements defined by Equations 4.12a and 4.12b. The associated reconstructables matrix can be seen in Equation 4.11. As was the case with the 12 measurement case, $m_{00}, m_{11}, m_{22}, m_{33}$, as well as $m_{01}, m_{02}, m_{03}, m_{10}, m_{20}$ and $m_{30}$ are reconstructable. The difference being the increased noise in $m_{00}, m_{22}, m_{20}, m_{02}, m_{33}, m_{30}$, and $m_{03}$.
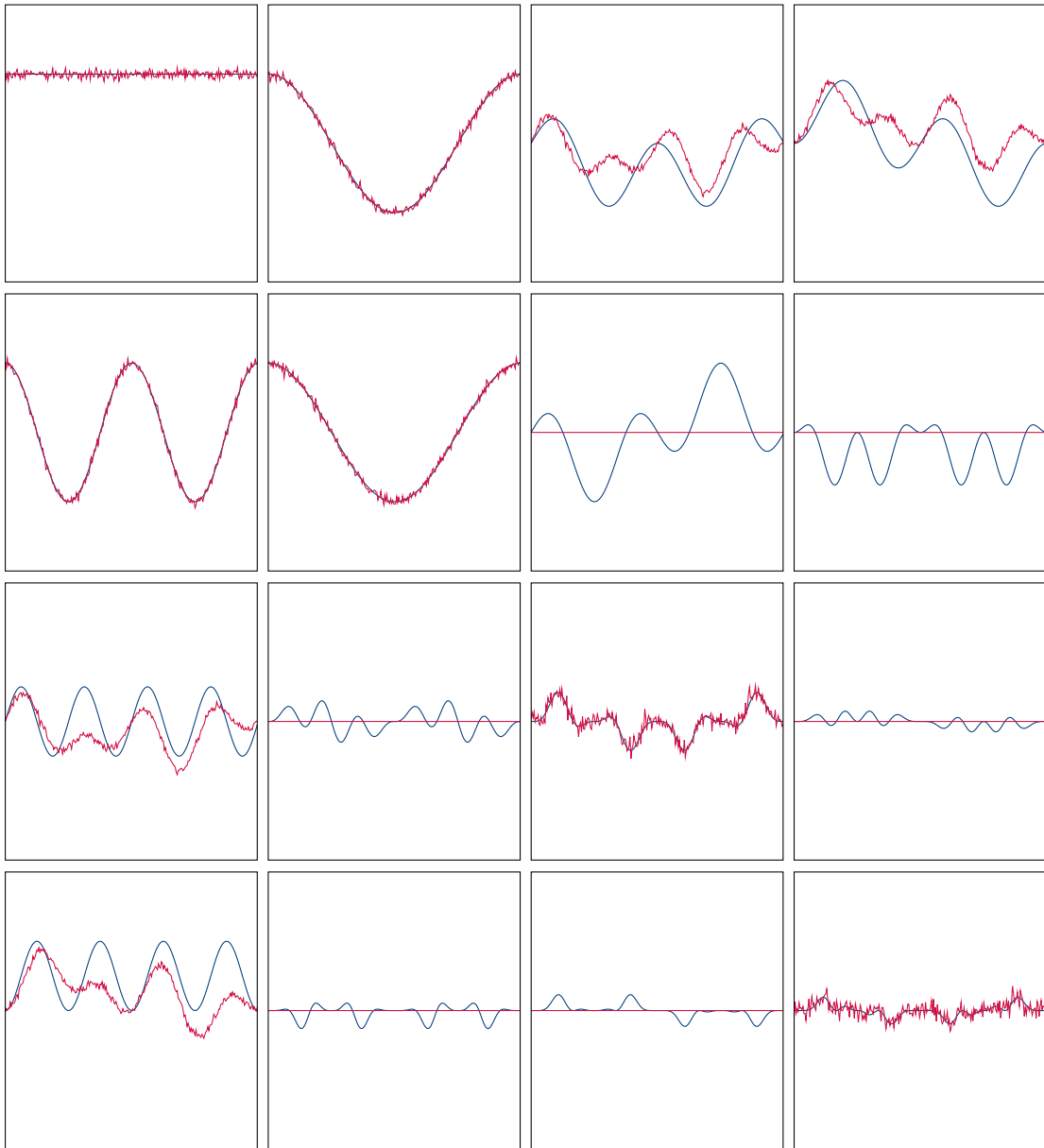
Figure 4.3: Partial reconstruction of a synthetic Mueller signal from the eight measurements defined by Equations 4.13a and 4.13b. The associated reconstructables matrix can be seen in Equation 4.14. The following elements are reconstructable: $m_{00}$, $m_{11}$, $m_{22}$, $m_{33}$, as well as $m_{01}$, $m_{10}$. Shown in Figure 4.4, are the two remaining linear combinations of elements that are also reconstructable.

(a) $\frac{1}{\sqrt{2}}\left[m_{02} + m_{20}\right]$        (b) $\frac{1}{\sqrt{2}}\left[m_{03} + m_{30}\right]$
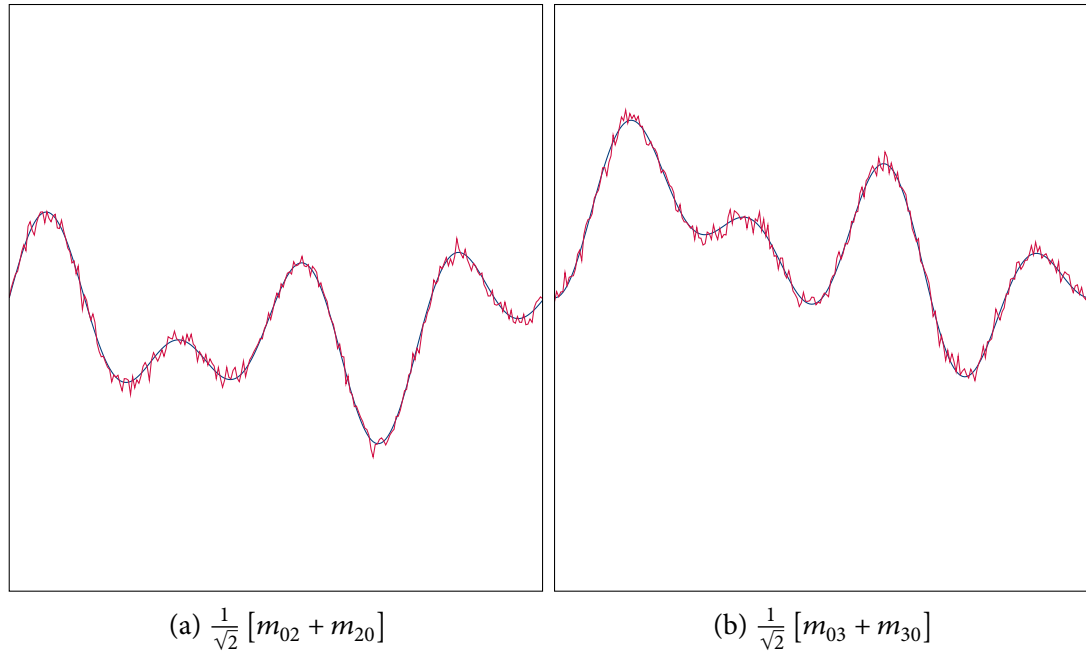
Figure 4.4: Reconstructions of linear combinations of Mueller elements that the polarimeter described by Equations 4.13a and 4.13b is able to reproduce.

## 4.4 Partial Mueller Matrix Polarimeter Design

Based on the understanding gained in Section 4.3, some prior constraints can be removed, and pMMP systems can be generalized to have arbitrary fully polarized PSG and PSA states within the requirement that $N = R$.

It is unclear from $\underline{\underline{\mathbf{B}}}$ alone which Mueller elements are grouped together into combinatorial channels. When a particular element of $\underline{\underline{\mathbf{B}}}$ is unity, then the corresponding Mueller matrix element can be reconstructed. But when it is other than unity, the element must appear in combination with other Mueller matrix elements. However, the fact that $\underline{\underline{\mathbf{B}}}$ is derived from the columns of $\underline{\underline{\mathbf{V}}}'$ provides insight into the overall subspace spanned by the pMMP. If two or more columns of $\underline{\underline{\mathbf{V}}}'$, say $\underline{\mathbf{v}}_n$ and $\underline{\mathbf{v}}_m$ correspond to equal singular values $\sigma_n = \sigma_m$, then they span a hyperplane with identical geometrical characteristics in the context of $\underline{\underline{\mathbf{W}}}$. In this case, any set of orthogonal basis vectors in that hyperplane can be used, allowing for a more intuitive grouping of Mueller matrix elements if desired.

All of the previous examples featured four-block measurements. Prior work was al-

ready familiar with $m_{00}/m_{i0}/m_{0j}/m_{ij}$ measurement, but a similar reconstruction exists for off-Mueller grid measurement. Consider the arbitrary analyzing and generating vectors:

$$\underline{\mathbf{A}}_{\pm} = \begin{bmatrix} 1 & \pm a_1 & \pm a_2 & \pm a_3 \end{bmatrix}, \tag{4.17a}$$

$$\underline{\mathbf{G}}_{\pm} = \begin{bmatrix} 1 & \pm g_1 & \pm g_2 & \pm g_3 \end{bmatrix}. \tag{4.17b}$$

A four-block polarimeter would go through the following four combinations of measurements:

$$\underline{\underline{\mathbf{A}}}_4 \Rightarrow \tfrac{1}{2} \begin{bmatrix} \underline{\mathbf{A}}_+ & \underline{\mathbf{A}}_+ & \underline{\mathbf{A}}_- & \underline{\mathbf{A}}_- \end{bmatrix}^{\mathrm{T}}, \tag{4.18a}$$

$$\underline{\underline{\mathbf{G}}}_4 \Rightarrow \begin{bmatrix} \underline{\mathbf{G}}_+ & \underline{\mathbf{G}}_- & \underline{\mathbf{G}}_+ & \underline{\mathbf{G}}_- \end{bmatrix}^{\mathrm{T}}. \tag{4.18b}$$

The resulting measurement matrix is

$$\underline{\underline{\mathbf{W}}}_4 = \begin{bmatrix} (\underline{\mathbf{A}}_+ \otimes \underline{\mathbf{G}}_+)^{\mathrm{T}} \\ (\underline{\mathbf{A}}_+ \otimes \underline{\mathbf{G}}_-)^{\mathrm{T}} \\ (\underline{\mathbf{A}}_- \otimes \underline{\mathbf{G}}_+)^{\mathrm{T}} \\ (\underline{\mathbf{A}}_- \otimes \underline{\mathbf{G}}_-)^{\mathrm{T}} \end{bmatrix}, \tag{4.19}$$

The SVD of $\underline{\underline{\mathbf{W}}}_4$ in Equation 4.19 will have four column-space vectors with four identical singular values. If a particular representation of $\underline{\mathbf{V}}$ is chosen, then there is only one $\underline{\underline{\mathbf{U}}}$ to go along with it. A linear combination of these vectors corresponds to rotation of the underlying vectors. This operation does not alter the space, but merely rotates the axes by which that space is described. It will be shown that a particular decomposition can be written down that is relatively easy to treat analytically. When faced with more complex $\underline{\underline{\mathbf{V}}}$ matrices that have non-equal singular values, adding and subtracting the underlying vectors is also possible, but special care needs to be taken.

For the four-block polarimeter, the column space can be described with the following

set of vectors

$$
\underline{\underline{V}}_4' =
\begin{bmatrix}
1 & 0 & 0 & 0 \\
0 & g_1 & 0 & 0 \\
0 & g_2 & 0 & 0 \\
0 & g_3 & 0 & 0 \\
0 & 0 & a_1 & 0 \\
0 & 0 & 0 & a_1 g_1 \\
0 & 0 & 0 & a_1 g_2 \\
0 & 0 & 0 & a_1 g_3 \\
0 & 0 & a_2 & 0 \\
0 & 0 & 0 & a_2 g_1 \\
0 & 0 & 0 & a_2 g_2 \\
0 & 0 & 0 & a_2 g_3 \\
0 & 0 & a_3 & 0 \\
0 & 0 & 0 & a_3 g_1 \\
0 & 0 & 0 & a_3 g_2 \\
0 & 0 & 0 & a_3 g_3
\end{bmatrix},
\tag{4.20}
$$

that correspond to four unity singular values and

$$
\underline{\underline{U}} = \frac{1}{2}
\begin{bmatrix}
1 & 1 & 1 & 1 \\
1 & -1 & 1 & -1 \\
1 & 1 & -1 & -1 \\
1 & -1 & -1 & 1
\end{bmatrix}.
\tag{4.21}
$$

The corresponding reconstructables matrix is

$$
\underline{\underline{B}}_4 =
\begin{bmatrix}
1 & g_1{}^2 & g_2{}^2 & g_3{}^2 \\
a_1{}^2 & a_1{}^2 g_1{}^2 & a_1{}^2 g_2{}^2 & a_1{}^2 g_3{}^2 \\
a_2{}^2 & a_2{}^2 g_1{}^2 & a_2{}^2 g_2{}^2 & a_2{}^2 g_3{}^2 \\
a_3{}^2 & a_3{}^2 g_1{}^2 & a_3{}^2 g_2{}^2 & a_3{}^2 g_3{}^2
\end{bmatrix}.
\tag{4.22}
$$

### 4.4.1  Additional Measurements

In order to expand the space coverage, more measurements need to be added. To do so while keeping system rank equal to the number of measurements means that each additional column in $\underline{\underline{V}}'$ needs to be orthogonal to every pre-existing one. Assuming the limit of using fully-polarized measurements, then the new analyzing vector pair $\underline{\underline{A}}_{2,\pm}$ needs to be orthogonal to the pre-existing analyzing vector pair $\underline{\underline{A}}_{1,\pm}$ in the Poincaré sphere space. Thus, once the first pair is selected, the new pair is bound to the space of the orthogonal circle. Once $\underline{\underline{A}}_{2,\pm}$ is chosen, there is only one more orthogonal set of vectors $\underline{\underline{A}}_{3,\pm}$ that can be added. This is shown in Figure 4.5.

It is important to make the connection between this general case and the one discussed in Section 4.B. If four measurements are made from each combination in $\underline{\underline{A}}_{1,\pm}$, $\underline{\underline{A}}_{2,\pm}$ and $\underline{\underline{A}}_{3,\pm}$, then the system will have $N = 12$ and $R = 10$, as is the case for the system described by Equations 4.10a and 4.10b. This is because each block is capable of reconstructing $m_{00}$ on its own and measuring it three times will have the effect of averaging, and thereby lowering the noise in its reconstruction. In order to keep $N = R$ only one four-measurement set specified by $\underline{\underline{A}}_{1,\pm}$ and up to two additional fewer-than-four measurements specified by $\underline{\underline{A}}_{2,\pm}$ and $\underline{\underline{A}}_{3,\pm}$ must be taken. This produces 16 possible measurement schemes. By denoting the set as $4ij$ and requiring that $4 > i \geq j$, the six redundant schemes can be ignored as can be seen in Fig. 4.6.

Purely for purposes of simplifying the notation, define the analyzing and generating vectors of the one-, two- and three-measurement cases as:

$$\underline{\underline{A}}_3 \Rightarrow \tfrac{1}{2} \begin{bmatrix} \underline{A}_+ & \underline{A}_- & \underline{A}_- \end{bmatrix}^{\mathrm{T}}, \tag{4.23a}$$

$$\underline{\underline{G}}_3 \Rightarrow \begin{bmatrix} \underline{G}_+ & \underline{G}_+ & \underline{G}_- \end{bmatrix}^{\mathrm{T}}, \tag{4.23b}$$

$$\underline{\underline{A}}_2 \Rightarrow \tfrac{1}{2} \begin{bmatrix} \underline{A}_+ & \underline{A}_- \end{bmatrix}^{\mathrm{T}}, \tag{4.23c}$$

$$\underline{\underline{G}}_2 \Rightarrow \begin{bmatrix} \underline{G}_+ & \underline{G}_- \end{bmatrix}^{\mathrm{T}}, \tag{4.23d}$$

$$\underline{\underline{A}}_1 \Rightarrow \tfrac{1}{2} \begin{bmatrix} \underline{A}_+ \end{bmatrix}^{\mathrm{T}}, \tag{4.23e}$$

$$\underline{\underline{G}}_1 \Rightarrow \begin{bmatrix} \underline{G}_+ \end{bmatrix}^{\mathrm{T}}. \tag{4.23f}$$

It can be shown that this selection considers all possible combinations. The $\pm$ only de-

Figure 4.5: Solid and dashed red vectors represent $\underline{\mathbf{A}}_{1,+}$ and $\underline{\mathbf{A}}_{1,-}$, respectively. Same principle is used to represent $\underline{\mathbf{A}}_{2,\pm}$ and $\underline{\mathbf{A}}_{3,\pm}$ with blue and green vectors, respectively. All three sets need to be orthogonal within the 3-space of the Poincaré sphere in order to maintain $N = R$. The animation shows how additional measurements constrain further vector selection. (Animation available in the digital version)
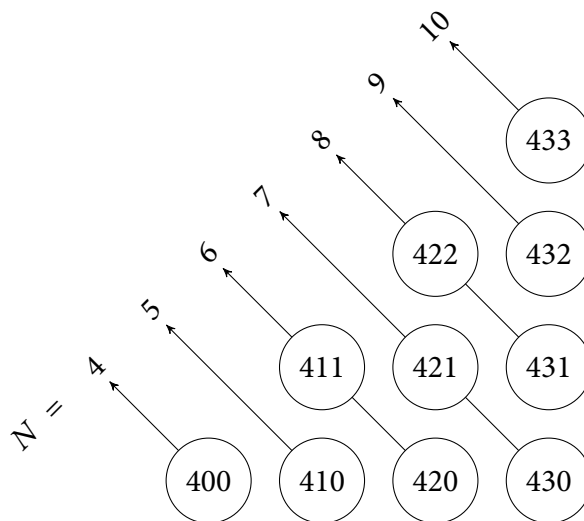


Figure 4.6: Possible sets of measurements that maintain the optimal $N = R$.

notes the operation on the $a_1/g_1$, $a_2/g_2$, and $a_3/g_3$, but a selection of a different vector can effectively construct all other combinations within the syntax implied by $\pm$.

The denoted characteristics of these measurements are only correct if $m_{00}$ is known. Thus, they can only be used as additional measurements and their measurement submatrices are:

$$\underline{\underline{W}}_3 = \begin{bmatrix} (\underline{A}_+ \otimes \underline{G}_+)^T \\ (\underline{A}_- \otimes \underline{G}_+)^T \\ (\underline{A}_- \otimes \underline{G}_-)^T \end{bmatrix}, \tag{4.24a}$$

$$\underline{\underline{W}}_2 = \begin{bmatrix} (\underline{A}_+ \otimes \underline{G}_+)^T \\ (\underline{A}_- \otimes \underline{G}_-)^T \end{bmatrix}, \tag{4.24b}$$

$$\underline{\underline{W}}_1 = \begin{bmatrix} (\underline{A}_+ \otimes \underline{G}_+)^T \end{bmatrix}, \tag{4.24c}$$

and the sub-reconstructables matrices are:

$$\underline{\underline{B}}_3 = \begin{bmatrix} 0 & g_1{}^2 & g_2{}^2 & g_3{}^2 \\ a_1{}^2 & a_1{}^2 g_1{}^2 & a_1{}^2 g_2{}^2 & a_1{}^2 g_3{}^2 \\ a_2{}^2 & a_2{}^2 g_1{}^2 & a_2{}^2 g_2{}^2 & a_2{}^2 g_3{}^2 \\ a_3{}^2 & a_3{}^2 g_1{}^2 & a_3{}^2 g_2{}^2 & a_3{}^2 g_3{}^2 \end{bmatrix}, \tag{4.25a}$$

$$\underline{\underline{B}}_2 = \frac{1}{2} \begin{bmatrix} 0 & g_1{}^2 & g_2{}^2 & g_3{}^2 \\ a_1{}^2 & 2a_1{}^2 g_1{}^2 & 2a_1{}^2 g_2{}^2 & 2a_1{}^2 g_3{}^2 \\ a_2{}^2 & 2a_2{}^2 g_1{}^2 & 2a_2{}^2 g_2{}^2 & 2a_2{}^2 g_3{}^2 \\ a_3{}^2 & 2a_3{}^2 g_1{}^2 & 2a_3{}^2 g_2{}^2 & 2a_3{}^2 g_3{}^2 \end{bmatrix}, \tag{4.25b}$$

$$\underline{\underline{B}}_1 = \frac{1}{3} \begin{bmatrix} 0 & g_1{}^2 & g_2{}^2 & g_3{}^2 \\ a_1{}^2 & a_1{}^2 g_1{}^2 & a_1{}^2 g_2{}^2 & a_1{}^2 g_3{}^2 \\ a_2{}^2 & a_2{}^2 g_1{}^2 & a_2{}^2 g_2{}^2 & a_2{}^2 g_3{}^2 \\ a_3{}^2 & a_3{}^2 g_1{}^2 & a_3{}^2 g_2{}^2 & a_3{}^2 g_3{}^2 \end{bmatrix}. \tag{4.25c}$$

The total measurement matrix of a $4ij$ system is

$$\underline{\underline{W}}_{4ij} = \begin{bmatrix} \underline{\underline{W}}_4^T & \underline{\underline{W}}_i^T & \underline{\underline{W}}_j^T \end{bmatrix}^T. \tag{4.26}$$

The constraints placed on $\underline{A}_{2,\pm}$ and $\underline{A}_{3,\pm}$ mean that the reconstructables matrix is the sum

of the sub-matrices

$$\underline{\underline{\mathbf{B}}}_{4ij} = \underline{\underline{\mathbf{B}}}_4 + \underline{\underline{\mathbf{B}}}_i + \underline{\underline{\mathbf{B}}}_j. \tag{4.27}$$

## 4.4.2   Structured Decomposition

As before, SVD can be performed on the matrix to find the space coverage and noise re-silience of any given polarimeter. However, in the case of being limited to the defined class of $4ij$ pMMP systems, a structured decomposition can be introduced

$$\underline{\underline{\mathbf{W}}}_{4ij} = \underline{\underline{\mathbf{U}}}_{s,4ij}\,\underline{\underline{\mathbf{\Sigma}}}_{s,4ij}\,\underline{\underline{\mathbf{V}}}_{s,4ij}^{\mathrm{T}}, \tag{4.28}$$

where $s$ differentiates this decomposition from the typical SVD. The goal of this decomposition is to be easily parsable by a human and provide an intuitive view of pMMP properties. The following are the structured matrices for any $4ij$ system:

$$\underline{\underline{\mathbf{U}}}_{s,4ij} = \left[\begin{array}{c|ccc} & \underline{\underline{\mathbf{U}}}_4' & \underline{\mathbf{0}}_{4\times i} & \underline{\mathbf{0}}_{4\times j} \\ \left[\sqrt{\frac{1}{N}}\right]_{N\times 1} & \underline{\mathbf{0}}_{i\times 3} & \underline{\underline{\mathbf{U}}}_i' & \underline{\mathbf{0}}_{i\times j} \\ & \underline{\mathbf{0}}_{j\times 3} & \underline{\mathbf{0}}_{j\times i} & \underline{\underline{\mathbf{U}}}_j' \end{array}\right], \tag{4.29}$$

$$\underline{\underline{\mathbf{\Sigma}}}_{s,4ij} = \sqrt{\frac{1}{4}}\,\mathrm{diag}\!\left(\ N\quad \vec{\varsigma}_4\quad \vec{\varsigma}_i\quad \vec{\varsigma}_j\ \right), \tag{4.30}$$

$$\underline{\underline{\mathbf{V}}}_{s,4ij} = \left[\ \underline{\underline{\mathbf{V}}}_4'\quad \underline{\underline{\mathbf{V}}}_i'\quad \underline{\underline{\mathbf{V}}}_j'\ \right], \tag{4.31}$$

where the left structured sub-matrices are:

$$\underline{\underline{\mathbf{U}}}_4' = \frac{1}{\sqrt{4}}\begin{bmatrix} 1 & 1 & 1 \\ -1 & 1 & -1 \\ 1 & -1 & -1 \\ -1 & -1 & 1 \end{bmatrix}, \tag{4.32a}$$

$$\underline{\underline{\mathbf{U}}}_3' = \frac{1}{\sqrt{3}}\begin{bmatrix} 1 & 1 & 1 \\ 1 & -1 & -1 \\ -1 & -1 & 1 \end{bmatrix}, \tag{4.32b}$$

$$\underline{\underline{\mathbf{U}}}_2' = \frac{1}{\sqrt{2}}\begin{bmatrix} 1 & 1 \\ -1 & 1 \end{bmatrix}, \tag{4.32c}$$

$$\underline{\underline{\mathbf{U}}}_1' = \frac{1}{\sqrt{1}}\begin{bmatrix} 1 \end{bmatrix}, \tag{4.32d}$$

the effectively rotated singular values are:

$$\vec{\zeta}_4 = \{4, 4, 4\}, \tag{4.33a}$$

$$\vec{\zeta}_3 = \{3, 3, 3\}, \tag{4.33b}$$

$$\vec{\zeta}_2 = \{4, 2\}, \tag{4.33c}$$

$$\vec{\zeta}_1 = \{3\}, \tag{4.33d}$$

while the right structured sub-matrices can be defined in terms of Equation 4.20. Expressing $\underline{\underline{V}}'_4 = \begin{bmatrix} \underline{v}_1 & \underline{v}_2 & \underline{v}_3 & \underline{v}_4 \end{bmatrix}$, leads to the corresponding structured sub-matrices:

$$\underline{\underline{V}}'_4 = \begin{bmatrix} \underline{v}_1 & \underline{v}_2 & \underline{v}_3 & \underline{v}_4 \end{bmatrix}, \tag{4.34a}$$

$$\underline{\underline{V}}'_3 = \begin{bmatrix} \underline{v}_2 & \underline{v}_3 & \underline{v}_4 \end{bmatrix}, \tag{4.34b}$$

$$\underline{\underline{V}}'_2 = \begin{bmatrix} \frac{1}{\sqrt{2}}\left(\underline{v}_2 + \underline{v}_3\right) & \underline{v}_4 \end{bmatrix}, \tag{4.34c}$$

$$\underline{\underline{V}}'_1 = \begin{bmatrix} \frac{1}{\sqrt{3}}\left(\underline{v}_2 + \underline{v}_3 + \underline{v}_4\right) \end{bmatrix}. \tag{4.34d}$$

Procedures defined above create matrices that are orthogonal in both dimensions, but normalizable only in one. To quantify noise resilience, knowledge of the product $\underline{\underline{\Sigma}}^+_{s,4ij}\underline{\underline{U}}^+_{s,4ij}$ is necessary. Calculating $\underline{\underline{\Sigma}}^+_{s,4ij}$ is trivial because $\underline{\underline{\Sigma}}_{s,4ij}$ is diagonal, while calculating $\underline{\underline{U}}^+_{s,4ij}$ is more challenging. However, for $4ij$ systems, it can be shown that

$$\underline{\underline{U}}^+_{s,4ij} = \begin{bmatrix} \overline{\left[\sqrt{\frac{N}{16}}\right]}_{1\times4} & \underline{0}_{1\times i} & \underline{0}_{1\times j} \\ \underline{\underline{U}}'^{+}_4 & \underline{0}_{3\times i} & \underline{0}_{3\times j} \\ \underline{\underline{R}}_i & \underline{\underline{U}}'^{+}_i & \underline{0}_{i\times j} \\ \underline{\underline{R}}_j & \underline{0}_{j\times i} & \underline{\underline{U}}'^{+}_j \end{bmatrix} \tag{4.35}$$

is a correct inverse, where

$$\underline{\underline{U}}'^{+}_4 = \underline{\underline{U}}'^{T}_4, \tag{4.36a}$$

$$\underline{\underline{U}}'^{+}_3 = \frac{\sqrt{3}}{2}\begin{bmatrix} 1 & 1 & 0 \\ 0 & -1 & -1 \\ 1 & 0 & 1 \end{bmatrix}, \tag{4.36b}$$

$$\underline{\underline{U}}'^{+}_2 = \underline{\underline{U}}'^{T}_2, \tag{4.36c}$$

$$\underline{\underline{U}}'^{+}_1 = \underline{\underline{U}}'^{T}_1, \tag{4.36d}$$

and

$$\underline{\underline{\mathbf{R}}}_3 = \sqrt{\frac{3}{16}} \begin{bmatrix} -1 & -1 & -1 & -1 \\ 1 & 1 & 1 & 1 \\ -1 & -1 & -1 & -1 \end{bmatrix}, \tag{4.37a}$$

$$\underline{\underline{\mathbf{R}}}_2 = \sqrt{\frac{2}{16}} \begin{bmatrix} 0 & 0 & 0 & 0 \\ -1 & -1 & -1 & -1 \end{bmatrix}, \tag{4.37b}$$

$$\underline{\underline{\mathbf{R}}}_1 = \sqrt{\frac{1}{16}} \begin{bmatrix} -1 & -1 & -1 & -1 \end{bmatrix}. \tag{4.37c}$$

### 4.4.3   Noise Resilience

Following the same additive noise model as prescribed by Equation 1.22, the noise can be projected into the respective directions of the *sensor space* (Wang et al. (2007)), $\mathcal{V}$:

$$\vec{\underline{\mathbf{n}}}' = \underline{\underline{\mathbf{W}}}^+_{4ij} \vec{\underline{\mathbf{n}}}, \tag{4.38}$$

where the pseudoinverse can be written within the context of $4ij$ systems as

$$\underline{\underline{\mathbf{W}}}^+_{4ij} = \underline{\underline{\mathbf{V}}}_{s,4ij} \underline{\underline{\mathbf{\Sigma}}}^+_{s,4ij} \underline{\underline{\mathbf{U}}}^+_{s,4ij} = \underline{\underline{\mathbf{V}}}_{s,4ij} \underline{\underline{\mathbf{L}}}_{\underline{\underline{\mathbf{V}}}_{s,4ij}}. \tag{4.39}$$

$\underline{\underline{\mathbf{L}}}_{\underline{\underline{\mathbf{V}}}_{s,4ij}}$ contains the mapping weights of information for each of the vectors of $\underline{\underline{\mathbf{V}}}_{s,4ij}$:

$$\underline{\underline{\mathbf{L}}}_{\underline{\underline{\mathbf{V}}}_{s,4ij}} = \begin{bmatrix} \underline{\boldsymbol{\ell}}^{\mathrm{T}}_{\underline{\mathbf{v}}_1} & \underline{\boldsymbol{\ell}}^{\mathrm{T}}_{\underline{\mathbf{v}}_2} & \cdots & \underline{\boldsymbol{\ell}}^{\mathrm{T}}_{\underline{\mathbf{v}}_N} \end{bmatrix}^{\mathrm{T}}. \tag{4.40}$$

Since the pMMP's sensor space contains $N$ vectors, $\underline{\underline{\mathbf{L}}}_{\underline{\underline{\mathbf{V}}}_{s,4ij}}$ also contains $N$ channels. The Euclidean length of each of those vectors represents the noise magnitude in each of the vectors of $\underline{\underline{\mathbf{V}}}_{s,4ij}$,

$$p_{\underline{\mathbf{v}}} = ||\underline{\boldsymbol{\ell}}_{\underline{\mathbf{v}}}||_2. \tag{4.41}$$

For each measurement set, the matrix multiplications reveal that each of the vectors making up $\underline{\underline{\mathbf{V}}}_{s,4ij}$ will have easily identifiable noise magnitudes:

$$\underline{\underline{\mathbf{P}}}_{\underline{\underline{\mathbf{V}}}_4} = \begin{bmatrix} 1 & 1 & 1 & 1 \end{bmatrix}^{\mathrm{T}}, \tag{4.42a}$$

$$\underline{\underline{\mathbf{P}}}_{\underline{\underline{\mathbf{V}}}_3} = \begin{bmatrix} \sqrt{3} & \sqrt{3} & \sqrt{3} \end{bmatrix}^{\mathrm{T}}, \tag{4.42b}$$

$$\underline{\underline{\mathbf{P}}}_{\underline{\underline{\mathbf{V}}}_2} = \begin{bmatrix} 1 & \sqrt{3} \end{bmatrix}^{\mathrm{T}}, \tag{4.42c}$$

$$\underline{\underline{\mathbf{P}}}_{\underline{\underline{\mathbf{V}}}_1} = \begin{bmatrix} \sqrt{\frac{5}{3}} \end{bmatrix}^{\mathrm{T}}. \tag{4.42d}$$

Finally, the total noise magnitude vector is the concatenation of the ones defined above,

$$\mathbf{P}_{\underline{\underline{V}}_{s,4ij}} = \left[ \begin{array}{ccc} \mathbf{P}_{\underline{\underline{V}}_4}^{\mathrm{T}} & \mathbf{P}_{\underline{\underline{V}}_i}^{\mathrm{T}} & \mathbf{P}_{\underline{\underline{V}}_j}^{\mathrm{T}} \end{array} \right]^{\mathrm{T}}. \tag{4.43}$$

However, since the intent of this exercise is to build systems that perform the best for a given task, it also follows that it would be desired to evaluate system performance not for the entire sensor space, but for the *scene space* instead (Wang et al. (2007)). This space is a collection of Mueller vector targets that are of interest for a given task and is to be compared with $\mathcal{V}$. Denote the scene space as $\Upsilon$ to match its computational representation, $\underline{\underline{Y}}$, and define a transformation to the sensor space,

$$\underline{\underline{T}} = \underline{\underline{Y}} \backslash \underline{\underline{V}}_{s,4ij}, \tag{4.44}$$

which can be used to combine $R$ supported vectors into the vectors approaching $\Upsilon$ or estimating $\underline{\underline{Y}}$,

$$\hat{\underline{\underline{Y}}}^{\mathrm{T}} = \underline{\underline{T}} \, \underline{\underline{V}}_{s,4ij}^{\mathrm{T}}. \tag{4.45}$$

Note that while $\mathbf{P}_{\underline{\underline{V}}_{s,4ij}}$ represents the noise magnitude for the reconstructable vectors represented by $\underline{\underline{V}}_{s,4ij}$, it would be incorrect to use these absolute magnitudes to map noise from reconstructables to the desired channels. Instead, the noise characteristics contained within $\underline{\underline{L}}_{\underline{\underline{V}}_{s,4ij}}$ need to be similarly mapped:

$$\underline{\underline{L}}_{\underline{\underline{Y}}} = \underline{\underline{T}} \, \underline{\underline{L}}_{\underline{\underline{V}}_{s,4ij}} = \left[ \begin{array}{cccc} \underline{\ell}_{\underline{\underline{y}}_1}^{\mathrm{T}} & \underline{\ell}_{\underline{\underline{y}}_2}^{\mathrm{T}} & \cdots & \underline{\ell}_{\underline{\underline{y}}_K}^{\mathrm{T}} \end{array} \right]^{\mathrm{T}}, \tag{4.46}$$

where $K$ is the total number of vectors in $\underline{\underline{Y}}$. The resulting noise magnitudes within those vectors can be evaluated in a philosophically equivalent way,

$$p_{\underline{\underline{y}}} = ||\underline{\ell}_{\underline{\underline{y}}}||_2, \tag{4.47}$$

and then can be combined into a total magnitude vector

$$\mathbf{P}_{\underline{\underline{Y}}} = \left[ \begin{array}{cccc} p_{\underline{\underline{y}}_1} & p_{\underline{\underline{y}}_2} & \cdots & p_{\underline{\underline{y}}_K} \end{array} \right]^{\mathrm{T}}. \tag{4.48}$$

### 4.4.4   Space Coverage

To properly evaluate a given partial system, it is important to know not only the system's noise resilience, but also the closeness of the sensor space to the scene space, which can

be described by $K$ ordered canonical angles $\zeta_1 \leq \zeta_2 \leq \ldots \leq \zeta_K$ Hotelling (1936). The first canonical angle $\zeta_1$ is

$$\zeta_1 = \cos^{-1}\left(\min_{\hat{\mathbf{v}}_1 \in \mathcal{V}, \hat{\mathbf{y}}_1 \in \Upsilon} \left(\hat{\underline{\mathbf{v}}}_1 \cdot \hat{\underline{\mathbf{y}}}_1\right)\right). \tag{4.49}$$

Subsequent canonical angles are computed by evaluating Equation 4.49 with the portions of subspace $\mathcal{V}$ remaining after the elimination of $\hat{\mathbf{v}}_1$. The best case scenario is when $\zeta_K = 0$, which means $\Upsilon \subset \mathcal{V}$, and the pMMP spans the desired channels.

While Equation 4.49 provides an intuitive interpretation of the canonical angles, there are more efficient ways of computing the angles, like forming the auxiliary matrix

$$\underline{\underline{\mathbf{X}}} = \underline{\underline{\mathbf{Y}}} - \underline{\underline{\mathbf{V}}}(\underline{\underline{\mathbf{V}}}^{\mathrm{T}}\underline{\underline{\mathbf{Y}}}) = \begin{bmatrix} \underline{\mathbf{x}}_1 & \underline{\mathbf{x}}_2 & \cdots & \underline{\mathbf{x}}_K \end{bmatrix}. \tag{4.50}$$

and computing the canonical angles its the singular values as (Knyazev and Argentati (2002))

$$\zeta_k = \arcsin(\sigma_{\underline{\mathbf{x}}_k}). \tag{4.51}$$

## 4.5   Example of pMMP Optimization

To find the best pMMP design for a given task, both noise resilience and space coverage need to be optimized. Because those properties are not inherently guaranteed to have overlapping minimums, the solution is invariably bound to be a point on the Pareto surface of a multi-objective optimization problem. The following metric

$$\arg\min_{\vec{\xi}} \left[ \underbrace{\sum_{k=1}^{K}(\alpha_k p_{\underline{\mathbf{y}}_k})^2}_{\varepsilon_1} + w \underbrace{\sum_{k=1}^{K}(\beta_k \sigma_{\underline{\mathbf{x}}_k})^2}_{\varepsilon_2} \right] \tag{4.52}$$

successfully finds appropriate pMMP designs. The choice of $w$, $\{\alpha_k\}$ and $\{\beta_k\}$ provides handles to adjust the importance of all the various parameters, while the optimization variable vector $\vec{\xi}$ contains six values to construct three generating and three analyzing vector pairs. The first four variables define $\phi_{\underline{\mathbf{G}}_1}$, $\theta_{\underline{\mathbf{G}}_1}$, $\phi_{\underline{\mathbf{A}}_1}$ and $\theta_{\underline{\mathbf{A}}_1}$ to produce vectors $\underline{\mathbf{G}}_{1,\pm}$ and $\underline{\mathbf{A}}_{1,\pm}$, while the second two variables define $\psi_G$ and $\psi_A$ to prescribe where $\underline{\mathbf{G}}_{2,\pm}$, $\underline{\mathbf{A}}_{2,\pm}$, $\underline{\mathbf{G}}_{3,\pm}$ and $\underline{\mathbf{A}}_{3,\pm}$ reside on the orthogonal circles with respect to $\underline{\mathbf{G}}_{1,\pm}$ and $\underline{\mathbf{A}}_{1,\pm}$.

To illustrate the design of pMMPs, consider the example presented in Hoover and Tyo (2007). Four different coupons of an ABS plastic material were exposed to different fluences of high energy laser energy, and the resulting damaged samples had their monostatic Mueller matrices measured at a range of angles from $-20°$ to $20°$. Performing SVD of the data reveals that the most fundamental three measurement channels are

$$\underline{\underline{Y}} = \begin{bmatrix}
-0.9204 & 0.3097 & 0.2378 \\
-0.0347 & 0.0410 & -0.2480 \\
-0.0010 & 0.0034 & -0.0136 \\
-0.0003 & 0.0007 & 0.0088 \\
-0.0318 & 0.0524 & -0.2356 \\
-0.2757 & -0.4730 & -0.4418 \\
-0.0010 & -0.0043 & -0.0050 \\
-0.0004 & 0.0033 & -0.0085 \\
0.0035 & -0.0039 & 0.0207 \\
0.0013 & -0.0043 & 0.0138 \\
0.2703 & 0.4860 & 0.3996 \\
-0.0019 & -0.0033 & -0.0220 \\
-0.0004 & 0.0008 & -0.0008 \\
0.0001 & 0.0023 & -0.0037 \\
0.0028 & 0.0017 & 0.0292 \\
0.0398 & 0.6630 & -0.6850
\end{bmatrix}. \tag{4.53}$$

Note that the original paper used covariance matrix principal component analysis that resulted in a different set of channels, which did not include $m_{00}$ in any of the measurements. If $m_{00}$ is added back, then the maximum canonical angle between the two spaces is $3.1011°$. The difference is small enough to be accounted for by the extra idealization step taken in Hoover and Tyo (2007).

MATLAB's built-in genetic algorithm routine is used together with Equation 5.24 to optimize each of the $4ij$ pMMP designs with $\alpha_k = \beta_k = 1$ and $w = 25$. Note that there is nothing fundamental about the choice of $w$ — a number of different weights between 1 and 100 were tried, and it was found that for this data set the value of 25 provided a good so-

lution where the space coverage penalty was just significant enough for the reconstruction of relevant information to be prioritized over the noise resilience.

Table 4.1 shows the system performances that were found for each of the defined classes of polarimeters. The space coverage seems to be marginally better for the 422 system than it is for the 432 or the 433, despite the latter two making more measurements and having a capacity only to expand the space coverage if the 422 design is used as the base. That, however, is purely an artifact of our choice of $w$, which leads to the optimizer finding a solution with slightly better noise resilience by sacrificing some space coverage. Practically, the designs should be evaluated on whether or not they can separate the different objects classes. To determine which of these pMMPs accomplish that, it is necessary to look at the object projections onto $\hat{\Upsilon}$. This can be captured by looking at how the proximity of each of the 25 objects from each of the four types of objects to the nearby classes changes. Instead of comparing data points directly, the comparison class is instead piece-wise interpolated and the separation for each object/class both in $\Upsilon$ and $\hat{\Upsilon}$ is determined as:

$$d_{\alpha,\beta,\gamma,\delta} = \frac{|(\vec{r}_{\alpha,\gamma} - \vec{r}_{\beta,\delta}) \times (\vec{r}_{\alpha,\gamma} - \vec{r}_{\beta,\delta+1})|}{|\vec{r}_{\beta,\delta+1} - \vec{r}_{\beta,\delta}|}, \tag{4.54a}$$

$$\hat{d}_{\alpha,\beta,\gamma,\delta} = \frac{|(\hat{\vec{r}}_{\alpha,\gamma} - \hat{\vec{r}}_{\beta,\delta}) \times (\hat{\vec{r}}_{\alpha,\gamma} - \hat{\vec{r}}_{\beta,\delta+1})|}{|\hat{\vec{r}}_{\beta,\delta+1} - \hat{\vec{r}}_{\beta,\delta}|}, \tag{4.54b}$$

where $\alpha$ and $\beta$ represent the object classes, $\gamma$ represents one of the 25 points within class $\alpha$, and $\delta$ represents one of the 24 line segments created for class $\beta$. Evaluate the geometric mean of the ratios of least separation,

$$h_{\alpha,\beta} = \left[\prod_{\gamma=1}^{25} \frac{\hat{d}_{\alpha,\beta,\gamma,\min}}{d_{\alpha,\beta,\gamma,\min}}\right]^{\frac{1}{25}}. \tag{4.55}$$

When $h_{\alpha,\beta} = 0$, classes $\alpha$ and $\beta$ have collapsed to lie on top of each other, while when $h_{\alpha,\beta} = 1$, the separation between classes $\alpha$ and $\beta$ has remained unchanged. In the case that $h_{\alpha,\beta} > 1$, the separation within the reconstruction is greater than the original separation. Although this presents a seemingly interesting scenario, this result is attributable to non-linearities introduced by the averaging of different space projections and would be compensated by another $h_{\alpha,\beta}$ elsewhere.

Examining the performance of each of the ten pMMPs optimized designs in Table 4.1 and Figures 4.7–4.16, it becomes clear that the 422 system is the first design of the defined range of systems that accomplishes the task of matching the space coverage and thereby separating the object projections adequately for object detection.

There is room to make the optimization routine more elaborate. For example, instead of matching the scene and sensor spaces of any given pMMP class, object identification can be done in the measurement space itself. This would require constructing a manifold as a model for the object distribution in the $N$-dimensional space, applying the proper noise model and looking at the separability of the classes within the measurement space. Performing all of this in each of the optimization instantiations is computationally intensive, as well as outside the scope of this development. A separate discussion is warranted to address that level of optimization properly.

## 4.6   pMMP Calibration

The amount of literature describing Mueller matrix calibration is limited. Compain's treatment is one that described the process for a general case in enough mathematical detail to suggest near optimal performance (Compain et al. (1999)). The drawback of the presented method in that work is the assumption that a complete measurement task is performed, which leads to a restrictive analysis that assumes that there are four analyzing and four generating vectors. Since this chapter is interested in constructing systems that perform partial measurements, a different approach suitable for calibration of pMMPs is required.

Rewrite Equation 1.20 as

$$\underline{\mathbf{I}}\,\underline{\mathbf{M}}^{'-1} = \underline{\underline{\mathbf{W}}}^{'}, \tag{4.56}$$

where, initially, $\underline{\mathbf{I}}$ is $N \times 1$ and $\underline{\mathbf{M}}^{'-1}$ is $1 \times 16$. Obviously, $\underline{\underline{\mathbf{W}}}^{'}$ cannot be deduced using only one $\underline{\mathbf{M}}^{'}$, i.e. one reference measurement object. Instead, considering $K$ Mueller vectors, which are formed into a matrix, $\underline{\underline{\mathbf{R}}}^{'}$. The measurement can then be written as

$$\underline{\underline{\mathbf{I}}}\,\underline{\underline{\mathbf{R}}}^{'-1} = \underline{\underline{\mathbf{W}}}^{'}, \tag{4.57}$$

where $\underline{\underline{\mathbf{R}}}^{'-1}$ is $K \times 16$ and thereby $\underline{\underline{\mathbf{I}}}$ is $N \times K$. With sufficiently large $K$, $\underline{\underline{\mathbf{W}}}^{'}$ can be determined with sufficient accuracy. With this in mind, creating a proper $\underline{\underline{\mathbf{R}}}^{'-1}$ requires a sufficiently

Table 4.1: Optimization results for the 10 pMMP system classes. The optimization targets, $\varepsilon_1$ and $\varepsilon_2$, are defined in Equation 5.24, while $\zeta_K$ represents the largest canonical angle. The values for $h_{\alpha,\beta}$ are calculated via Equation 4.55. Because of the way that the four classes are distributed in $\Upsilon$, knowledge of $h_{1,2}$, $h_{2,3}$ and $h_{3,4}$ may suffice.

| Design | N | $\varepsilon_1$ | $\varepsilon_2$ | $\varepsilon_1 + w\varepsilon_2$ | $\zeta_K$ | $h_{1,2}$ | $h_{2,3}$ | $h_{3,4}$ | $h_{1,3}$ | $h_{2,4}$ | $h_{1,4}$ |
|---|---|---|---|---|---|---|---|---|---|---|---|
| 400 | 4 | 1.911 | 1.089 | 29.142 | 89.65° | 0.0003 | 0.0006 | 0.0006 | 0.0001 | 0.0001 | 0.0000 |
| 410 | 5 | 2.546 | 0.717 | 20.475 | 56.90° | 0.1747 | 0.2207 | 0.2698 | 0.3144 | 0.1922 | 0.0355 |
| 411 | 6 | 2.669 | 0.556 | 16.569 | 47.53° | 0.1770 | 0.2417 | 0.4435 | 0.2232 | 0.4506 | 0.1438 |
| 420 | 6 | 3.520 | 0.469 | 15.247 | 43.18° | 0.5305 | 0.4743 | 0.5594 | 0.2750 | 0.5191 | 0.5163 |
| 421 | 7 | 3.528 | 0.248 | 9.727 | 29.78° | 0.5184 | 0.2960 | 0.8056 | 0.2087 | 0.8787 | 0.5441 |
| 422 | 8 | 3.967 | 0.002 | 4.011 | 2.32° | 1.0852 | 0.9811 | 0.9652 | 0.9893 | 0.9922 | 0.9851 |
| 430 | 7 | 3.318 | 0.469 | 15.042 | 43.17° | 0.5133 | 0.4793 | 0.5625 | 0.2705 | 0.5435 | 0.5151 |
| 431 | 8 | 3.493 | 0.249 | 9.713 | 29.84° | 0.5155 | 0.3029 | 0.8132 | 0.1998 | 0.8583 | 0.5302 |
| 432 | 9 | 3.932 | 0.002 | 3.987 | 2.60° | 1.0940 | 0.9921 | 0.9632 | 0.9893 | 0.9914 | 0.9869 |
| 433 | 10 | 3.897 | 0.002 | 3.949 | 2.57° | 1.1676 | 0.9966 | 0.9637 | 0.9925 | 1.0005 | 0.9863 |
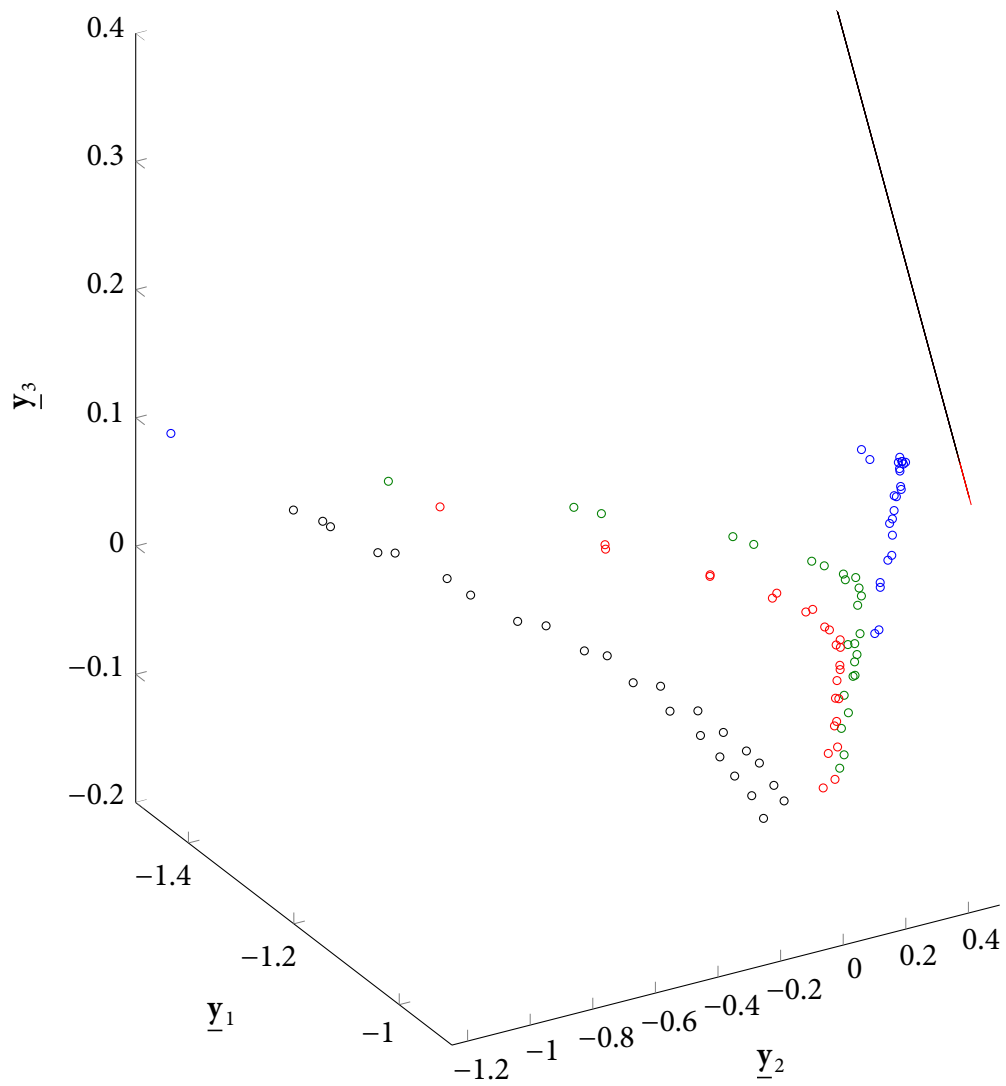
Figure 4.7: Space coverage of 400 pMMP, $N = 4$.
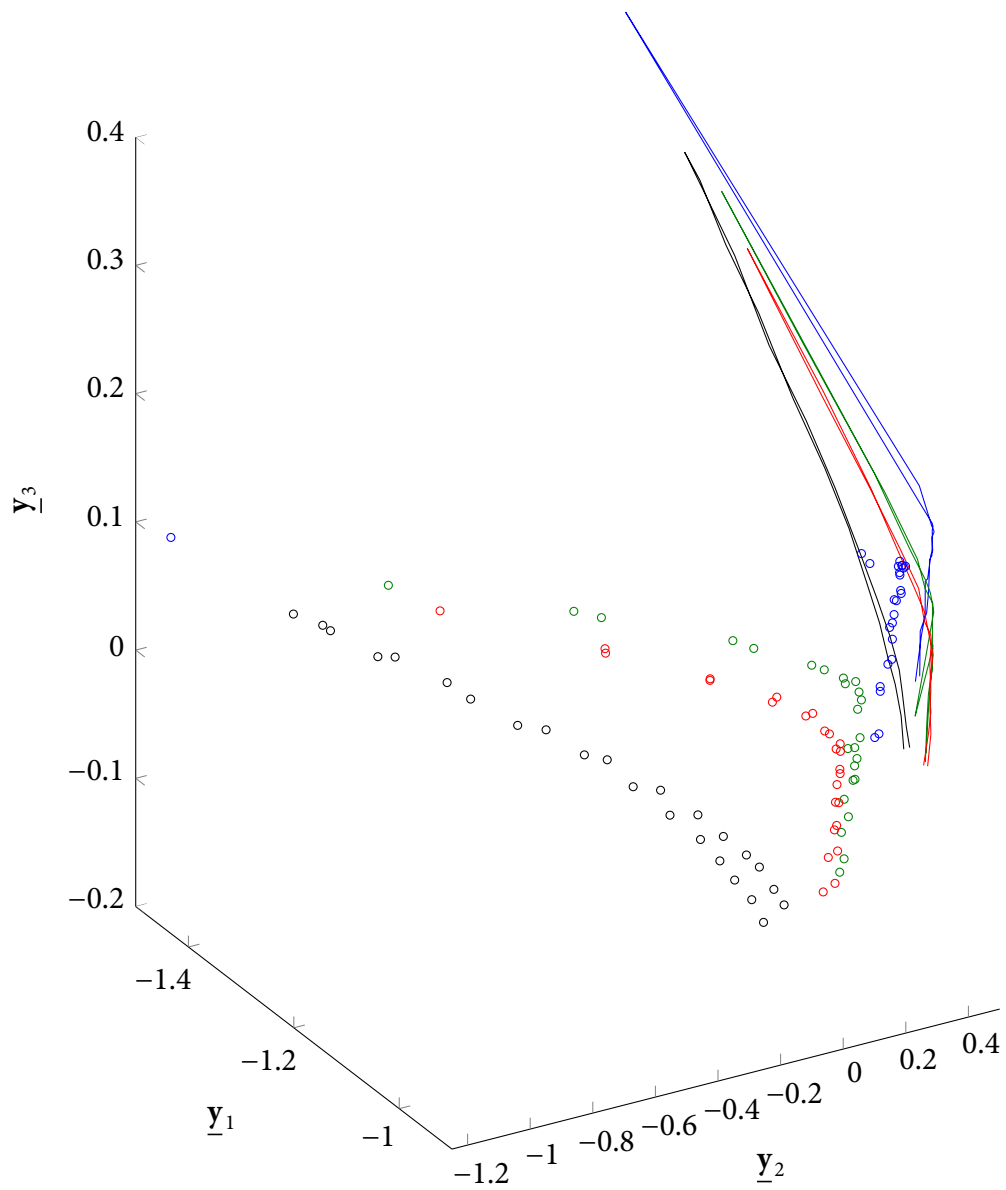
Figure 4.8: Space coverage of 410 pMMP, $N = 5$.
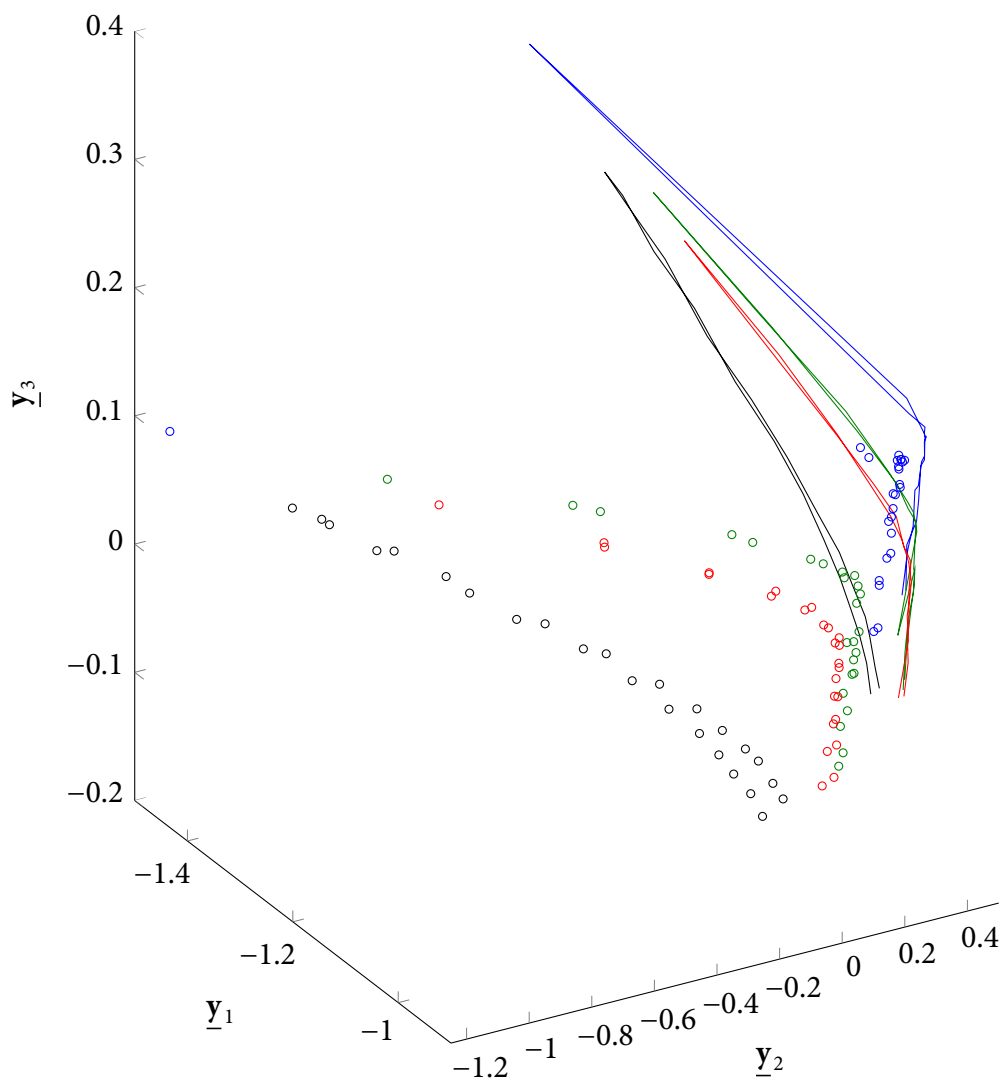
Figure 4.9: Space coverage of 411 pMMP, $N = 6$.
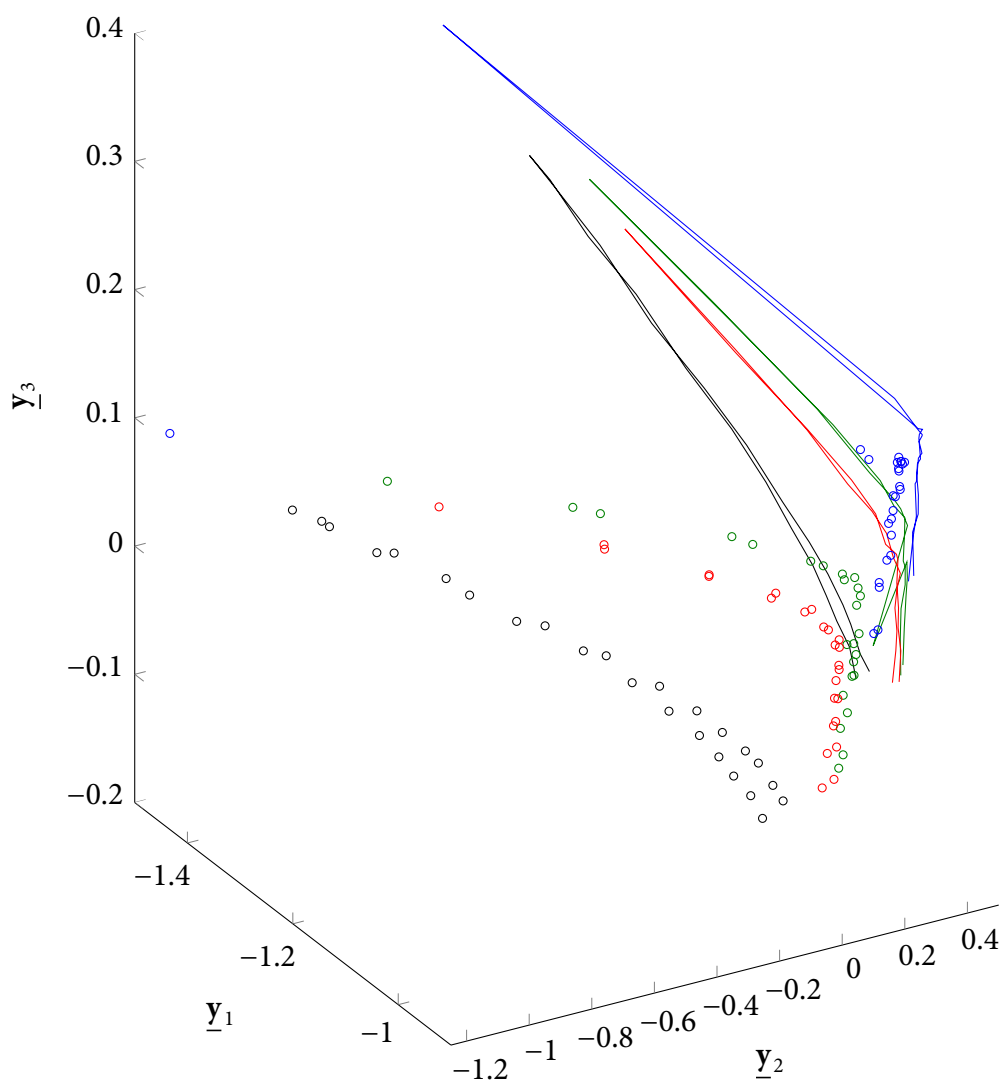
Figure 4.10: Space coverage of 420 pMMP, $N = 6$.
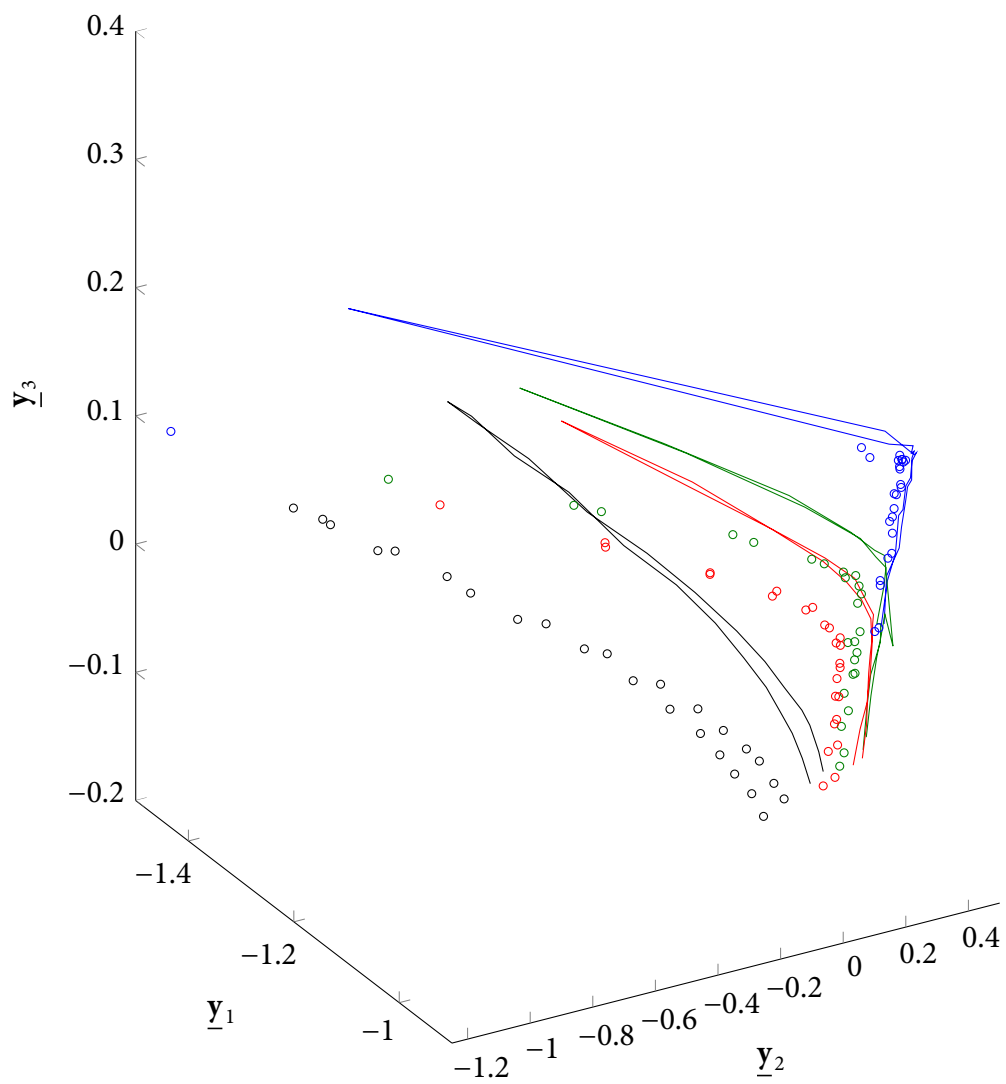
Figure 4.11: Space coverage of 421 pMMP, $N = 7$.
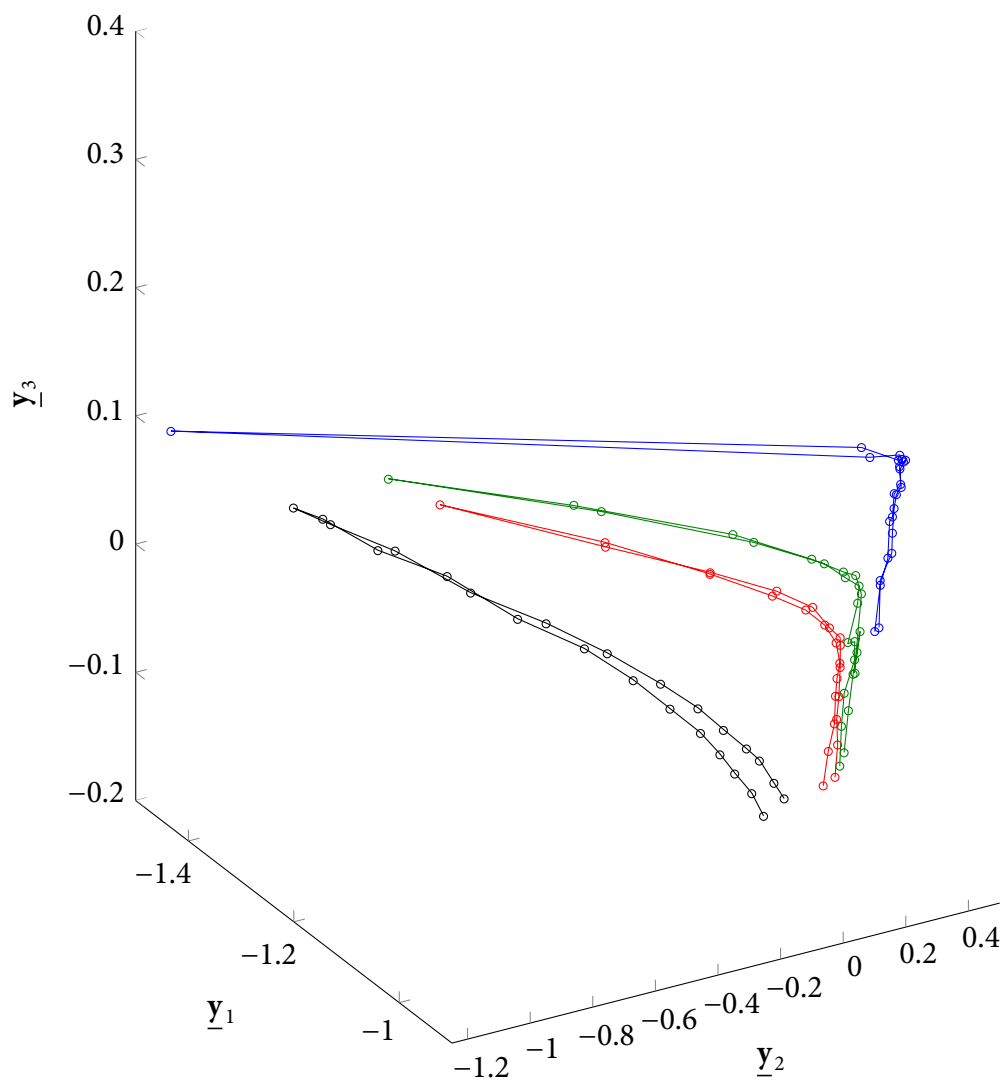
Figure 4.12: Space coverage of 422 pMMP, $N = 8$.
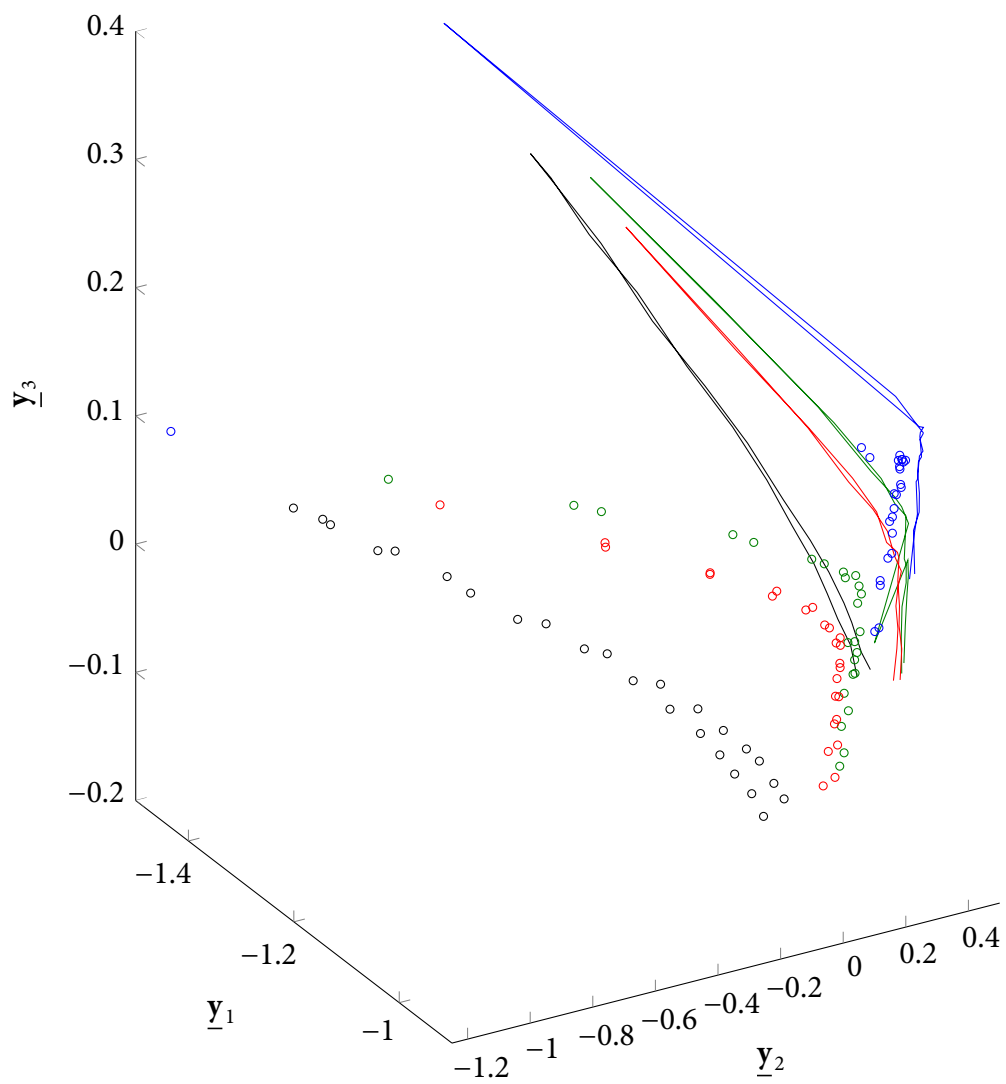
Figure 4.13: Space coverage of 430 pMMP, $N = 7$.
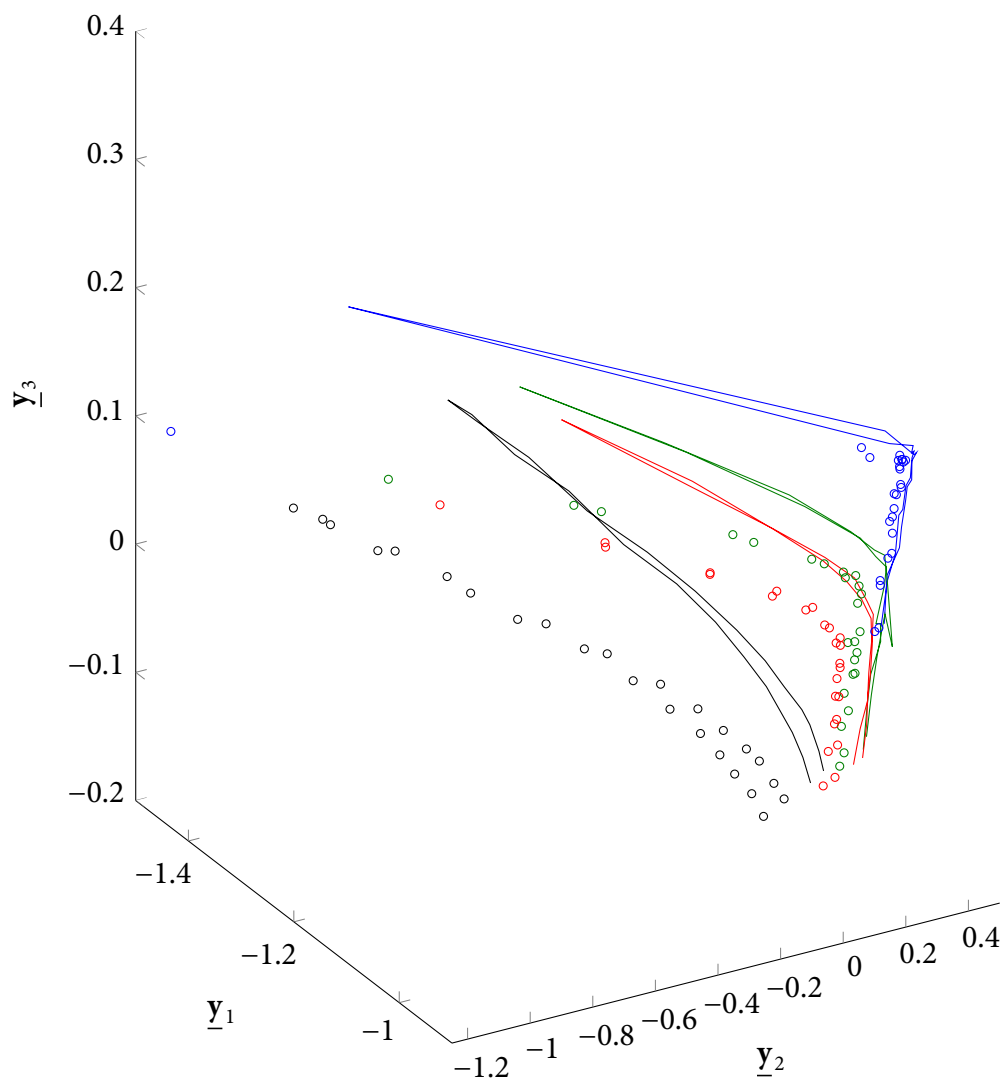
Figure 4.14: Space coverage of 431 pMMP, $N = 8$.
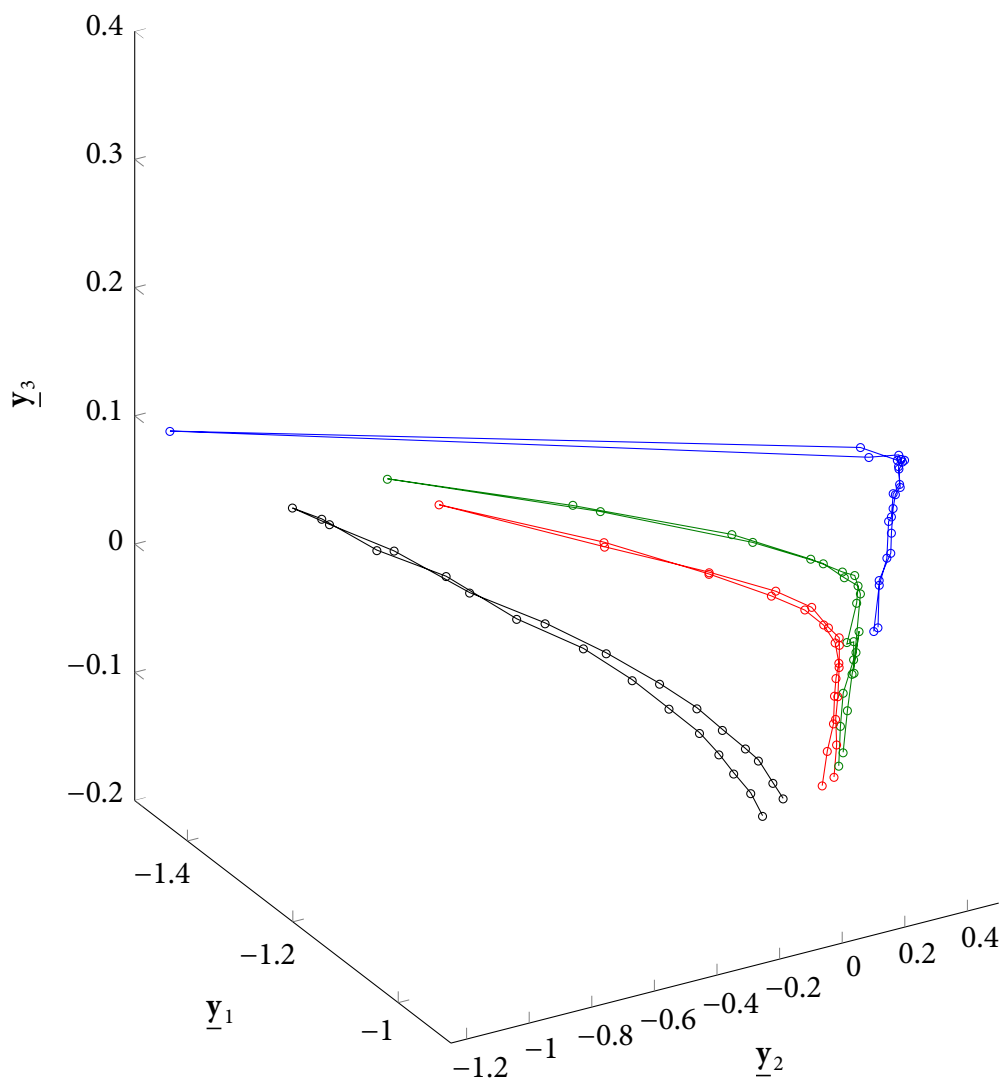
Figure 4.15: Space coverage of 432 pMMP, $N = 9$.
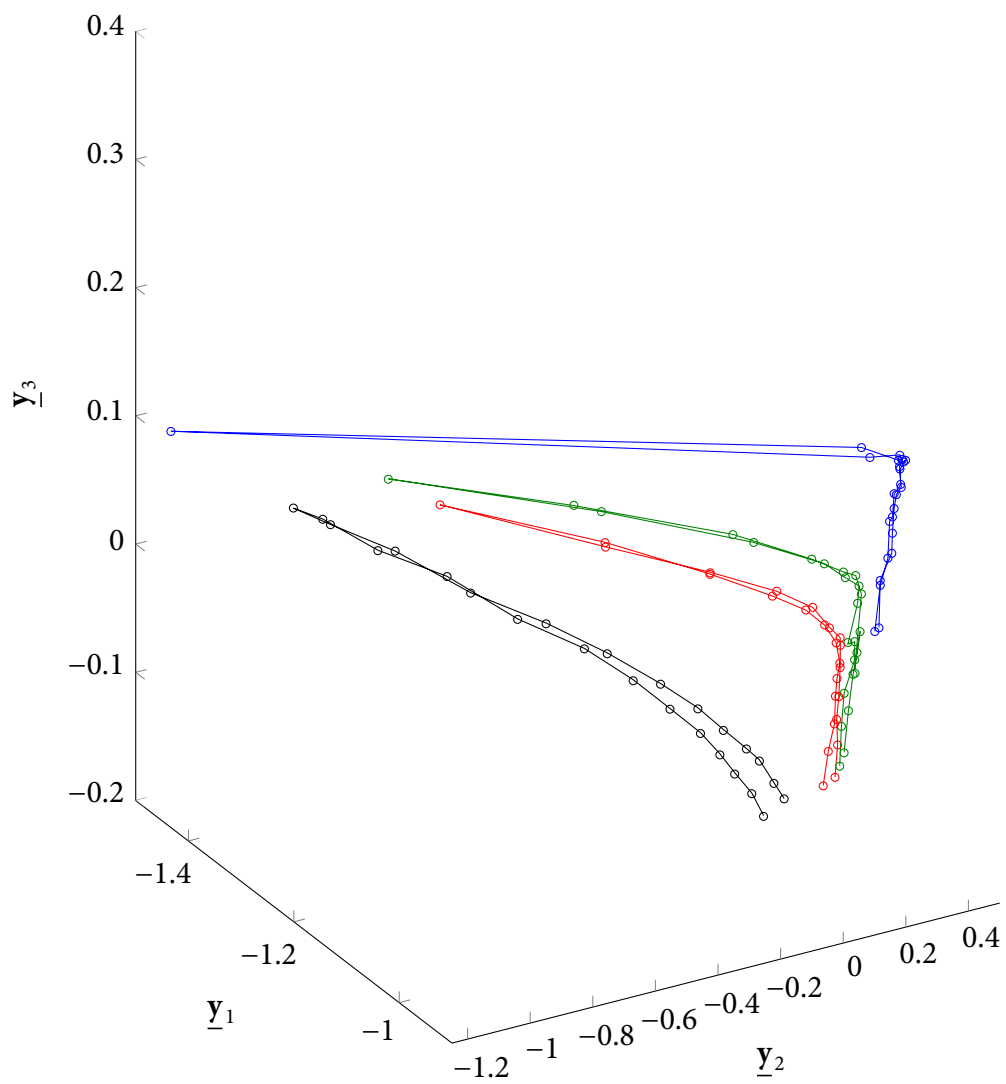
Figure 4.16: Space coverage of 433 pMMP, $N = 10$.

diverse family of $\underline{\mathbf{M}}'$s, which mirrors the requirements of the measurement matrix. Thus, the goal is to create an invertible set of Mueller vectors, $\underline{\mathbf{R}}'$.

The elements that are chosen for calibration are to be assumed to be ideal, thus it is best to use elements that approximate their ideal counterparts well. A linear diattenuator is perhaps one of the better elements by virtue of the existence of Glan-Thompson and Wollaston polarizers that can provide around $10^{-6}$ extinction. The Mueller matrix for a linear diattenuator can be seen in Equation 1.28, while its idealized polarizer form can be seen in Equation 1.29. From the Mueller matrix, it can be clearly seen that the polarizer can only span the linear–linear 3×3 block of the Mueller matrix. To add more Mueller elements to the calibration, retarders can be introduced, the Mueller matrix of which can be seen in Equation 1.30. In the most general case, calibration can be performed via insertion of a black box that is the ideal polarizer sandwiched between two retarders

$$\underline{\underline{\mathbf{X}}} = \underline{\underline{\mathbf{M}}}_{\mathrm{LR}}(\delta_2,\phi_2)\,\underline{\underline{\mathbf{M}}}_{\mathrm{LP}}(\theta)\,\underline{\underline{\mathbf{M}}}_{\mathrm{LR}}(\delta_1,\phi_1), \qquad (4.58)$$

where $\delta_i$s and $\phi_i$s are the retardances and the orientations of the two retarders, and $\theta$ is the orientation of the polarizer in the middle. Following Equation 1.19, the Mueller matrix

can be rewritten as a Mueller vector

$$\underline{\mathbf{X}}' = \frac{1}{2} \begin{bmatrix} 1 \\ c(2\theta)(c(2\phi_1)^2 + c(\delta_1)s(2\phi_1)^2) - c(2\phi_1)s(2\phi_1)s(2\theta)(c(\delta_1) - 1) \\ s(2\theta)(c(\delta_1)c(2\phi_1)^2 + s(2\phi_1)^2) - c(2\phi_1)c(2\theta)s(2\phi_1)(c(\delta_1) - 1) \\ c(2\phi_1)s(2\theta)s(\delta_1) - c(2\theta)s(2\phi_1)s(\delta_1) \\ c(2\theta)(c(2\phi_2)^2 + c(\delta_2)s(2\phi_2)^2) - c(2\phi_2)s(2\phi_2)s(2\theta)(c(\delta_2) - 1) \\ (c(2\theta)^2(c(2\phi_1)^2 + c(\delta_1)s(2\phi_1)^2) - c(2\phi_1)c(2\theta)s(2\phi_1)s(2\theta)(c(\delta_1) - 1))(c(2\phi_2)^2 + c(\delta_2)s(2\phi_2)^2) \\ -c(2\phi_2)s(2\phi_2)(c(\delta_2) - 1)(c(2\theta)s(2\theta)(c(2\phi_1)^2 + c(\delta_1)s(2\phi_1)^2) - c(2\phi_1)s(2\phi_1)s(2\theta)^2(c(\delta_1) - 1)) \\ (c(2\theta)s(2\theta)(c(\delta_1)c(2\phi_1)^2 + s(2\phi_1)^2) - c(2\phi_1)c(2\theta)^2s(2\phi_1)(c(\delta_1) - 1))(c(2\phi_2)^2 + c(\delta_2)s(2\phi_2)^2) \\ -c(2\phi_2)s(2\phi_2)(c(\delta_2) - 1)(s(2\theta)^2(c(\delta_1)c(2\phi_1)^2 + s(2\phi_1)^2) - c(2\phi_1)c(2\theta)s(2\phi_1)s(2\theta)(c(\delta_1) - 1)) \\ -(c(2\theta)^2s(2\phi_1)s(\delta_1) - c(2\phi_1)c(2\theta)s(2\theta)s(\delta_1))(c(2\phi_2)^2 + c(\delta_2)s(2\phi_2)^2) \\ -c(2\phi_2)s(2\phi_2)(c(\delta_2) - 1)(c(2\phi_1)s(2\theta)^2s(\delta_1) - c(2\theta)s(2\phi_1)s(2\theta)s(\delta_1)) \\ s(2\theta)(c(\delta_2)c(2\phi_2)^2 + s(2\phi_2)^2) - c(2\phi_2)c(2\theta)s(2\phi_2)(c(\delta_2) - 1) \\ (c(2\theta)s(2\theta)(c(2\phi_1)^2 + c(\delta_1)s(2\phi_1)^2) - c(2\phi_1)s(2\phi_1)s(2\theta)^2(c(\delta_1) - 1))(c(\delta_2)c(2\phi_2)^2 + s(2\phi_2)^2) \\ -c(2\phi_2)s(2\phi_2)(c(\delta_2) - 1)(c(2\theta)^2(c(2\phi_1)^2 + c(\delta_1)s(2\phi_1)^2) - c(2\phi_1)c(2\theta)s(2\phi_1)s(2\theta)(c(\delta_1) - 1)) \\ (s(2\theta)^2(c(\delta_1)c(2\phi_1)^2 + s(2\phi_1)^2) - c(2\phi_1)c(2\theta)s(2\phi_1)s(2\theta)(c(\delta_1) - 1))(c(\delta_2)c(2\phi_2)^2 + s(2\phi_2)^2) \\ -c(2\phi_2)s(2\phi_2)(c(\delta_2) - 1)(c(2\theta)s(2\theta)(c(\delta_1)c(2\phi_1)^2 + s(2\phi_1)^2) - c(2\phi_1)c(2\theta)^2s(2\phi_1)(c(\delta_1) - 1)) \\ (c(2\phi_1)s(2\theta)^2s(\delta_1) - c(2\theta)s(2\phi_1)s(2\theta)s(\delta_1))(c(\delta_2)c(2\phi_2)^2 + s(2\phi_2)^2) \\ +c(2\phi_2)s(2\phi_2)(c(\delta_2) - 1)(c(2\theta)^2s(2\phi_1)s(\delta_1) - c(2\phi_1)c(2\theta)s(2\theta)s(\delta_1)) \\ c(2\theta)s(2\phi_2)s(\delta_2) - c(2\phi_2)s(2\theta)s(\delta_2) \\ -c(2\phi_2)s(\delta_2)(c(2\theta)s(2\theta)(c(2\phi_1)^2 + c(\delta_1)s(2\phi_1)^2) - c(2\phi_1)s(2\phi_1)s(2\theta)^2(c(\delta_1) - 1)) \\ +s(2\phi_2)s(\delta_2)(c(2\theta)^2(c(2\phi_1)^2 + c(\delta_1)s(2\phi_1)^2) - c(2\phi_1)c(2\theta)s(2\phi_1)s(2\theta)(c(\delta_1) - 1)) \\ -c(2\phi_2)s(\delta_2)(s(2\theta)^2(c(\delta_1)c(2\phi_1)^2 + s(2\phi_1)^2) - c(2\phi_1)c(2\theta)s(2\phi_1)s(2\theta)(c(\delta_1) - 1)) \\ +s(2\phi_2)s(\delta_2)(c(2\theta)s(2\theta)(c(\delta_1)c(2\phi_1)^2 + s(2\phi_1)^2) - c(2\phi_1)c(2\theta)^2s(2\phi_1)(c(\delta_1) - 1)) \\ -c(2\phi_2)s(\delta_2)(c(2\phi_1)s(2\theta)^2s(\delta_1) - c(2\theta)s(2\phi_1)s(2\theta)s(\delta_1)) \\ -s(2\phi_2)s(\delta_2)(c(2\theta)^2s(2\phi_1)s(\delta_1) - c(2\phi_1)c(2\theta)s(2\theta)s(\delta_1)) \end{bmatrix}, \quad (4.59)$$

where $c(x) = \cos(x)$ and $s(x) = \sin(x)$. By adjusting $\theta$, $\phi_1$ and $\phi_2$, all Mueller non-$m_{00}$ elements can be modulated, therefore obtaining a reference object that spans the entire space. Those variables can be optimized such that the Mueller objects create $\underline{\underline{\mathbf{R}}}'$ that is as well conditioned as possible.

Before jumping into the optimization, it can be recognized that this process will effectively feature the same math as the measurement optimization, which has been performed many times. The optimally sampled sixteen-reference measurement will then correspond to a tetrahedron in both the $\underline{\underline{\mathbf{A}}}$ and $\underline{\underline{\mathbf{G}}}$ equivalents. Jumping directly to the optimal answer:

$$\delta_1 = \delta_2 = \arccos\left(-2/3\right) \approx 131.810°, \tag{4.60a}$$

$$\phi_1 = \phi_2 = \{-\psi_2, -\psi_1, +\psi_1, +\psi_2\}, \tag{4.60b}$$

where

$$\psi_1 = \frac{\pi}{2} - \frac{1}{5}\arccos\left(\frac{1 - 2\sqrt{3}}{5}\right) \approx 51.6925°, \tag{4.61a}$$

$$\psi_2 = \arccos\left(\sqrt{\frac{1 + \sqrt{\frac{\sqrt{3}+2}{5}}}{2}}\right) \approx 15.1185°. \tag{4.61b}$$

In order to obtain retarders with very accurate retardance, custom Fresnel rhombs can be manufactured and by stacking two of them together, the optical axis can be maintained. The advantage of using such a construction is that the Mueller matrix can be calculated directly based on the index of refraction, $n(\lambda)$, and the face angle of the rhomb, $\alpha$ (different from $\alpha = q + r$ that was used before).

Consider the pMMP polarimeter at Dayton AFRL. For the purposes of this exercise, it is sufficient to describe the system in terms of its PSG and PSA designs. The PSG can be equivalently described with a RR hand that is described in Section 1.6.1, while the PSA is a rotating analyzer (RA) hand, which only has access to linear polarization. This corresponds to the reconstructables matrix

$$\underline{\underline{\mathbf{B}}} = \begin{bmatrix} 1 & 1 & 1 & 1 \\ 1 & 1 & 1 & 1 \\ 1 & 1 & 1 & 1 \\ 0 & 0 & 0 & 0 \end{bmatrix}, \tag{4.62}$$

which suggests that the reference-object modulation in the bottom row is unnecessary. Thus, the second retarder provides no utility, leaving only

$$\underline{\underline{\mathbf{X}}} = \underline{\underline{\mathbf{M}}}_{\mathrm{LP}}(\theta)\underline{\underline{\mathbf{M}}}_{\mathrm{LR}}(\delta_1, \phi_1), \tag{4.63}$$

or

$$
\underline{\mathbf{X}}' = \frac{1}{2}
\begin{bmatrix}
1 \\
\cos(2\theta)(\cos(2\phi_1)^2 + \cos(\delta_1)\sin(2\phi_1)^2) - \cos(2\phi_1)\sin(2\phi_1)\sin(2\theta)(\cos(\delta_1) - 1) \\
\sin(2\theta)(\cos(\delta_1)\cos(2\phi_1)^2 + \sin(2\phi_1)^2) - \cos(2\phi_1)\cos(2\theta)\sin(2\phi_1)(\cos(\delta_1) - 1) \\
\cos(2\phi_1)\sin(2\theta)\sin(\delta_1) - \cos(2\theta)\sin(2\phi_1)\sin(\delta_1) \\
\cos(2\theta) \\
\cos(2\theta)^2(\cos(2\phi_1)^2 + \cos(\delta_1)\sin(2\phi_1)^2) - \cos(2\phi_1)\cos(2\theta)\sin(2\phi_1)\sin(2\theta)(\cos(\delta_1) - 1) \\
\cos(2\theta)\sin(2\theta)(\cos(\delta_1)\cos(2\phi_1)^2 + \sin(2\phi_1)^2) - \cos(2\phi_1)\cos(2\theta)^2\sin(2\phi_1)(\cos(\delta_1) - 1) \\
\cos(2\phi_1)\cos(2\theta)\sin(2\theta)\sin(\delta_1) - \cos(2\theta)^2\sin(2\phi_1)\sin(\delta_1) \\
\sin(2\theta) \\
\cos(2\theta)\sin(2\theta)(\cos(2\phi_1)^2 + \cos(\delta_1)\sin(2\phi_1)^2) - \cos(2\phi_1)\sin(2\phi_1)\sin(2\theta)^2(\cos(\delta_1) - 1) \\
\sin(2\theta)^2(\cos(\delta_1)\cos(2\phi_1)^2 + \sin(2\phi_1)^2) - \cos(2\phi_1)\cos(2\theta)\sin(2\phi_1)\sin(2\theta)(\cos(\delta_1) - 1) \\
\cos(2\phi_1)\sin(2\theta)^2\sin(\delta_1) - \cos(2\theta)\sin(2\phi_1)\sin(2\theta)\sin(\delta_1) \\
0 \\
0 \\
0 \\
0
\end{bmatrix}
\tag{4.64}
$$

The optimal $\delta$ is still $\arccos(-2/3)$, however, calibration does not need to be performed as measurements themselves, thus there is less pressure to take as few reference measurements as possible. Many can be taken with the calibration system overdeterminining the reconstruction of the system's $\underline{\underline{\mathbf{W}}}'$, while using widely available $\frac{\lambda}{4}$ Fresnel rhombs. This would leave

$$
\underline{\mathbf{X}}' = \frac{1}{2}
\begin{bmatrix}
1 \\
\cos(2\theta)\cos(2\phi_1)^2 + \sin(2\phi_1)\sin(2\theta)\cos(2\phi_1) \\
\sin(2\theta)\sin(2\phi_1)^2 + \cos(2\phi_1)\cos(2\theta)\sin(2\phi_1) \\
\cos(2\phi_1)\sin(2\theta) - \cos(2\theta)\sin(2\phi_1) \\
\cos(2\theta) \\
\cos(2\phi_1)^2\cos(2\theta)^2 + \sin(2\phi_1)\sin(2\theta)\cos(2\phi_1)\cos(2\theta) \\
\cos(2\phi_1)\cos(2\theta)^2\sin(2\phi_1) + \sin(2\theta)\cos(2\theta)\sin(2\phi_1)^2 \\
\cos(2\phi_1)\cos(2\theta)\sin(2\theta) - \cos(2\theta)^2\sin(2\phi_1) \\
\sin(2\theta) \\
\cos(2\theta)\cos(2\phi_1)^2\sin(2\theta) + \sin(2\phi_1)\cos(2\phi_1)\sin(2\theta)^2 \\
\sin(2\phi_1)^2\sin(2\theta)^2 + \cos(2\phi_1)\cos(2\theta)\sin(2\phi_1)\sin(2\theta) \\
\cos(2\phi_1)\sin(2\theta)^2 - \cos(2\theta)\sin(2\phi_1)\sin(2\theta) \\
0 \\
0 \\
0 \\
0
\end{bmatrix},
\tag{4.65}
$$

which would result in a Mueller vector that can be stacked and optimized to provide a set of objects to provide a base for the reconstruction of the necessary channels. The drawback

of $\frac{\lambda}{4}$-plate is that the SNR will not be equally distributed among channels, but as alluded to before, the accuracy of our calibration can be increased by increasing the number of measurements.

Define the following set of reference-objects:

$$\underline{\underline{\mathbf{R}}}' = \left[\ \underline{\mathbf{X}}'_{1,1}\ \ \underline{\mathbf{X}}'_{1,2}\ \ \cdots\ \ \underline{\mathbf{X}}'_{1,M}\ \ \underline{\mathbf{X}}'_{2,1}\ \ \cdots\ \ \underline{\mathbf{X}}'_{L,1}\ \ \cdots\ \ \underline{\mathbf{X}}'_{L,M}\ \right]^{\mathrm{T}}, \qquad (4.66)$$

where $M$ is the number of polarizer orientations and $L$ is the number of retarder orientations. For each object, the polarimeter would be cycled through the $N$ measurements, which would would correspond to a matrix of intensities, $\underline{\underline{\mathbf{I}}}$, that is $N \times (M \times L)$. Multiplying it by $\underline{\underline{\mathbf{R}}}'^{-1}$ will reveal the experimental $\underline{\underline{\mathbf{W}}}'_{\mathrm{exp}}$.

If 36 reference objects are desired, that can be done by taking measurements at every combination of six $\theta$s and six $\phi_1$s. Since $\theta$ is varied only to change the linear states, the optimal distribution is that of equally distributed vectors along the equator of the Poincarè sphere. The Stokes-CN for that will be equal to $\sqrt{2}$. The $\phi_1$ would need to be varied through $\{\pm 10.8572, \pm 38.0991, \pm 57.8539\}$[1] to produce a Stokes-CN of $\sim 3.2645$. The net result would be a set of reference objects, with a Total-CN (a product of analyzer Stokes-CN and generator Stokes-CN) of 4.6167. However, if 12 reference objects are desired, that can be done by taking measurements at every combination of three $\theta$s and four $\phi_1$s. Assuming that an ideal retarder with $\delta = \arccos(-2/3)$ is used, it would be possible to get a Total-CN of $\sqrt{6} \sim 2.4495$. The results can be further improved by determining the potential errors that can deviate the $\underline{\underline{\mathbf{W}}}'$. An example of this consideration follows.

Any calibration attempt needs to be applicable to any generic system that requires calibration of all 16 elements. Without calibration, and provided diligent effort in system's construction, the best assumption that can be made is that $\underline{\underline{\mathbf{W}}}_{\mathrm{cal}} = \underline{\underline{\mathbf{W}}}_{\mathrm{ideal}}$. The goal of calibration is then to identify the deviations within $\underline{\underline{\mathbf{W}}}_{\mathrm{true}}$ from $\underline{\underline{\mathbf{W}}}_{\mathrm{ideal}}$, so that the correct measurement matrix can be used, i.e., $\underline{\underline{\mathbf{W}}}_{\mathrm{cal}} \to \underline{\underline{\mathbf{W}}}_{\mathrm{true}}$. A metod of enumerated errors is introduced here to limit the subspace, which the system might occupy. In order to evaluate

---

[1]minimized for $\ell_2$ norm

the proximity of the calibrated matrix to the true matrix, define the following metric,

$$\varepsilon(\underline{\underline{\mathbf{W}}}'_{\text{cal}}, \underline{\underline{\mathbf{W}}}'_{\text{true}}, \underline{\underline{\mathbf{R}}}', \underline{\underline{\mathbf{R}}}'_{\text{true}}) = \left\|\underline{\underline{\mathbf{W}}}'^{+}_{\text{cal}} \underbrace{\underline{\underline{\mathbf{W}}}'_{\text{true}} \underline{\underline{\mathbf{R}}}'_{\text{true}}}_{\underline{\underline{\mathbf{I}}}'} - \underline{\underline{\mathbf{W}}}'^{+}_{\text{true}} \underbrace{\underline{\underline{\mathbf{W}}}'_{\text{true}} \underline{\underline{\mathbf{R}}}'}_{\underline{\underline{\mathbf{I}}}'}\right\|_{\text{Fro}} \quad (4.67)$$

$$= \left\|\underline{\underline{\mathbf{W}}}'^{+}_{\text{cal}} \underline{\underline{\mathbf{I}}}' - \underline{\underline{\mathbf{R}}}'\right\|_{\text{Fro}}, \quad (4.68)$$

where $\underline{\underline{\mathbf{R}}}'_{\text{true}}$ represents the true set of objects in order to differentiate it from the assumed $\underline{\underline{\mathbf{R}}}'$. This will allow to incorporate the ability to evaluate the required precision of the reference objects. The first form of the metric includes the term $\underline{\underline{\mathbf{W}}}'^{+}_{\text{true}} \underline{\underline{\mathbf{W}}}'_{\text{true}}$ to provide automatic masking of $\underline{\underline{\mathbf{R}}}'$ in case of a partial Mueller matrix polarimeter. This is not critical for a full system, but must be performed for a pMMP like in the case of the AFRL polarimeter defined above. The discussion provided tools to treat calibration of a partial system, however a calibration of a full system is probably most useful to denote here. Define the parameters that will determine the polarimeter by its generator and analyzer parameters,

$$\vec{\xi}^{G} = \left\{q^{G}, r^{G}, \vec{\theta}^{G}_{\text{LR}}, \delta^{G}_{\underline{\underline{\mathbf{LR}}}_{1}}, \vec{\theta}^{G}_{\text{LR}_{1}}, \delta^{G}_{\text{LR}_{2}}, \vec{\theta}^{G}_{\text{LR}_{2}}\right\}, \quad (4.69a)$$

$$\vec{\xi}^{A} = \left\{q^{A}, r^{A}, \vec{\theta}^{A}_{\text{LR}}, \delta^{A}_{\underline{\underline{\mathbf{LR}}}_{1}}, \vec{\theta}^{A}_{\text{LR}_{1}}, \delta^{A}_{\text{LR}_{2}}, \vec{\theta}^{A}_{\text{LR}_{2}}\right\}. \quad (4.69b)$$

The full set of parameters is then: $\vec{\xi} = \left\{\vec{\xi}^{G}, \vec{\xi}^{A}\right\}$ and in the case of the AFRL polarimeter calibration, the variables can be appropriately constrained to collapse a non-existing element into an identity matrix.

Suppose that a function $f$ can be written to map $\vec{\xi}$ into the corresponding $\underline{\underline{\mathbf{W}}}'$, the metric can be rewritten in terms of that function,

$$\underset{\Delta\vec{\xi}_{ic}}{\arg\min}\left[\varepsilon\left(f(\vec{\xi}_{ic}), f(\vec{\xi}_{\text{true}}), \underline{\underline{\mathbf{R}}}', \underline{\underline{\mathbf{R}}}'_{\text{true}}\right)\right], \quad (4.70)$$

where $\Delta\vec{\xi}_{ic}$ represents the enumerated errors within each parameter from the idealized set to the calibrated set as a collection of optimization variables. The simulation tested a number ($K = 1$ to $K = 16$) of different random non-depolarizing object sets. These diattenuators were perturbed with Gaussian noise of specified width to produce $\underline{\underline{\mathbf{R}}}'_{\text{true}}$. After

$\underline{\mathbf{W}}'_c$ was found, it was put through an optimally conditioned full collection of sixteen objects. Simulation was run with ten instantiation of $\underline{\mathbf{R}}'$. The results can be seen in Figure 4.17.

Unsurprisingly, Figure 4.17 shows that in order to calibrate the system well, the reference objects need to be known pretty well — errors beyond 0.1° lead to questionable performance. Enumerating the errors had the effect of constraining the system in a way that even a small number of measurements is sufficient to calibrate the system. The results show that $K = 3$ may be enough.

## 4.7   Conclusion

Mueller matrix polarimeters have demonstrated utility recently to assist in target identification, and the use of partial Mueller matrix polarimeters provides a way to develop a sensor that measures the polarization features needed for a particular detection or classification task without having to measure the full Mueller matrix. Previous designs of pMMPs have been ad hoc, in that the polarimeters were developed by hand. In some instances, there was no real attention paid to whether or not the pMMP was even physically realizable.

This chapter developed the theory of pMMPs that enables the structure of a pMMP to be determined from the actual generator/analyzer pairs used to form its instrument matrix $\underline{\mathbf{W}}$. By proper analysis of $\underline{\mathbf{W}}$, it is possible to determine the portion of Mueller matrix space that a particular pMMP measures. The introduced metrics of optimality for pMMPs are based on balancing their SNR performance with their closeness to the particular scene space at hand. The performance of this optimization method was demonstrated for a case previously presented in the literature (Hoover and Tyo (2007)).

Note that this chapter constructed pMMPs using the typical PSG and PSA with an implied temporal modulation manifested through different alignments of linear polarizers and linear retarders. This results in an effective dyadic basis for the pMMP measurement, which is not guaranteed to be ideal. A future study can include a different set of target projections that would result in a different basis and would thereby require another analysis.
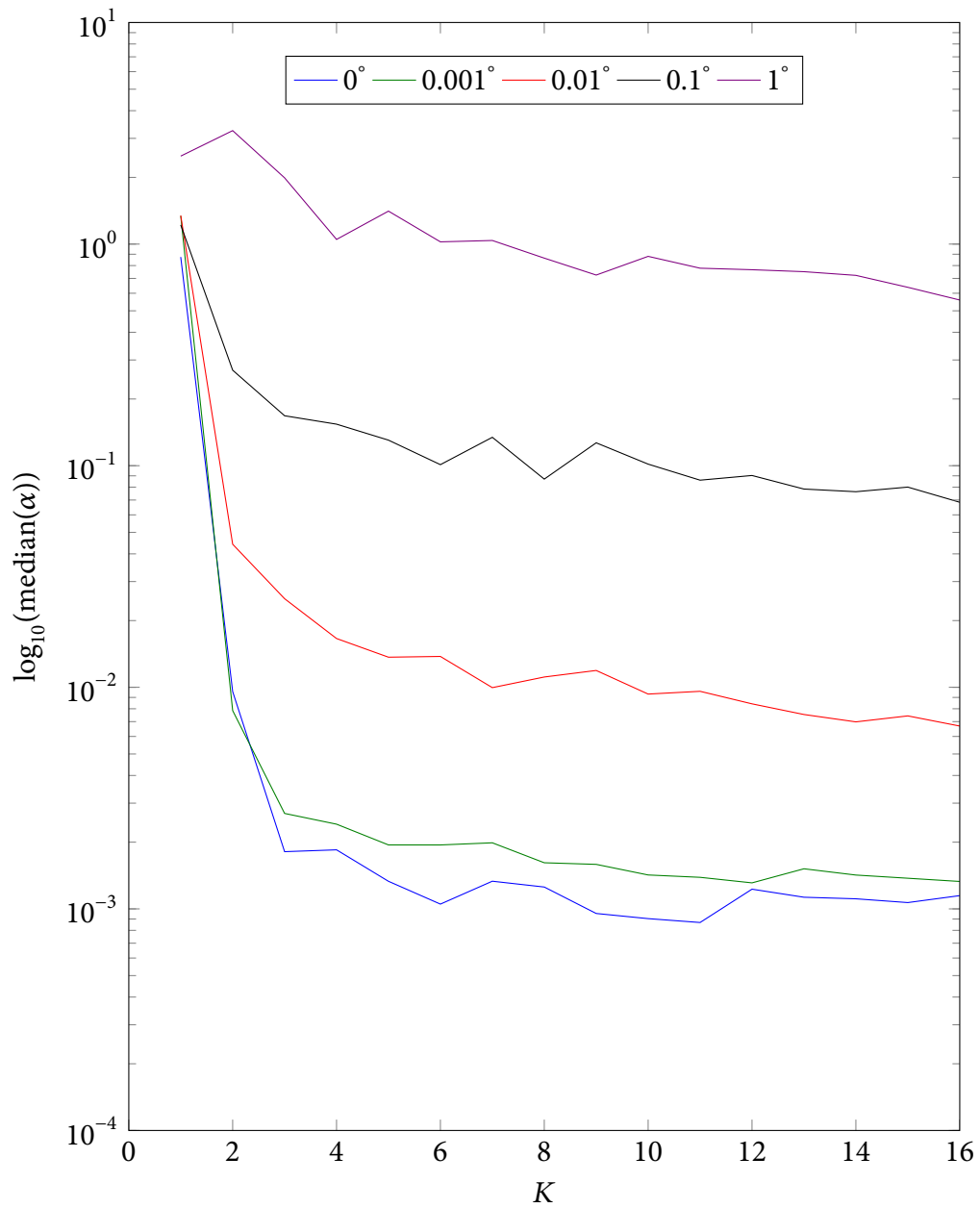
Figure 4.17: Calibration convergence with different number of Mueller objects $K$ under different reference precision. Note that the errors were not administered to the polarization components, but to the spherical coordinates of each analyzing and generating vector.

CHAPTER 5

CHANNELED PARTIAL POLARIMETRY

Chapters 3 and 4 introduced the concepts of channeled polarimetry and partial polarime-
try, respectively. Each of those chapters developed its own set of tools that were useful for
describing the systems and leveraging the gained understanding of the matrix structure
to develop optimal systems. In this chapter, the concepts involved in each of these topics
are combined to describe chaneled partial Mueller matrix polarimeters (c-pMMPs). Given
what has been learned from Chapter 3 with respect to modulation frequencies determin-
ing the set of potential solutions, there remains a fairly small subspace of systems that was
left uncovered. In order to analyze these systems, this chapter will introduce structured
decomposition matrices akin to those used in Chapter 4.

## 5.1  Initial Evaluation

From Chapter 3, a full polarimeter was evaluated by calculating the covariance matrix of
the reduction matrix,

$$\underline{\underline{\mathbf{K}}}_{\underline{\mathbf{Q}}^+} = \underline{\underline{\mathbf{Q}}}^+ \underline{\underline{\mathbf{Q}}}^{+\dagger}. \tag{5.1}$$

The covariance matrix of $\underline{\underline{\mathbf{Q}}}^+$ is $16 \times 16$ matrix that contains the covariance of each com-
bination of the reconstruction vectors. Its diagonal contains the squares of the singular
values of $\underline{\underline{\mathbf{Q}}}$, which are often used to determine the noise resilience of the system. For a
full system, EWV provides a way to consider performance uniformly across all the polar-
ization degrees of freedom by adding all of the variances together. However, if the intent
is to build a partial system, then it is necessary to adjust the evaluation metric to allow
preferential treatment of information. A primitive way to do it would be with a weighing
vector, $\underline{\mathbf{u}}$, that can be introduced to calculate a Weighted Variance (WV) as

$$\text{WV} = \underline{\mathbf{u}}^{\text{T}} \text{diag}\left[\underline{\underline{\mathbf{K}}}_{\underline{\mathbf{Q}}^+}\right] = \sum_{k=0}^{15} u_k / \sigma^2_{\underline{\mathbf{Q}}^+,k}. \tag{5.2}$$

Of course, that metric can only be useful for weighing isolated Mueller matrix element preferences. However, as Chapter 4 made obvious, Mueller matrix space imposes a set of measurement constraints and it might not be physically possible to measure exactly the set of elements that you need. Instead, certain elements might be available as a linear combinations of elements. In order to achieve the complete utility of understanding the resulting conglomeration, singular value decomposition of $\underline{\underline{Q}}$ is necessary. A similar derivation to the one in Chapter 4 will be followed here to introduce the necessary notation in the context of channeled systems. As before, $\underline{\underline{Q}}$ can be written as

$$\underline{\underline{Q}} = \underline{\underline{U}}_{\underline{\underline{Q}}} \underline{\underline{\Sigma}}_{\underline{\underline{Q}}} \underline{\underline{V}}_{\underline{\underline{Q}}}^{\dagger}, \tag{5.3}$$

where the matrices $\underline{\underline{U}}$ and $\underline{\underline{V}}$ are $N \times N$ and $16 \times 16$ complex, orthogonal matrices, respectively, and $\underline{\underline{\Sigma}}$ is a $N \times 16$ reduced diagonal matrix containing the $N$ singular values $\sigma_1 \geq \sigma_2 \geq \ldots \geq \sigma_N > 0$. In this context, $N$ is the number of channels created and the pseudoinverse can be written as

$$\underline{\underline{Q}}^{+} = \underline{\underline{V}}_{\underline{\underline{Q}}} \underline{\underline{\Sigma}}_{\underline{\underline{Q}}}^{+} \underline{\underline{U}}_{\underline{\underline{Q}}}^{\dagger}, \tag{5.4}$$

where $\underline{\underline{\Sigma}}^{+}$ is the $16 \times N$ reduced diagonal matrix containing the inverse of the singular values. The rank of the measurement can be calculated as,

$$R_{\underline{\underline{Q}}} = \text{tr}(\underline{\underline{Q}}^{+} \underline{\underline{Q}}). \tag{5.5}$$

However, instead of providing a summary statistic, it is interesting to look at the diagonal elements of this covariance matrix to see how the information from the $N$ channels is distributed in the estimated Mueller matrix. Define the "reconstructables" matrix

$$\underline{\underline{B}}^{'} = \text{vec}(\underline{\underline{B}}) = \text{diag}(\underline{\underline{Q}}^{+} \underline{\underline{Q}}). \tag{5.6}$$

For each Mueller $k$-th element $(m_k^{'})$, $\sqrt{b_k^{'}}$ tells the fraction of energy that is maintained after reconstruction. When $b_k^{'} = 0$, then $m_k^{'} \perp \mathcal{R}$ and the information lies in the null space of the measurement (LaCasse et al. (2011a, 2012)). When $b_k^{'} = 1$, then $m_k^{'} \subseteq \mathcal{R}$ and the information can be reconstructed to within noise limitations. It can be shown that $\sum_0^{k=15} b_k^{'} = R$, where $R$ is the rank of $\underline{\underline{Q}}$ and is always an integer. Therefore, if a particular

$b_k'$ is not an integer, it implies that the corresponding $k$-th element must be available for reconstruction as a member of a linear combination of Mueller elements. To investigate those details, the concept of structured decomposition needs to be ported over from partial systems of Chapter 4 and applied to the channeled systems of Chapter 3.

## 5.2  Structured Decomposition

As in Chapter 4, a structured decomposition of $\underline{\underline{Q}}$ can be postulated. Its desired feature is to be more parsable by humans, and after seeing the structured matrices for non-channeled pMMPs, it is expected that these matrices would also have an analytically predictable form. The benefit of that form is the ability to represent the system with variables, allowing for direct calculation of the system needed to cover a given scene space. In this dissertation, however, the analytical form is not demonstrated and will remain a topic of a future discussion. The structured decomposition for $\underline{\underline{Q}}$ is

$$\underline{\underline{Q}} = \underline{\underline{U}}_{s,\underline{\underline{Q}}}\,\underline{\underline{\Sigma}}_{s,\underline{\underline{Q}}}\,\underline{\underline{V}}_{s,\underline{\underline{Q}}}^{\dagger} = \underline{\underline{L}}_{s,\underline{\underline{Q}}}^{+}\,\underline{\underline{V}}_{s,\underline{\underline{Q}}}^{\dagger}, \tag{5.7}$$

where $\underline{\underline{U}}_{s,\underline{\underline{Q}}}$ is $N \times R$ matrix containing left-column vectors, $\underline{\underline{\Sigma}}_{s,\underline{\underline{Q}}}$ is $R \times R$ matrix containing structured singular values and $\underline{\underline{V}}_{s,\underline{\underline{Q}}}$ is $16 \times R$ matrix containing the right-column vectors and representing the sensor space, $\mathcal{V}$. As before, $\underline{\underline{\Sigma}}_{s,\underline{\underline{Q}}}$ cannot be used on its own to determine the noise resilience, but instead must be mapped with $\underline{\underline{U}}_{s,\underline{\underline{Q}}}$. The decomposition can be derived from SVD through a prescribed procedure. First, the null space partition of $\underline{\underline{V}}$ is cropped away to produce $\underline{\underline{V}}'$, which spans the sensor space. Then, using Gaussian elimination, $\underline{\underline{V}}'^{\mathrm{T}}$ can be rewritten in its reduced row echelon form. That operation is performed using the MATLAB code shown in Algorithm 5.1.

---

**Algorithm 5.1** Reduced Row Echelon Form MATLAB Code

```
function A = rreff(A)
[m,n] = size(A);
i = 1;
j = 1;
while (i <= m) && (j <= n)
    [~,k] = max(abs(A(i:m,j))); k = k+i-1;
```

```
    A([i k],j:n) = A([k i],j:n);
    A(i,j:n) = A(i,j:n)/A(i,j);
    for k = [1:i-1 i+1:m]
        A(k,j:n) = A(k,j:n) - A(k,j)*A(i,j:n);
    end
    i = i + 1;
    j = j + 1;
end
```

Lastly, each column is normalized and the resultant matrix is denoted as $\underline{\underline{\mathbf{V}}}_{s,\mathbf{Q}}$, which is significantly simplified with the similar caveat from Chapter 4, that it is no longer normalizable in both dimensions and is therefore non-unitary. Though this may seem unfavorable, the complexity of dealing with non-unitary matrices is easily overcome as will be shown.

Since $\underline{\underline{\mathbf{Q}}}$ is known from the steps denoted in Chapter 3 and $\underline{\underline{\mathbf{V}}}_{s,\mathbf{Q}}$ is derived from the SVD decomposition, it is trivial to calculate the auxiliary matrix, $\underline{\underline{\mathbf{L}}}^{+}_{s,\mathbf{Q}}$:

$$\underline{\underline{\mathbf{L}}}^{+}_{s,\mathbf{Q}} = \underline{\underline{\mathbf{Q}}} / \underline{\underline{\mathbf{V}}}^{\dagger}_{s,\mathbf{Q}}, \tag{5.8}$$

which can be further decomposed into the product $\underline{\underline{\mathbf{U}}}_{s,\mathbf{Q}} \underline{\underline{\mathbf{\Sigma}}}_{s,\mathbf{Q}}$, where $L_2$ norm of each column of $\underline{\underline{\mathbf{L}}}^{+}_{s,\mathbf{Q}}$ can be extracted into the corresponding effective singular value of $\underline{\underline{\mathbf{\Sigma}}}_{s,\mathbf{Q}}$. The reason that $\underline{\underline{\mathbf{L}}}$ is introduced as its pseudoinverse, rather than the forward matrix, is to mirror the matrix of the same kind being introduced in Chapter 4, for which the decomposition in terms of $\underline{\underline{\mathbf{Q}}}$ still holds:

$$\underline{\underline{\mathbf{L}}}_{s,\mathbf{Q}} = \underline{\underline{\mathbf{\Sigma}}}^{+}_{s,\mathbf{Q}} \underline{\underline{\mathbf{U}}}^{+}_{s,\mathbf{Q}} = \left[ \begin{array}{cccc} \underline{\boldsymbol{\ell}}^{\mathrm{T}}_{\underline{\mathbf{v}}_1} & \underline{\boldsymbol{\ell}}^{\mathrm{T}}_{\underline{\mathbf{v}}_2} & \cdots & \underline{\boldsymbol{\ell}}^{\mathrm{T}}_{\underline{\mathbf{v}}_R} \end{array} \right]. \tag{5.9}$$

### 5.2.1 Noise Resilience

With the structured decomposition at hand, it is now possible to evaluate the system in more detail. First, the noise performance is given by the Euclidean length of each of the vectors of $\underline{\underline{\mathbf{L}}}_{s,\mathbf{Q}}$,

$$p_{\underline{\mathbf{v}}} = ||\underline{\boldsymbol{\ell}}_{\underline{\mathbf{v}}}||_2. \tag{5.10}$$

Concatenating them together into a noise magnitude vector describes the system's noise resilience for each of the reconstructable element combinations specified by the vectors of $\underline{\underline{\mathbf{V}}}_{s,\underline{\underline{\mathbf{Q}}}}$:

$$\underline{\mathbf{P}}_{s,\underline{\underline{\mathbf{Q}}}} = \begin{bmatrix} p_{\underline{\mathbf{v}}_1} & p_{\underline{\mathbf{v}}_2} & \cdots & p_{\underline{\mathbf{v}}_R} \end{bmatrix}^{\mathrm{T}}. \tag{5.11}$$

Because the reconstructed elements are generally generally derived through different combinations of the same channels, the previously uncorrelated noise of each measurement is now correlated between reconstructed elements. Thus, when looking for evaluating system performance for any given subspace of interest, or scene space, $\underline{\underline{\mathbf{Y}}}$, the noise characteristics needs to be mapped through a transformation,

$$\underline{\underline{\mathbf{T}}} = \underline{\underline{\mathbf{Y}}} \backslash \underline{\underline{\mathbf{V}}}_{s,\underline{\underline{\mathbf{Q}}}}, \tag{5.12}$$

which combines $R$ reconstructables into the vectors approaching $\Upsilon$ or estimating $\underline{\underline{\mathbf{Y}}}$,

$$\hat{\underline{\underline{\mathbf{Y}}}}^{\mathrm{T}} = \underline{\underline{\mathbf{T}}}\,\underline{\underline{\mathbf{V}}}_{s,4ij}^{\mathrm{T}}. \tag{5.13}$$

As before, $\underline{\mathbf{L}}_{s,\underline{\underline{\mathbf{Q}}}}$ needs to be mapped into the appropriate space

$$\underline{\mathbf{L}}_{\underline{\underline{\mathbf{Y}}}} = \underline{\underline{\mathbf{T}}}\,\underline{\mathbf{L}}_{\underline{\underline{\mathbf{V}}}_{s,4ij}} = \begin{bmatrix} \underline{\ell}_{\underline{\mathbf{y}}_1}^{\mathrm{T}} & \underline{\ell}_{\underline{\mathbf{y}}_2}^{\mathrm{T}} & \cdots & \underline{\ell}_{\underline{\mathbf{y}}_K}^{\mathrm{T}} \end{bmatrix}^{\mathrm{T}}, \tag{5.14}$$

where $K$ is the total number of vectors in $\underline{\underline{\mathbf{Y}}}$. The resulting noise magnitudes within those vectors can be evaluated in a philosophically equivalent way,

$$p_{\underline{\mathbf{y}}} = \|\underline{\ell}_{\underline{\mathbf{y}}}\|_2, \tag{5.15}$$

and then can be combined into a total magnitude vector

$$\underline{\mathbf{P}}_{\underline{\underline{\mathbf{Y}}}} = \begin{bmatrix} p_{\underline{\mathbf{y}}_1} & p_{\underline{\mathbf{y}}_2} & \cdots & p_{\underline{\mathbf{y}}_K} \end{bmatrix}^{\mathrm{T}}. \tag{5.16}$$

### 5.2.2   Space Coverage

Because $\underline{\underline{\mathbf{V}}}_{s,\underline{\underline{\mathbf{Q}}}}$ is structured into a purely real space, evaluating the space proximity for a partial system is no different than it is for a partial channeled system. The matrix,

$$\underline{\underline{\mathbf{X}}} = \underline{\underline{\mathbf{Y}}} - \underline{\underline{\mathbf{V}}}_{s,\underline{\underline{\mathbf{Q}}}} \left( \underline{\underline{\mathbf{V}}}_{s,\underline{\underline{\mathbf{Q}}}}^{\mathrm{T}} \underline{\underline{\mathbf{Y}}} \right), \tag{5.17}$$

contains canonical angles within the singular values of its SVD,

$$\zeta_k = \arcsin(\sigma_{\underline{\mathbf{x}}_k}). \tag{5.18}$$

### 5.2.3 Example Decomposition

As an example, consider the 1D modulation channeled system with the same element alignment as Hagen et al. (2007) and $\underline{\mathbf{d}} = \{1, 1, 1, 1\}$. After performing the SVD, and simplifying the column-space, the structured right-column matrix is

$$
\underline{\underline{\mathbf{V}}}_{s,\underline{\underline{\mathbf{Q}}}_{\{1,1,1,1\}}} =
\begin{bmatrix}
\frac{1}{\sqrt{2}} & 0 & 0 & 0 & 0 & 0 & 0 & 0 \\
0 & \frac{1}{\sqrt{2}} & 0 & 0 & 0 & 0 & 0 & 0 \\
0 & 0 & \frac{1}{2} & 0 & 0 & 0 & 0 & 0 \\
0 & 0 & 0 & \frac{1}{\sqrt{2}} & 0 & 0 & 0 & 0 \\
0 & \frac{1}{\sqrt{2}} & 0 & 0 & 0 & 0 & 0 & 0 \\
\frac{1}{\sqrt{2}} & 0 & \frac{1}{2} & 0 & 0 & 0 & 0 & 0 \\
0 & 0 & 0 & 0 & \frac{1}{\sqrt{2}} & 0 & 0 & 0 \\
0 & 0 & 0 & 0 & 0 & \frac{1}{\sqrt{2}} & 0 & 0 \\
0 & 0 & \frac{1}{2} & 0 & 0 & 0 & 0 & 0 \\
0 & 0 & 0 & 0 & \frac{1}{\sqrt{2}} & 0 & 0 & 0 \\
0 & 0 & 0 & 0 & 0 & 0 & \frac{1}{\sqrt{2}} & 0 \\
0 & 0 & 0 & 0 & 0 & 0 & 0 & \frac{1}{\sqrt{2}} \\
0 & 0 & 0 & \frac{1}{\sqrt{2}} & 0 & 0 & 0 & 0 \\
0 & 0 & 0 & 0 & 0 & \frac{1}{\sqrt{2}} & 0 & 0 \\
0 & 0 & 0 & 0 & 0 & 0 & 0 & \frac{1}{\sqrt{2}} \\
0 & 0 & \frac{1}{2} & 0 & 0 & 0 & \frac{1}{\sqrt{2}} & 0
\end{bmatrix},
\tag{5.19}
$$

where certain measurement symmetries emerge. Because the PSG and the PSA contain the same modulation frequencies, the measurements have a symmetric presence across the Mueller matrix diagonal. The sensor space described by $\underline{\underline{\mathbf{V}}}_{s,\underline{\underline{\mathbf{Q}}}_{\{1,1,1,1\}}}$ can be interpreted

to contain the following vectors:

$$\underline{\mathbf{v}}_1 = \frac{1}{\sqrt{2}}\left(m_{00} + m_{11}\right) \tag{5.20a}$$

$$\underline{\mathbf{v}}_2 = \frac{1}{\sqrt{2}}\left(m_{01} + m_{10}\right) \tag{5.20b}$$

$$\underline{\mathbf{v}}_3 = \frac{1}{2}\left(m_{02} + m_{11} + m_{20} + m_{33}\right) \tag{5.20c}$$

$$\underline{\mathbf{v}}_4 = \frac{1}{\sqrt{2}}\left(m_{03} + m_{30}\right) \tag{5.20d}$$

$$\underline{\mathbf{v}}_5 = \frac{1}{\sqrt{2}}\left(m_{12} + m_{21}\right) \tag{5.20e}$$

$$\underline{\mathbf{v}}_6 = \frac{1}{\sqrt{2}}\left(m_{13} + m_{31}\right) \tag{5.20f}$$

$$\underline{\mathbf{v}}_7 = \frac{1}{\sqrt{2}}\left(m_{22} + m_{33}\right) \tag{5.20g}$$

$$\underline{\mathbf{v}}_8 = \frac{1}{\sqrt{2}}\left(m_{23} + m_{32}\right) \tag{5.20h}$$

within the system's sensor space. The corresponding auxiliary matrix is

$$\underline{\underline{\mathbf{L}}}^{+}_{s,\underline{\underline{\mathbf{Q}}}_{\{1,1,1,1\}}} = \begin{bmatrix} 0 & 0 & 0 & 0 & 0 & 0 & \frac{1}{8\sqrt{2}} & \frac{-i}{8\sqrt{2}} \\ 0 & 0 & 0 & 0 & \frac{-1}{4\sqrt{2}} & \frac{i}{4\sqrt{2}} & 0 & 0 \\ 0 & 0 & \frac{-1}{2} & \frac{i}{\sqrt{8}} & 0 & 0 & -\frac{1}{\sqrt{8}} & \frac{i}{4\sqrt{2}} \\ 0 & \frac{1}{\sqrt{2}} & 0 & 0 & \frac{1}{4\sqrt{2}} & \frac{i}{4\sqrt{2}} & 0 & 0 \\ \sqrt{2} & 0 & 1 & 0 & 0 & 0 & \frac{3}{2\sqrt{8}} & 0 \\ 0 & \frac{1}{\sqrt{2}} & 0 & 0 & \frac{1}{4\sqrt{2}} & \frac{-i}{4\sqrt{2}} & 0 & 0 \\ 0 & 0 & \frac{-1}{2} & \frac{-i}{\sqrt{8}} & 0 & 0 & -\frac{1}{\sqrt{8}} & \frac{-i}{4\sqrt{2}} \\ 0 & 0 & 0 & 0 & \frac{-1}{4\sqrt{2}} & \frac{-i}{4\sqrt{2}} & 0 & 0 \\ 0 & 0 & 0 & 0 & 0 & 0 & \frac{1}{8\sqrt{2}} & \frac{i}{8\sqrt{2}} \end{bmatrix}, \tag{5.21}$$

which is clearly non-unitary and unnormalized in both dimensions. Normalizing its columns and pulling those normalization factors into the diagonal of $\underline{\underline{\mathbf{\Sigma}}}_{s,\underline{\underline{\mathbf{Q}}}_{\{1,1,1,1\}}}$ allows the

auxiliary matrix to be further decomposed into the structured singular values,

$$
\underline{\underline{\Sigma}}_{s,\underline{\underline{\mathbf{Q}}}_{\{1,1,1,1\}}} =
\begin{bmatrix}
\sqrt{2} & 0 & 0 & 0 & 0 & 0 & 0 & 0 \\
0 & 1 & 0 & 0 & 0 & 0 & 0 & 0 \\
0 & 0 & \sqrt{\frac{3}{2}} & 0 & 0 & 0 & 0 & 0 \\
0 & 0 & 0 & \frac{1}{2} & 0 & 0 & 0 & 0 \\
0 & 0 & 0 & 0 & \frac{1}{\sqrt{8}} & 0 & 0 & 0 \\
0 & 0 & 0 & 0 & 0 & \frac{1}{\sqrt{8}} & 0 & 0 \\
0 & 0 & 0 & 0 & 0 & 0 & \frac{\sqrt{35}}{8} & 0 \\
0 & 0 & 0 & 0 & 0 & 0 & 0 & \frac{\sqrt{5}}{8}
\end{bmatrix},
\tag{5.22}
$$

and the left-column matrix,

$$
\underline{\underline{\mathbf{U}}}_{s,\underline{\underline{\mathbf{Q}}}_{\{1,1,1,1\}}} =
\begin{bmatrix}
0 & 0 & 0 & 0 & 0 & 0 & \frac{1}{\sqrt{70}} & \frac{-i}{2\sqrt{5}} \\
0 & 0 & 0 & 0 & \frac{-1}{2} & \frac{i}{2} & 0 & 0 \\
0 & 0 & \frac{-1}{\sqrt{6}} & \frac{i}{\sqrt{2}} & 0 & 0 & -\sqrt{\frac{8}{35}} & \frac{i}{\sqrt{5}} \\
0 & \frac{1}{\sqrt{2}} & 0 & 0 & \frac{1}{2} & \frac{i}{2} & 0 & 0 \\
1 & 0 & \sqrt{\frac{2}{3}} & 0 & 0 & 0 & \sqrt{\frac{18}{35}} & 0 \\
0 & \frac{1}{\sqrt{2}} & 0 & 0 & \frac{1}{2} & \frac{-i}{2} & 0 & 0 \\
0 & 0 & \frac{-1}{\sqrt{6}} & \frac{-i}{\sqrt{2}} & 0 & 0 & -\sqrt{\frac{8}{35}} & \frac{-i}{\sqrt{5}} \\
0 & 0 & 0 & 0 & \frac{-1}{2} & \frac{-i}{2} & 0 & 0 \\
0 & 0 & 0 & 0 & 0 & 0 & \frac{1}{\sqrt{70}} & \frac{i}{2\sqrt{5}}
\end{bmatrix},
\tag{5.23}
$$

which is still non-unitary, but unnormalized only in one dimension.

## 5.3   c-pMMP Performance

In this section, the performance of a number of channeled-partial systems is investigated. In order to accomplish this task, the construction of $\underline{\underline{\mathbf{Q}}}$ follows the framework of Chapter 3, while evaluation principles are adapted from Chapter 4 into their channeled equivalents

described in Sections 5.2.1 and 5.2.2. This chapter employs the same metric,

$$
\arg\min_{\vec{\xi}} \left[ \underbrace{\sum_{k=1}^{K} (\alpha_k p_{\underline{\mathbf{y}}_k})^2}_{\varepsilon_1} + w \underbrace{\sum_{k=1}^{K} (\beta_k \sigma_{\underline{\mathbf{x}}_k})^2}_{\varepsilon_2} \right], \tag{5.24}
$$

where $\varepsilon_1$ is the noise resilience term, $\varepsilon_2$ is the space coverage term, and $w$ is the weighing factor introduced to select the trade-off along the Pareto surface of the multi-objective optimization. The same value of 25 is used here because the scene space is the same as in Chapter 4:

$$
\underline{\underline{\mathbf{Y}}} = \begin{bmatrix}
-0.9204 & 0.3097 & 0.2378 \\
-0.0347 & 0.0410 & -0.2480 \\
-0.0010 & 0.0034 & -0.0136 \\
-0.0003 & 0.0007 & 0.0088 \\
-0.0318 & 0.0524 & -0.2356 \\
-0.2757 & -0.4730 & -0.4418 \\
-0.0010 & -0.0043 & -0.0050 \\
-0.0004 & 0.0033 & -0.0085 \\
0.0035 & -0.0039 & 0.0207 \\
0.0013 & -0.0043 & 0.0138 \\
0.2703 & 0.4860 & 0.3996 \\
-0.0019 & -0.0033 & -0.0220 \\
-0.0004 & 0.0008 & -0.0008 \\
0.0001 & 0.0023 & -0.0037 \\
0.0028 & 0.0017 & 0.0292 \\
0.0398 & 0.6630 & -0.6850
\end{bmatrix}. \tag{5.25}
$$

The system performances within the $4 \times 4 \times 4 \times 4$ sub-volume corresponding to the four frequencies making up $\underline{\mathbf{d}}$ ranging from 1 to 4 can be seen in Tables 5.1–5.3. From the results presented in Tables 5.1–5.3, the systems with $\underline{\mathbf{d}} = (\ 1\ \ 1\ \ 1\ \ 1\ )$, $\underline{\mathbf{d}} = (\ 1\ \ 1\ \ 2\ \ 2\ )$, $\underline{\mathbf{d}} = (\ 2\ \ 1\ \ 3\ \ 1\ )$, and $\underline{\mathbf{d}} = (\ 3\ \ 1\ \ 3\ \ 1\ )$ are examined further.

Table 5.1: Noise resilience, represented by $\epsilon_1$ in Equation 5.24, of 256 systems within the described $4\times4\times4\times4$ volume of systems.

| $d_3$ → | | 1 | 1 | 1 | 1 | 2 | 2 | 2 | 2 | 3 | 3 | 3 | 3 | 4 | 4 | 4 | 4 |
| $d_1$ | $d_2$ \ $d_4$ | 1 | 2 | 3 | 4 | 1 | 2 | 3 | 4 | 1 | 2 | 3 | 4 | 1 | 2 | 3 | 4 |
|---|---|---|---|---|---|---|---|---|---|---|---|---|---|---|---|---|---|
| 1 | 1 | 65.91 | 71.48 | 84.28 | 93.52 | 118.4 | 74.36 | 76.51 | 87.82 | 197 | 122.9 | 255 | 174.9 | 95.9 | 122.9 | 85.89 | 371.1 |
| 1 | 2 | 65.19 | 130.8 | 194 | 173.7 | 122.1 | 119.6 | 98.45 | 75.3 | 206.3 | 95.43 | 104.5 | 61.41 | 137.6 | 55.52 | 87.94 | 69.06 |
| 1 | 3 | 95.35 | 134 | 171.3 | 161.9 | 204.2 | 135.5 | 97.77 | 90.31 | 88.11 | 130.9 | 61.56 | 82.43 | 2960 | 363.9 | 74.36 | 112.2 |
| 1 | 4 | 98.46 | 134.5 | 163.3 | 130.6 | 137.3 | 89.54 | 87.93 | 62.3 | 37.14 | 49.31 | 85.55 | 60.36 | 26.73 | 41.45 | 51.06 | 61.56 |
| 2 | 1 | 72.42 | 65.71 | 37.2 | 69.54 | 128.5 | 66.55 | 146.4 | 89.68 | 129.6 | 162.4 | 154.9 | 95.46 | 130.2 | 212.1 | 147.8 | 129.9 |
| 2 | 2 | 67.12 | 75.49 | 94 | 191.5 | 117 | 65.91 | 67.73 | 71.48 | 228.3 | 87.84 | 155.1 | 82.25 | 86.3 | 118.4 | 86.56 | 74.36 |
| 2 | 3 | 89.02 | 163.1 | 67.37 | 86.84 | 97.08 | 92.27 | 146.4 | 133.7 | 131.9 | 37.11 | 61.56 | 64.3 | 48.77 | 333.3 | 67.7 | 158.4 |
| 2 | 4 | 69.27 | 109.8 | 68.1 | 272.4 | 59.79 | 65.19 | 58.29 | 130.8 | 371.8 | 333.2 | 96.04 | 102.7 | 42.71 | 122.1 | 49.62 | 119.6 |
| 3 | 1 | 94.84 | 45.69 | 29.12 | 48.89 | 189.7 | 69.34 | 47.11 | 30.76 | 171.4 | 66.55 | 55.86 | 102.7 | 161.7 | 63.2 | 27.57 | 196.6 |
| 3 | 2 | 85.18 | 144.2 | 47.75 | 191.3 | 98.45 | 67.44 | 32.18 | 109.9 | 98.99 | 146.7 | 55.86 | 155 | 87.96 | 55.03 | 69.05 | 69.06 |
| 3 | 3 | 254.9 | 157.8 | 54.26 | 54.9 | 103.3 | 153.9 | 54.26 | 165.1 | 61.7 | 61.7 | 65.91 | 61.7 | 84.36 | 95.71 | 54.26 | 145.9 |
| 3 | 4 | 87.28 | 148.7 | 27.31 | 102.1 | 87.97 | 87.65 | 68.91 | 84.66 | 73.78 | 68.08 | 55.86 | 90.13 | 2053 | 48.76 | 26.73 | 61.56 |
| 4 | 1 | 95.16 | 71.92 | 47.77 | 28.93 | 165.7 | 79.44 | 191.9 | 50.96 | 161.8 | 86.46 | 57.37 | 32.38 | 129.7 | 266.8 | 102.5 | 55.86 |
| 4 | 2 | 103.3 | 90.45 | 29.34 | 50.99 | 72.15 | 72.42 | 108.5 | 65.71 | 86.67 | 130.5 | 164.8 | 169.9 | 64.38 | 128.5 | 87.6 | 66.55 |
| 4 | 3 | 180.5 | 98.91 | 106.9 | 32.76 | 61.27 | 86.25 | 152.9 | 172.4 | 85.38 | 64.22 | 61.56 | 28.52 | 60.97 | 105 | 90.65 | 55.86 |
| 4 | 4 | 373.6 | 129.3 | 197.4 | 54.26 | 67.8 | 67.12 | 67.8 | 75.49 | 113.2 | 152.8 | 146 | 54.26 | 61.7 | 117 | 61.7 | 65.91 |

Table 5.2: Space Coverage, represented by $\varepsilon_2$ in Equation 5.24, of 256 systems within the described $4 \times 4 \times 4 \times 4$ volume of systems.

| | $d_3$ → | 1 | 2 | 3 | 4 | 1 | 2 | 3 | 4 | 1 | 2 | 3 | 4 | 1 | 2 | 3 | 4 |
| $d_1$ | $d_2$ \ $d_4$ → | 1 | 1 | 1 | 1 | 2 | 2 | 2 | 2 | 3 | 3 | 3 | 3 | 4 | 4 | 4 | 4 |
|---|---|---|---|---|---|---|---|---|---|---|---|---|---|---|---|---|---|
| 1 | 1 | 1.163 | 1.187 | 1.214 | 0.962 | 0.781 | 0.946 | 0.985 | 0.615 | 0.708 | 0.682 | 0.633 | 0.397 | 0.584 | 0.781 | 0.000 | 0.346 |
| 2 | 1 | 0.780 | 0.653 | 0.179 | 0.127 | 0.497 | 0.865 | 0.001 | 0.000 | 0.183 | 0.053 | 0.000 | 0.000 | 0.161 | 0.118 | 0.000 | 0.000 |
| 3 | 1 | 0.689 | 0.502 | 0.001 | 0.000 | 0.198 | 0.523 | 0.000 | 0.044 | 0.497 | 0.382 | 0.491 | 0.000 | 0.495 | 0.351 | 0.000 | 0.000 |
| 4 | 1 | 0.574 | 0.555 | 0.000 | 0.001 | 0.161 | 0.552 | 0.000 | 0.124 | 0.080 | 0.000 | 0.000 | 0.000 | 0.497 | 0.000 | 0.000 | 0.491 |
| 1 | 2 | 1.172 | 0.497 | 0.882 | 0.804 | 0.649 | 0.620 | 0.127 | 0.623 | 0.505 | 0.333 | 0.207 | 0.000 | 0.556 | 0.342 | 0.049 | 0.374 |
| 2 | 2 | 0.943 | 0.631 | 0.826 | 0.839 | 0.885 | 1.163 | 0.501 | 1.187 | 0.537 | 0.521 | 0.577 | 0.670 | 0.568 | 0.781 | 0.183 | 0.946 |
| 3 | 2 | 0.674 | 0.337 | 0.662 | 0.001 | 0.054 | 0.505 | 0.001 | 0.502 | 0.375 | 0.497 | 0.491 | 0.000 | 0.000 | 0.058 | 0.000 | 0.374 |
| 4 | 2 | 0.774 | 0.335 | 0.662 | 0.372 | 0.127 | 0.780 | 0.127 | 0.653 | 0.337 | 0.051 | 0.000 | 0.000 | 0.000 | 0.497 | 0.000 | 0.865 |
| 1 | 3 | 1.194 | 0.879 | 0.497 | 0.461 | 0.165 | 0.819 | 0.161 | 0.734 | 0.001 | 0.670 | 0.496 | 0.461 | 0.000 | 0.670 | 0.001 | 0.346 |
| 2 | 3 | 0.981 | 0.133 | 0.161 | 0.097 | 0.001 | 0.491 | 0.497 | 0.000 | 0.000 | 0.001 | 0.496 | 0.000 | 0.000 | 0.118 | 0.161 | 0.000 |
| 3 | 3 | 0.635 | 0.218 | 0.507 | 0.632 | 0.000 | 0.575 | 0.507 | 0.113 | 0.501 | 0.501 | 1.163 | 0.501 | 0.000 | 0.000 | 0.507 | 0.000 |
| 4 | 3 | 0.000 | 0.055 | 0.001 | 0.000 | 0.000 | 0.178 | 0.161 | 0.124 | 0.000 | 0.000 | 0.496 | 0.001 | 0.115 | 0.000 | 0.497 | 0.491 |
| 1 | 4 | 0.945 | 0.801 | 0.469 | 0.497 | 0.118 | 0.822 | 0.088 | 0.161 | 0.000 | 0.001 | 0.630 | 0.001 | 0.001 | 0.383 | 0.000 | 0.496 |
| 2 | 4 | 0.605 | 0.629 | 0.735 | 0.161 | 0.000 | 1.172 | 0.000 | 0.497 | 0.040 | 0.505 | 0.105 | 0.261 | 0.121 | 0.649 | 0.121 | 0.620 |
| 3 | 4 | 0.396 | 0.000 | 0.454 | 0.001 | 0.000 | 0.662 | 0.000 | 0.258 | 0.000 | 0.000 | 0.491 | 0.497 | 0.000 | 0.000 | 0.001 | 0.496 |
| 4 | 4 | 0.351 | 0.384 | 0.351 | 0.507 | 0.000 | 0.943 | 0.000 | 0.631 | 0.000 | 0.384 | 0.000 | 0.507 | 0.501 | 0.885 | 0.501 | 1.163 |

Table 5.3: Weighted sum of noise resilience and space coverage with $w = 25$ of 256 systems within the described $4 \times 4 \times 4 \times 4$ volume of systems.

| | | $d_3$ = 1 | | | | $d_3$ = 2 | | | | $d_3$ = 3 | | | | $d_3$ = 4 | | | |
|---|---|---|---|---|---|---|---|---|---|---|---|---|---|---|---|---|---|
| $d_1$ | $d_2\backslash d_4$ | 1 | 2 | 3 | 4 | 1 | 2 | 3 | 4 | 1 | 2 | 3 | 4 | 1 | 2 | 3 | 4 |
| 1 | 1 | 94.98 | 101.1 | 114.6 | 117.6 | 138 | 98.01 | 101.1 | 103.2 | 214.7 | 139.9 | 270.8 | 184.8 | 110.5 | 142.4 | 85.89 | 379.8 |
| 2 | 1 | 84.69 | 147.1 | 198.5 | 176.8 | 134.5 | 141.2 | 98.46 | 75.3 | 210.8 | 96.75 | 104.5 | 61.41 | 141.6 | 58.47 | 87.94 | 69.06 |
| 3 | 1 | 112.6 | 146.5 | 171.3 | 161.9 | 209.1 | 148.6 | 97.77 | 91.42 | 100.5 | 140.4 | 73.84 | 82.43 | 2972 | 372.7 | 74.36 | 112.2 |
| 4 | 1 | 112.8 | 148.4 | 163.3 | 130.6 | 141.3 | 103.3 | 87.93 | 65.4 | 39.13 | 49.31 | 85.55 | 60.36 | 39.15 | 41.45 | 51.06 | 73.84 |
| 1 | 2 | 101.7 | 78.12 | 59.24 | 89.64 | 144.7 | 82.06 | 149.5 | 105.3 | 142.3 | 170.7 | 160 | 95.46 | 144.1 | 220.7 | 149 | 139.2 |
| 2 | 2 | 90.69 | 91.26 | 114.7 | 212.5 | 139.1 | 94.98 | 80.25 | 101.1 | 241.8 | 100.9 | 169.5 | 99 | 100.5 | 138 | 91.14 | 98.01 |
| 3 | 2 | 105.9 | 171.6 | 83.93 | 86.85 | 98.42 | 104.9 | 146.4 | 146.3 | 141.3 | 49.53 | 73.84 | 64.31 | 48.77 | 334.7 | 67.7 | 167.7 |
| 4 | 2 | 88.63 | 118.1 | 84.66 | 281.7 | 62.97 | 84.69 | 61.47 | 147.1 | 380.2 | 334.5 | 96.04 | 102.7 | 42.72 | 134.5 | 49.62 | 141.2 |
| 1 | 3 | 124.7 | 67.65 | 41.53 | 60.41 | 193.8 | 89.82 | 51.13 | 49.11 | 171.4 | 83.29 | 68.25 | 114.2 | 161.7 | 79.95 | 27.61 | 205.2 |
| 2 | 3 | 109.7 | 147.6 | 51.77 | 193.7 | 98.47 | 79.71 | 44.59 | 109.9 | 98.99 | 146.8 | 68.25 | 155 | 87.96 | 57.99 | 73.08 | 69.06 |
| 3 | 3 | 270.8 | 163.2 | 66.94 | 70.72 | 103.3 | 168.3 | 66.94 | 167.9 | 74.22 | 74.22 | 94.98 | 74.22 | 84.36 | 95.71 | 66.94 | 145.9 |
| 4 | 3 | 87.28 | 150 | 27.34 | 102.1 | 87.97 | 92.11 | 72.93 | 87.77 | 73.78 | 68.08 | 68.25 | 90.15 | 2056 | 48.76 | 39.15 | 73.84 |
| 1 | 4 | 118.8 | 91.95 | 59.49 | 41.35 | 168.6 | 100 | 194.1 | 54.99 | 161.8 | 86.48 | 73.11 | 32.41 | 129.7 | 276.3 | 102.5 | 68.25 |
| 2 | 4 | 118.5 | 106.2 | 47.71 | 55.01 | 72.16 | 101.7 | 108.5 | 78.12 | 87.66 | 143.1 | 167.4 | 176.4 | 67.4 | 144.7 | 90.62 | 82.06 |
| 3 | 4 | 190.4 | 98.91 | 118.2 | 32.79 | 61.27 | 102.8 | 152.9 | 178.9 | 85.38 | 64.22 | 73.84 | 40.93 | 60.97 | 105 | 90.66 | 68.25 |
| 4 | 4 | 382.3 | 138.9 | 206.2 | 66.94 | 67.8 | 90.69 | 67.8 | 91.26 | 113.2 | 162.4 | 146 | 66.94 | 74.22 | 139.1 | 74.22 | 94.98 |

Table 5.4: $h_{12}$ for 256 systems within the described $4 \times 4 \times 4 \times 4$ volume of systems.

| | $d_3$ | 1 | 2 | 3 | 4 | 1 | 2 | 3 | 4 | 1 | 2 | 3 | 4 | 1 | 2 | 3 | 4 |
|---|---|---|---|---|---|---|---|---|---|---|---|---|---|---|---|---|---|
| $d_1$ | $d_2 \backslash d_4$ | 1 | 1 | 1 | 1 | 2 | 2 | 2 | 2 | 3 | 3 | 3 | 3 | 4 | 4 | 4 | 4 |
| 1 | 1 | 0.780 | 0.703 | 0.670 | 0.881 | 2.885 | 4.572 | 3.126 | 4.442 | 0.469 | 0.476 | 0.317 | 0.761 | 0.543 | 1.115 | 1.000 | 1.469 |
| 2 | 1 | 1.475 | 0.968 | 0.745 | 0.284 | 1.000 | 0.509 | 0.999 | 1.001 | 0.944 | 1.230 | 1.000 | 1.000 | 0.558 | 1.243 | 1.000 | 1.000 |
| 3 | 1 | 0.556 | 0.621 | 1.083 | 0.753 | 0.344 | 0.526 | 1.000 | 2.026 | 1.000 | 0.718 | 1.993 | 1.001 | 0.244 | 1.551 | 1.000 | 1.000 |
| 4 | 1 | 0.401 | 0.655 | 1.000 | 1.083 | 1.295 | 0.784 | 1.000 | 1.229 | 2.748 | 1.000 | 1.000 | 1.000 | 1.000 | 1.001 | 1.001 | 1.993 |
| 1 | 2 | 0.404 | 1.000 | 0.475 | 0.326 | 0.924 | 0.479 | 0.636 | 1.608 | 1.168 | 0.231 | 2.648 | 0.944 | 0.481 | 0.165 | 1.119 | 0.962 |
| 2 | 2 | 0.375 | 0.531 | 0.459 | 0.467 | 0.556 | 0.780 | 2.042 | 0.703 | 0.562 | 0.332 | 0.961 | 0.609 | 3.620 | 2.885 | 1.315 | 4.572 |
| 3 | 2 | 0.457 | 0.397 | 0.630 | 0.914 | 1.034 | 0.471 | 1.083 | 0.556 | 0.639 | 1.000 | 1.993 | 1.001 | 1.000 | 0.291 | 1.000 | 0.962 |
| 4 | 2 | 0.277 | 0.653 | 0.630 | 1.046 | 0.284 | 1.475 | 0.284 | 0.968 | 0.476 | 0.488 | 1.000 | 1.000 | 1.001 | 1.000 | 1.001 | 0.509 |
| 1 | 3 | 0.176 | 0.572 | 1.000 | 0.911 | 1.730 | 1.045 | 0.558 | 1.262 | 1.083 | 0.609 | 0.584 | 0.637 | 1.000 | 0.609 | 0.952 | 1.469 |
| 2 | 3 | 1.530 | 0.541 | 1.295 | 0.934 | 1.227 | 1.993 | 1.000 | 1.001 | 1.000 | 1.083 | 0.584 | 1.000 | 1.000 | 1.243 | 0.558 | 1.000 |
| 3 | 3 | 0.295 | 2.145 | 0.410 | 1.109 | 1.000 | 1.693 | 0.410 | 2.046 | 2.042 | 2.042 | 0.780 | 2.042 | 1.000 | 1.000 | 0.410 | 1.000 |
| 4 | 3 | 1.000 | 0.909 | 0.952 | 1.000 | 1.000 | 1.786 | 1.295 | 1.229 | 1.000 | 1.000 | 0.584 | 1.083 | 0.605 | 1.001 | 1.000 | 1.993 |
| 1 | 4 | 0.434 | 0.383 | 0.390 | 1.000 | 1.243 | 0.331 | 1.240 | 0.558 | 1.076 | 0.914 | 0.831 | 0.952 | 1.083 | 0.544 | 1.000 | 0.584 |
| 2 | 4 | 1.300 | 0.538 | 0.619 | 1.295 | 1.001 | 0.404 | 1.001 | 1.000 | 1.975 | 0.349 | 1.775 | 0.555 | 0.663 | 0.924 | 0.663 | 0.479 |
| 3 | 4 | 0.492 | 1.017 | 0.335 | 0.952 | 1.000 | 0.630 | 1.000 | 0.604 | 1.001 | 1.001 | 1.993 | 1.000 | 1.000 | 1.000 | 1.083 | 0.584 |
| 4 | 4 | 1.181 | 0.411 | 1.181 | 0.410 | 1.000 | 0.375 | 1.000 | 0.531 | 1.000 | 0.411 | 1.000 | 0.410 | 2.042 | 0.556 | 2.042 | 0.780 |

Table 5.5: $h_{23}$ for 256 systems within the described $4 \times 4 \times 4 \times 4$ volume of systems.

| $d_3$ → | | 1 | 1 | 1 | 1 | 2 | 2 | 2 | 2 | 3 | 3 | 3 | 3 | 4 | 4 | 4 | 4 |
|---|---|---|---|---|---|---|---|---|---|---|---|---|---|---|---|---|---|
| $d_1$ | $d_2$ \ $d_4$ | 1 | 2 | 3 | 4 | 1 | 2 | 3 | 4 | 1 | 2 | 3 | 4 | 1 | 2 | 3 | 4 |
| 1 | 1 | 1.021 | 0.832 | 0.562 | 0.890 | 1.179 | 1.415 | 1.650 | 1.395 | 0.430 | 0.336 | 0.526 | 0.335 | 0.777 | 0.513 | 1.000 | 1.145 |
| 2 | 1 | 0.530 | 0.298 | 0.790 | 0.692 | 0.718 | 0.545 | 0.979 | 0.991 | 0.798 | 0.578 | 1.000 | 1.000 | 0.643 | 0.511 | 1.000 | 1.000 |
| 3 | 1 | 0.499 | 0.487 | 0.991 | 0.992 | 0.665 | 0.854 | 1.000 | 1.097 | 0.718 | 0.456 | 0.900 | 0.991 | 0.212 | 0.694 | 1.000 | 1.000 |
| 4 | 1 | 0.870 | 0.421 | 1.000 | 0.991 | 0.525 | 0.890 | 1.000 | 0.588 | 1.134 | 1.000 | 1.000 | 1.000 | 0.718 | 0.991 | 0.991 | 0.900 |
| 1 | 2 | 0.744 | 0.718 | 0.622 | 0.180 | 0.320 | 0.280 | 0.426 | 0.236 | 0.511 | 0.290 | 0.838 | 0.857 | 0.281 | 0.227 | 0.506 | 0.697 |
| 2 | 2 | 0.780 | 0.395 | 0.770 | 0.232 | 0.691 | 1.021 | 1.403 | 0.832 | 1.115 | 0.487 | 1.203 | 0.511 | 1.474 | 1.179 | 1.554 | 1.415 |
| 3 | 2 | 0.672 | 0.157 | 0.757 | 0.992 | 0.866 | 0.654 | 0.991 | 0.528 | 0.665 | 0.718 | 0.900 | 0.991 | 1.000 | 0.444 | 1.000 | 0.697 |
| 4 | 2 | 0.863 | 0.541 | 0.757 | 0.581 | 0.692 | 0.530 | 0.692 | 0.298 | 0.386 | 0.370 | 1.000 | 1.000 | 0.991 | 0.718 | 0.991 | 0.545 |
| 1 | 3 | 0.411 | 0.642 | 0.718 | 0.632 | 0.679 | 0.545 | 0.643 | 0.305 | 0.991 | 0.511 | 0.783 | 0.479 | 1.000 | 0.511 | 0.991 | 1.145 |
| 2 | 3 | 0.507 | 0.615 | 0.525 | 0.763 | 0.986 | 0.900 | 0.718 | 0.991 | 1.000 | 0.991 | 0.783 | 1.000 | 1.000 | 0.511 | 0.643 | 1.000 |
| 3 | 3 | 0.451 | 1.120 | 0.481 | 0.341 | 1.000 | 1.236 | 0.481 | 1.092 | 1.403 | 1.403 | 1.021 | 1.403 | 1.000 | 1.000 | 0.481 | 1.000 |
| 4 | 3 | 1.000 | 0.922 | 0.991 | 1.000 | 1.000 | 1.177 | 0.525 | 0.588 | 1.000 | 1.000 | 0.783 | 0.991 | 0.541 | 0.991 | 0.718 | 0.900 |
| 1 | 4 | 0.618 | 0.257 | 0.355 | 0.718 | 0.511 | 0.411 | 0.511 | 0.643 | 1.006 | 0.992 | 0.581 | 0.991 | 0.991 | 0.437 | 1.000 | 0.783 |
| 2 | 4 | 1.119 | 0.276 | 0.412 | 0.525 | 0.991 | 0.744 | 0.991 | 0.718 | 1.136 | 0.483 | 1.169 | 0.334 | 0.549 | 0.320 | 0.549 | 0.280 |
| 3 | 4 | 0.450 | 0.993 | 0.645 | 0.991 | 1.000 | 0.757 | 1.000 | 0.287 | 0.991 | 0.991 | 0.900 | 0.718 | 1.000 | 1.000 | 0.991 | 0.783 |
| 4 | 4 | 1.070 | 0.351 | 1.070 | 0.481 | 1.000 | 0.780 | 1.000 | 0.395 | 1.000 | 0.351 | 1.000 | 0.481 | 1.403 | 0.691 | 1.403 | 1.021 |

Table 5.6: $h_{34}$ for 256 systems within the described $4 \times 4 \times 4 \times 4$ volume of systems.

| | $d_3$ | 1 | 2 | 3 | 4 | 1 | 2 | 3 | 4 | 1 | 2 | 3 | 4 | 1 | 2 | 3 | 4 |
| $d_1$ | $d_2 \backslash d_4$ | 1 | 1 | 1 | 1 | 2 | 2 | 2 | 2 | 3 | 3 | 3 | 3 | 4 | 4 | 4 | 4 |
|---|---|---|---|---|---|---|---|---|---|---|---|---|---|---|---|---|---|
| 1 | 1 | 0.548 | 0.627 | 0.723 | 0.843 | 0.461 | 0.718 | 0.477 | 0.846 | 0.420 | 0.403 | 0.585 | 0.825 | 0.707 | 0.534 | 1.000 | 0.883 |
| 2 | 1 | 0.597 | 0.577 | 1.117 | 1.054 | 0.530 | 0.458 | 1.000 | 1.002 | 0.550 | 0.656 | 1.000 | 1.000 | 0.471 | 0.723 | 1.000 | 1.000 |
| 3 | 1 | 0.446 | 0.669 | 0.996 | 0.968 | 0.509 | 0.696 | 1.000 | 0.970 | 0.530 | 0.746 | 0.803 | 1.002 | 0.469 | 0.760 | 1.000 | 1.000 |
| 4 | 1 | 0.665 | 0.538 | 1.000 | 0.996 | 0.538 | 0.728 | 1.000 | 0.659 | 1.010 | 1.000 | 1.000 | 1.000 | 0.530 | 1.002 | 1.002 | 0.803 |
| 1 | 2 | 0.299 | 0.530 | 0.311 | 0.450 | 0.773 | 0.566 | 0.986 | 0.763 | 0.773 | 0.472 | 0.838 | 0.964 | 0.442 | 0.432 | 0.703 | 0.707 |
| 2 | 2 | 0.555 | 0.299 | 0.453 | 0.072 | 0.859 | 0.548 | 1.068 | 0.627 | 0.736 | 0.588 | 0.663 | 0.607 | 0.903 | 0.461 | 1.121 | 0.718 |
| 3 | 2 | 0.504 | 0.449 | 0.505 | 0.973 | 0.887 | 0.542 | 0.996 | 0.656 | 0.740 | 0.530 | 0.803 | 1.002 | 1.000 | 0.530 | 1.000 | 0.707 |
| 4 | 2 | 0.504 | 0.415 | 0.505 | 0.763 | 1.054 | 0.597 | 1.054 | 0.577 | 0.900 | 0.544 | 1.000 | 1.000 | 1.002 | 0.530 | 1.002 | 0.458 |
| 1 | 3 | 0.338 | 0.535 | 0.530 | 0.706 | 0.722 | 0.537 | 0.471 | 0.598 | 0.996 | 0.607 | 0.651 | 0.784 | 1.000 | 0.607 | 0.965 | 0.883 |
| 2 | 3 | 0.299 | 0.660 | 0.538 | 0.722 | 1.003 | 0.803 | 0.530 | 1.002 | 1.000 | 0.996 | 0.651 | 1.000 | 1.000 | 0.723 | 0.471 | 1.000 |
| 3 | 3 | 0.603 | 0.901 | 0.710 | 0.823 | 1.000 | 0.773 | 0.710 | 0.969 | 1.068 | 1.068 | 0.548 | 1.068 | 1.000 | 1.000 | 0.710 | 1.000 |
| 4 | 3 | 1.000 | 0.909 | 0.965 | 1.000 | 1.000 | 1.023 | 0.538 | 0.659 | 1.000 | 1.000 | 0.651 | 0.996 | 0.577 | 1.002 | 0.530 | 0.803 |
| 1 | 4 | 0.477 | 0.445 | 0.842 | 0.530 | 0.723 | 0.301 | 0.717 | 0.471 | 1.002 | 0.973 | 0.502 | 0.965 | 0.996 | 0.845 | 1.000 | 0.651 |
| 2 | 4 | 0.769 | 0.426 | 0.759 | 0.538 | 1.002 | 0.299 | 1.002 | 0.530 | 1.009 | 0.730 | 1.022 | 0.434 | 1.055 | 0.773 | 1.055 | 0.566 |
| 3 | 4 | 0.567 | 0.953 | 0.721 | 0.965 | 1.000 | 0.505 | 1.000 | 0.474 | 1.002 | 1.002 | 0.803 | 0.530 | 1.000 | 1.000 | 0.996 | 0.651 |
| 4 | 4 | 0.776 | 0.791 | 0.776 | 0.710 | 1.000 | 0.555 | 1.000 | 0.299 | 1.000 | 0.791 | 1.000 | 0.710 | 1.068 | 0.859 | 1.068 | 0.548 |

Figure 5.1: Reconstruction of $\underline{\mathbf{d}} = (\,1\;\;1\;\;1\;\;1\,)$ c-pMMP. This system has $N = 9$ and $R = 8$. Circles represent the different objects classes, corresponding to different damage states. Lines represent their approximation. Reconstructions of object classes corresponding to the red and green lines intersect.

Figure 5.2: Reconstruction of $\underline{\mathbf{d}} = (\ 1\quad 1\quad 2\quad 2\ )$ c-pMMP. This system has $N = 13$ and $R = 11$. Circles represent the different objects classes, corresponding to different damage states. Lines represent their approximation. Reconstruction of the stray green object is now separable from the red class.

Figure 5.3: Reconstruction of $\underline{\mathbf{d}} = (\;2\quad 1\quad 3\quad 1\;)$ c-pMMP. This system has $N = 15$ and $R = 14$. Circles represent the different objects classes, corresponding to different damage states. Lines represent their approximation. By virtue of being an almost full rank system, the space is even closer to intended.
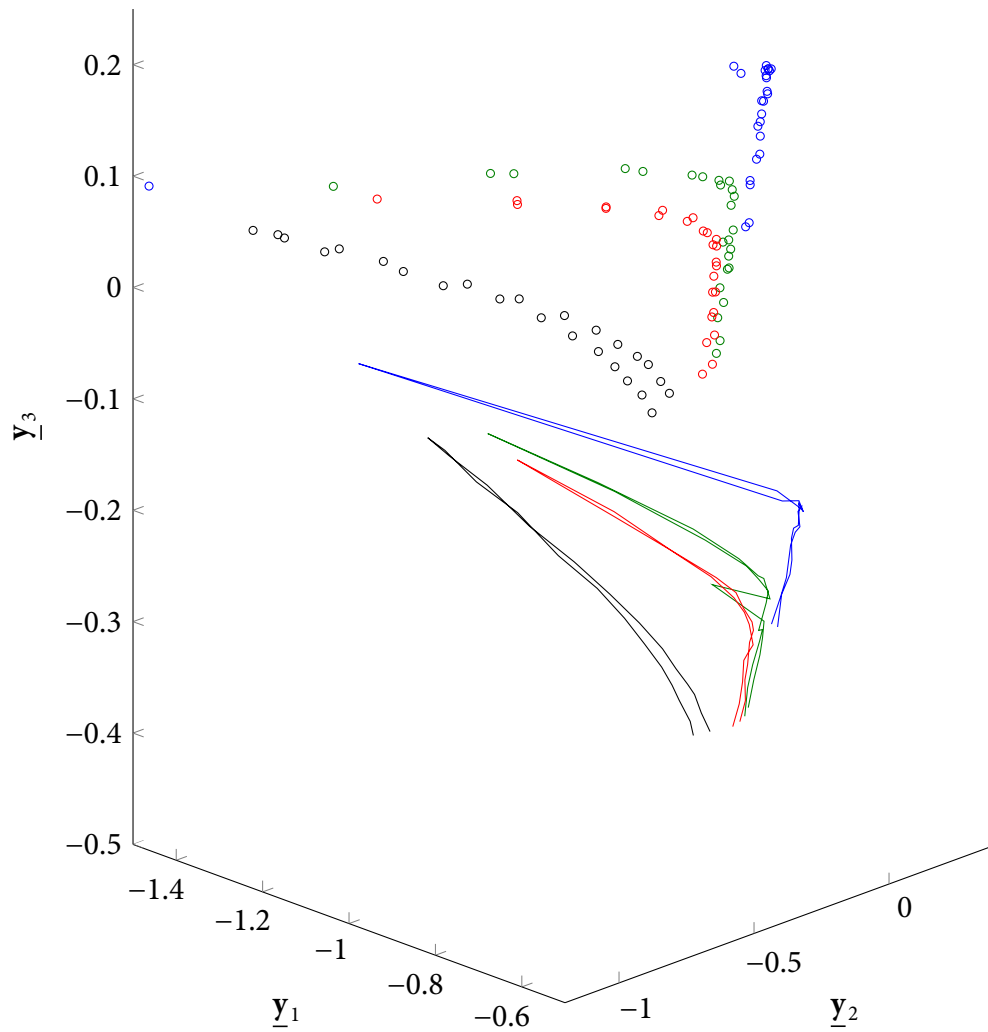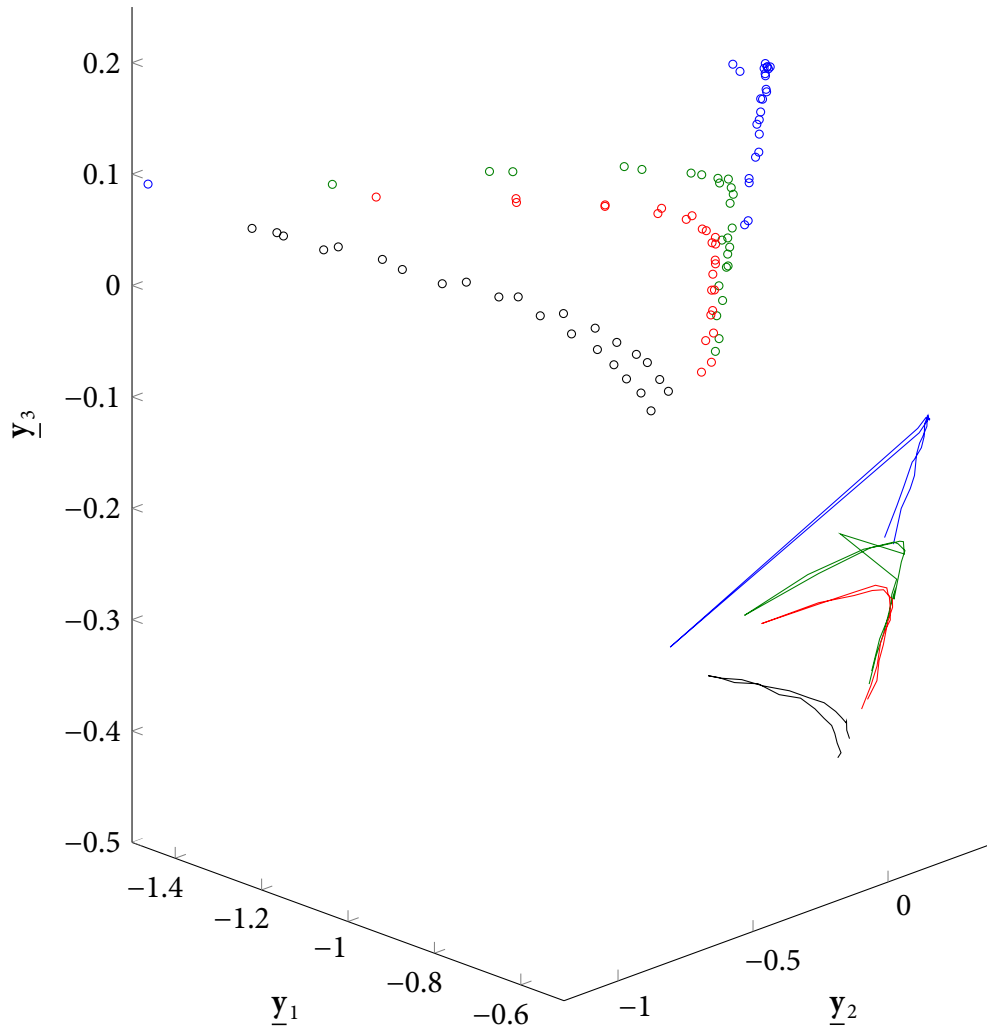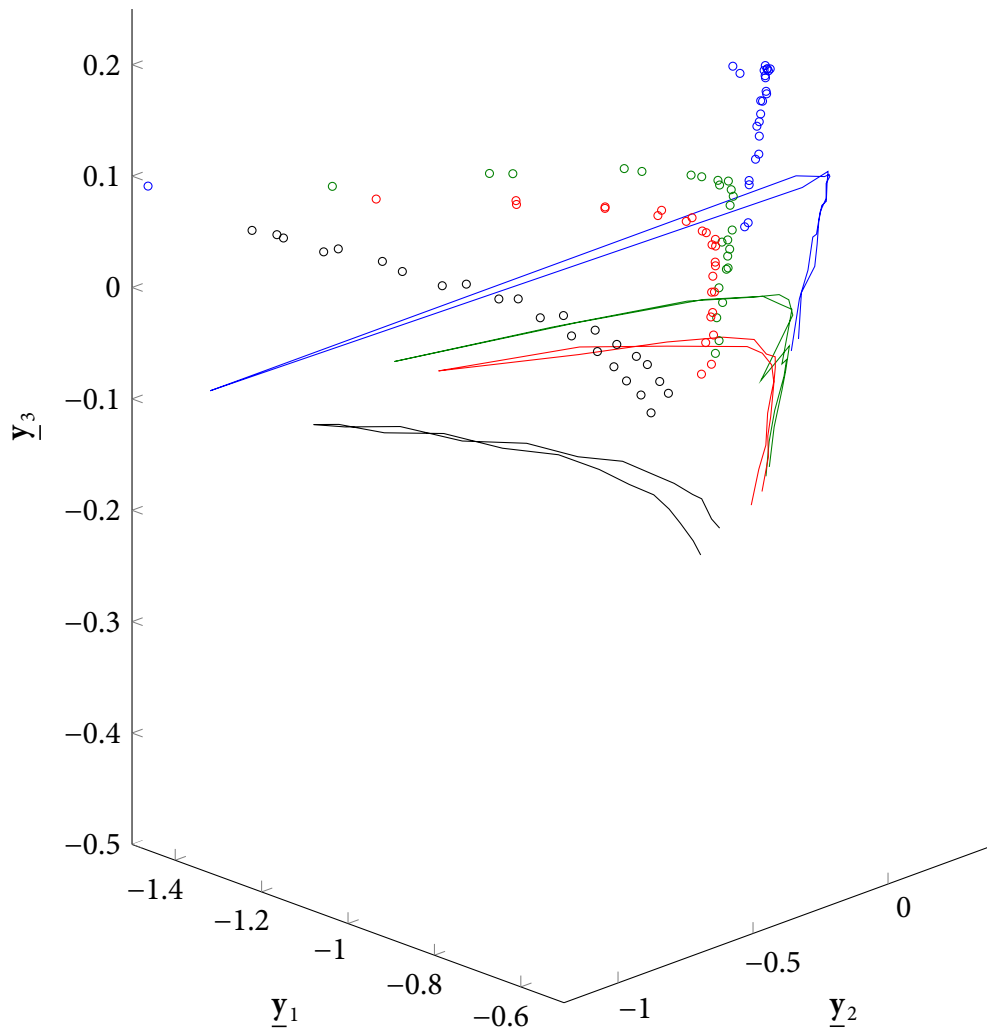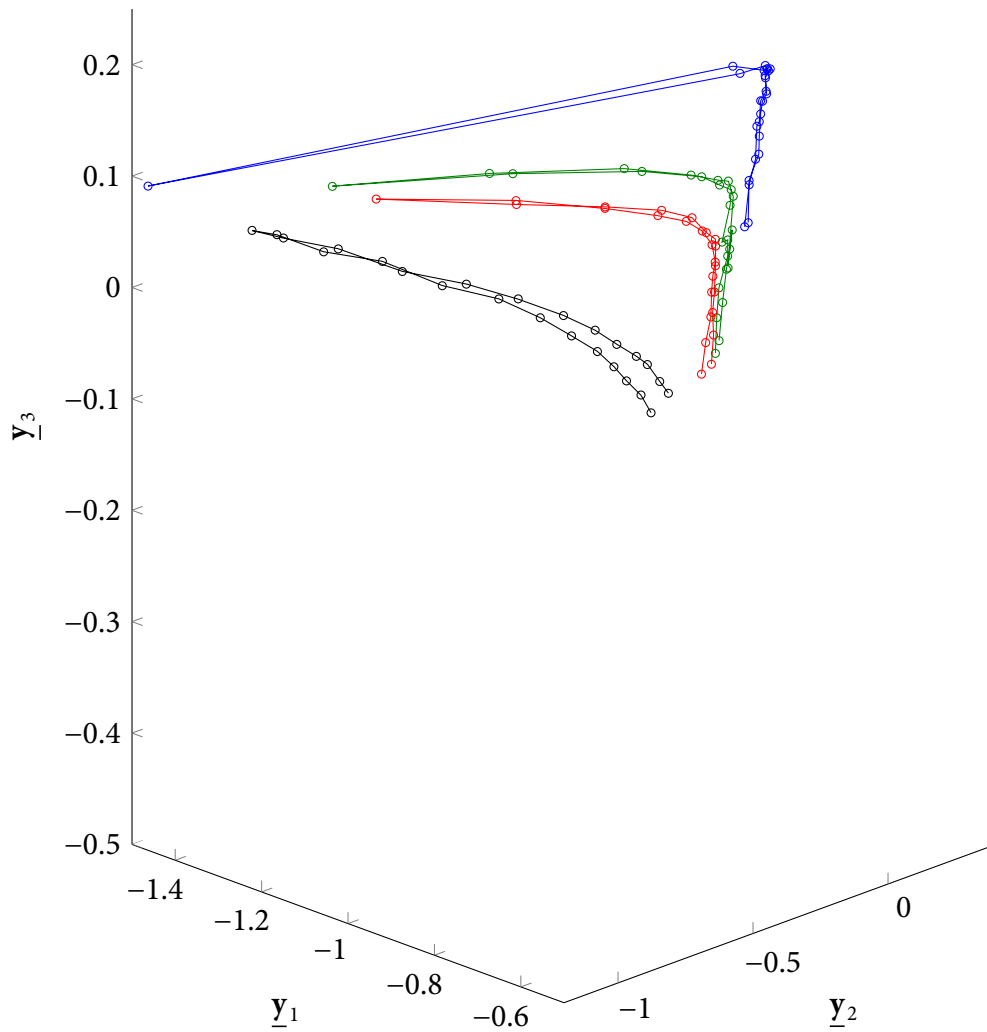
Figure 5.4: Reconstruction of $\underline{\mathbf{d}}$ = ( 3  1  3  1 ) c-pMMP. This system has $N$ = 17 and $R$ = 15. Circles represent the different objects classes, corresponding to different damage states. Lines represent their approximation. This system manages to align the reconstruction with the object classes.

## 5.4 Discussion

It has been shown that studying structured matrices within the context of partial systems is beneficial. However these matrices can further elucidate previously studied concepts from Chapter 3. When applied to full systems, $\underline{\underline{V}}_{s,\underline{\underline{Q}}}$ is a $16 \times 16$ identity matrix and $\underline{\underline{\Sigma}}_{s,\underline{\underline{Q}}} = \mathrm{diag}(1, \frac{1}{\sqrt{2}}, \frac{1}{2}, \frac{1}{2}, \frac{1}{\sqrt{2}}, \frac{1}{2}, \frac{1}{\sqrt{8}}, \frac{1}{\sqrt{8}}, \frac{1}{2}, \frac{1}{\sqrt{8}}, \frac{1}{4}, \frac{1}{4}, \frac{1}{2}, \frac{1}{\sqrt{8}}, \frac{1}{4}, \frac{1}{4})$. Note that $\sum_{i=1}^{16} \frac{1}{\sigma_{s,i}^2} = 121$, which corresponds to the ideal EWV of channeled systems in terms of the number of modulations within each Mueller element. Thus, the non-optimality is completely contained within $\underline{\underline{U}}_{s,\underline{\underline{Q}}}$ and the optimal full system must have a unitary $\underline{\underline{U}}_{s,\underline{\underline{Q}}}$.

The results shown in Tables 5.1–5.3 and Figures 5.1–5.4 indicate that channeled-partial Mueller matrix polarimeters can be successful in the task of object discrimination while reducing the number of channels and thereby increasing the resolution of the domain (in this case spectral) with which the polarization shares the bandwidth. The data set at hand contains the default state as well as three damage states, which are more arbitrary than intrinsically principal to detection. The difference between the red and green classes is particularly minimal, which leads to the realization that this optimization scenario is not ideal because the initial selection of classes of objects did not concern itself with the pMMP or c-pMMP design-ability. For optimal results, the class selection and pMMP or c-pMMP design needs to be performed at the same time for the system to be balanced. Having said that, it is clear that even the c-pMMP with $\underline{d} = (\,1\quad 1\quad 1\quad 1\,)$ is capable of providing separability to the classes and with proper calibration could be useful. Though only the $\underline{d} = (\,3\quad 1\quad 3\quad 1\,)$ system with $R = 15$ was able to approximate the space with low maximum canonical angles, note that the $\underline{d} = (\,1\quad 1\quad 1\quad 1\,)$ system with $R = 8$ was also able to separate the different damage state classes. The net separation as denoted by the respective $h_{\alpha,\beta}$ values seen in Tables 5.4–5.6 shows that the classes got closer: $h_{12} = 0.780$, $h_{23} = 1.021$ and $h_{34} = 0.548$. It is conceivable to adjust the space within which the target identification is performed, thereby allowing to use fairly sparse number of channels for the task. The c-pMMPs with $\underline{d} = (\,1\quad 1\quad 2\quad 2\,)$, $\underline{d} = (\,2\quad 1\quad 3\quad 1\,)$ and $\underline{d} = (\,3\quad 1\quad 3\quad 1\,)$ represent steps from the system with the most minimal modulation scheme to systems that have rank gradually approaching that of a full system. Table 5.7 shows $\underline{\underline{B}}$, $\underline{\underline{Q}}$, as well as the

structured form of measurable vectors $\underline{\mathbf{v}}_{s,i}$ and the corresponding noise variances $\sigma_{s,i}^2$ of the four c-pMMP systems.

## 5.5   Conclusion

The concepts of channeled and partial polarimetry were combined to enable the design of channeled-partial Mueller matrix polarimeters (c-pMMPs). By introducing structured decomposition, the measurement matrix $\underline{\underline{\mathbf{Q}}}$ is further investigated to provide the user with handles for evaluating the system's noise resilience and space coverage directly from the measurement matrix. As a result, the utility of c-pMMPs has been increased. Finally, this chapter demonstrated the applicability of the developed tools on the data set used in Chapter 4.

Table 5.7: Reconstruction properties of the four c-pMMP systems of interest.

| $\underline{d}^{\mathrm{T}}$ | $\underline{\underline{B}}$ | $\underline{\underline{Q}}$ | $64\sigma^2_{s,i}$ | $\underline{v}_{s,i}$ |
|---|---|---|---|---|
| $\begin{bmatrix}1\\1\\1\\1\end{bmatrix}$ | $\begin{bmatrix}\frac{7}{12}&\frac{1}{2}&\frac{1}{3}&\frac{1}{2}\\\frac{1}{2}&\frac{7}{12}&\frac{1}{2}&\frac{1}{2}\\\frac{1}{3}&\frac{1}{2}&\frac{7}{12}&\frac{1}{2}\\\frac{1}{2}&\frac{1}{2}&\frac{1}{2}&\frac{7}{12}\end{bmatrix}$ | | 128 | $\frac{1}{\sqrt{2}}\left[m_{00}+m_{11}\right]$ |
| | | | 64 | $\frac{1}{\sqrt{2}}\left[m_{01}+m_{10}\right]$ |
| | | | 96 | $\frac{1}{\sqrt{4}}\left[m_{02}+m_{11}+m_{20}+m_{33}\right]$ |
| | | | 16 | $\frac{1}{\sqrt{2}}\left[m_{03}+m_{30}\right]$ |
| | | | 8 | $\frac{1}{\sqrt{2}}\left[m_{12}+m_{21}\right]$ |
| | | | 8 | $\frac{1}{\sqrt{2}}\left[m_{13}+m_{31}\right]$ |
| | | | 35 | $\frac{1}{\sqrt{2}}\left[m_{22}+m_{33}\right]$ |
| | | | 5 | $\frac{1}{\sqrt{2}}\left[m_{23}+m_{32}\right]$ |
| $\begin{bmatrix}1\\1\\2\\2\end{bmatrix}$ | $\begin{bmatrix}\frac{16}{21}&\frac{16}{21}&\frac{16}{21}&\frac{3}{4}\\1&1&1&1\\\frac{11}{42}&\frac{5}{14}&\frac{23}{43}&\frac{11}{16}\\\frac{11}{16}&\frac{3}{16}&\frac{11}{16}&\frac{23}{43}\end{bmatrix}$ | | 128 | $\frac{1}{\sqrt{2}}\left[m_{00}+m_{11}\right]$ |
| | | | 32 | $\left[m_{01}\right]$ |
| | | | 240 | $\frac{1}{\sqrt{10}}\left[m_{02}-2m_{11}+2m_{20}+m_{33}\right]$ |
| | | | 16 | $\frac{1}{\sqrt{2}}\left[m_{03}+m_{32}\right]$ |
| | | | 16 | $\left[m_{11}\right]$ |
| | | | 84 | $\frac{1}{\sqrt{6}}\left[m_{12}+2m_{20}+m_{33}\right]$ |
| | | | 12 | $\frac{1}{\sqrt{6}}\left[m_{13}+2m_{30}+m_{32}\right]$ |
| | | | 12 | $\left[m_{21}\right]$ |
| | | | 14 | $\frac{1}{\sqrt{2}}\left[m_{22}+m_{33}\right]$ |
| | | | 10 | $\frac{1}{\sqrt{2}}\left[m_{23}+m_{32}\right]$ |
| | | | 4 | $\left[m_{31}\right]$ |
| $\begin{bmatrix}2\\1\\3\\1\end{bmatrix}$ | $\begin{bmatrix}\frac{21}{22}&\frac{21}{22}&\frac{2}{3}&1\\\frac{2}{3}&\frac{2}{3}&\frac{3}{11}&1\\\frac{9}{11}&1&1&1\\1&1&1&1\end{bmatrix}$ | | 80 | $\frac{1}{\sqrt{5}}\left[2m_{00}-m_{20}\right]$ |
| | | | 40 | $\frac{1}{\sqrt{5}}\left[2m_{01}+m_{20}\right]$ |
| | | | 32 | $\frac{1}{\sqrt{2}}\left[m_{02}-m_{11}\right]$ |
| | | | 16 | $\left[m_{03}\right]$ |
| | | | 64 | $\frac{1}{\sqrt{2}}\left[m_{10}+m_{11}\right]$ |
| | | | 30 | $\frac{1}{\sqrt{5}}\left[m_{12}+2m_{20}\right]$ |
| | | | 10 | $\left[m_{13}\right]$ |
| | | | 10 | $\left[m_{21}\right]$ |
| | | | 3 | $\left[m_{22}\right]$ |
| | | | 3 | $\left[m_{23}\right]$ |
| | | | 16 | $\left[m_{30}\right]$ |
| | | | 6 | $\left[m_{31}\right]$ |
| | | | 7 | $\left[m_{32}\right]$ |
| | | | 3 | $\left[m_{33}\right]$ |
| $\begin{bmatrix}3\\1\\3\\1\end{bmatrix}$ | $\begin{bmatrix}1&1&\frac{1}{2}&1\\1&1&1&1\\\frac{1}{2}&1&1&1\\1&1&1&1\end{bmatrix}$ | | 64 | $\left[m_{00}\right]$ |
| | | | 32 | $\left[m_{01}\right]$ |
| | | | 32 | $\frac{1}{\sqrt{2}}\left[m_{02}+m_{20}\right]$ |
| | | | 16 | $\left[m_{03}\right]$ |
| | | | 32 | $\left[m_{10}\right]$ |
| | | | 16 | $\left[m_{11}\right]$ |
| | | | 4 | $\left[m_{12}\right]$ |
| | | | 12 | $\left[m_{13}\right]$ |
| | | | 4 | $\left[m_{21}\right]$ |
| | | | 9 | $\left[m_{22}\right]$ |
| | | | 3 | $\left[m_{23}\right]$ |
| | | | 16 | $\left[m_{30}\right]$ |
| | | | 12 | $\left[m_{31}\right]$ |
| | | | 3 | $\left[m_{32}\right]$ |
| | | | 1 | $\left[m_{33}\right]$ |

CHAPTER 6

MEASUREMENT DIVERSITY

In order to reconstruct the state of light's polarization, a polarimeter must take several measurements. As described in Chapter 1, each measurement performs a projection of the state of the light onto each of the analyzing vectors. Every additional measurement provides a particular constraint on how the two vectors relate, thereby shrinking the space of polarization states that the measured light can potentially occupy. Each constraint takes the form of a 4-dimensional hyperplane, which can be easily seen from

$$I_n = a_0 s_0 + a_1 s_2 + a_2 s_2 + a_3 s_3, \tag{6.1}$$

where the Stokes parameters can be thought of as a set of 4-dimensional axes. Equivalently to the methods of reconstruction described in Section 1.4, the purpose of having multiple analyzing vectors is to construct at least four 4-dimensional hyperplanes. Provided that these hyperplanes are different, they will have one intersection point — the solution to the system of equations that the measurements present. Given that the Stokes parameters being measured are constant, the additional hyperplane constraints arising from taking more than four measurements will still contain the previous solution.

Naturally, even if the analyzing vectors are known with infinite precision, there are additional sources of noise. These sources of error can be applied by adding uncertainty to the hyperplane. The case of additive noise is easy to imagine as it turns the hyperplanes into thin clouds or "thickened" planes. When these clouds intersect the volume enclosed in that intersection may be significant if the effective hyperplanes are not sufficiently different. As a result, in order for the intersection to be well defined, it is necessary for the separation angles to be large, ideally orthogonal, or $\frac{\pi}{2}$.

To evaluate a polarimeter's performance, it is necessary to accurately understand the mathematical steps involved to predict the effective noise resilience. The most straightforward and brute force method is to construct an artificial Stokes scene, pass it through

the system's known analyzing vectors to obtain detector intensities, and after adding a representative kind of noise, use the pseudoinverse to get to the underlying Stokes data. With original and reconstructed data at hand, one can then evaluate some sort of error metric between the images, like

$$\varepsilon = \sum_{i=0}^{3} a_i \sqrt[b]{\frac{1}{XY} \sum_{x=1}^{X} \sum_{y=1}^{Y} \left| s_{i,\text{original}}(x, y) - s_{i,\text{reconstructed}}(x, y) \right|^b}, \tag{6.2}$$

where $a_i$ allows to weigh different Stokes parameters differently and $b$ allows to average the errors in a more arbitrary space. This method, however, is computationally intensive and, depending on the noise model, may cause some experimental bias if the scene that is generated is not representative of the one that will be measured.

As an alternative to the brute force evaluation, one can instead attempt to identify the mathematical quantities in the reconstruction process which are responsible for determining the noise resilience of the system. Much like there is no correct $b$ for Equation 6.2, there is no "correct" mathematical space in which to weigh the noise characteristics. Although the approaches to the global optimum between the different metrics can be different, all the useful ones must have the intent of orthogonalizing the reconstruction hyperplanes. Given a set of measurements,

$$\underline{\mathbf{I}} = \begin{bmatrix} a_{0,0}s_0 + a_{1,0}s_2 + a_{2,0}s_2 + a_{3,0}s_3 \\ a_{0,1}s_0 + a_{1,1}s_2 + a_{2,1}s_2 + a_{3,1}s_3 \\ \vdots \\ a_{0,N}s_0 + a_{1,N}s_2 + a_{2,N}s_2 + a_{3,N}s_3 \end{bmatrix}, \tag{6.3}$$

with $N \geq 4$, the pseudoinvese will remix $a_{i,n}s_i$ products to form a $4 \times N$ reconstruction matrix, $\underline{\mathbf{W}}^+$, which to the best of author's knowledge cannot be effectively represented for the completely general case of $N \geq 4$. In order to solve a reverse-problem by way of a matrix multiplication, it is necessary to consider the intersection of exactly four $N$-dimensional hyperplanes — the rows of $\underline{\mathbf{W}}^+$. For $N = 4$ the inversion does not alter the geometry significantly, but for $N > 4$, there exist $N - 4$ extra degrees of freedom in which the hyperplanes can rotate.

## 6.1 Established Evaluation Metrics

One of the first metrics to be used in determining polarimeter's performance was the Condition Number (CN) and was introduced by Tyo (2002). It can be calculated as

$$\text{CN} = \left\| \underline{\underline{\mathbf{W}}} \right\| \cdot \left\| \underline{\underline{\mathbf{W}}}^+ \right\| = \left| \frac{\lambda_{\max}(\underline{\underline{\mathbf{W}}})}{\lambda_{\min}(\underline{\underline{\mathbf{W}}})} \right|, \tag{6.4}$$

which has the needed effect of orthogonalizing the rows of the pseudoinverse $\underline{\underline{\mathbf{W}}}^+$ when used as a minimization target. Tyo (2002) showed that the minimum CN for a Stokes polarimeter is $\sqrt{R-1}$, where $R$ is the number of Stokes parameters being reconstructed. Through PSG/PSA independence, it can be easily shown that for a Mueller matrix polarimeter, the minumum CN is $\sqrt{(R_G - 1)(\sqrt{R_A - 1})}$, with $R_G$ and $R_A$ are the numbers of Mueller columns and rows being reconstructed, respectively. In this chapter, the focus is on overdetermined Stokes systems, and $R = 4$ is assumed.

Another often used evaluation metric is the Equally Weighted Variance (EWV), which can be calculated as

$$\text{EWV} = \text{tr}\left( \underline{\underline{\mathbf{W}}}^{+\text{T}} \underline{\underline{\mathbf{W}}}^+ \right) = \sum_{i=0}^{3} \frac{1}{\sigma_{i,\underline{\mathbf{W}}}^2} \tag{6.5}$$

was introduced by Sabatke et al. (2000) and Twietmeyer and Chipman (2008) for purposes of evaluating Stokes and Mueller polarimeters, respectively. By minimizing EWV, the mean square error between input and reconstruction is minimized. As it was prefaced before, CN and EWV are often corollary — if the theoretical minimum exists in one, then that optimal system will also be at the theoretical minimum of the other. The only difference lies in the slope at which the minimum is approached and the effective weighing implied, which may lead to a discrepancy when the theoretical minimum is unavailable given the variable space specified.

## 6.2 Diversity Metrics

CN and EWV are perfectly sufficient for evaluating the system if additive noise is the only one present. In this section, overdetermined systems will be specifically studied to see if there is any benefit in more carefully shaping the analyzing vectors. Essentially, the attempt

is to see if the extra $(N − 4)$-dimensions of freedom contain solutions that are not only optimal with respect to CN and EWV, but also provide improved performance for different kinds of noise.

As mentioned before, once the noise becomes data dependent, there is a possibility for experimental bias to affect the design of the polarimeter. Although it's possible to construct a set of measurements, given the distribution of objects to be measured and the noise encountered, this method will provide overly specific designs. Instead, the goal of this chapter is to assume that the systems are equally likely to measure all kinds of polarizations and base the experiment on a spherical distribution of states, covering the Poincaré sphere.

This section will investigate if a system that performs a more diverse set of measurements is any better at reconstructing the scene than a system of the same CN/EWV that does not consider the measurement diversity. As was shown by Goudail and Tyo (2011), partially polarized measurements never improve contrast, thus justifying limiting all analyzing vectors to lie on a sphere of $a_0$ radius. Linking the radius allows a simplification to a 3-dimensional quantity,

$$\underline{\mathbf{v}} = [\ a_1 \quad a_2 \quad a_3\ ]^{\mathrm{T}}, \tag{6.6}$$

from where, the diversity can be based on the relationship of each of the available vector pairs. One way to evaluate that relationship is the Eucledean distance,

$$d_{k\ell} = \|\underline{\mathbf{v}}_k - \underline{\mathbf{v}}_\ell\| = \sqrt{(v_{kx} - v_{\ell y})^2 + (v_{ky} - v_{\ell y})^2 + (v_{kz} - v_{\ell z})^2}, \tag{6.7}$$

while another way is the arclength separation,

$$\alpha_{k\ell} = \arccos(\hat{v}_k \cdot \hat{v}_\ell). \tag{6.8}$$

The metrics that will be proposed in this chapter will all depend on either of the two measures of separation.

### 6.2.1 Valence Shell Electron Pair Repulsion Theory

In chemistry, molecule shapes are determined by multiple co-existing repulsion forces between all of the electric charges in the vicinity. The number of atom's valence shell electrons

predetermines certain geometries. Mirroring this theory, analyzing vectors can be treated as electrons in the valence shell and their proximities to one another leading to repulsion forces. Adding all of the forces present, allows the optimization to search for the "easiest", or lowest-energy configuration. Mathematically, it can be written as

$$\text{VTR} = \frac{1}{N^2} \sum_{k=1}^{N-1} \sum_{\ell=k+1}^{N} \frac{C}{d_{k\ell}^2}, \tag{6.9}$$

where the summation limits prevent double-counting and $C$ is a constant that carries the proper units for VTR to have units of force. Note that because $d_{k\ell}$ is in the denominator, this metric heavily punishes systems that take the same measurements. And although taking the same measurement might not be ideal, giving such systems a score approaching infinity is unlikely to be justifiable. Instead, this metric is likely to be useful only for determining arrangements where the extreme constraints are appropriate.

To remedy this limitation, the metric can be adjusted,

$$\text{VTA} = \frac{1}{N^2} \sum_{k=1}^{N-1} \sum_{\ell=k+1}^{N} \frac{C}{(d_{k\ell} + a)^2}, \tag{6.10}$$

where $a$ is added to $d_{k\ell}$ to stabilize division. This adjustment will invariably change the optimization result and will depend heavily on $a$. However, it is not easy to justify a particular value for $a$.

### 6.2.2 Arclength Anti-proximity

Another way to spread the measurements' analyzing vectors around is to consider their arclength separation on the surface of the Poincaré sphere. The maximum separation occurs when the measurements are orthogonal, meaning $\alpha_{k\ell} = \pi$. Since the maximum arclength separation is known, using that maximum to bias all the separations is not arbitrary. Hence, in this metric, normalized arclength anti-proximity (shortness) is calculated between each measurement pair and added, or

$$\text{AAP} = \sqrt{\frac{1}{N^2} \left[ \sum_{k=1}^{N-1} \sum_{\ell=k+1}^{N} \left( 1 - \frac{\alpha_{k\ell}}{\pi} \right)^2 \right]}, \tag{6.11}$$

where the summation limits prevent double-counting as before. Unlike VTR, this metric does not punish repeated measurements infinitely. As a result, this metric has a weaker forcing towards the minimum and is thus definitely flatter overall.

### 6.2.3 Solid Angle Intersection

VTR and AAP are relatively straight-forward in that they provide a continuous punishment for two measurements being close to one another. Depending on the way the metric is constructed, it is easy to punish similar measurement too much or too little. To provide a potentially more balanced approach, one can start punishing against a measurement only when it gets within a certain range of another. One way to do that is to construct cones with spherical caps around each analyzing vector's point on the Poincaré sphere. By giving each measurement's cone a solid angle of $\Omega_{\mathbf{v}_k} = \frac{4\pi}{N}$ ensures that the intersections are extant, yet not overly abundant. Using Oleg Mazonka's derivation (Mazonka (2012)), unqiue solid angle intersections are added,

$$\text{SAI} = \sum_{k=1}^{N-1} \sum_{\ell=k+1}^{N} 4\mathbb{R}\left[\arccos\left(\frac{\sin(\alpha_{k\ell}/2)}{\sin(\beta)}\right) - \cos(\beta)\arccos\left(\frac{\tan(\alpha_{k\ell}/2)}{\tan(\beta)}\right)\right], \qquad (6.12)$$

where the summation limits prevent double-counting as before and $\beta$ is the arclength radius of each cone and can be easily shown to be $\arccos(1 - \frac{2}{N})$ given the $\Omega_{\underline{\mathbf{v}}_k}$ from before.

### 6.2.4 Empty Sphere Volume

Finally, instead of looking at measurement relationships one by one and adding them together, the whole collection can be looked at as an ensemble and the property that can be used to group them together is the volume that the polyhedron encloses between all those analyzing vectors. Although deriving a calculation for a volume given all the points within the set should be possible, breaking up the volume into constituent pieces and calculating the volume of each one is easier. To do that, the 3D distribution of $\underline{\mathbf{v}}$s is Delaunay triangulated first, which forms $M$ simplices. For the 3-dimensional $\underline{\mathbf{v}}$s, those simplices are referred to as tetrahedra. For each tetrahedron, a sub-volume is calculated and added

together. The result is then subtracted from a normalized sphere,

$$\text{ESV} = 1 - \frac{1}{\pi} \sum_{m=1}^{M} \left| \det \left( \ \underline{\mathbf{v}}_{m,1} - \underline{\mathbf{v}}_{m,4} \quad \underline{\mathbf{v}}_{m,2} - \underline{\mathbf{v}}_{m,4} \quad \underline{\mathbf{v}}_{m,3} - \underline{\mathbf{v}}_{m,4} \ \right) \right|. \tag{6.13}$$

One difference of this metric is in how it treats a repeated measurement. If all other metrics punish repetition directly, ESV simply maintains the volume of that configuration. Whether this is a drawback is likely to depend on the constraints placed on measurement selection.

## 6.3   Example

These metrics can yield a better system only for systems with $N > 4$. To justify a larger than required number of measurements, the information modulation technique that is utilized needs to bode well to speedy capture times and should represent a reasonable, rather than an extravagant design. As a result, to test these metrics, a hybrid scheme was selected, where both spatial and temporal modulations are used.

The selected setup features a microgrid detector, and two rotating retarders in front of it. The system can be seen in Figure 6.1a, while the system's analyzing vector can be shown to be

$$\underline{\mathbf{A}}(\vec{\xi}) = \left( \begin{bmatrix} 1 & 0 & 0 & 0 \end{bmatrix} \underline{\underline{\mathbf{M}}}_{\text{LP}}(\phi) \underline{\underline{\mathbf{M}}}_{\text{LR},2}(\delta_2, \theta_2) \underline{\underline{\mathbf{M}}}_{\text{LR},1}(\delta_1, \theta_1) \right)^{\text{T}} =$$

$$= \frac{1}{2} \begin{bmatrix} 1 \\[6pt] \begin{aligned} &+ \cos(2\phi)[\psi_1\psi_2 - \sin(2\theta_1)\sin(2\theta_2)\sin(\delta_1)\sin(\delta_2) + \sin(4\theta_1)\sin(4\theta_2)\sin^2(\delta_1/2)\sin^2(\delta_2/2)] \\ &+ \sin(2\phi)[\sin(4\theta_1)\sin^2(\delta_1/2)\psi_2 + \sin(4\theta_2)\sin^2(\delta_2/2)\psi_1 + \sin(2\theta_1)\cos(2\theta_2)\sin(\delta_1)\sin(\delta_2)] \end{aligned} \\[12pt] \begin{aligned} &+ \sin(2\phi)[\psi_1\psi_2 - \cos(2\theta_1)\cos(2\theta_2)\sin(\delta_1)\sin(\delta_2) + \sin(4\theta_1)\sin(4\theta_2)\sin^2(\delta_1/2)\sin^2(\delta_2/2)] \\ &+ \cos(2\phi)[\sin(4\theta_1)\sin^2(\delta_1/2)\psi_2 + \sin(4\theta_2)\sin^2(\delta_2/2)\psi_1 + \cos(2\theta_1)\sin(2\theta_2)\sin(\delta_1)\sin(\delta_2)] \end{aligned} \\[12pt] \begin{aligned} &+ \sin(2\phi)[\cos(2\theta_1)\sin(\delta_1)\zeta_2 + \cos(2\theta_2)\cos(\delta_1)\sin(\delta_1) - \sin(2\theta_1)\sin(4\theta_2)\sin(\delta_1)\sin^2(\delta_2/2)] \\ &- \cos(2\phi)[\sin(2\theta_1)\sin(\delta_1)\psi_2 + \sin(2\theta_2)\cos(\delta_1)\sin(\delta_2) + \cos(2\theta_1)\sin(4\theta_2)\sin(\delta_1)\sin^2(\delta_2/2)] \end{aligned} \end{bmatrix}, \tag{6.14}$$

where $\psi_i = \cos^2(2\theta_i) + \cos(\delta_i)\sin^2(2\theta_i)$, $\zeta_i = \sin^2(2\theta_i) + \cos(\delta_i)\cos^2(2\theta_i)$ and $(\vec{\xi}) = (\phi, \delta_1, \delta_2, \theta_1, \theta_2)$ and $\phi$ represents the angle of the polarizer on a particular pixel. For this example, microgrid's pattern of polarimeter orientations is customized to form a trapezoid over the superpixel's set of four pixels, an illustration of which can be seen in Figure 6.1c.

The customization introduces two parameters, $\alpha$ and $\beta$ to determine the applied pattern. Forgoing the Instantaneous Field of View (IFOV) problems, each snapshot of the system can be described by the following sub-$\underline{\underline{\mathbf{W}}}$:

$$\underline{\underline{\mathbf{W}}}(t) = \begin{bmatrix} \underline{\mathbf{A}}\left(-\frac{\pi}{2} + \alpha + \beta, \delta_1, \delta_2, \theta_1(t), \theta_2(t)\right)^{\mathrm{T}} \\ \underline{\mathbf{A}}\left(\ 0 - \alpha + \beta, \delta_1, \delta_2, \theta_1(t), \theta_2(t)\right)^{\mathrm{T}} \\ \underline{\mathbf{A}}\left(\ 0 + \alpha - \beta, \delta_1, \delta_2, \theta_1(t), \theta_2(t)\right)^{\mathrm{T}} \\ \underline{\mathbf{A}}\left(+\frac{\pi}{2} - \alpha - \beta, \delta_1, \delta_2, \theta_1(t), \theta_2(t)\right)^{\mathrm{T}} \end{bmatrix}, \tag{6.15}$$

which creates the polarizer array seen in Figure 6.1c and traces out the edge of a trapezoid within the Poincaré $a_1/a_2$ plane as shown in Figure 6.1b. While assuming a fairly limited temporal bandwidth of the measured scene, multiple snapshots can be combined to form the total $\underline{\underline{\mathbf{W}}}$:

$$\underline{\underline{\mathbf{W}}} = \begin{bmatrix} \underline{\underline{\mathbf{W}}}^{\mathrm{T}}(t = t_1) & \cdots & \underline{\underline{\mathbf{W}}}^{\mathrm{T}}(t = t_L), \end{bmatrix}^{\mathrm{T}} \tag{6.16}$$

where $L$ is the number of snapshots taken. In this example, $L = 3$, constituting a total of 12 measurements. Figure 6.2 shows how $\alpha$ and $\beta$ affect each of the discussed metrics, while Table 6.1 shows 49 different resulting polyhedra that the analyzing vectors enclose.

In order to test how these metrics perform when presented with non-Gaussian noise, a simulation was run, where a Stokes scene was measured with multiplicative noise, where noise variance grows with signal strength. In order to ignore the high frequency error and focus on the underlying structure, the scene was low-pass-filtered to include the lowest $\frac{1}{8}$ of frequencies to judge the overall shape of the reconstruction. The Structural Similarity (Wang et al. (2004)) was then adapted to calculate how similar the structures between the reconstruction and the object are. The metric is defined as

$$\mathrm{SSIM}(x, y) = \frac{(2\mu_x\mu_y + c_1)(2\sigma_{xy} + c_2)}{(\mu_x^2 + \mu_y^2 + c_1)(\sigma_x^2 + \sigma_y^2 + c_2)}, \tag{6.17}$$

where $\mu_x$ and $\mu_y$ are the averages of $x$ and $y$, respectively, $\sigma_x^2$ and $\sigma_y^2$ are the standard deviations of $x$ and $y$, respectively, $\sigma_{xy}$ is the covariance of $x$ and $y$ and $c_1$ and $c_2$ are additional variables to stabilize division. In order to collapse SSIM into a single number, all the values of SSIM are averaged,

$$\mathrm{MSSIM} = \frac{1}{N_x N_y} \sum_{x=1}^{N_x} \sum_{y=1}^{N_y} \mathrm{SSIM}(x, y), \tag{6.18}$$

which effectively assumes a rectangular window. This selection might not be ideal, but given the artificially periodic nature of the scene, it should suffice for the purposes of this exercise. Additionally, since a Stokes image contains four images corresponding to each of the parameters, the scores need to be combined. This is done by multiplying MSSIMs of each of the channels, i.e.,

$$\text{MSSIM}_{\text{total}} = \text{MSSIM}_{s_0} \cdot \text{MSSIM}_{s_1} \cdot \text{MSSIM}_{s_2} \cdot \text{MSSIM}_{s_3}. \tag{6.19}$$

The results presented in Table 6.2 show how it is less than ideal to repeat optimal four measurements three times. The reconstruction resulting from a polyhedron that constructs an icosahedron provides an advantage. The system that produces that distribution consisted of two rotating retarders with $\delta_1 = \pi$, $\delta_2 = \pi - \arccos\left(\frac{1}{\sqrt{3}}\right)$, with rotation rate of the second retarder being double that of the first and the initial offset from $\text{LR}_1$ to $\text{LR}_2$ being $\frac{\pi}{32}$. The microgrid that produces described by $\alpha = \frac{1}{2}\tan\left(\frac{2}{1+\sqrt{5}}\right)$ and $\beta = 0$.

## 6.4 Conclusion

In this chapter, the class of overdetermined Stokes polarimeters was investigated. It was found that ensuring measurement diversity in their relation to the spherecity of the enclosed polyhedron, parallels a reconstruction that is favorable under non-additive noises, while provides no disadvantage when dealing with additive noise. This discussion provides the most minimal of gains and should only be considered if the conditions absolutely require an overdetermined kind of system. Nonetheless, it is interesting to discover how various polarimetric quantities relate to the geometrical fundamentals.
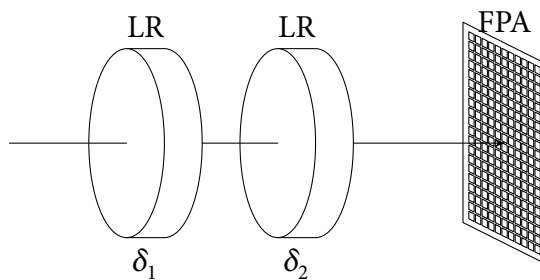
(a) System Layout
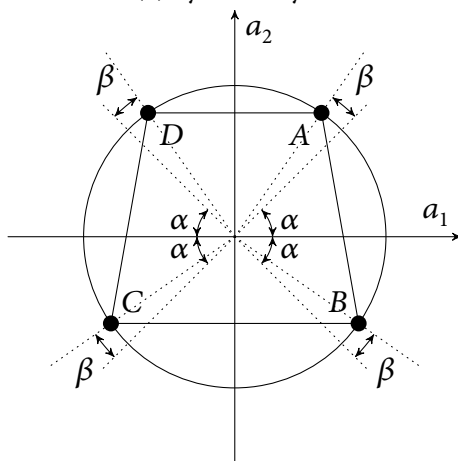


(b) Measurements plotted on top of Poincaré $a_1/a_2$ plane (equator)
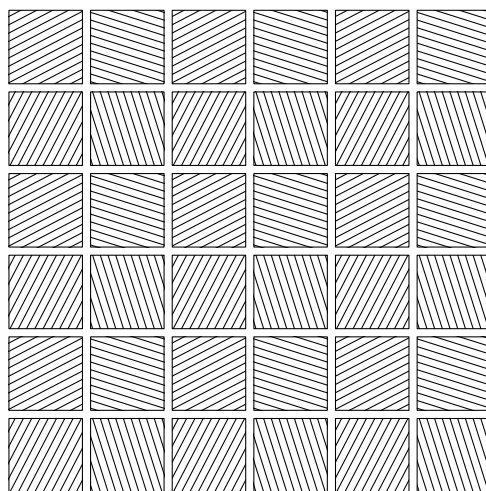


(c) Resultant FPA detector polarizer orientation pattern

Figure 6.1: System configuration. The measurements and the custom microgrid pattern are shown with $\alpha = 22.5°$ and $\beta = 5°$.
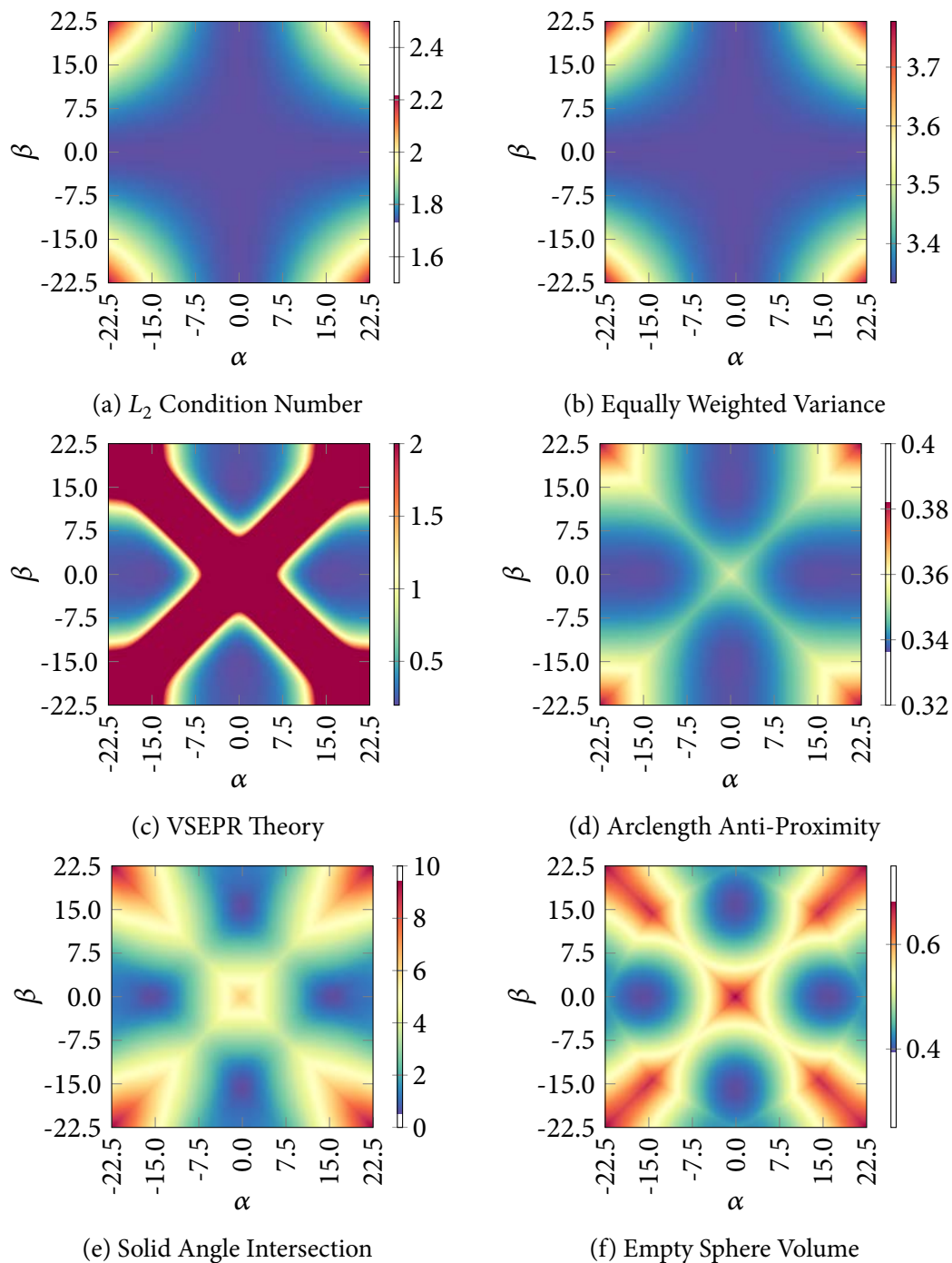
(a) $L_2$ Condition Number

(b) Equally Weighted Variance

(c) VSEPR Theory

(d) Arclength Anti-Proximity

(e) Solid Angle Intersection

(f) Empty Sphere Volume

Figure 6.2: Simulation results for $\alpha/\beta$ sweep for two established metrics, as well as four newly introduced diversity-based metrics.

Table 6.1: Representative samples of measurement Poincaré structures. Colored with SAI.
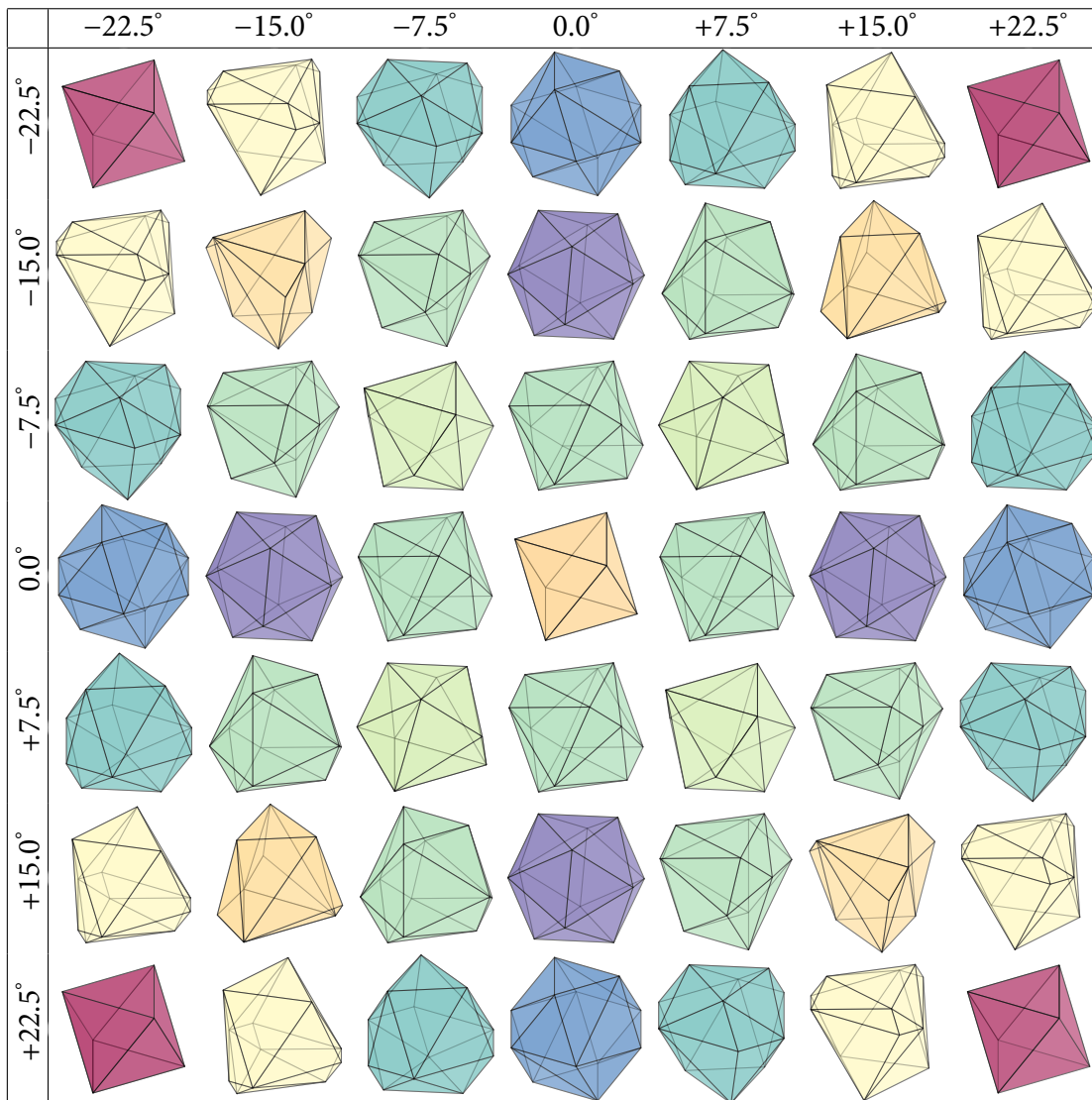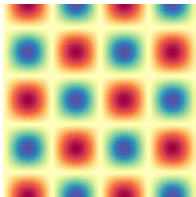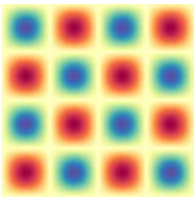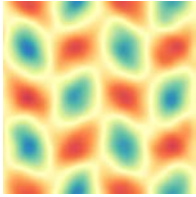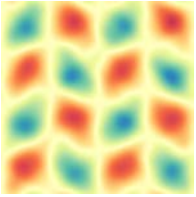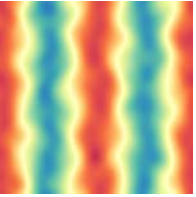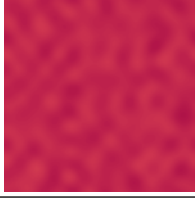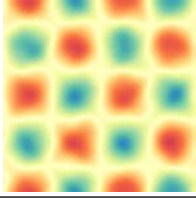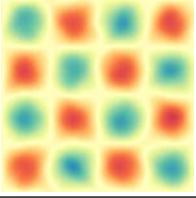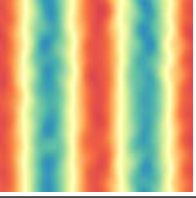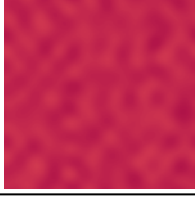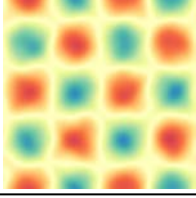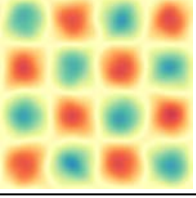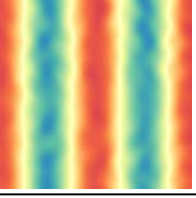
Table 6.2: Reconstruction of different polyhedra under multiplicative noise. To gauge the underlying shape, simulated images are filtered to include only the bottom $\frac{1}{8}$ frequencies.

| | $s_0$ | $s_1$ | $s_2$ | $s_3$ | MSSIM |
|---|---|---|---|---|---|
| Original Scene | | | | | 1.000 |
| | | | | | 1.000 |
| | | | | | 1.000 |
| | | | | | 1.000 |
| | | | | | **1.000** |
| $3 \times$ Tetrahedron | | | | | 0.703 |
| | | | | | 0.641 |
| | | | | | 0.741 |
| | | | | | 0.801 |
| | | | | | **0.267** |
| Cuboctahedron | | | | | 0.734 |
| | | | | | 0.851 |
| | | | | | 0.861 |
| | | | | | 0.875 |
| | | | | | **0.471** |
| Icosahedron | | | | | 0.760 |
| | | | | | 0.868 |
| | | | | | 0.869 |
| | | | | | 0.888 |
| | | | | | **0.509** |

CHAPTER 7

CLOSING REMARKS

This dissertation investigated the classes of channeled Mueller matrix polarimeters in Chapter 3, partial Mueller matrix polarimeters in Chapter 4, and the combined class of channeled-partial Mueller matrix polarimeters in Chapter 5. The manuscript opened with relevant pieces of prior work by Tyo, Sabatke and Twietmeyer that introduced concepts by which to evaluate Stokes and Mueller polarimeters and later broached the subject of channeled systems that were popularized by Oka, as well as the subject of partial systems that were introduced by Hoover and Tyo. The work in this dissertation recognized the patterns in the generalized versions of the systems pertaining to each class to construct the necessary framework by which to evaluate each given system. Overall, this dissertation introduces several novel concepts listed below.

First, Chapter 3 introduced measurement matrix $\underline{\underline{\mathbf{Q}}}$, which related Fourier domains of the modulations instead of intensities. Besides maximizing quality of reconstruction by virtue of using linear system manipulations rather than arithmetic derived by hand, a completely parallel concept of EWV was developed for channeled systems, which lead to the discovery of optimal channeled systems as well as the discovery that even very superficial changes to existing designs can improve their performance drastically. Introduction of FPM as a way to calculate the coefficients of delta functions within the Fourier transform of an arbitrary multiplication of sinusoidal functions trivialized the construction of the measurement matrix. Additionally, leveraging an already optimal system, a redistribution of error between reconstruction channels is possible. The completely generalized nature of this development serves incredible utility to any further work intending to design a channeled polarimeter

Second, Chapter 4 developed the concepts of structured decomposition and the reconstructables matrix, which provide immediate insight into system's space coverage and yield a pMMP basis that allow the formation of ten classes of pMMP systems. The evaluation of

such systems was aided by timely introduction of space mapping through auxiliary matrices developed as a part of structured decomposition. Instead of looking at noise variances within Mueller elements, pMMPs need to consider the noise variance within the linear combination of elements of interest. Additionally, the analysis needs to include the proximity of the reconstructed linear combination to the intended one. The prescription given within this scheme achieves these needs and enables the user to design a pMMP given the provided basis, as well as leaves enough pieces in place for the user to construct a basis of their own based on different assumptions.

Third, Chapter 5 combined the concepts of Chapters 3 and 4 and paved way for a new topic of channeled-partial Mueller matrix polarimeters. Combining the $\underline{\underline{\mathbf{Q}}}$ formalism with structured decomposition allowed for proper evaluation of noise resilience and space coverage of channeled partial system. Though the analytic form of the decomposition is not provided here, it is computed instead. The downside is that the space coverage is not trivial to calculate, thereby increasing the optimization time and potentially reducing the applicability of inserting the c-pMMP design constraints into the hypothetical measurement selection step. The derivation of the analytical form of structured decomposition for c-pMMPs will have to be a part of a future discussion.

Fourth, Chapter 6 introduced polarimeter performance evaluation metrics, the optimization of which showed that diverse geometrical distributions of analyzing vectors provide an improved reconstruction for overdetermined Stokes polarimeters under a non-additive noise model.

APPENDIX A

DIVERSITY OPTIMIZATION

This appendix shows results of a number of optimization runs that minimized the metrics introduced in Chapter 6, which attempt to make the design of Stokes polarimeters with $N > 4$ to produce more accurate results under non-additive noise. As before, the optimization minimized each of the metrics using MATLAB's built-in genetic algorithm. However, this time the optimization variables were not constrained to any particular system design and instead represented free-floating fully-polarized analyzing vectors on the surface of the Poincaré sphere.

Figures A.1, A.2, A.3 and A.4 show results for VTR, AAP, SAI and ESV, respectively. Despite the final optimizations results settling in rotated distributions with respect to one another, several connections can be made. For $N = 4$, $N = 6$, $N = 12$ and $N = 24$, VTR, AAP and SAI produce the same solutions corresponding to the identifiable polyhedrons of tetrahedron, octahedron, icosahedron and snub cube, respectively. ESV agrees with the other metrics for $N = 4$, $N = 6$, $N = 12$, but provides a different solution for $N = 24$. It is valuable to know the underlying geometric properties of each of those polyhedrons because a design parameter will often be related. For example, to achieve a tetrahedral distribution, one needs to use a rotating retarder with retardance, $\delta = \arccos\left(-\frac{2}{3}\right)$, which is not disconnected from the dihedral angle of the tetrahedron, $\varphi = \arccos\left(\frac{1}{3}\right)$. To achieve a cuboctahedral distribution, one needs a typical microgrid with a rotating retarder with retardance, $\delta = \arccos(-\frac{1}{\sqrt{3}})$, which is equal to the dihedral angle of the cuboctahedron. The same retarder can be used to achieve a regular icosahedral distribution by changing the polarizers' orientations in the microgrid such that the default four measurements create a rectangle within the Poincaré sphere's equator that has the aspect ratio of the golden ratio. Within the notation of custom microgrid designs that is introduced in Chapter 6, that means $\alpha = \frac{1}{2}\arctan\left(\frac{2}{1+\sqrt{5}}\right)$ and $\beta = 0$.

(a) $N = 4$

(b) $N = 5$

(c) $N = 6$

(d) $N = 7$

(e) $N = 8$

(f) $N = 9$

(g) $N = 10$

(h) $N = 11$

(i) $N = 12$

(j) $N = 16$

(k) $N = 20$

(l) $N = 24$
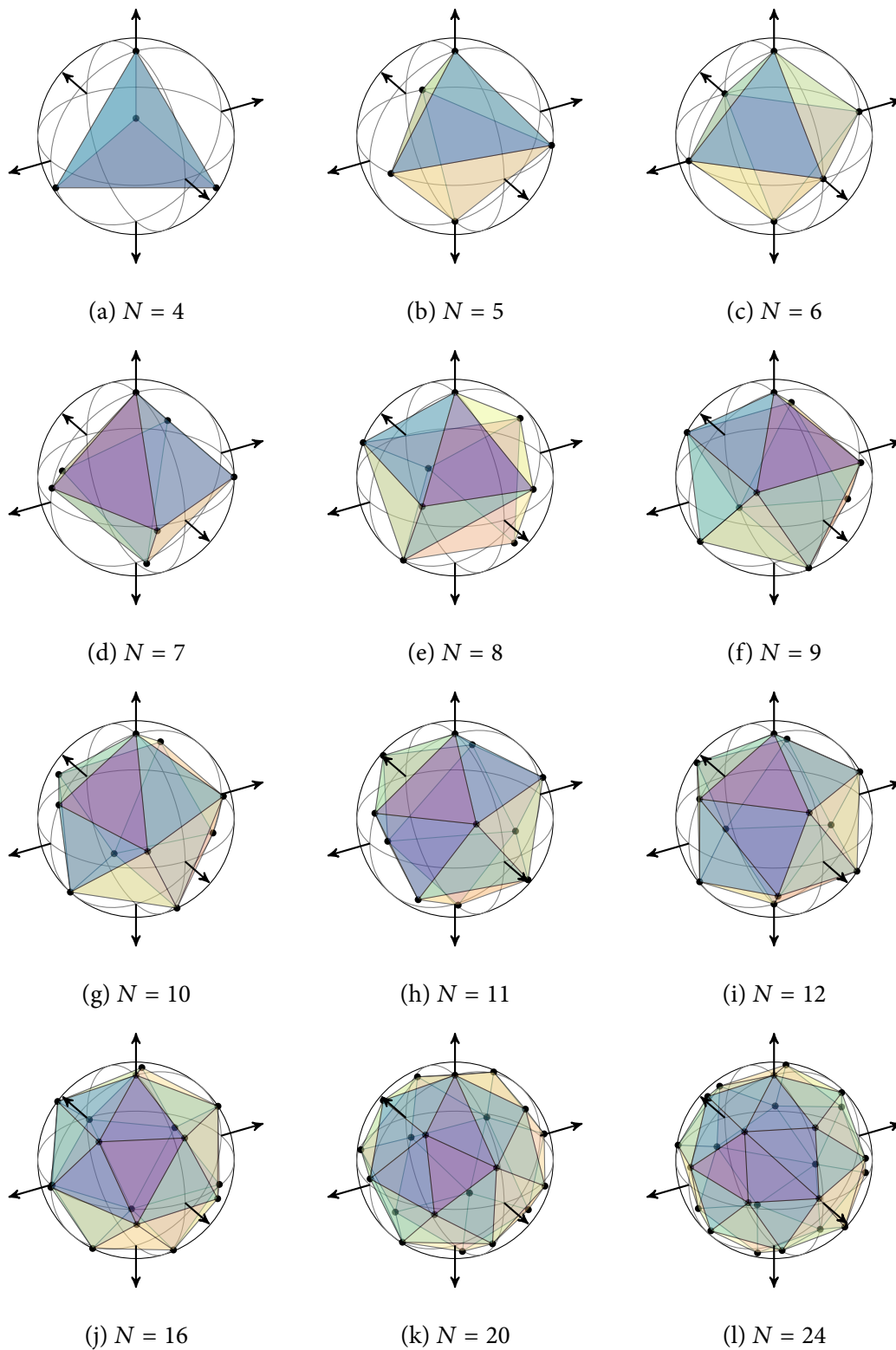
Figure A.1: Optimizations with different number of measurements for VTR.

(a) $N = 4$

(b) $N = 5$

(c) $N = 6$

(d) $N = 7$

(e) $N = 8$

(f) $N = 9$

(g) $N = 10$

(h) $N = 11$

(i) $N = 12$

(j) $N = 16$

(k) $N = 20$

(l) $N = 24$
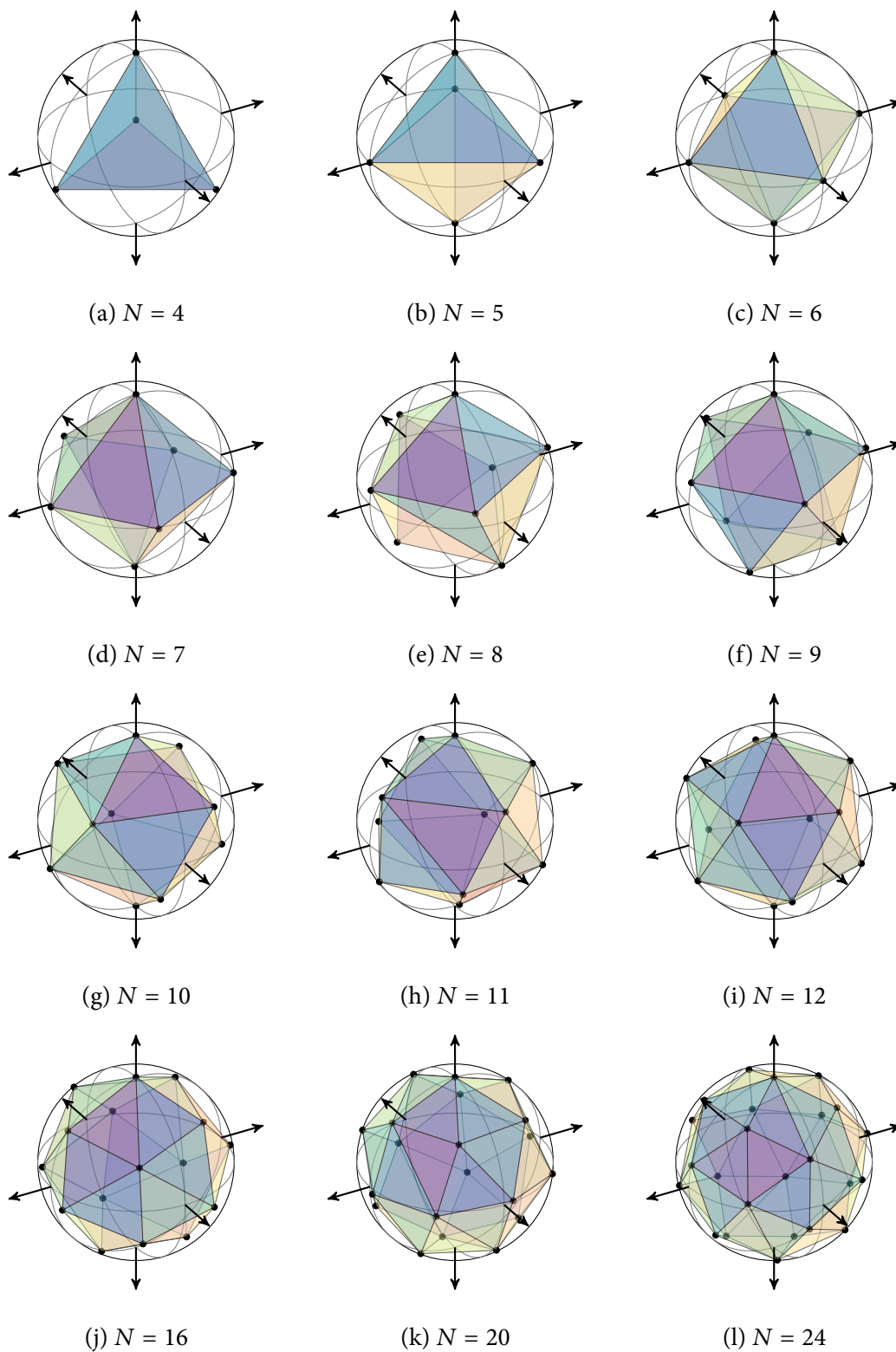
Figure A.2: Optimizations with different number of measurements for AAP.

(a) $N = 4$

(b) $N = 5$

(c) $N = 6$

(d) $N = 7$

(e) $N = 8$

(f) $N = 9$

(g) $N = 10$

(h) $N = 11$

(i) $N = 12$

(j) $N = 16$

(k) $N = 20$

(l) $N = 24$
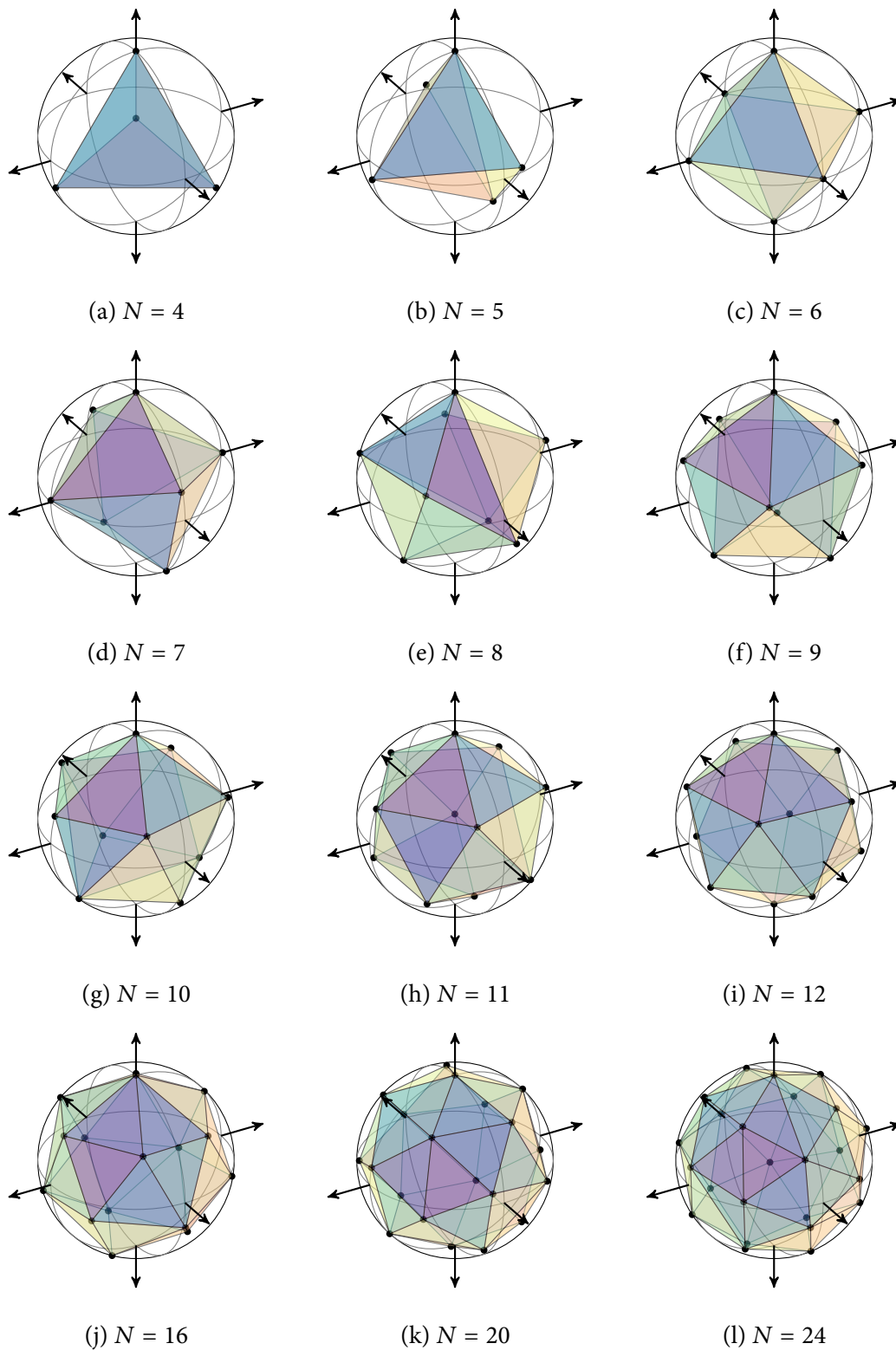
Figure A.3: Optimizations with different number of measurements for SAI.

(a) $N = 4$

(b) $N = 5$

(c) $N = 6$

(d) $N = 7$

(e) $N = 8$

(f) $N = 9$

(g) $N = 10$

(h) $N = 11$

(i) $N = 12$

(j) $N = 16$

(k) $N = 20$

(l) $N = 24$

Figure A.4: Optimizations with different number of measurements for ESV.

# REFERENCES

Alenin, A. S. and J. S. Tyo (2012). Task-specific snapshot Mueller matrix channeled spectropolarimeter optimization. In *8364*, pp. 836402–836402–13. SPIE, Bellingham, WA. doi:10.1117/12.921911.

Alenin, A. S. and J. S. Tyo (2014). Generalized channeled polarimetry. *J. Opt. Soc. Am. A*, **31**(5), pp. 1013–1022. doi:10.1364/JOSAA.31.001013.
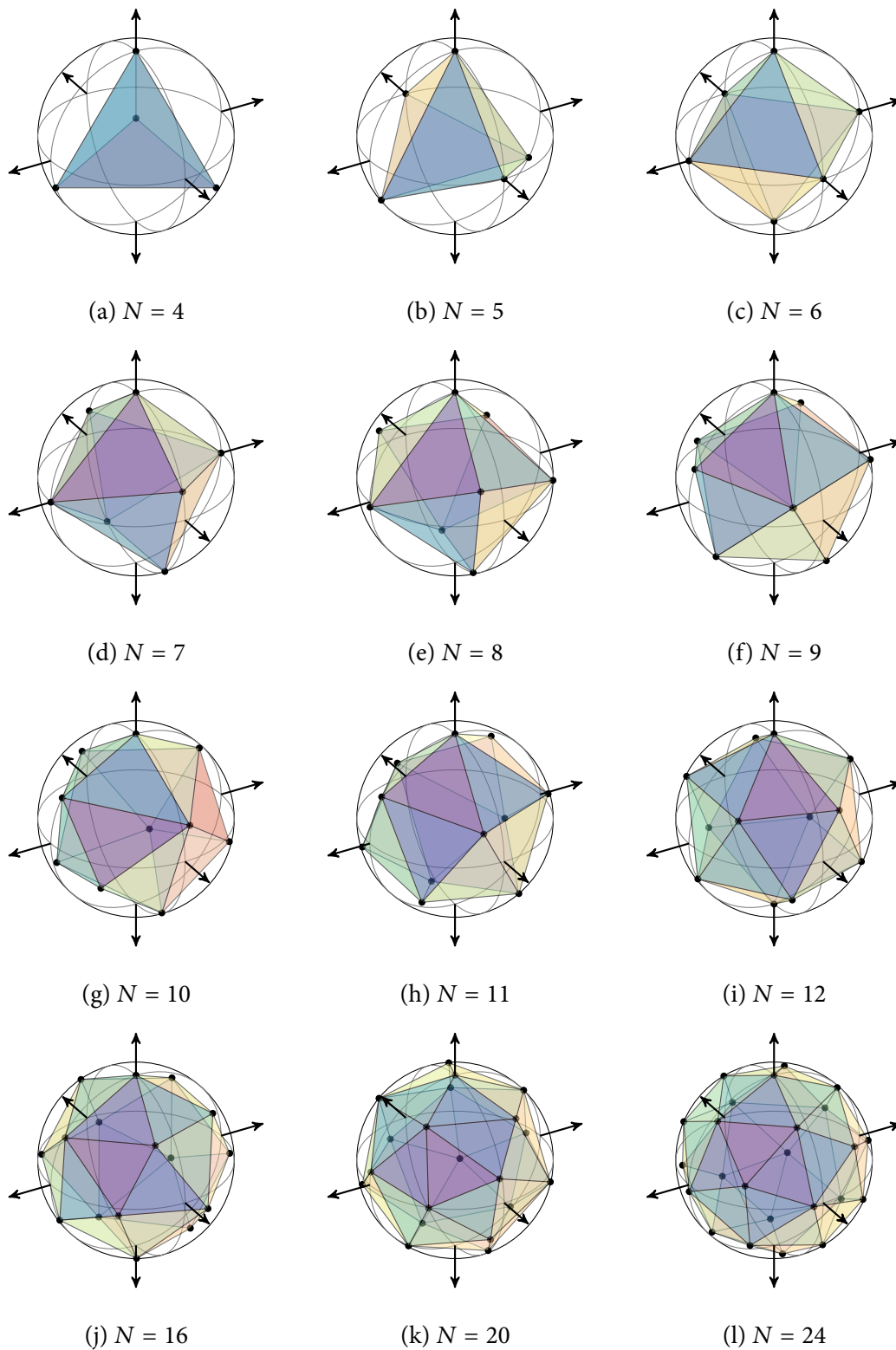
Anna and Goudail (2012). Optimal Mueller matrix estimation in the presence of Poisson shot noise. *Opt. Express*, **20**, pp. 21331 – 21340.

Anna, G., F. Goudail, and D. Dolfi (2011a). Optimal discrimination of multiple regions with an active polarimetric imager. *Opt. Express*, **19**(25), pp. 25367–25378. doi:10.1364/OE.19.025367.

Anna, G., F. Goudail, and D. Dolfi (2011b). Polarimetric target detection in the presence of spatially fluctuating Mueller matrices. *Opt. Lett.*, **36**(23), pp. 4590–4592. doi:10.1364/OL.36.004590.

Baldwin, A. M. (2004). *Mueller matrix imaging for skin cancer detection*. Master's thesis, Texas A&M University.

Cheng, L. J., M. Hamilton, C. Mahoney, and G. Reyes (1994). Analysis of AOTF Hyperspectral Imaging. In Iverson, A. (ed.) *Proceedings of SPIE Vol. 2231, Algorithms for Multispectral and Hyperspectral Imagery*, pp. 158–166. SPIE, Bellingham, WA.

Chipman, R. A. (2005). Metrics for Depolarization. In Shaw, J. A. and J. S. Tyo (eds.) *Proceedigns of SPIE vol. 5888: Polarizaiton Science and Remote Sensing II*, p. 58880L. SPIE, Bellingham, WA.

Chipman, R. A. (2009a). *Handbook of Optics*, volume 1, chapter 15, pp. 15.1–15.41. McGraw Hill, third edition.

Chipman, R. A. (2009b). Mueller Matrices. In *Handbook of Optics*, volume 1, chapter 14, pp. 14.1–14.44. McGraw Hill, third edition.

Chipman, R. A. (2009c). Polarimetry. In *Handbook of Optics*, volume 1, chapter 15, pp. 15.1–15.46. McGraw-Hill, third edition.

Cloude, S. R. (1986). Group theory and polarization algebra. *Optik (Stuttgart)*, **75**, pp. 26–36.

Cloude, S. R. and E. Pottier (1996). A review of target decomposition theorems in radar polarimetry. *Geoscience and Remote Sensing, IEEE Transactions on*, **34**(2), pp. 498–518.

Compain, E. and B. Drevillon (1998). Broadband division-of-amplitude polarimeter based on uncoated prisms. *Appl. Opt.*, **37**(25), pp. 5938–5944. doi:10.1364/AO.37.005938.

Compain, E., S. Poirier, and B. Drevillon (1999). General and self-consistent method for the calibration of polarization modulators, polarimeters, and Mueller-matrix ellipsometers. *Appl. Opt.*, **38**, pp. 3490–3502.

Diner, D. J., A. Davis, B. Hancock, G. Gutt, R. A. Chipman, and B. Cairns (2007). Dual-photoelastic-modulator-based polarimetric imaging concept for aerosol remote sensing. *Appl. Opt.*, **46**(35), pp. 8428–8445. doi:10.1364/AO.46.008428.

Dubreuil, M., S. Rivet, B. L. Jeune, and J. Cariou (2007). Snapshot Mueller matrix polarimeter by wavelength polarization coding. *Opt. Express*, **15**(21), pp. 13660–13668. doi:10.1364/OE.15.013660.

Gil, J. J. (2007). Polarimetric characterization of light and media. *Eur. Phys. J. Appl. Phys.*, **40**(1), pp. 1–47. doi:10.1051/epjap:2007153.

Golub, G. H. and C. F. van Loan (1983). *Matrix Computations*, chapter 2, pp. 11–29. Johns Hopkins University Press, Baltimore, MD.

Goudail, F. (2009). Comparative study of the best achievable contrast in scalar, Stokes and Mueller images. In *First NanoCharm workshop on advanced polarimetric instrumentation*. NanoCharm: Multifunctional Nanomaterials Characterization Exploiting EllipsoMetry and Polarimetry.

Goudail, F. and A. Beniere (2009). Optimization of the contrast in polarimetric scalar images. *Opt. Lett.*, **34**, pp. 1471 – 1473.

Goudail, F. and J. S. Tyo (2011). When is polarimetric imaging preferable to intensity imaging for target detection? *J. Opt. Soc. Am. A*, **28**(1), pp. 46–53. doi:10.1364/JOSAA.28.000046.

Hagen, N., K. Oka, and E. L. Dereniak (2007). Snapshot Mueller matrix spectropolarimeter. *Opt. Lett.*, **32**(15), pp. 2100–2102. doi:10.1364/OL.32.002100.

Hoover, B. G. and J. S. Tyo (2007). Polarization components analysis for invariant discrimination. *Appl. Opt.*, **46**(34), pp. 8364–8373. doi:10.1364/AO.46.008364.

Hotelling, H. (1936). Relations between two sets of variates. *Biometrika*, **28**, pp. 312 – 377.

Jacques, S. L., J. R. Roman, and K. Lee (1999). Imaging Superficial Tissues With Polarized Light. *Lasers in Surgery and Medicine*, pp. 119–129.

Knyazev, A. and M. Argentati (2002). Principal Angles between Subspaces in an A-Based Scalar Product: Algorithms and Perturbation Estimates. *SIAM Journal on Scientific Computing*, **23**(6), pp. 2008–2040. doi:10.1137/S1064827500377332.

Kudenov, M. W., M. J. Escuti, N. Hagen, E. L. Dereniak, and K. Oka (2012). Snapshot imaging Mueller matrix polarimeter using polarization gratings. *Opt. Lett.*, **37**(8), pp. 1367–1369. doi:10.1364/OL.37.001367.

Kudenov, M. W., N. A. Hagen, E. L. Dereniak, and G. R. Gerhart (2007). Fourier transform channeled spectropolarimetry in the MWIR. *Opt. Express*, **15**(20), pp. 12792–12805. doi:10.1364/OE.15.012792.

LaCasse, C. F., R. A. Chipman, and J. S. Tyo (2011a). Band limited data reconstruction in modulated polarimeters. *Opt. Express*, **19**(16), pp. 14976–14989. doi:10.1364/OE.19.014976.

LaCasse, C. F., T. Ririe, R. A. Chipman, and J. S. Tyo (2011b). Spatio-temporal modulated polarimetry. *SPIE*, pp. 81600K–81600K–11. doi:10.1117/12.896068.

LaCasse, C. F., J. S. Tyo, and R. A. Chipman (2012). Role of the null space of the DRM in the performance of modulated polarimeters. *Opt. Lett.*, **37**(6), pp. 1097–1099. doi:10.1364/OL.37.001097.

Lemaillet, P., S. Rivet, and B. L. Jeune (2008). Optimization of a snapshot Mueller matrix polarimeter. *Opt. Lett.*, **33**(2), pp. 144–146. doi:10.1364/OL.33.000144.

Lu, S.-Y. and R. A. Chipman (1996). Interpretation of Mueller matrices based on the polar decomposition. *J. Opt. Soc. Am. A*, **13**, pp. 1106–1113.

Mazonka, O. (2012). Solid Angle of Conical Surfaces, Polyhedral Cones, and Intersecting Spherical Caps. *ArXiv e-prints*.

Noble, H. D. and R. A. Chipman (2012). Mueller matrix roots algorithm and computational considerations. *OX*, **20**, pp. 17 – 31.

Oka, K. and T. Kaneko (2003). Compact complete imaging polarimeter using birefringent wedge prisms. *Opt. Express*, **11**(13), pp. 1510–1519. doi:10.1364/OE.11.001510.

Oka, K. and T. Kato (1999). Spectroscopic polarimetry with a channeled spectrum. *Opt. Lett.*, **24**(21), pp. 1475–1477. doi:10.1364/OL.24.001475.

Okabe, H., M. Hayakawa, H. Naito, A. Taniguchi, and K. Oka (2007). Spectroscopic polarimetry using channeled spectroscopic polarization state generator (CSPSG). *Opt. Express*, **15**(6), pp. 3093–3109. doi:10.1364/OE.15.003093.

Ossikovski, R. (2009). Analysis of depolarizing Mueller matrices through a symmetric decomposition. *J. Opt. Soc. Am. A*, **26**, pp. 1109 – 1118.

Ossikovski, R. (2011). Differential matrix formalism for depolarizing anisotropic media. *Opt. Lett.*, **36**, pp. 2330 – 2332.

Ossikovski, R. (2012). Differential and product Mueller matrix decompositions: a formal comparison. *Opt. Lett.*, **37**, pp. 220 – 222.

Peltzer, J. J., P. D.Flammer, T. E. Furtak, R. T. Collins, and R. E. Hollingsworth (2011). Ultra-high extinction ratio micropolarizers using plasmonic lenses. *Opt. Express*, **19**, pp. 18072 – 18079.

Sabatke, D. S., M. R. Descour, E. L. Dereniak, W. C. Sweatt, S. A. Kemme, and G. S. Phipps (2000). Optimization of retardance for a complete Stokes polarimeter. *Opt. Lett.*, **25**(11), pp. 802–804. doi:10.1364/OL.25.000802.

Twietmeyer, K. M. and R. A. Chipman (2008). Optimization of Mueller matrix polarimeters in the presence of error sources. *Opt. Express*, **16**(15), pp. 11589–11603. doi: 10.1364/OE.16.011589.

Tyo, J. S. (2002). Design of Optimal Polarimeters: Maximization of Signal-to-Noise Ratio and Minimization of Systematic Error. *Appl. Opt.*, **41**(4), pp. 619–630. doi:10.1364/AO. 41.000619.

Tyo, J. S., D. L. Goldstein, D. B. Chenault, and J. A. Shaw (2006). Review of passive imaging polarimetry for remote sensing applications. *Appl. Opt.*, **45**(22), pp. 5453–5469. doi:10. 1364/AO.45.005453.

Tyo, J. S., M. P. Rowe, J. E. N. Pugh, and N. Engheta (1996). Target detection in optically scattering media by polarization-difference imaging. *Appl. Opt.*, **35**(11), pp. 1855–1870. doi:10.1364/AO.35.001855.

Tyo, J. S., Z. Wang, S. J. Johnson, and B. G. Hoover (2010). Design and optimization of partial Mueller matrix polarimeters. *Appl. Opt.*, **49**(12), pp. 2326–2333. doi:10.1364/ AO.49.002326.

Vaughn, I., B. G. Hoover, and J. S. Tyo (2012a). Classification using active polarimetry. In Chenault, D. B. and D. H. Goldstein (eds.) *Proc. SPIE vol. 8364: Polarization Measurement, Analysis, and Remote Sensing X*, p. 83610S. SPIE, Bellingham, WA.

Vaughn, I. J. and B. G. Hoover (2008). Noise reduction in a laser polarimeter based on discrete waveplate rotations. *Opt. Express*, **16**, pp. 2091 – 2108.

Vaughn, I. J., B. G. Hoover, and J. S. Tyo (2012b). Classification using active polarimetry. *SPIE*, pp. 83640S–83640S–13. doi:10.1117/12.922623.

Wang, Z., A. Bovik, H. Sheikh, and E. Simoncelli (2004). Image quality assessment: from error visibility to structural similarity. *Image Processing, IEEE Transactions on*, **13**(4), pp. 600–612. ISSN 1057-7149. doi:10.1109/TIP.2003.819861.

Wang, Z., J. S. Tyo, and M. M. Hayat (2007). Data interpretation for spectral sensors with correlated bands. *J. Opt. Soc. Am. A*, **24**, pp. 2864 – 2870.

Zhao, Y., L. Zhang, and Q. Pan (2009). Spectropolarimetric imaging for pathological analysis of skin. *Appl. Opt.*, **48**(10), pp. D236–D246.